Magnetic Hydrogels for Bone Tissue Engineering

Emma Jackson
BSc (Hons)

Submitted in fulfilment of the requirements
for the degree of Doctor of Philosophy (PhD)

Centre for the Cellular Microenvironment
Advanced Research Centre
School of Molecular Biosciences
College of Medical, Veterinary & Life Sciences
University of Glasgow

September 2025

University of Glasgow

Abstract

Bone injuries represent a significant healthcare burden, with autograft transplantation currently considered the gold standard treatment. However, autografts are limited by donor site morbidity, pain, and restricted availability. Bone tissue engineering offers a promising alternative by combining stem cells, biomaterial scaffolds, and bioactive cues to promote regeneration. External stimulation, such as magnetic fields, has also emerged as a strategy to enhance bone healing and tissue regeneration. In this study, a magnetic hydrogel model was developed to explore the therapeutic potential and mechanisms of magnetic field stimulation in bone repair.

The effects of static and dynamic magnetic fields on mesenchymal stromal cells (MSCs) were first investigated, with a focus on osteogenic differentiation, mechanotransductive signaling and pathway activation. A magnetic hydrogel was then fabricated using gelatin methacryloyl (GelMA) combined with iron oxide magnetic nanoparticles (MNPs). MSCs were encapsulated either as dispersed cells or in spheroid form. The hydrogels were extensively characterised, demonstrating tunable mechanical properties, appropriate porosity, and long-term biocompatibility. To evaluate osteogenic potential, MSC-laden hydrogels were exposed to either static or dynamic magnetic fields for up to 28 days. Gene expression, mineralisation and hydrogel stiffness were assessed as markers of osteogenic activity and environmental remodeling. Stemness markers were also monitored to evaluate stem cell renewal capacity.

Intermittent static magnetic field (SMF) exposure for 1 hour per day emerged as the most effective regime, enhancing osteogenic gene expression in 2D culture, and further evidenced within 3D cultures in combination with MNPs showing increased mineralisation. Incorporation of MNPs or application of intermittent SMF also led to stiffening of the hydrogel model over 28 days. In addition, intermittent SMF exposure supported stem cell population renewal over 28 days

This thesis demonstrates that GelMA based magnetic hydrogels, particularly under intermittent SMFs can direct MSC osteogenesis. These findings support the development of smart biomaterials that integrate biophysical cues for next generation bone tissue engineering and regenerative medicine.

Table of Contents

List of Tables

List of Figures

Acknowledgements

My first and most heartfelt thank you goes to my wonderful supervisor, Catherine. Thank you so much for giving me this opportunity. Life has been something of a rollercoaster over the last few years, and I could not have made it through without your kind support and guidance. It has been a true pleasure working with you over the past four years, and I will sincerely miss your unwavering enthusiasm. Thank you for believing in me.

Thank you to my second supervisor, Manuel, for your support and guidance. Thank you to my unofficial supervisor, Matt, for giving me many opportunities to contribute meaningfully and make my voice heard. Thank you to Claire for your friendship, kindness, and encouragement over the years.

I would like to thank lifETIME-CDT including my lovely cohort, the extended family, and the administrative and management teams. You created a friendly, encouraging space for researchers to grow and support each other. I used to believe that doing a PhD would be a lonely journey, and I was delighted to be proven wrong. A big thank you to my most reluctant friend Conor — meeting you was a highlight of my PhD. Thank you for being the sensible voice to my occasionally overly emotional one. Thank you to Michelle, Aimee, and Monika for your friendship along the way. Likewise, thank you to all the friends I've made in CeMi — there are, fortunately, too many to mention. A big thank you to Monica for all your help and technical advice, and most importantly for your friendship throughout it all.

Thank you to Gloria, Arantxa, and Jose for your guidance and support during my placement in Valencia. Thank you for being so kind and helping me navigate a new research lab. A big thank you to Juan for helping me feel a little more at home, and for your weekend trip recommendations!

Thank you to the Anatomy department. I began my academic journey with you, and I am grateful to have been able to continue that journey with you as an educator. Thank you for your ongoing support, for the many opportunities you've offered for career development, and for always being a safe haven.

To my friend Lou: as you said, "the road from strangers to friends has never been shorter". You consistently lifted my spirits with your infectious smile, strategic coffee breaks, and

shenanigans. I'm glad to report that not even SwissAir prices have kept us apart over the last few years.

To my lovely sister, Sarah, who has endured enough of my tears and self-doubt for a lifetime: thank you for believing in me every time I forgot to believe in myself. I'm lucky to have you. And a huge thank you to my sister's boyfriend, Alastair, what a job you've had being my personal mechanic, dog sitter, plumber, removal service, and life coach. Thank you for being an absolute legend.

Thank you to my family for all the support, meals, laundry, dog sitting, car repairs, home moves, and everything you've provided over the years. Thank you, Mum, for being my rock. To Katie and Rosie, thank you for always being up for shenanigans and reminding me how important it is to laugh.

Julia and Siobhan, two thirds of the aptly named Ovary Achievers, I feel incredibly lucky not only to have met you both during my undergraduate years but also to have maintained such a wonderful friendship with you since. You both mean the world to me. Thank you for always being my biggest fangirls.

To Watson, my lab partner, who may never understand how his joyful greeting at the door after long workdays made my worries melt away. Your goofy smile and wagging tail are the best kind of therapy.

And to my wonderful nana, who sadly isn't here to witness the conclusion of this journey, this thesis is dedicated to you. I miss you more than words can express, but I know you would be proud.

Authors Declaration

I hereby declare that the research reported within this thesis is my own work, unless otherwise stated, and that at the time of submission is not being considered elsewhere for any other academic qualification.

Emma Jackson
September 2025

This work was supported by Science Foundation Ireland 18/EPSRC-CDT/3583 and the Engineering and Physical Sciences Research Council EP/S02347X/1. CÚRAM is co-funded by the European Regional Development Fund and Science Foundation Ireland under Ireland's European Structural and Investment Fund Grant Number 13/RC/2073

Abbreviations

ACAN - Aggrecan

ALP – Alkaline phosphatase

ANG1 – Angiopoietin-1

BCP – Biphasic calcium phosphate

β-TCP – β-tricalcium phosphate

BMP – Bone morphogenetic protein

BMPR – Bone morphogenetic protein receptors

BMU - Basic multicellular unit

BSA - Bovine serum albumin

BSP - Bone sialoprotein

BTE – Bone tissue engineering

C/EBPα - CCAAT/enhancer-binding protein alpha

ccRCC – Renal carcinoma cell

CDKs – Cyclin-dependent kinases

cDNA – Complementary DNA

CI - Carbonyl iron

Col1/Col1A1 – Collagen 1 / Collagen type 1 alpha 1

COX-2 - Cyclooxygenase 2

CREB - cAMP response element binding protein

DNA – Deoxyribonucleic acid

DKK1 –Dickkopf-1

DMEM – Dulbecco's Modified Eagles Medium

DMF – Dynamic magnetic field

DMSO - Dimethyl sulfoxide

DPSCs – Dental pulp stem cells

ECM – Extracellular matrix

EDTA - Ethylenediaminetetraacetic acid

EPCs – Endothelial progenitor cells

ERK – Extracellular signal-regulated kinase

EthD-1 – Ethidium homodimer-1

EVs – Extracellular vesicles

FAK – Focal adhesion kinase

FBS – Foetal bovine serum

Fe_3O_4 – Iron oxide (Magnetite)

FGF – Fibroblast growth factor

FLRT – Fibronectin leucine-rich transmembrane protein

FOXP1 – Forkhead box p1

GelMA – Gelatin methacryloyl

GFAP – Glial fibrillary acidic protein

GFP – Green fluorescent protein

HA - Hydroxyapatite

HES – Hairy/enhancer-of-split

HEY - Hairy/enhancer-of-split related with YRPW

HIF1/2 – Hypoxia-inducible factors 1 and 2

hMSCs – Human mesenchymal stromal cells

HSC – Haematopoietic stem cell

ID1/2 – Inhibitors of DNA binding 1 / 2

IFC – Integrated fluidic circuit

IL – Interleukin

IFN-β – Interferon-β

ITGA5 – Integrin α-5

LAP - Lithium phenyl-2,4,6-trimethylbenzoylphosphinate

LDV – Laser doppler vibrometry

LIPU – Low intensity pulsed ultrasound

LEF1 - Lymphoid enhancer binding factor

MA-CS - Methacrylated chondroitin sulphate

MAF – MAF bZIP transcription factor

MAPK - Mitogen-activated protein kinase

MCP-1 - Monocyte chemoattractant protein-1

MicroCT – Micro Computed Tomography

MMP - Matrix metalloproteinase

MNP – Magnetic nanoparticle

MRSA - Methicillin-resistant *Staphylococcus aureus*

MSC – Mesenchymal stromal cell

MSK – Musculoskeletal

MSX2 – msh homeobox 2

MyoD – Myogenic differentiation 1

NdFeB – Neodymium iron boron

NICD – Notch intracellular domain

NTA – Nanoparticle tracking analysis

OA – Osteoarthritis

OCN – Osteocalcin

OGM – Osteogenic media

OI – Osteogenesis imperfecta

OPG – Osteoprotegerin

OPN – Osteopontin

PBS – Phosphate-buffered solution

PCL - Polycaprolactone

PDLA - Poly(DL-lactic acid)

PDLSCs - Periodontal ligament stem cells

PDMS – Polydimethylsiloxane

PEG - Polyethylene glycol

PGA - Polyglycolic acid

PL – Platelet lysate

PLA - Poly(lactic acid)

PLLA - Poly(L-lactic acid)

PPARγ - Peroxisome proliferator-activated receptor gamma

PVA - Polyvinyl alcohol

PVP - Poly(vinyl pyrrolidone)

Rac1 – Ras-related C3 botulinum toxin substrate 1

Rb - Retinoblastoma protein

RhoA - Ras homolog gene family, member A

RNA – Ribonucleic acid

RT-qPCR - Real-time quantitative reverse transcription polymerase chain reaction

RUNX – Runt-related transcription factor

SASP – Senescence-associated secretory phenotype

SDF-1 - Stromal cell derived factor-1

SEM - Scanning electron microscope

SFRP1 – Secreted frizzled-related protein 1

SHH – Sonic hedgehog

SMF – Static magnetic field

SOX - SRY-box transcription factor

SQUID – Superconducting quantum interference device

STA – Specific target amplification

subVOIs – Sub Volumes of Interest

SVF – Stromal vascular fraction

TAZ - PDZ binding motif

TCF – T cell factor family

TEM – Transmission electron microscopy

TF – Transcription factor

TIMP - Tissue inhibitor of metalloproteinases

TLE – Transducin-like enhancer of split proteins

TRPS – Tunable resistive pulse sensing

TRPV4 - Transient receptor potential vanilloid 4

UV – Ultraviolet

VEGF - Vascular endothelial growth factor

VSM – Vibrating sample magnetometer

WCA – Water contact angle

YAP – Yes-associated Protein

Chapter 1: Introduction

1.1 Bone Tissue

Bone tissue is a calcified connective tissue in the human body, providing essential structural and physiological functions. It comprises most of the skeletal system, with the remaining composed primarily of cartilage (Drake, et al., 2024). Bone tissue is characterised by a mineralised intracellular matrix, rich in type 1 collagen fibres which is continuously maintained and remodelled by a co-ordinated network of cells, including osteoblasts, osteoclast, osteocytes, and haematopoietic cells (Selvaraj, et al., 2024). Osteoblasts are responsible for bone formation; osteoclasts mediate bone resorption, osteocytes function as mechanosensory and haemopoietic cells contribute to immune and haematological functions within the bone marrow niche (Clarke, 2008; Hart, et al., 2020).

1.1.1 Anatomy, Embryology and Physiology

1.1.1.1 Anatomy

Bone tissue can be broadly classified by its density and internal structure into spongy or compact bone, also known as trabecular and cortical bone respectively (Lin & Kang, 2021). Spongy bone is light and porous, while compact bone is dense and rigid (Drake, et al., 2024). Spongy bone is formed from a lattice like network of beams, called trabeculae, filled with bone marrow, which plays an important role in the formation of haematopoietic tissue, such as erythrocytes and platelets (Taichman, 2005). Spongy bone is found at the end of long bones and within other bones such as vertebrae. Compact bone contains subunits called osteons, or Harversian systems. Each osteon consists of a concentric layer of calcified matrix, called lamellae, which surrounds a cylindrical canal (Haversian canal). These canals contain blood vessels, facilitating the transportation of nutrients and removal of waste products, and nerves which regulate skeletal homeostasis (Kim, et al., 2015).

Bones are further classified into one of five categories, based on their morphology: long, short, flat, irregular and sesamoid (Drake, et al., 2024). Long bones, also called tubular bones, are longer than they are wide, and consist of a shaft (diaphysis) with two bulky ends (epiphyses). Most long bones are found in upper and lower limbs. The diaphysis is primarily composed of compact bone with areas of spongy bone at the distal and proximal epiphyses (Augusto, et al., 2022; Clarke, 2008). In contrast, short bones have near equal dimensions of length, width and thickness. The carpals and tarsals of hands and feet respectively are short

bones. Short bones are primarily spongy bone surrounded by a thin layer of compact bone. Flat bones are thin, flattened and often curved, and these bones compose most of the cranium and facial bones (Clarke, 2008). Their structure is two parallel layers of compact bone with an enclosed thin layer of spongy bone. Irregular bones include those that do not fit into previously mentioned categories. Their structures vary but are often consist primarily of spongy bone encased within layer of compact bone (Drake, et al., 2024). The final classification is a unique small round and nodular shaped bone, called sesamoid bones, usually formed within tendons at joints. These classifications divide bones based on their morphology, however despite their variation in shape, all bones are comprised of compact and spongy bone in varying proportions (Clarke, 2008; Drake, et al., 2024).

1.1.1.2 Embryology

The embryological origins of the skeletal system are diverse, arising from three primary lineages: neural crest cells, somites and the lateral plate mesoderm (Hirasawa & Kuratani, 2015)**.** These progenitor populations give rise to mesenchymal precursors, differentiating into bone forming cells through highly regulated developmental pathways. The process of bone formation, or osteogenesis, begins between weeks six and seven of embryonic development and continues until mid-twenties (Drake, et al., 2024)**.** Two district mechanisms govern ossification: Intramembranous ossification and Endochondral ossification (Nowlan, et al., 2010).

Intramembranous ossification occurs directly from mesenchymal tissue and is primarily responsible for the formation of flat bones. During intramembranous ossification, mesenchymal stromal cells (MSCs) differentiate to osteoblasts and mineralise tissue by secreting osteoid (**Figure 1-1A**) (Jabalee, et al., 2013; Nowlan, et al., 2010). Endochondral ossification instead produces bone tissue by gradually replacing hyaline cartilage and is the predominate mechanism in the formation of long bones (Nowlan, et al., 2010). It begins when MSCs differentiate into chondrocytes that lay down hyaline cartilage. In long bones, primary ossification develops in the diaphysis, with secondary ossification occurring in the later stages in the epiphyses (**Figure 1-1B**) (Mackie, et al., 2008; Drake, et al., 2024).

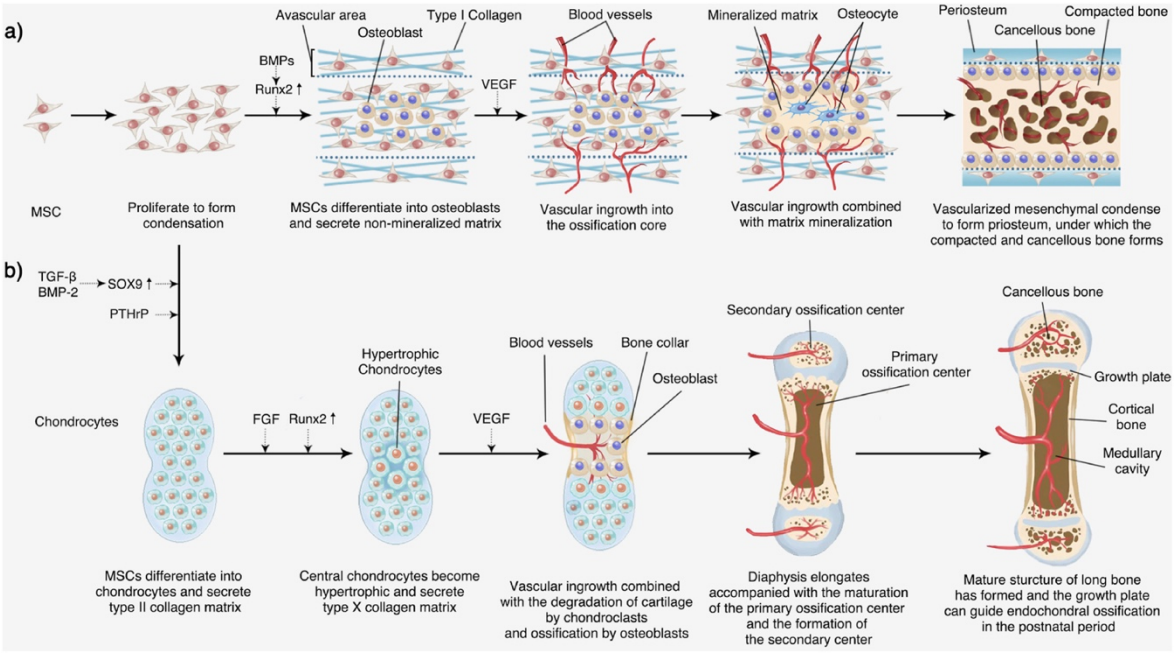

Figure 1-1: Schematic of embryonic bone development (ossification)

Embryonic bone development occurs via two distinct processes: [A] Intramembranous ossification: mesenchymal stromal cells (MSCs) condense and differentiate into osteoblasts. These osteoblasts secrete osteoid (unmineralised matrix), initiating mineralisation. This is followed by vascular invasion, bringing nutrients and additional progenitor cells. Subsequently the matrix becomes mineralised, resulting in formation of mature bone tissue. [B] Endochondral ossification: MSCs differentiate into chondrocytes, forming a hyaline cartilage template. The cartilage undergoes proliferation and hypertrophy, followed by matrix calcification and vascular invasion into the diaphysis, leading to formation of a primary ossification centre. Over time the process expands towards along the bone, leading to mature long bone development. Figure reproduced from Zhu, et al., 2021.

1.1.1.3 Physiology

Bone tissue performs several essential functions within the body, critical to maintaining homeostasis and enabling movement. As part of the skeletal system, bone provides structural support by forming a stable framework for the attachment of muscles, tendons and ligaments (Shea & Miller, 2005). In addition, it protects vital organs including the central nervous system enclosed within the cranium and the vertebral column, and the cardiovascular and respiratory system protected by the rib cage. Bones also facilitate movement, or locomotion, acting as levels for muscles to pull on enabling motor function (Su, et al., 2019). Bone tissue acts as a dynamic reservoir for essential minerals, primarily calcium and phosphate which are critical to various physiological processes (Shea & Miller, 2005). Mineral homeostasis is maintained through co-ordinated activity of osteoclasts which reabsorb bone to release minerals, and osteoblasts which deposit minerals during bone formation (Al-Bari & Mamun, 2020; Hart, et al., 2020). Haematopoiesis, the continuous production of blood cells, occurs

in red bone marrow within spongy bone. This process originates with a multipotent precursor haematopoietic stem cell (HSC), and gives rise to erythrocytes, leukocytes and platelets, supporting immune function and nutrient transfer (Doulatov, et al., 2012).

Bone is a highly dynamic tissue, with the ability to adapt to mechanical forces. Osteocytes, acting as mechanosensors, detect mechanical strain and co-ordinate bone remodelling (Clarke, 2008). In addition to its structural and metabolic functions, bone possesses the ability to repair and remodel itself in response to damage, including microcracks. This process is known as bone remodelling and is tightly regulated cellular response of osteoclasts and osteoblasts, cooperating as a basic multicellular unit (BMU), with osteoclasts reabsorbing damaged bone and osteoblasts responsible for laying down new healthy bone through differentiation into osteocytes and new lining cells (**Figure 1-2**) (Hart, et al., 2020).

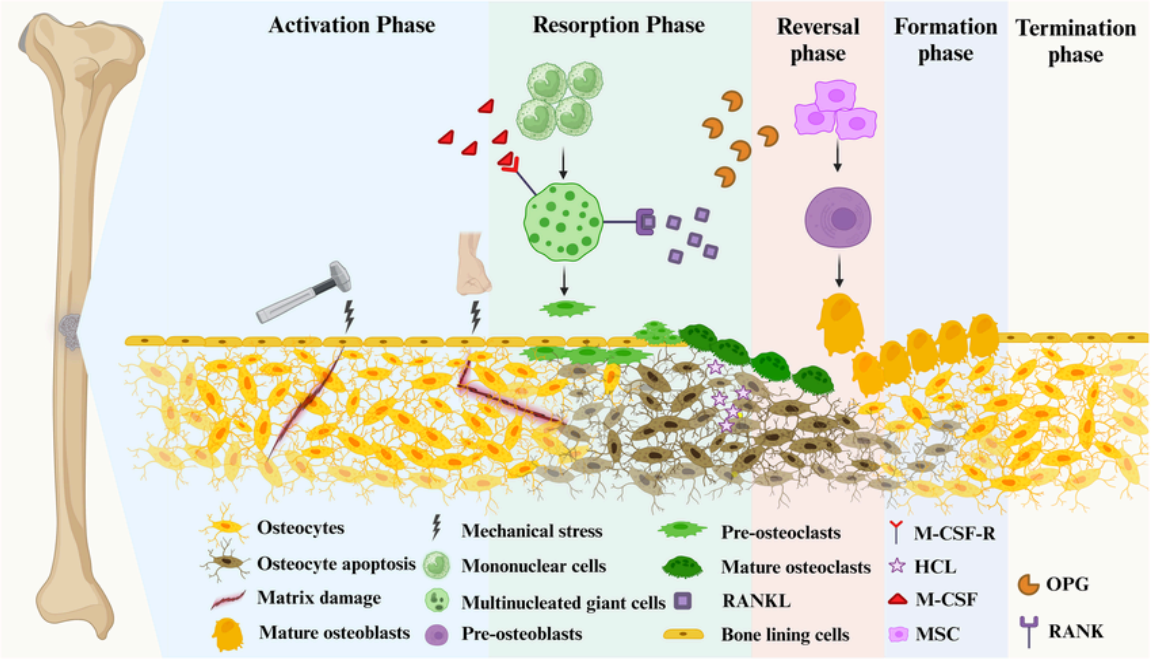

Figure 1-2: Schematic of the bone remodelling cycle

Starting on the left (activation phase), bone resorption by osteoclasts is triggered by microdamage, such as microcracks or trauma, which induces osteocyte apoptosis. Signals released by apoptotic osteocytes and bone lining cells recruit osteoblast precursors to the site of damage. Following resorption, osteoblasts are recruited to initiate the formation phase, and then some differentiate into new lining cells or become embedded within the matrix as osteocytes. Figure reproduced from Li, et al., 2024.

1.1.2 Bone Disease and Defects

Like other tissues in the body, bone tissue is susceptible to damage and defects resulting from a variety of conditions. Musculoskeletal (MSK) disorders are considered the leading

cause of disability worldwide, with treatment costs rapidly increasing. In 2021, the global burden of treatment for MSK disorders cost in excess of $96 billion, with costs expected to increase as the population ages (Guan, et al., 2025). Bone diseases and defects can either be congenital, present at birth, or acquired later in life. Bone tissue is the second most transplanted tissue worldwide, second only to blood transplants (Hochmann, et al., 2023). More than 4 million operations occur globally each year to treat bone defects caused by fractures, critical size defects, skeletal malformation & abnormalities, surgical/tumour excision and disease (International Osteoporosis Foundation, 2021). **Table 1-1** outlines some of the common diseases and conditions affecting bone tissue, alongside their associated socioeconomic costs.

Congenital bone disorders, such as osteogenesis imperfecta (OI), can often lead to progressive degeneration and deformity of the skeletal system, due to a genetic mutation impacting the synthesis of, or ability to modify and transport, type I collagen. OI affects around 1 in 15,000 individuals with clinical presentations ranging from mild to severe phenotypes and affects collagen type I synthesis or processing (Selvaraj, et al., 2024). OI is characterised by low bone mass, reduced strength and an increased susceptibility of fractures often from mild trauma (Forlino, et al., 2012). The healthcare burden of OI is significant, with one study in Spain reporting an average annual treatment cost of €5,207 per patient for hospital admissions alone, with fractures being the most common cause of admission including a 7% readmission rate (Darbà & Marsà, 2020). The economic burden of OI extends beyond direct admission costs, and includes high healthcare usage, lost productivity, and significant out of pocket expenses with adults experiencing five times more missed work days and substantially higher unemployment rates than the general population (Hart, et al., 2024).

Acquired bone conditions include metabolic disorders, infections, benign and malignant tumours, and damage from trauma and toxic exposures. These conditions may result in structural degradation, impaired healing or the need for surgical removal of bone tissue. One of the most prevalent acquired diseases is osteoporosis, which is characterised by the loss of bone density due to deterioration of bone microstructure leaving tissue vulnerable to damage (Jaworski, 1981). While primarily associated with aging, osteoporosis can also be secondary to other chronic medical conditions or treatments, such as 1 diabetes (Wu, et al., 2022). Over 200 million people worldwide have some degree of osteoporosis, with over 50% of post-menopausal women developing secondary osteoporosis (Charde, et al., 2023). The cost of

managing osteoporotic fractures in Europe was €57 billion in 2019 (International Osteoporosis Foundation, 2021).

Condition	Pathophysiology	Socioeconomic Cost	References
Osteogenesis Imperfecta	Genetic mutation affecting type I collagen synthesis/ processing, leading to bone fragility and deformity	$5k per patient annually (hospital admissions)	(Darbà & Marsà, 2020; Hart, et al., 2024; Selvaraj, et al., 2024)
Osteoporosis	Loss of bone density and microstructure deterioration, increased fracture risk, often age related and can also be secondary to other diseases	$56.9 billion annually in Europe	(Charde, et al., 2023; International Osteoporosis Foundation, 2021; Jaworski, 1981; Wu, et al., 2022)
Osteoarthritis	Chronic joint disorder with cartilage denegation, subchondral bone changes and inflammation leading to joint dysfunction	£1 billion in UK (2010, no recent updated estimate)	(Allen, et al., 2022; Chen, et al., 2012; Kurtz, et al., 2009; World Health Organization, 2023)
Osteomyelitis	Bone infection, causes osteonecrosis, chronic infection and often requires surgical debridement	Varies on case, up to £100k per patient, estimated towards £1.5 billion over 5 years	(Pimentel de Araujo, et al., 2021; Restrepo, et al., 2014; Shirley, et al., 2018; Sia & Berbari, 2006)
Non-union fractures / critical size defects	Failure of bone healing after fracture, requiring surgical reconstruction and grafting, mainly affects weight bearing bones	Excess of £70k per patient in UK, $120k in Germany	(Ekegren, et al., 2018; Maisenbacher, et al., 2025; Nauth, et al., 2018; Schemitsch, 2017)
Osteosarcoma	Primary bone cancer linked to genetic mutations, mainly affects younger populations, often near knee/humerus	Cancer care costs the NHS over £6 billion in (2010), with lack of recent data on cancer treatment but acknowledgement that costs were estimated to grow by 9% each year	(Beird, et al., 2022; Brookes, et al., 2021; Eaton, et al., 2020; Wills, et al., 2024)
Secondary bone tumours	Metastasis from breast, prostate and lung cancers, causing bone destruction, pathological fractures. Often requires surgical resection and grafts		

Table 1-1: Summary of common bone diseases and defects

Overview of common bone disease and defects, their underlying pathophysiology and associated socioeconomic costs.

Another common age-related degenerative bone disorder is osteoarthritis (OA), a chronic joint disorder characterised by cartilage degeneration, subchondral bone changes and inflammation. OA affects an estimated 528 million individuals worldwide with progressive degeneration in joint structures (World Health Organization, 2023). In 2010 the UK estimated health costs to treat OA was over £1 billion (Chen, et al., 2012), but despite increasing prevalence and patient numbers, there are no recent comprehensive estimates on the economic burden available. While OA is a disease associated with mechanical wear and tear of the cartilage in joints over time, other contributing factors include obesity, genetic predisposition and it is also commonly observed following joint injury (Allen, et al., 2022). Subchondral bone undergoes continuous remodelling to maintain its structure and function; however abnormal mechanical loading due to loss of joint cartilage leads to increased turnover of subchondral bone (Hu, et al., 2021). Treatment for OA involves pharmacological treatment and self-management of risk factors, with surgical interventions reserved for patients who do not respond to other treatments. With an aging population, there has been significant increase in the demand for surgical intervention among individuals over 65 years old due to age related bone degeneration. Interestingly, joint replacements surgeries have also seen a noticeable increase in patients under 65 years old between 1993 and 2006, with projections indicating that younger patients may represent the majority of joint replacement demand by 2030 (Kurtz, et al., 2009).

Osteomyelitis is a serious bone infection that can arise following trauma, surgical procedures or through hematogenous spread from systemic infections. It is most commonly caused by *Staphylococcus aureus*, including methicillin-resistant strains (MRSA) (Pimentel de Araujo, et al., 2021), and can result in severe complications such as osteonecrosis (bone death), chronic infection and impaired skeletal growth (Pimentel de Araujo, et al., 2021; Restrepo, et al., 2014). Management often involves surgical debridement of infected and necrotic bone tissue leading to potential need for tissue grafts and reconstruction surgeries to restore structural integrity (Sia & Berbari, 2006). Cost of treatment varies between patients and subsequent reinfection, reaching around £100,000 in some incidences (Shirley, et al., 2018).

Damage to bone tissue such as fractures, blast injuries or infection, can lead to the formation of a critical size defect, defined as bone loss that will not heal spontaneously and requires surgical reconstruction. These are most commonly observed in non-union fractures, where a substantial loss of bone tissue necessitates the use of bone grafts (Schemitsch, 2017). Non-union most commonly affects weight bearing bones, such as femur and tibia. In the UK the cost of in-patient medical treatment and therapies for non-union exceeds £70,000 per patient

(Ekegren, et al., 2018). In Europe, a report from the German healthcare system identified treatment of non-union fractures as a significant healthcare burden, with socioeconomic cost over €120,000 per treated patient (Maisenbacher, et al., 2025). Long term, these patients often require additional operations, frequently with the limitation of reduced functionality in the reconstructed bone (Nauth, et al., 2018).

Bone, like other tissues, is susceptible to tumour development, both from primary and secondary cancers. Osteosarcoma is the most common primary tumour observed in bone tissue, most commonly presenting around the knee in lower limbs and humerus in the upper limbs (Beird, et al., 2022). It most often presents in younger patient populations, perhaps due to its link to periods of rapid bone growth. Although the exact cause is not fully understood, genetic alterations in tumour suppressor genes such as to TP53 and RB are present in most cases (Eaton, et al., 2020). In Europe, osteosarcomas account for 2-3% of cancer diagnoses each year in individuals under 24 years old (Beird, et al., 2022). In addition, bone is a frequent site for secondary (metastatic) tumours, from highly prevalent cancers such as breast, prostate and lung, which unfortunately spread to bone tissue (Brookes, et al., 2021). Secondary tumours can significantly affect bone integrity leading to pathological fractures and loss of function. Surgical tumour resection is a difficult balance between clear margins and preservation of surrounding structures. Depending on the extend of tissue removal, bone grafts may be necessary to restore function and promote regeneration (Brookes, et al., 2021).

With the global increase in life expectancy, age related bone disorders are becoming an escalating public health concern. Worldwide, healthcare services will be required to manage an increasing prevalence of conditions such as osteoporosis and OA that disproportionately affect older adults (Fehlings, et al., 2015). The rising demand for surgical interventions, including bone grafts, reflects the growing burden of degenerative diseases in aging populations (Kurtz, et al., 2009; Reginster & Burlet, 2006).

1.1.3 Graft Treatments for Bone Injury

Bone injuries, such as fractures, are very common with 178 million new fractures recorded in 2019, and a further 455 million cases experiencing complications relating to fractures. Since 1990, these cases have increasing by 33% and 70% respectively (GBD 2019 Fracture Collaborators, 2021). Non-union of fractures is a complication which often requires surgical intervention. The GBD 2019 Fracture Collaborates found non-union prevalences varies by

anatomical region, occurring in approximately 2.1% of radial fractures but up to 14% in tibia or fibula fractures (2019).

The treatment for non-union, or critical size defects commonly involves bone grafting. It is estimated that over two million bone graft surgeries occur annually worldwide, with a quarter performed in the US alone (Zhang, et al., 2019). Autografts, where bone tissue is harvested from the patient's own body, are considered the clinical 'gold standard' treatment (Turnbull, et al., 2018). Bone tissue is harvested from a donor site in a prior surgery, usually from the iliac crest of the pelvis. Using the patient's own bone tissue promotes excellent osseointegration of the graft and minimises immune rejection by providing biologically relevant grafts with the patient's own osteogenic cells. Autografts are also capable of supporting vascularisation (Amini & Lari, 2021). However, graft size is limited to preserve function at the donor site, and the additional harvest surgery is often associated with donor site morbidity and pain, and potential infection (Zhang, et al., 2019).

The alternative is the allograph transplant; utilising bone tissue harvested from cadavers. Allografts comprise one third of all bone grafts used in North America due to the variety of morphology available (Wang & Yeung, 2017). This donor tissue is more readily available, especially for larger grafts, and eliminates the need for a second surgery on the patient. Allografts are decellularised to reduce risk of infection; however, this process also diminishes their osteogenic capacity, and infection risk cannot be fully eliminated (Turnbull, et al., 2018). Furthermore, allograft transplants have a higher risk of immune rejection than autograft transplants and exhibit inferior healing compared to autografts. (Turnbull, et al., 2018; Wang & Yeung, 2017).

A less common approach is the use of xenograft transplants, essentially an allograft sourced form a different species. This method has largely been abandoned in orthopaedic practices due to high rates of graft failure and immune rejection (Amini & Lari, 2021). However, a systematic review by Amini & Lari (2021), suggests that decellularised xenograft derived bone scaffolds have shown promising results in *in vivo* studies demonstrating good biocompatibility, osteoconductivity and the ability to promote migration and proliferation in osteoblasts. In some cases, a total joint replacement may be necessary, especially for degenerative diseases of joint tissue such as OI. This surgical procedure involves replacing the damaged joint surfaces with prosthetic components to restore function, reduce pain and improve quality of life when conservative treatments have failed (Katz, 2006).

Tissue engineering is an evolving approach to bone regeneration that aims to overcome the limitations of traditional graft treatments. By utilising biomaterials scaffolds designed to promote new bone formation, tissue engineering seeks to restore tissue function more effectively and reduce complications associated with traditional grafts. These scaffolds can be combined with stem cells, and growth factors, to enhance osteogenesis and vascularisation, representing a promising frontier in regenerative medicine. The application of engineered scaffolds will be discussed in section *1.3 Bone Tissue Engineering*.

1.2 Mesenchymal Stromal Cells in Regenerative Medicine

MSCs are multipotent stromal cells that play a fundamental role in the development, maintenance and repair of skeletal tissues. As described in the process of osteogenesis during embryonic development, MSCs are the progenitor cells that give rise to osteoblasts during both intramembranous and endochondral ossification pathways (Drake, et al., 2024; Mackie, et al., 2008; Nowlan, et al., 2010). After birth, MSCs retain the capacity for self-renew and multilineage differentiation, giving rise to multiple cell types, including osteoblasts, chondrocytes and adipocytes. This plasticity underpins their essential role in bone homeostasis, facilitating continuous bone remodelling, adaption to mechanical stress and repair following injury (Sheng, 2015). Given their ability to differentiate into multiple skeletal cell types, and support tissue repair, MSCs hold great potential in regenerative medicine, particularly when combined with biomaterial scaffolds to enhance bone regeneration and restore function in damaged tissues.

Within this thesis, this cell population is referred to as mesenchymal stromal cells. The terminology used to describe these cells remains controversial with several variations of the acronym ‘MSC’ used in the literature, including ‘multipotent stem cells’ (Rodriguez, et al., 2005), ‘medicinal signalling cells’ (Leisengang, et al., 2022) alongside ‘mesenchymal stem cells’ (Meinel, et al., 2004) and ‘mesenchymal stromal cells’ (Meinel, et al., 2004). While the term ‘mesenchymal stem cell’ has been widely used, many researchers agree that ‘mesenchymal stromal cell’ is more appropriate as not all MSC populations in adult tissue meets the strict criterial for stemness *in vivo* (Yan, et al., 2025). Instead, these cells primarily mediate tissue repair through paracrine signalling and immunomodulatory effects (García-Bernal, et al., 2021; Kusuma, et al., 2017). Their stromal functions, rather than their stemness potential, form the rationale for referring to these cells as mesenchymal stromal cells (Bianco, 2014; Fitzimmons, et al., 2018).

Some researchers also question the term ‘mesenchymal’, proposing that this cell population relevant to the postnatal skeleton is more accurately described as a skeletal stem cell (SSCs) (Bianco & Robey, 2015). SSCs are tissue resident progenitor cells within the bone marrow that are capable of self-renewal and generating all the major skeletal linages (Bianco, 2014; Li, et al., 2022). Current evidence suggests that genuine stem cells for skeletal tissue are found in the bone marrow, whereas MSC like populations isolated from other tissues including periosteum, are biologically different and should not be automatically considered SSCs (Bianco & Robey, 2015; Viswanathan, et al., 2019). However, it is important to note that these strictly defined SSC populations represent only a small and highly specialised subset of cells and do not reflect the broader, heterogenous populations that are typically isolated and expanded for experimental or therapeutic use (Bianco & Robey, 2015; Li, et al., 2022). However, even within bone marrow sources, some degree of heterogeneity occurs within MSC populations. Bühring, et al. (2009), demonstrated that primary bone marrow MSCs from the same donor comprise at least two phenotypically and functionally distinct subsets. Furthermore, they reported that MSCs exhibit altered surface marker expression following *in vitro* culture compared with their *in vivo* counterparts (Bühring, et al., 2009).

The discussion on nomenclature is important as researchers advocate for the terminology to reflect the true biology of the cells rather than historical usage (Li, et al., 2022; Yan, et al., 2025). To address this ambiguity the International Society for Cellular Therapy (ISCT) proposed minimal criteria for defining mesenchymal stromal cells *in vitro* (Dominici, et al., 2006), but these do not completely resolve questions surrounding the *in vivo* identity, heterogeneity and true stem cell status, meaning the nomenclature remains debated (Yan, et al., 2025).

In 2006, a position paper from the ISCT outlined the minimal criterial for defining multipotent MSCs used in biomedical research (Dominici, et al., 2006). Three criteria were proposed:

1. **Plastic adherence**: they must have the ability to adhere and grow on standard tissue culture plastic.
2. **Surface antigen expression**: MSC populations must express CD105, CD73, CD90 and lack expression of CD45, CD34, CD14 or CD11b, CD79α, or CD19 and HLA class II.
3. **Multipotent differentiation:** MSCs must have ability to differentiate into adipogenic, chondrogenic and, osteogenic lineages *in vitro*

For use in biomedical research, MSCs can be isolated from a variety of adult connective tissues primarily bone marrow and periosteum, as well as adipose tissue, peripheral blood, menstrual blood, synovial membranes and dental pulp (Liu, et al., 2022). MSCs can also be harvested from muscles, tendons and ligaments with the latter being the least studied source of MSCs (Čamernik, et al., 2018). In additional, foetal sources such as the placenta, amniotic fluid, umbilical cord, and cord blood also provide rich reservoirs of MSCs (Han, et al., 2019).

MSCs isolated from non-bone marrow tissues often differ in terms of gene expression profile, differentiation bias and immunomodulatory capacity, highlighting that the term MSC encompasses a heterogenous group of stromal cell populations rather than a single universal cell type (Elahi, et al., 2016; Raicevic, et al., 2011; Xu, et al., 2017). In response to these issues, the ISCT issued an updated position statement to further clarify MSC nomenclature (Viswanathan, et al., 2019). Further criteria were proposed:

1. MSC origin should be stated in order to recognise tissue specific biological properties
2. MSCs should be interpreted as "stromal" cells unless rigorous evidence of stemness both *in vivo* and *in vitro* is demonstrated
3. MSCs should be accompanied by a robust matrix of functional assays appropriate to the intended therapeutic mechanism of action

For this reason, the term mesenchymal stromal cell is adopted throughout this thesis, as it acknowledges this heterogeneity and avoids implying properties of stemness that have not been definitively demonstrated *in vivo*. In the context of this thesis, all experiments were performed using human bone marrow derived MSCs (PromoCell GmbH, Germany). The cells were sourced commercially where they were verified to meet the ISCT minimal criterial, including differentiation potential and marker expression profile (PromoCell, 2026). As such, the MSC populations used in this work represent well defined bone marrow stromal cells, while acknowledging that MSCs derived from other sources may exhibit distinct biological properties.

1.2.1 MSC Ability to Regenerate and Repair Tissue

Focusing on bone tissue, MSCs contribute to bone regeneration and remodelling through multiple mechanisms. Most directly, they differentiate into osteoblasts, bone forming cells

responsible for matrix deposition and mineralisation. However, they also play a paracrine role, secreting bioactive factors and extracellular vesicles (EVs), that modulate bone environment. These include chemokines and cytokines that attract immune cells and support endothelial cells to form new vasculature. MSCs also exhibit a homing ability, migrating to sites of injury where they support tissue repair and modulate inflammation.

MSCs maintain a tightly regulated cell cycle to balance self-renewal with differentiation potential. However, during *in vitro* expansion, prolonged culture and increasing passage number can lead to a progressive decline in MSC functionality. This is largely governed by the retinoblastoma protein (Rb)/p16 and p53/p21 pathways, which play critical roles in controlling MSC proliferation, cell cycle progression and entry into senescence (**Figure 1-3**) (Turinetto, et al., 2016). Dysregulation of these pathways can impair regenerative capacity or lead to unwanted differentiation. Functional decline in MSCs is characterised by reduced proliferation, loss of multipotency and onset of cellular senescence (Liu, et al., 2022; Kwon, et al., 2021). Senescent MSCs exhibit morphological changes and molecular changes, including a flattened and enlarged morphology, typically following cell cycle arrest in the G1 phase (Li, et al., 2017). In addition to altered morphology, senescent MSCs adopt a pro-inflammatory senescence-associated secretory phenotype (SASP). This includes elevated secretion of cytokines and enzymes such as interlukin-6 (IL-6), interlukin-8 (IL-8), interferon-β (INF-β), monocyte chemoattractant protein-1 (MCP-1), matrix metalloproteinase-2 (MMP-2) and tissue inhibitor of metalloproteinases-2 (TIMP-2) (Kwon, et al., 2021). These factors can negatively influence the surrounding microenvironment, contributing to organ degeneration, accelerated aging and chronic inflammation (Liu, et al., 2022). This highlights the potential of MSCs in pathogenesis, particularly when cell cycle regulation is disrupted and senescence becomes dysregulated (Liu & Chen, 2020).

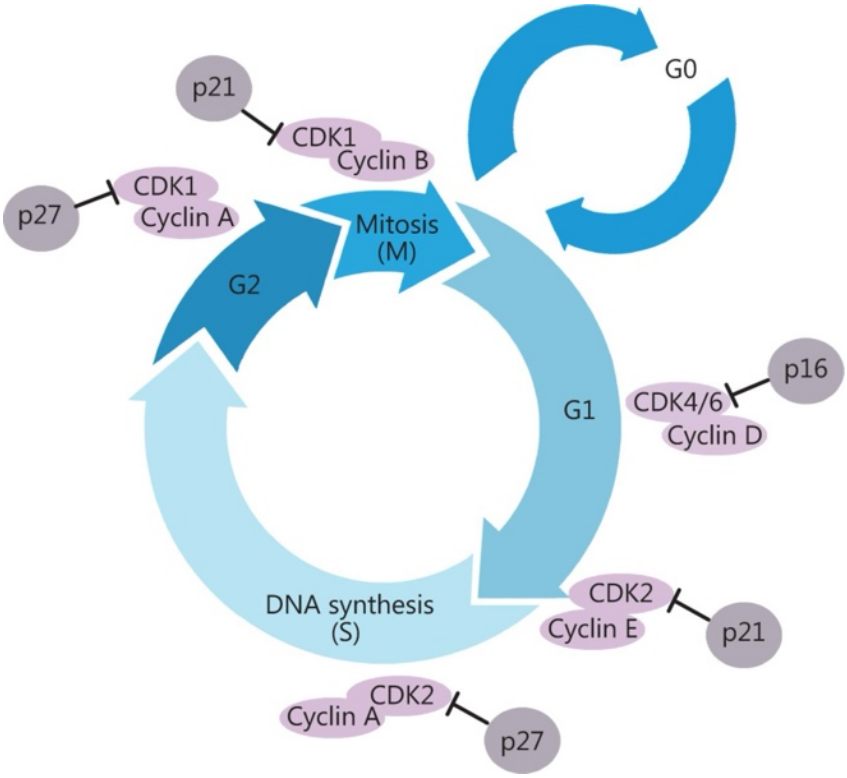

Figure 1-3: Schematic of the cell cycle

Summary of cell cycle, including phases (G1, S, G2, M, G0) showing key cyclin-dependent kinases (CDKs) and their regulatory proteins. The retinoblastoma protein (Rb)/p16 pathway inhibits CDK4/6 activity to enforce G1 phase arrest, preventing progression to S phase. Similarly, the p53/p21 pathway responds to cellular stress by activating p21, which inhibits CDK2 and halts the cell cycle at the G1/S checkpoint. Together these pathways tightly regulate mesenchymal stromal cell proliferation and senescence. Figure reproduced from Bai, et al., 2017.

While MSCs can significantly influence their local microenvironment through the secretion of bioactive factors, they are also highly responsive to external cues. The behaviour and fate of MSCs are strongly influenced by their local microenvironment, including mechanical stimuli, oxygen tension and biochemical signals (Bruels, et al., 2008; Krinner, et al., 2009). In tissue engineering and regenerative medicine, biomaterials are designed to mimic the extracellular matrix (ECM) providing both structural support and instructive cues that guide MSC behaviour (Leach & Whitehead, 2017). One of the most critical material properties is scaffold stiffness, which can direct lineage specific differentiation; stiffer substrates tend to promote osteogenic differentiation, while softer substrates favour adipogenic or neurogenic pathways (Yi, et al., 2022; Young, et al., 2014). Additionally surface topography and architecture in 2D can modulate MSC adhesion, morphology and cytoskeletal organisation, all of which influence downstream gene expression and differentiation. Disordered micropatterned nanostructures for example, have been shown to promote osteogenic commitment in MSCs (Dalby, et al., 2007).

MSCs migrate to sites of tissue damage and defects, where they play a crucial role in facilitating bone regeneration. MSCs can replenish local cell populations, and release trophic factors that suppress inflammation, promote re-epithelialisation and stimulate angiogenesis**.** A study has shown that conditioned media from human MSCs can enhance recruitment of MSCs to bone defect sites *in vivo*, as demonstrated in rat models (Osugi, et al., 2012). In cases of non-union fractures, insufficient migration of MSCs to the injury site has been identified as a key contributor to the formation of critical size defect (Oryan, et al., 2017). These findings highlight the importance of MSC presence and mobilisation in effective bone repair and regeneration.

Bone regeneration is intimately linked with angiogenesis, the formation of new blood vessels. MSCs play an active role in promoting angiogenesis, primarily through paracrine secretion of pro-angiogenic factors such as vascular endothelial growth factor (VEGF) and fibroblast growth factor-2 (FGF-2) which stimulate endothelial cell proliferation and new vessel formation (Ge, et al., 2017; Oryan, et al., 2017). Secretion of chemokine stromal cell derived factor-1 (SDF-1) is upregulated by MSCs in injured tissues and supports mobilisation of pro-angiogenic cells (Petit, et al., 2007). During bone repair, adequate vascularisation is essential to ensure proper nutrient delivery, oxygenation and waste removal. Beyond their individual contributions, MSCs have been shown to work synergistically with endothelial progenitor cells (EPCs) to enhance both angiogenesis and osteogenesis (Shi, et al., 2022). EPCs are mobilised into peripheral blood following fractures and trauma, secreting cytokines, VEGF and stromal SDF-1 to further support vascular repair. When introduced to a bone defect model, EPCs also upregulate bone morphogenetic protein 2 (BMP-2) expression suggesting a role in osteogenic differentiation (Li, et al., 2014). The crosstalk between MSCs and EPCs *via* paracrine signalling contributes to the coupling of angiogenesis and osteogenesis (Shi, et al., 2022; Xu, et al., 2020)

1.2.1.1 Osteogenic Differentiation

The differentiation of MSCs into osteoblasts for new bone formation is a tightly regulated process controlled by a complex network of signalling pathways and transcription factors (TFs) responding to mechanical and biochemical signalling (Liu, et al., 2023). The process occurs in four progressive stages: commitment, proliferation, maturation and mineralisation (**Figure 1-4**). As indicated in the commitment stage in **Figure 1-4**, MSCs possess multipotent differentiation potential, with commitment to myogenic, chondrogenic and adipogenic lineages regulated by the expression of key TFs: myogenic differentiation 1

(MyoD), SRY-box transcription factor 9 (SOX9) and Peroxisome proliferator-activated receptor gamma (PPARγ) respectfully (**Figure 1-4**). These linage specific pathways are further discussed in section *1.2.1.2 Commitment to Other Lineages*. The following text expands on **Figure 1-4** and described the key molecules and pathways involved in osteogenesis.

Osteogenic Differentiation: Runt-related TF 2 (RUNX2) is a key TF in in osteoblast differentiation (Lin & Hankenson, 2011), with support of other factors including downstream TF SP7/Osterix (Chan, et al., 2021). RUNX2 is considered the master TF, as it is present in the absence of SP7/Osterix, however SP7/Osterix expression is not observed in the absence of RUNX2 (Chan, et al., 2021; Liu, et al., 2023). RUNX2 expression begins in MSCs and is upregulated during MSC commitment and proliferation to pre-osteoblasts, with expression reducing in mature osteoblasts (Chan, et al., 2021). SP7/Osterix is responsible for proliferation of osteoprogenitor cells to osteoblasts, with support of β-Catenin promoting differentiation from pre-osteoblasts to osteoblasts (Liu, et al., 2020). TFs MAF bZIP (MAF) Msh homeobox 2 (MSX2) and Forkhead box P1 (FOXP1) regulate and promote MSC differentiation to osteoprogenitor cells, with the latter two also contributing to osteoblast calcification and mineralisation respectively (Liu, et al., 2023). Differentiation from pre-osteoblast to mature osteoblast is supported by β-Catenin, which also upregulates activating transcription factor 4 (ATF4) to promote osteoblast differentiation (**Figure 1-4**) (Liu, et al., 2023). Pre-osteoblasts begin adapting their environment by secreting alkaline phosphatase (ALP) and collagen, type I, alpha 1 (Col1A1). Expression of ALP and Col1A1 are induced with upregulation of both RUNX2 and SP7/OSX (Lang, et al., 2025). Expression of osteopontin (OPN), osteocalcin (OCN) and bone sialoprotein (BSP) are elevated in mature osteoblasts (Zhu, et al., 2024). The combination of these proteins works together to control bone mineralisation, OCN & BSP promote mineral deposition and strengthen bone matrix, while OPN prevents abnormal or excessive calcification ensuring proper bone formation (**Figure 1-4**) (Liu, et al., 2023).

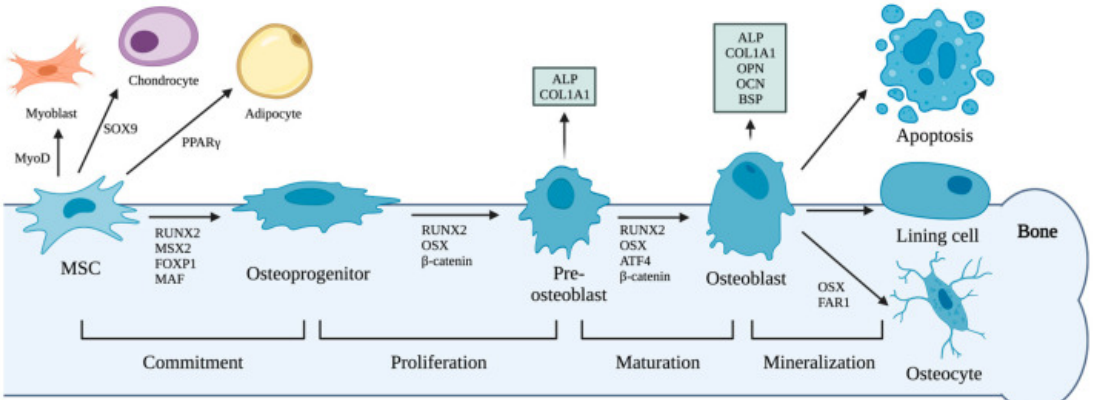

Figure 1-4: Schematic of mesenchymal stromal cell differentiation towards new bone formation

The process of osteogenesis occurs over four stages: commitment, proliferation, maturation and mineralisation. During these stages, mesenchymal stromal cells transition to osteoprogenitors, pre-osteoblasts, osteoblasts and finally osteocytes respectively. Transcription factors responsible for each stage are indicated by the arrows, and markers corresponding to (pre)osteoblast are indicated by boxes above the cells. Figure reproduced from Liu, et al., 2023.

Bone morphogenetic proteins (BMP): BMPs are proteins and growth factors, that belong to the transforming growth factor-β superfamily, playing a role in bone and cartilage formation; particularly BMP2, BMP6 and BMP9 which guide MSC differentiation into osteoblasts, with BMP4, BMP5, and BMP7 supporting both intramembranous and endochondral embryonic bone formation (Rahman, et al., 2015). BMPs receptors (BMPRs) activate the SMAD/1/5/8 signalling cascade which induces expression of RUNX2 (**Figure 1-5**), the master TF required for osteoblast differentiation (Chan, et al., 2021; Rahman, et al., 2015). Not all forms of BMP promote osteogenesis; BMP3 antagonises BMP2 activity, acting as inhibit to osteogenic BMPs by competing for downstream signalling within TGF-β and BMP pathways (Bahamonde & Lyons, 2001; James, 2013). *In vitro*, recombinant human BMP2 (rhBMP-2) is a commonly used osteogenic treatment (Lin & Hankenson, 2011; Matsumoto, et al., 2015).

Wnt/β-Catenin pathway: Activation of the Wnt/β-Catenin pathway enhances osteogenic differentiation while supressing adipogenic fate. β-Catenin accumulates and is translocated to cell nucleus, where it forms complexes with TCF/LEF TFs which drives osteogenic gene expression (**Figure 1-5**), including upregulation of RUNX2, supporting osteoblast maturation (Lin & Hankenson, 2011). Activation of Wnt/β-Catenin also enhances bone formation by increasing osteoprotegerin (OPG) expression and decreasing RANKL expression (Chan, et al., 2021). The shift in OPG/RANKL ratio inhibits osteoclast

differentiation and activity, preserving bone mass (James, 2013). Non-canonical Wnt ligands, such as Wnt5a, reinforce osteogenesis by supressing adipogenic TFs (D'Alimonte, et al., 2013; James, 2013; Lin & Hankenson, 2011).

Sonic Hedgehog (SHH) / Groucho/TLE axis: SHH signalling supports early osteogenic differentiation of MSCs acting through canonical SHH pathway mediated by Gli TFs. SHH activity enhances bone formation in part through a positive feedback loop with BMP signalling, where Gli-2 driven upregulation of BMP2 further amplifies osteogenic gene expression including ALP (James, 2013; Lin & Hankenson, 2011). SHH effects are not observed in committed osteoprogenitor cells, suggesting SHH plays its role early in fate development (James, 2013).

Notch Signalling: The role of notch signalling in osteogenesis is context dependent, with its effects varying based on cellular environment and stage of differentiation. Notch is a transmembrane receptor, that interacts with membrane bound ligands Delta or Jagged on adject cells (**Figure 1-5**) (Lin & Hankenson, 2011). Notch can promote proliferation of early osteoprogenitor cells or inhibit osteoblast differentiation by interfering with RUNX2 activity; notably through Hairy/enhancer-of-split (HES) and Hairy/enhancer-of-split related with YRPW (HEY) activity, which in turn inhibit RUNX2 expression (Lin & Hankenson, 2011). Furthermore, the dynamic approach of Notch activity means it will not necessarily enhance bone formation, despite supporting osteoblast maturation (Lin & Hankenson, 2011).

Pathway Crosstalk: In summary, osteoblast differentiation is orchestrated by multiple signalling pathways that ultimately regulate RUNX2 expression. BMP and canonical Wnt signalling both promote RUNX2 expression and activity, supporting early commitment of MSCs to an osteogenic lineage (Arya, et al., 2024). In canonical Wnt/β-Catenin signalling, β-Catenin nuclear translocation leads to TCF/LEF complexes, which drive expression of osteogenic genes. BMP signalling can also enhance Wnt signalling by upregulating Wnt ligands and receptors, while Wnt can stabilise SMAD proteins to prolong BMP activity (Arya, et al., 2024; Lin & Hankenson, 2011). SHH signalling also enhances early osteogenic commitment, in part through upregulation of RUNX2, and synergistic activation of osteogenic markers, ALP and OCN, when combined with BMPs (James, 2013; Lin & Hankenson, 2011). SHH acts upstream of Wnt, facilitating β-Catenin activation and thereby promoting later stages of osteoblast differentiation (James, 2013). In turn, canonical Wnt signalling is required downstream of SHH to support osteoblast maturation (Day & Yingzi, 2008). In contrast Notch appears to play a context dependent role, promoting profileration

of immature osteoblasts, but inhibiting terminal differentiation by supressing RUNX2 activity *via* HES/HEY transcriptional repressors. Notch can also antagonise Wnt and BMP signalling by reducing β-Catenin levels (Lou, et al., 2019), and inducing Hey-1, which represses BMP/SMAD mediated transcription (Lin & Hankenson, 2011).

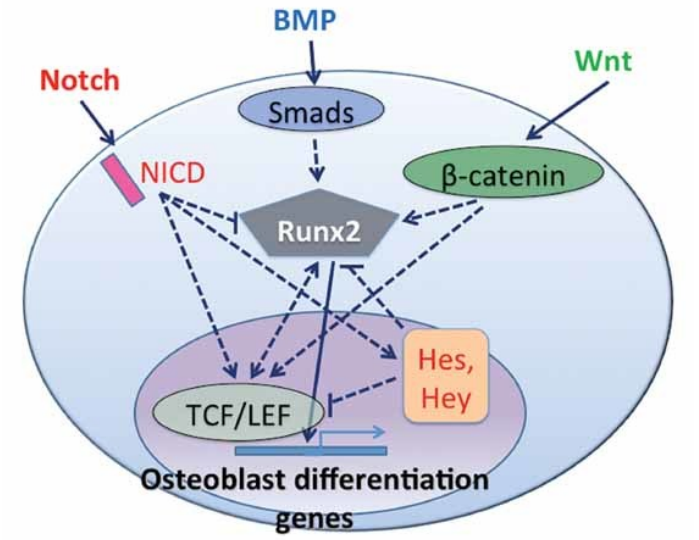

Figure 1-5: Summary of signalling pathway crosstalk in the regulation of osteogenesis

Schematic summarising the interactions of Notch, bone morphogenetic protein (BMP) and Wnt signalling pathways in the regulation of master osteogenic transcription factor runt-related transcription factor 2 (RUNX2). Notch signalling activates the Notch intracellular domain (NICD) which inhibits RUNX2 directly, while promoting transcription factors T-cell factor/lymphoid enhancer factor (TCF/LEF) and Hairy/enhancer of split and Hairy/enhancer of split related with YRPW (HES and HEY respectively). HES/HEY negatively regulate osteoblast differentiation and TCF/LEF's role is modulated through interaction with Wnt signalling. BMP signalling activates signal transducers and transcriptional modulators (SMAD) proteins, which enhance RUNX2 expression, promoting osteoblast differentiation and bone formation. Wnt signalling stabilises β-catenin, which translocates to the nucleus to promote RUNX2 expression and osteoblastogenesis, as well as activating TCF/LEF. The complex crosstalk between these pathways finely tunes osteoblast differentiation through direct and indirect regulation of RUNX2 and its downstream targets. Figure reproduced from Lin & Hankenson, 2011.

Together these pathways regulate osteoblast differentiation, by coordinating the timing and extent of RUNX2 activity, and its downstream effectors such as SP7/Osterix ultimately regulating osteoblast commitment, differentiation and matrix mineralisation.

1.2.1.2 Commitment to Other Lineages

As illustrated in the commitment stage of **Figure 1-4**, MSCs are also capable to differentiating down other cell lineages.

Adipogenesis: MSC commitment to the adipogenic lineage is primarily driven by TF PPARγ (**Figure 1-4**), in co-ordination with CCAAT/enhancer-binding protein alpha (C/EBPα) (Ghaben & Scherer, 2019). These TFs activate expression of adipocyte specific genes, involved in lipid metabolism and storage (Prestwich & MacDougald, 2007). BMP signalling promotes adipogenic differentiation through SMAD-dependent transcription, particularly *via* BMP4 while plays a key role in the formation of white adipose tissue by upregulating PPARγ. The Wnt/β-Catenin pathway inhibits adipogenesis, with β-Catenin stabilisation represses PPARγ and C/EBPα expression in preadipocytes, redirecting MSCs towards alternative linages (Ghaben & Scherer, 2019; Prestwich & MacDougald, 2007). Similarly, Hedgehog signally antagonises adipogenesis by interfering with BMP and insulin pathways, shifting cells towards an osteogenic fate (Ghaben & Scherer, 2019). During osteogenic differentiation, RUNX2 is upregulated, which in turn supresses adipogenic differentiation (Robert, et al., 2020).

Chondrogenesis: MSC commitment to a chondrogenic lineage is primarily regulated by SOX9 expression, an essential TF for chondrocyte development and cartilage formation (**Figure 1-4**). BMP signalling, particularly BMP1 and BMP2, promotes osteogenic commitment through SMAD1/5/8 mediated activation of SOX5, SOX6 and SOX9, which subsequently act in collaboration to drive cartilage gene expression (Li & Dong, 2016). One of the key downstream targets of SOX9 is aggrecan (ACAN), a key component of cartilage ECM (Peffers, et al., 2010). Canonical Wnt/β-Catenin signalling supresses chondrogenesis by downregulating SOX9 through β-Catenin expression, favouring osteogenic differentiation (Day, et al., 2005). In contrast, non-canonical Wnt/β-Catenin has been observed to support chondrogenic differentiation, particularly Wnt5a, and Wnt11 in coordination with TGF-β (Li & Dong, 2016; Robert, et al., 2020).

Myogenesis: Myogenetic differentiation is driven by expression of TF MyoD **(Figure 1-4**), with MSCs differentiating under exposure to demethylating agent 5-azacytidine in culture (Testa, et al., 2020). MyoD expression can be regulated by Canonical Wnt/β-Catenin signalling, (Wnt1 and Wnt7) through activation of protein kinase A and subsequent phosphorylation of cAMP response element binding protein (CREB). CREB phosphorylation supports expression of myogenic TFs including MyoD. BMP signalling plays a dynamic role in myogenesis, with early activation of the pathway supporting the progenitor pool including satellite cells, while BMP pathway suppression is required for progression into myogenic differentiation and muscle fibre formation (Borok, et al., 2020). Additionally, while Wnt/β-Catenin and BMP pathways, seem to promote myogenesis during

torso muscle development, they exert antagonist effects in craniofacial muscle formation, highlighting complex region-specific regulation during embryonic development (Yusuf & Brand-Saberi, 2012).

1.2.2 Induced Osteogenesis

In biomedical applications, osteogenesis can be induced through a variety of stimuli, including chemical, physical, mechanical, electrical and magnetic, many of which mimic or amplify physiological conditions found *in vivo* through the process of mechanotransduction. Understanding the cellular and molecular mechanisms behind these cues is essential for developing effective strategies in bone tissue engineering (BTE).

1.2.2.1 Chemical Induction

Biochemical cues are foundational in directing MSCs towards a potential lineage. Osteoinductive supplements, such as ascorbic acid, β-glycerophosphate and dexamethasone are commonly used in cell culture media to initiate osteogenic differentiation *in vitro* (Langenbach & Handschel, 2013; Mostafa, et al., 2012). These agents modulate intracellular paths to upregulate osteogenic markers such as ALP, RUNX2, and OCN (Langenbach & Handschel, 2013; Mostafa, et al., 2012). Dexamethasone has been recognised as the most efficient supplement to promote osteogenesis, however high concentrations also correlate with increased adipogenesis (Mostafa, et al., 2012).

Additionally, targeted delivery of growth factors such as recombinant human BMP-2 and BMP-7 (rhBMP-2, rhBMP-7), TGF-β and VEGF *via* culture media or bioengineered scaffolds can support and enhance osteogenic induction (Liu, et al., 2023; Lv, et al., 2015; Matsumoto, et al., 2015). Growth factors can also be delivered *via* biodegradable sustained release microcarriers, such as polyhedral microcrystals packaged with rhBMP-2 and rhBMP-7 (Matsumoto, et al., 2012; Matsumoto, et al., 2015; Whitty, et al., 2022). These factors are released slowly from polyhedral microcrystals through enzyme degradation of surrounding cells, supporting sustained release *in vivo* (Matsumoto, et al., 2012).

1.2.2.2 Physical Induction

Physical properties of the cell culture substrate, such as surface roughness, and biomaterial stiffness play a vital role in stem cell fate decisions. Faia-Torres, et al. (2015) examined various surface roughness levels and found that modifying the surface topography within an

optimal range can serve as an osteogenic cue, even in the absence of osteogenic media supplements. This optimal surface roughness effectively triggers and supports enhanced mineralisation in MSCs compared to common tissue culture plastic (Faia-Torres, et al., 2015). Yang, et al. (2016), observed that modifying surface roughness of hydroxyapatite enhanced osteogenic differentiation, particularly when combined with an optimal range of topographical nanopeaks. The MSCs responded through mechanotransduction mechanisms involving modulation of the Yes-associated protein (YAP) and PDZ binding motif (TAZ) signalling pathways (Yang, et al., 2016).

Nanoscale patterning of cell substrates can influence cell adhesion and osteoblast differentiation. Dalby, et al. (2007), observed highly ordered nanotopographies negatively impacted these factors, while disordered nanotopography acts as a significant osteogenic cue. Nanotopographies such as nanopillars, nanopits and nanogrooves act like mechanical stimuli that are converted to intracellular cues by mechanotransduction (Dobbenga, et al., 2016).

Substrate stiffness has an undeniable impact on MSC behaviour and differentiation potential. On soft hydrogels (13-16 kPa), MSCs are driven towards an adipogenic lineage, with high expression of adipogenic markers PPARγ and C/EBPα. MSCs undergo myogenic differentiation in hydrogels at 48-53 kPa and within stiffer hydrogels, MSCs favour an osteogenic lineage (El-Rashidy, et al., 2021). Scaffold architecture, including porosity, directly impact cell adhesion, profileration and gene expression. High porosity hydrogels allow enhanced nutrient and oxygen circulation, and subsequent osteogenic differentiation and mineralisation (Hao, et al., 2021), while small pore scaffolds promote chondrogenesis both *in vivo* and *in vitro* (Gupte, et al., 2018).

1.2.2.3 Mechanical Stimulation

Mechanical forces such as compressive and tensile strength, ultrasonic and fluid sheer stress can drive osteogenic lineage commitment. Such stimuli can be delivered using bioreactors or dynamic culture systems designed to mimic functional loading environments. These cues can stimulate *in vivo* conditions, transducing to intracellular biochemical signalling, promoting osteogenic differentiation. Low intensity pulsed ultrasound (LIPU) stimulates MSC proliferation and mineralisation by modulating mechanosensitive signalling pathways, including YAP/TAZ and calcium influx. LIPU at varying intensities can contribute to

enhanced mineralisation, ALP activity and collagen synthesis in osteoblasts, particularly in combination with 3D printed and hydroxyapatite (HA) scaffolds (Shuai, et al., 2018).

Mechanical stress stimulation, including cyclic stretching, cyclic compression and fluid sheer stress all influence MSC, osteoblast and osteocyte behaviour. Cyclic stretching of MSCs has been observed to promote osteogenic gene expression dependent on stretching magnitude, with low magnitudes supporting osteogenic commitment. Cyclic compression was observed to increase expression of bone remodelling genes, cyclooxygenase 2 (COX-2) and IL-6. Fluid sheer stress influences cell alignment, cytoskeleton organisation and enhances activity of osteogenic markers like ALP (Shuai, et al., 2018). Nanokicking is an emerging nanoscale mechanical stimulation technique, that applies extremely low amplitude, high-frequency vibrations to cells in culture. This method has been shown to direct MSC differentiation towards an osteogenic or chondrogenic lineage, in the absence of chemical differentiation factors. In response to nano vibrations, MSCs show morphology nuclear and cytoskeleton morphology changes. Upregulation of SP7/Osterix and ALP has been observed in MSCs under the application of nanokicking (Nikukar, et al., 2013; Robertson, et al., 2018).

1.2.2.4 Magnetic Stimulation

Magnetic fields have emerged as non-invasive biophysical stimuli for directing cell behaviour. Application of external magnetic fields have been shown to promote MSC proliferation and mineralisation. Similarly, the use of internal components, such as magnetic nanoparticles (MNPs) promote cell differentiation (Shuai, et al., 2018; Yuan, et al., 2018). Effects of magnetic stimulation will be further discussed in *1.4.3 Magnetic Stimulation for Bone Tissue Engineering.*

1.2.2.5 Electrical Stimulation

Electrical stimulation varies from invasive, semi-invasive and non-invasive techniques, producing electrical currents (biphasic, direct and alternative) to generate biochemical reactions. Continuous biphasic currents have positive effect on osteoblast profileration mode. Under an electrical field, cells have been observed to migrate and align towards the electrical field, with electrical stimulation driving osteogenic gene expression in MSCs. Combining electrical stimulation with 3D scaffolds also enhances osteoblast activity by promoting osteoblast proliferation and differentiation (Shuai, et al., 2018).

1.2.2.6 Mechanotransduction

Mechanotransduction is the process by which cells convert mechanical stimuli into biochemical signals, and it is fundamental to many of the induction strategies described above. Focal adhesion molecules, including vinculin and talin, transmit mechanical forces to intracellular signalling by activating proteins like focal adhesion kinase (FAK) (Dahl, et al., 2008; Sun, et al., 2022). The mitogen-activated protein kinase (MAPK) signalling pathway promotes osteogenesis through translocation of extracellular signal-regulated kinase (ERK) from cytoplasm to nucleus. Similarly, the Ras homolog gene family, member A (RhoA) pathway drives YAP/TAZ nuclear translocation, promoting osteogenesis. Mechanosensitive ion channels, transient receptor potential vanilloid 4 (TRPV4) and Piezo1, also act on YAP/TAZ activity. Upregulation of YAP/TAZ has been linked to enhanced expression of osteogenic markers (**Figure 1-6**) (Sun, et al., 2022). Additionally, nuclear morphology changes, such as nuclear flattening or elongation, occur as a result of mechanotransduction events, influencing chromatin organisation and transcriptional activity. Proteins such as lamin within the nuclear envelope play a role in sensing mechanical cues and affect nuclear morphology, contributing to osteogenic differentiation (Dahl, et al., 2008).

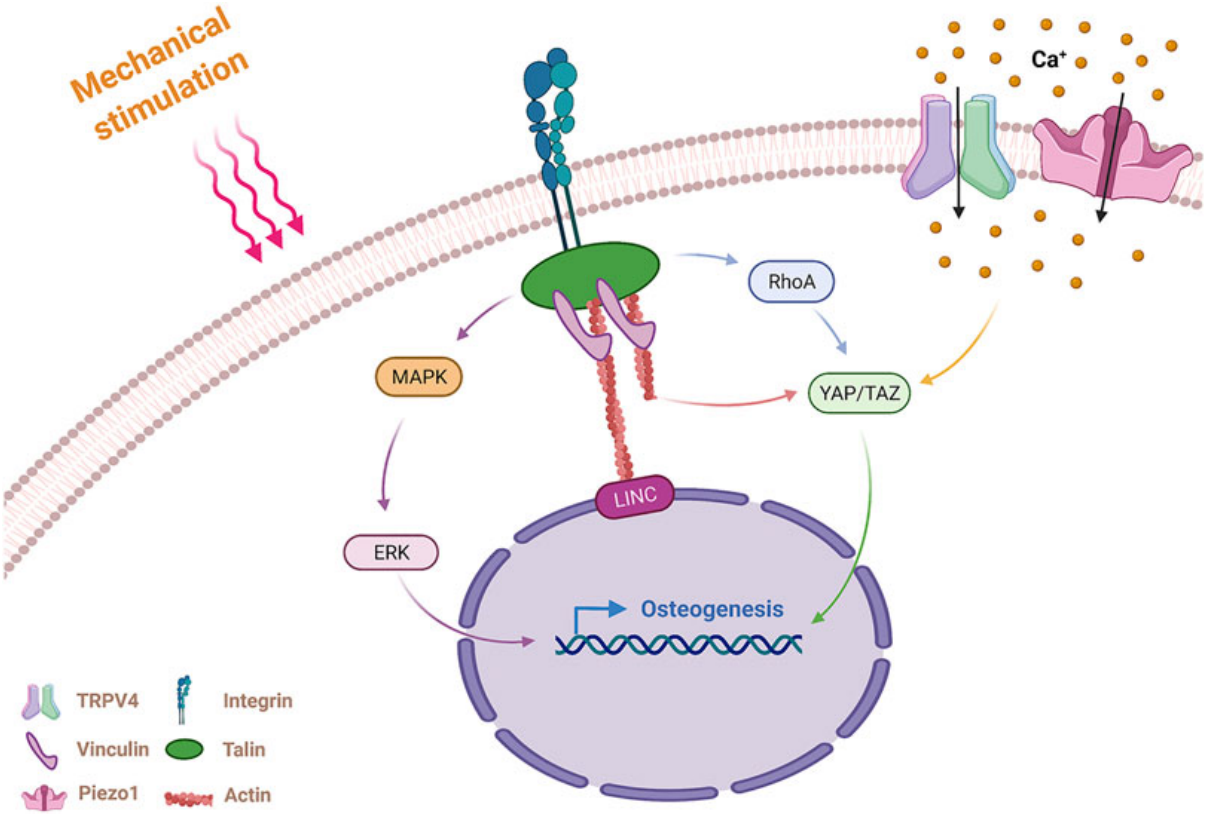

Figure 1-6: Schematic representation of mesenchymal stromal cells responding to mechanical stimulation

Mesenchymal stromal cells detect mechanical signals *via* integrins and mechanosensitive ion channels, which trigger pathway activation. Integrins activate Ras homolog family member A (RhoA) and mitogen-activated protein kinase (MAPK) pathways, promoting nuclear translocation of Yes-associated protein (YAP), transcriptional co-activator with PDZ-binding motif (TAZ) and extracellular signal-regulated kinase (ERK) respectively, leading to osteogenic gene expression. Mechanosensitive ion channels generate an intracellular calcium influx, aiding nuclear translocation of YAP/TAZ. Figure reproduced from Sun, et al., 2022.

1.2.3 Paracrine Signalling

Paracrine signalling is increasingly recognised as a major contributor to the therapeutic effect of MSCs, often exerting a greater influence than direct cell replacement or differentiation (Kusuma, et al., 2017). MSCs secret a diverse array of bioactive factors, including cytokines, growth factors, chemokines and most notably EVs which act on molecular pathways and influence cell fate (**Figure 1-7**) (Foo, et al., 2021).

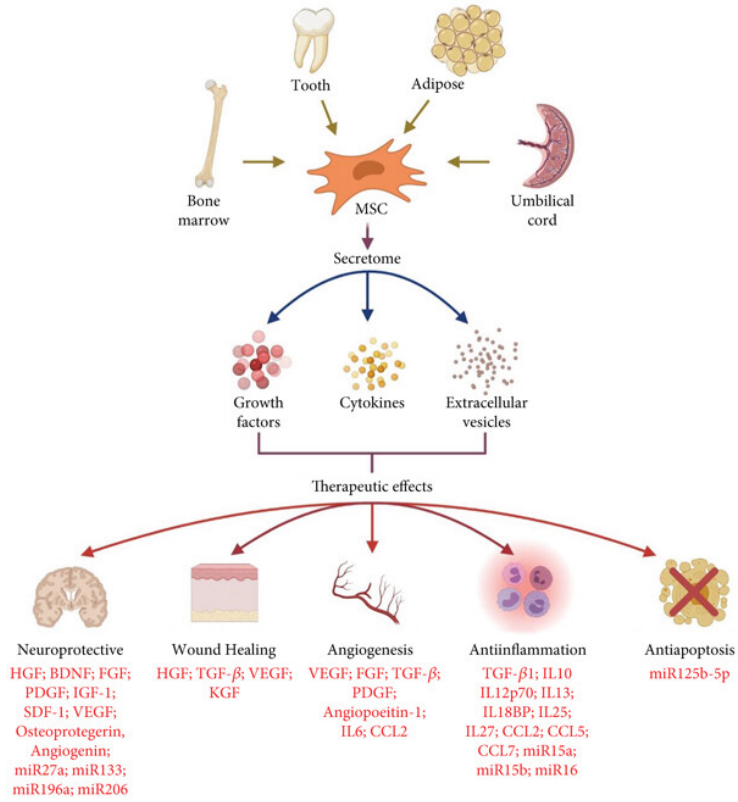

Figure 1-7: Mesenchymal stromal cell therapeutic effects

Schematic highlights common mesenchymal stromal cell (MSC) sources, and the composition of their paracrine signalling. MSCs can be isolated from multiple tissues, including bone marrow, adipose tissue, and umbilical cord. Their secretome is a complex mixture of growth factors, cytokines and extracellular vesicles (EVs) that mediate diverse therapeutic activities. These include neuroprotection, promotion of wound healing, angiogenesis, anti-inflammatory effects, and inhibition of apoptosis, collectively contributing to tissue repair and regeneration. Figure reproduced from Foo, et al., 2021.

EVs are small, phospholipid membrane bound particles released by MSCs that facilitate intercellular communication. These vesicles include both exosomes (30-150 nm) and macrovesicles (100-1000 nm), varying in their cell origins and content (**Figure 1-8**). MSC derived EVs carry a cargo of proteins, lipids and nucleic acids, including osteogenic and immunomodulatory micro ribonucleic acid (microRNA) which can be transferred to target cells to modulate their behaviour (Presen, et al., 2019). MSC-EVs act as key paracrine mediators in maintaining bone metabolic balance by delivering bioactive molecules, such as microRNAs and GFs, to promote osteogenesis and inhibit osteoclast mediated bone reabsorption (Tang, et al., 2024). In bone damage, paracrine signalling and EV release by MSCs promote angiogenesis, recruit host progenitor cells and modulate the local immune response to adopt a pro-regenerative phenotype (Kou, et al., 2022). This immunomodulatory effect is mediated in part by cytokines such as IL-6, a multifunctional cytokine secreted by

MSCs that plays a dual role regulating inflammation and contributing to osteoclast differentiation (Lee, et al., 2008).

Figure 1-8: Schematic of mesenchymal stromal cell-derived extracellular vesicle release

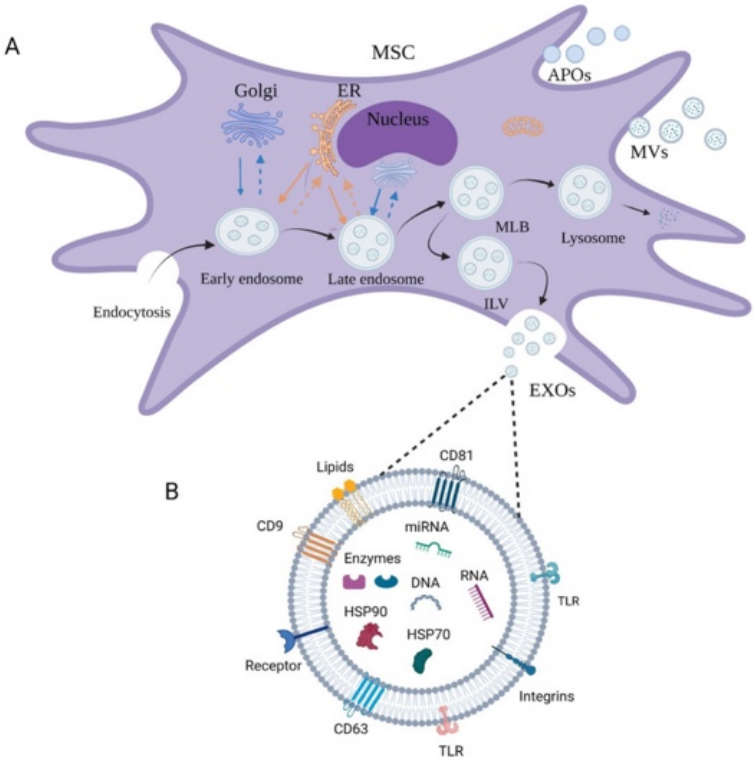

Mesenchymal stromal cells secrete extracellular vesicles (EVs) as part of paracrine signalling [A] The biogenesis of the three main types of EVs are indicated; EXO (exosomes), MV (microvesicles) and APO (apoptotic bodies). [B] An EV, showing the membrane composition including key marker proteins and the internal cargo components, such as RNA and various small molecules Figure reproduced from Kou, et al., 2022.

1.3 Bone Tissue Engineering

BTE is the fastest growing field within tissue engineering, primarily aimed at repairing and regenerating bone defects. BTE utilises scaffolds, pre-osteogenic cells, bioactive growth factors and external stimulation to promote regeneration and repair (**Figure 1-9**) (Perez, et al., 2018). In addition, maintaining cells in a 3D matrix allows for formation of 3D cell organisations such as spheroids, which promote osteoblast cell maturation in MSC populations (Yuan, et al., 2018).

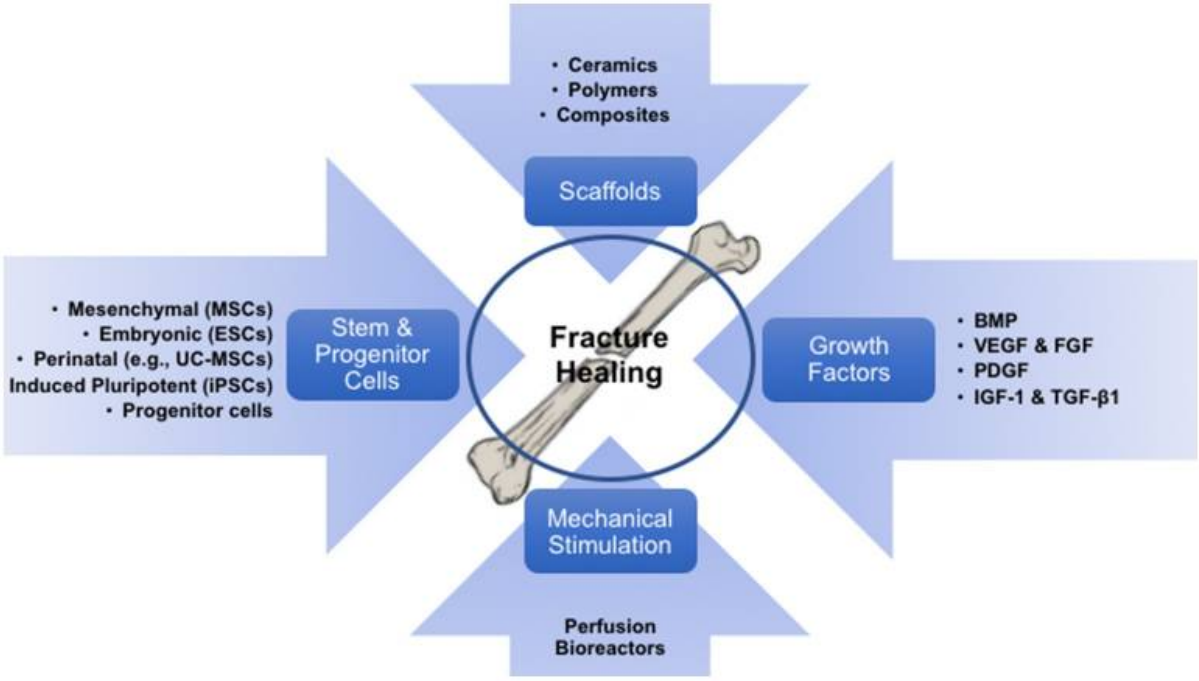

Figure 1-9: Schematic of components commonly used in bone tissue engineering

Tissue engineering harnesses the synergistic effects of multiple components to promote tissue regeneration. Scaffolds act as three-dimensional frameworks that mimic the extracellular matrix, providing structural support and guiding new tissue formation. Stem cells and progenitor cells are incorporated to aid or replace native cell populations during tissue repair. Additionally, growth factors can be used to direct tissue lineage, while mechanical stimulation mimics *in vivo* conditions to enhance regeneration through mechanotransductive effects. Figure reproduced from Perez, et al., 2018.

1.3.1 Established Bone Tissue Engineering Scaffolds

As previously discussed, a growing need for bone grafts has focused research towards developing alternative bioengineered grafts. BTE utilises biomaterials in the development of suitable scaffolds, serving as temporary 3D framework that mimics the ECM, with the aim to guide new tissue formation. Bioengineered scaffolds need to meet certain criteria for successful integration; they must be biocompatible, biodegradable, have compatible surface properties and porosity, and they must be osteoconductive. Scaffolds should also support vascularisation, mechanical integrity and osteointegration (Manzini, et al., 2021; Perez, et al., 2018; Xue, et al., 2022). Scaffolds can be classified based on their material type: ceramics, polymers, compositions and metals. Most recently BTE has supported the development of biomaterials such as hydrogels for use as scaffolds (Perez, et al., 2018).

Ceramics such as HA, bioactive glass, β-tricalcium phosphate (β-TCP) and biphasic calcium phosphate (BCP), exhibit excellent biocompatibility leading to their frequent use in repair of critical size defects (Perez, et al., 2018; Zhang, et al., 2019). Among these, bioactive glass

is particularly noted for forming a surface layer similar to HA, facilitating strong bonding with surrounding bone tissue. Similarly, calcium phosphate scaffolds, including β-TCP and BCP, gained promise with development of 3D printing technologies, which enable precise control of internal architecture, improving scaffold porosity while maintaining excellent biocompatibility. However, bioactive glass and calcium phosphate scaffolds are brittle, limiting their clinical use to non-weight bearing bones (Xu, et al., 2024; Zhang, et al., 2019). Additionally, slow or incomplete biodegradability in some ceramics, such as HA has limited their clinical use despite their excellent osteogenic potential (Xu, et al., 2024; Zhang, et al., 2019). Research efforts in ceramics now aim to improve their osteoinductivity through surface coating or application of nanotopographies (Perez, et al., 2018).

Polymers can be broadly categorised as natural or synthetic. Natural polymers such as animal derived collagen and gelatin, and plant-based alginate and cellulose are fundamentally biocompatible, supporting cell adhesion and proliferation (Xu, et al., 2024). Collagen is a key component in natural bone while gelatin is obtained from the hydrolysis of collagen, leading to both polymers having outstanding biocompatibility with native bone. However, both suffer from weak mechanical properties and poor degradation control (Perez, et al., 2018; Wu, et al., 2024). Synthetic degradable polymers, such as poly(L-lactic acid) (PLLA), poly(DL-lactic acid) (PDLA), polyglycolic acid (PGA) and polycaprolactone (PCL), allow for tuneable degradation rates and consistent manufacturing quality, minimising batch variability. Despite these benefits, some synthetic polymers may lack intrinsic bioactivity leading to poor cell adhesion, and their degradation products can sometimes cause local pH changes that may impact cell behaviour and induce inflammation (Perez, et al., 2018) (Xu, et al., 2024).

Composite materials are the combination of polymers and ceramics, a method aimed to reduce limitations of both categories through combined use, while maximising their strengths including bioactivity and biocompatibility (Xu, et al., 2024). Resorbable composites, such as HA/PLA are commonly used in maxillofacial surgeries but lack sufficient strength for orthopaedic surgeries due to increased degradability. Composite performance can be tuned using fibres and surface coatings to improve compressive strength, embedded cell proliferation and osteogenesis (Perez, et al., 2018).

1.3.2 Hydrogels for Tissue Engineering

While ceramics, conventional polymers and composites have demonstrated considerable potential in BTE, each material type presents limitations, such as insufficient mechanical strength and lack of bioactivity, that can compromise scaffold performance. Hydrogels have emerged as promising and versatile biomaterials for BTE applications (Nallusamy & Das, 2021). While technically a subclass of polymers, they possess unique characteristics that distinguish them from traditional polymer-based scaffolds.

Hydrogels are three dimensional networks of natural or synthetic polymers that are capable of absorbing large volumes of water, due to crosslinking between polymer chains. Hydrogels have tissue like viscoelasticity and the ability to encapsulate cells and bioactive molecules, making them particularly attractive for mimicking the native ECM (Liu, et al., 2020; Markey, et al., 2016; Manzini, et al., 2021). Their inherent hydrophilicity supports efficient nutrient diffusion and cell viability supporting 3D growth of cells for both *in vitro* and *in vivo* tissue engineering (Bashir, et al., 2020; Markey, et al., 2016).

Hydrogels are generally simple to fabricate, mainly by crosslinking of the polymer network (Hu, et al., 2019). A key advantage in using hydrogels is that they are tuneable in terms of their mechanical properties, which allows the support of cell adhesion, migration, and differentiation mimicking a variety of tissues such as the bone marrow (Liu, et al., 2020). As well as mechanical properties, hydrogels are developed to ensure efficient swelling and degradation to support ECM development (Silva, et al., 2018). Hydrogels are typically highly biocompatible, allowing for safe integration with host tissue without immune response (Bashir, et al., 2020).

Many hydrogels are injectable, enabling minimally invasive administration into irregular bone defects where pre-formed scaffolds may not be practical (Wang, et al., 2023). Additionally injectable hydrogels can be laden with biomolecules such as growth factors, BMP-2 or VEGF, enabling controlled and localised release (Salama, et al., 2025). Many hydrogels are also printable as bioinks, enabling fabrication of highly controlled, specific scaffolds (Li, et al., 2018).

There are many types of hydrogels for use in BTE. In addition to the classifications in **Figure 1-10**, hydrogels can be further classified by their preparation method and crosslinking method (Bashir, et al., 2020; Yue, et al., 2020).

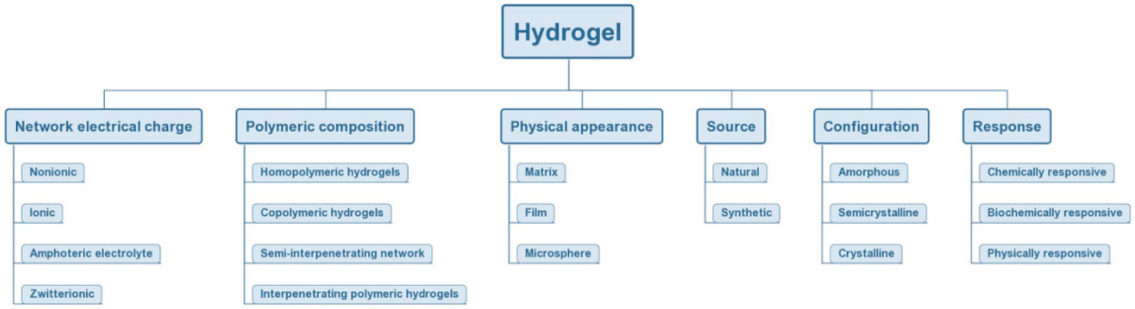

Figure 1-10: Classification of hydrogels by different properties

Hydrogels can be classified based on their network electrical charge, polymeric composition, physical appearance, source, configuration, and response. Figure reproduced from Yue, et al., 2020.

Natural source hydrogels such as chitosan, collagen, sodium alginate and gelatin, are derived from biological sources including animal tissues or plant materials, and are known for their high biocompatible, non-toxicity and biological relevance (Bashir, et al., 2020; Gomez-Florit, et al., 2020). Due to their natural tissue origins, these hydrogels closely mimic the structure and composition of the native ECM, supporting cell adhesion, proliferation and integration (Gomez-Florit, et al., 2020; Yue, et al., 2020). Additionally, they are relatively inexpensive and readily available, making them attractive for a wide range of biomedical applications (Bashir, et al., 2020). However, natural hydrogels generally display poor mechanical properties and may elicit variable immune response *in vivo*, limiting their clinical utility (Xue, et al., 2021).

Synthetic hydrogels are a viable alternative to natural source hydrogels, with excellent mechanical strength in comparison to natural hydrogels (Bashir, et al., 2020). Common examples of synthetic hydrogels including polyethylene glycol (PEG), poly (lactic acid) (PLA), polyvinyl alcohol (PVA) and poly (vinyl pyrrolidone) (PVP) (Bashir, et al., 2020)**.** These are chemically well defined which improves consistency and negates the possibility of batch variation due to tight control over production (Clough, et al., 2021). Synthetic hydrogels are easy to modulate; they can be functionalised with integrin binding sequence or can have fluorescence added to aid analysis (Faroni, et al., 2019). However, despite their versatility, in comparison to natural hydrogels, biocompatibility and toxicity of synthetic materials falls short (Yue, et al., 2020).

Hybrid hydrogels combine natural polymers with synthetic polymers, aiming to overcome the individual limitations of each. This approach generates biocompatible hydrogels with enhanced mechanical strength (Bashir, et al., 2020). A widely studied example is gelatin methacryloyl (GelMA), which is derived from gelatin and functionalised with a

methacryloyl group to enable photocrosslinking under UV light. This gives GelMA the bioactivity of a natural polymer, supporting cell adhesion and proliferation, while also enabling mechanical stability, a characteristic of synthetic biomaterials (Zhou, et al., 2023). GelMA is widely used in BTE, bioprinting and drug delivery applications, where both biological compatibility and mechanical properties are essential considerations (Mamidi, et al., 2023; Zhou, et al., 2023).

For this project, GelMA was selected over other commonly used hydrogels including synthetic peptide hydrogels and PEG based systems, because it combines intrinsic biocompatibility with tuneable mechanical properties and allows for straightforward incorporation of internal components such as MNPs (Zhou, et al., 2023). Unlike fully synthetic hydrogels, GelMA retains natural cell-adhesive motifs that support MSC attachment and cell spreading, facilitating homogenous cell dispersal throughout the hydrogel (Xiao, et al., 2019). GelMA has a demonstrated osteogenic potential, making it a suitable biomaterial for examining the regenerative capacity of applied magnetic fields (Lee, et al., 2020; Lin, et al., 2018). In addition, the crosslinking method enables control over stiffness and degradation rate by adjusting polymer concentration and crosslinking conditions (Sharifi, et al., 2021). Previous studies have successfully developed GelMA bioprinting strategies, which is advantageous for potential translation of the model (Zhu, et al., 2023). During preliminary testing, synthetic hydrogels were also explored; however, challenges associated with MNP dispersion and low MSC viability led to their discontinued use in favour of GelMA. While there are many positives to utilising these biomaterials, GelMA hydrogels still have limitations, including batch to batch variability, and potential cytotoxicity associated with UV exposure (Garces, et al., 2023; Zennifer, et al., 2023). Additionally, GelMA hydrogels do not have intrinsic mineralisation capacity, with previous studies incorporating ceramic additives to support mineralisation (Han, et al., 2024). Over extended culture periods, gelatin-based hydrogels can lose mechanical strength, due to rapid enzymatic activity of embedded cells degrading the hydrogel (Lestari, et al., 20216). This is particularly important for long term studies, including differentiation studies, where mechanotransduction outcomes may be influenced by time dependent matrix remodelling. Taken together GelMA provides a biologically active, tuneable biocompatible hydrogel and its known limitations conditions were carefully considered in the selection for this model.

1.4 Magnetic Stimulation for Bone Tissue Engineering

1.4.1 Magnetic Nanoparticles

MNPs are particles typically ranging in size from 1-100 nm, with some applications of particles up to 500 nm (Ali, et al., 2021; Lu, et al., 2007). These particles are commonly composed of magnetic materials such as iron oxide (Fe_3O_4), cobalt or nickel, with iron oxide being the most widely used due to its superior biocompatibility (Ali, et al., 2021; Lu, et al., 2007). To enhance stability MNPs are often coated with organic or inorganic materials such as silica, dextran, PEG or other polymers (Fathi-Achachelouei, et al., 2019; Lu, et al., 2007). These coatings not only prevent aggregates forming, they also provide functional groups for possible conjugation with biomolecules (Ali, et al., 2021; Fathi-Achachelouei, et al., 2019; Lu, et al., 2007). Particles between 76 nm to 128 nm generally maintain single domain cores, although this can depend on particle shape, while larger particles, such as 200 nm, form multidomain cores (Li, et al., 2017). While single domain particles tend to be utilised within engineering studies, multidomain particles are favoured for biomedical research applications as their structure prevents particle agglomeration and supports colloidal stability (Nowak, et al., 2014).

Furthermore, MNPs have shown to be biocompatible and non cyto-toxic making them ideal candidates for tissue engineering (Ali, et al., 2021; Fathi-Achachelouei, et al., 2019). Depending on size and coating, MNPs can be internalised by cells; the application of an external static magnetic field (SMF) has been observed to significantly enhance the uptake of MNPs into fibroblasts (Chaudhary, et al., 2013). MNPs have also been incorporated into cells prior to generating cell spheroids, to enable magnetic manipulation of the spheroid shape and assembly into larger 3D tissue like structures (Mattix, et al., 2014). The variability in size and core structure can have significant biological consequences; smaller particles (37 – 100 nm) are more readily internalised by cells which can influence cellular behaviour and fate (Hoshyar, et al., 2016). Depending on the experimental context, MNP uptake may be a desired feature to facilitate magnetic manipulation, or it could be an unintended consequence of culture conditions, potentially influence cell behaviour. Despite numerous studies investigating particle uptake by cells, there is no clear consensus on the ‘critical’ particle size, as uptake depends not only on particle dimensions but also on core structure, surface coating and physiochemical properties as well as the intrinsic dynamics of the specific cell type. This complexity makes it challenging to predict internalisation efficiency and

emphasises the need for careful characterisation of nanoparticles in each experimental context.

Particle coating can also significantly influence MNP and cellular responses, with effects depending on coating composition and hydrophilicity. Hydrophilic coatings, such as dextran or PEG, have generally been used to improve stability and biocompatibility. However, studies have shown that these coatings can still aggregate in the presence of cell media components, including foetal bovine serum, and that this aggregation can be influenced by the electrical charge of the particle coating (Eberbeck, et al., 2010). Such aggregation may alter particle uptake and intracellular processing, highlighting that even commonly used coatings can have context dependent effects on biological performance (Yue, et al., 2011). Additionally, the molecular weight of coatings, such as dextran, can affect MNP colloid stability with increasing weight affecting their magnetisation (Hong, et al., 2008). Hong et al. (2008), observed that increasing the ratio of dextran to iron oxide decreased saturation magnetisation, indicting reduced magnetic strength of the MNPs. In addition, dextran coatings are not strongly bound to MNPs, which can result in detachment of dextran and subsequent particle aggregation (Singh, et al., 2010). This trade-off between coating stability and magnetisation is a careful consideration for biomedical applications.

Studies report a wide range of MNP concentrations in the applications of iron oxide MNPs used in cell culture research, yet there is no clear consensus on optimal concentration (Liu, et al., 2020; Wang, et al., 2024). Particle concentration influences magnetic stimulation relayed to cells, however increasing MNP concentration can promotes interparticle interactions leading to MNP aggregations, which also affects cellular uptake and subsequently impacts cell viability (Hong, et al., 2011; Hoshyar, et al., 2016). Hong et al. (2011) identified a maximum concentration of 500ppm to maintain cell viability, and suggested MNP concentration to be the most critical factor affecting cell viability in cell culture applications. The variability in MNP concentration further complicates comparisons across studies and highlights the need to balance concentration dependent-magnetisation effects with biocompatibility.

One of the defining properties of MNPs are their ability to respond to an external magnetic field, allowing spatial and temporal control over attached biomolecules or cells (Fathi-Achachelouei, et al., 2019). In tissue engineering, this non-invasive method of stimulation has led to opportunities for manipulating cell and material behaviour. Importantly, due to their size, many MNPs are superparamagnetic, exhibiting magnetic behaviour only in

response to an external field, minimising aggregation after field removal (Ali, et al., 2021). Magnetic ability of MNPs can be influenced by the particle dimensions (single or multidomain cores), and aggregation behaviour. (Lu, et al., 2007), both of which can be further influenced by MNP concentration (Hoshyar, et al., 2016). In contrast, to superparamagnetic nanoparticles, larger or aggregated particles may exhibit paramagnetic or ferromagnetic behaviour, retaining residual magnetisation after field removal (Issa, et al., 2018). Interestingly Superparamagnetism has been observed to occur in ferromagnetic nanoparticles when particle dimensions are reduced to the single domain core (Ha, et al., 2018). While this may enhance magnetic responsiveness, it also increases the risk of particle aggregation and uneven distribution within hydrogels, which can compromise hydrogel stability. As such, careful considering of MNP behaviour is critical when designing magnetic hydrogels.

In this study, we opted to use iron oxide dextran coated MNPs around 200 nm in size to embed within hydrogels. These nanoparticles, fluidMAG-Dx, exhibit superparamagnetic behaviour, becoming magnetised under an applied magnetic field and showing no remnant magnetism once the field is removed, essentially enabling reversible control of magnetic stimulation applied to cultured cells (chemicell, 2025). The dextran coating was chosen for its proven biocompatibility in cell culture applications and its ability to maintain colloidal stability (Eberbeck, et al., 2010; Hong, et al., 2008; Thorat, et al., 2013), while the 200 nm size supports the superparamagnetic behaviour and limits cellular uptake (Chithrani, et al., 2006; He, et al., 2010; Nowak, et al., 2014).

1.4.2 Magnetic Stimulation for Bone Tissue Engineering

Both the ECM and cell membranes have diamagnetic properties, and their structure and orientation can be modified by magnetic fields. Targeted external forces can remotely influence membrane flux in cells, and their behaviour within their ECM (Paun, et al., 2018). Magnetic actuation has been shown to increase the expression of integrin alpha-5 (ITGA5), as well as active downstream signalling pathways such as RhoA and MAPK. Additionally magnetic stimulation can trigger BMP2 signalling, and subsequent activation of SMAD1/5/8. Together these pathways promote expression of osteogenic TFs RUNX2 and SP7/Osterix, leading to osteoblast differentiation (Filippi, et al., 2019; Xia, et al., 2018). Consequently, magnetic stimulation has been shown to enhance both cell proliferation and direct stem cell differentiation (Henstock, et al., 2014; Paun, et al., 2018; Silva, et al., 2018).

However, these effects are highly dependent on both the type and parameters of the applied magnetic field, as well as the specific cell population and ECM environment used in each study. For example, Zheng et al. (2018) observed that application of 1 mT SMF to dental pulp stem cells increases cell proliferation, while application of a 2 mT or 4 mT field for the same duration has no observed effect on cell proliferation. Similarly, Boda et al. (2015) applied a constant SMF (100 mT) for 7 days to MSCs and observed reduced cell proliferation; however, a later study by Marędziak et al. (2017) applied a 500 mT field constantly for the same period to MSCs and observed cell proliferation increased. In addition, Cois et al. (2021), observed cell dependent effects in rental cell lines under a DMF (4.5 mT, 50 Hz). Over 72 hours, the magnetic field induced cell cycle arrest in a renal carcinoma cell line while healthy kidney cells were unaffected by the applied regime (Cios, et al., 2021). These field and cell dependent effects underly the need to distinguish between different magnetic stimulation regimes.

Magnetic fields are typically categorised as either static or dynamic, with static fields remaining constant and dynamic fields varying over time (Fan, et al., 2020). SMFs maintain a consistent strength and field orientation, while dynamic fields use induce periodic changes in magnetic field intensity (Castro, et al., 2020).

A static field can be classified by field strength, which is typically measured in Tesla (T) or milliTesla (mT). Field strengths below 1 mT are considered weak, while those between 1 mT to 1 T are classified as moderate. For context, a common fridge magnet has a field strength of approximately 1 mT. Strong magnetic fields range from 1 T to 5 T and are commonly used in modern MRI machines. Fields exceeding 5 T are considered ultra strong (Marycz, et al., 2018). It should be noted that the ‘moderate’ category spans a very wide range (1 mT to 1 T), encompassing strengths that may elicit substantially different biological effects. As such the terminology can be inconsistent across studies, potentially contributing to variability in reported cellular responses between weak, moderate and strong fields. While some studies report magnetic field strength in Oersted (Oe), Gauss (G) and kiloampere/Meter (kA/m) this thesis uses T or mT for consistency with conversions as follows: 1 G = 0.1 mT, 1 Oe = 0.1 mT, 1 kA/m = 1.26 mT (Maurer Magnetic, 2025).

SMFs have been widely utilised in bone tissue engineering to promote osteogenic lineage commitment and maintenance. Exposure to SMFs has been shown to promote osteoblast proliferation, migration and differentiation through mechanotransduction processes (Paun, et al., 2018; Yuan, et al., 2018). Similarly, magnetic exposure of 50 mT for one week resulted

in increased expression of RUNX2, SP7/Osterix and Col1A1 in stromal vascular fraction population, including MSCs (Filippi, et al., 2019). Paun, et al. (2018), observed that SMFs between 100-250 mT accelerated osteogenic differentiation, with higher field strengths correlating with earlier onset of differentiation. Additionally, SMF actuation inhibited activity of osteocytes due to significantly reduced Sost expression (Zhang, et al., 2018). Despite these promising findings there is a substantial heterogeneity in magnetic field strength in previous studies, limiting direct comparison and making it difficult to define an optimal or clinically relevant stimulation window. In addition, the use a variety of biological models, and cell populations complicates interpretation of cell specific responses. For example, utilising a moderate magnetic field, 4 mT, Zhang et al. (2018), found whole body exposure to a SMF over 16 weeks prevented bone deterioration in a diabetic rat model, instead prompting bone formation through elevated levels of RUNX2, OCN and BMP2. Application of magnetic field to whole body models induces potential systemic and indirect effects that are difficult to isolate and translate to *in vitro* models, complicating direct comparisons between studies.

Notably, static magnetic stimulation is typically applied continuously for the duration of the experiment duration (ranging from hours to weeks), with limited consideration of intermittent exposure. As a result, potential hormetic effects of magnetic stimulation remain under explored. Romeo, et al. (2016) compared constant and intermittent SMF application to determine potential permanent or transient effects on cells and found both application methods support cell viability and DNA integrity (Romeo, et al., 2016). However, whether intermittent exposure can modulate osteogenic differentiation or mechanotransduction more effectively than continuous stimulation remains unclear.

In our study we opted for use of a 370 mT neodymium iron boron static magnetic plate in both 24 well and 96 well formations. The 96 well plate is compatible with all standard cell culture plates and flasks except a 24 well; therefore, a dedicated 24 well magnetic plate was also used to enable experiments in this format (chemicell, 2026). This set up ensured magnetic exposure was consistent across all experimental conditions and allows reproducible stimulation of cells cultured in monolayer or embedded within hydrogels. The choice of field strength was based on observations that moderate magnetic fields accelerate osteogenic differentiation and promote proliferation in MSCs and osteoblasts (Filippi, et al., 2019; Paun, et al., 2018). We investigated two SMF regimes, a constant SMF applied for the full duration of the experimental protocol, and intermittent SMF applied for 1 hour per day, in order to compare sustained vs time limited magnetic stimulation and assess if intermittent

exposure could elicit distinct cellular responses while reducing prolong magnetic stimulation.

Dynamic magnetic fields (DMF) are an umbrella term for many dynamic modes of stimulation, including pulsed or alternating magnetic fields, and magnetically driven dynamic culture systems (Hao, et al., 2021; Tsai, et al., 2019; Varani, et al., 2021). In general, studies suggest that DMFs combined with MNPs can promote osteogenic differentiation although the underlying mechanism not clearly defined. Wang, et al., (2022) embedded iron oxide MNPs (~60-70 nm) into agarose hydrogels and applied a dynamic magnetic field (1.26 mT), observing upregulation in osteogenic genes via PI3K/AKT and MAPK signalling pathways (Wang, et al., 2022). Kim et al., (2014) however observed that DMF exposure (1 mT, 45 Hz) in combination with iron oxide MNPs (12 nm) significantly upregulated osteogenic gene expression through activation of the BMP signalling pathway (Kim, et al., 2015). The activation of multiple pathways in previous literature suggests the method of promoting osteogenic differentiation is dependent on the parameters of the applied field.

Other studies highlight additional nuances, including effect on other differentiation pathways, observed in MSCs and related progenitor populations. Lu et al., (2015) observed DMF (20 Hz, 2 mT) stimulation promoted osteogenic differentiation and inhibited angiogenic differentiation in MSC over 10 days, with increased OCN expression at day 3, and OPN at day 9. They also observed downregulation of adipogenic markers, including adipokine and AP-2 (Lu, et al., 2015). Yin et al., (2018) reported a DMF (1mT, 50Hz) significantly enhanced osteogenic differentiation in ASCs. At 7 days, ALP activity and early osteogenic gene expression was increased (ALP, BMP2, RUNX2), and later osteogenic genes were expressed by day 14 (Yin, et al., 2018). Ongaro et al observed the effect of a DMF (75 Hz, 1.6mT) on both MSCs and ASCs. They observed that a DMF increased early (ALP) and late (OCN) osteogenic markers and promoted matrix mineralisation in both cell types (Ongaro, et al., 2014). Taken together these studies indicate that DMF can be a powerful tool to drive osteogenesis but the diversity in frequency, amplitude, cell type and nanoparticles make it difficult to draw generalisations.

While these results show promise for dynamic culture systems at promoting osteogenic differentiation, some studies do not report essential parameters clearly, making direct comparisons challenging and limiting reproducibility. For example, Henstock et al. (2014), reported that exposure to a 25 mT field in combination with nanoparticles increased mineralisation and matrix density in an *ex vivo* chick foetal femur model. However, this

study did not provide all experimental parameters, making comparison with high or low frequency studies difficult despite the reported positive outcomes. Similarly, Wang et al. reported magnetic field strength (1.26 mT) but not applied frequency, again limiting comparison to similar field dynamic system.

DMF studies employ a wide variety of culture systems, from simple oscillating magnets to more complex culture systems, introducing variability in mechanical cues and local field distribution. In systems using bioreactors or dynamic magnetic actuation, secondary effects such as local heating, fluid sheer or mechanical vibration are often not measured, which may contribute to observed cellular responses independent of magnetic stimulation. For example, Wang et al, (2022) induced mild hyperthermia through application of an alternating magnetic field. While the primary aim of their study was to induce hyperthermia, it highlights that dynamic fields can generate thermal effects, which may also unintendedly occur in other DMF studies where such effects are not investigated. To account for these potential confounders, more robust controls are required. Aldebs et al. (2020) cultured their control groups on their dynamic field system without activating dynamic displacement, allowing distinction between the effects of the magnetic field itself and secondary mechanical or thermal influences. As with static magnetic fields, effects are highly dependent on cell type, limiting generalisation of results across different systems.

Interestingly, transitioning from a static field application to dynamic field application does not necessarily produce equivalent results, even when most parameters remain same. For example, Manjua et al. (2021), observed that exposure of MSCs to a 450 mT constant SMF for 24 hours increases cell proliferation, whereas application of a 450 mT dynamic field (0.25 Hz) for the same duration resulted in decreased proliferation. This highlights that field dynamics can critically influence cellular responses, underscoring the need for careful optimisation and reporting of all dynamic magnetic stimulation parameters.

In this thesis we utilised custom built dynamic magnetic field bioreactor. Based on research by Guillot-Ferriols, M. *et al.* (PhD, 2024), a frequency of 0.3 Hz and 10 mm displacement were applied on a programme with a 16-hour active stimulation period, followed by 8 hours of rest during which the cells were exposed to a low SMF of approximately 23 mT. These parameters have been observed to stimulate MSCs to induce osteogenic gene expression when cultured on piezoelectric films over 3 days (Guillot-Ferriols, et al., 2024). In this study, the effects of these dynamic fields were investigated on both monolayer MSCs and cells embedded within magnetic hydrogels.

In summary, both static and dynamic fields have the potential to enhance osteogenic differentiation, especially in combination with MNPs. However, responses are highly dependent on magnetic field parameters, cell type, and exposure regime.

1.4.3 Magnetic Hydrogels for Bone Tissue Engineering

Recent advancements in bone tissue engineering also make use of external magnetic fields and internal magnetic components, to promote osteogenesis and bone repair (Paun, et al., 2018). The benefits of both hydrogels and MNPs can be combined, generating magnetic hydrogels. Magnetic hydrogels are composed of a matrix hydrogel with an additional magnetic component, the combination of which is more effective than if each component is used in isolation (Yuan, et al., 2018). With the addition of a magnetic component, such as nanoparticles, the hydrogels respond to an external magnetic field. The adaption of hydrogels into magnetically responsive hydrogels improves regulation of tuneable properties within the cellular environment and improves biological activity of the cells and tissues (Liu, et al., 2020).

There are various methods for the fabrication of magnetic hydrogels including blending, *in situ* precipitation, and grafting. The blending method is used to fabricate magnetic hydrogels when the magnetic particles and hydrogels have been produced separately. Magnetic particles and hydrogels are blended with to spread magnetic particles throughout the hydrogel (**Figure 1-11, A**) (Liu, et al., 2020). The *in situ* precipitation method synthesises the magnetic particles within the hydrogel. Magnetic precursors (Fe2, Fe3) are added to a hydrogel which has been prepared *via* a crosslinking reaction. The mixture undergoes alkalinisation which induces crystallisation of magnetite, forming the magnetic hydrogel (**Figure 1-11, B**). The grafting-onto method forms magnetic hydrogels through the formation of covalent bonds between grafted magnetic particles and the polymers within the hydrogel (**Figure 1-11, C**). The grafting-onto method produces hydrogels with high stability and good mechanical properties; however, it is costly and time consuming limiting its potential use (Liu, et al., 2020). The choice of preparation method can significantly influence MNP retention. Both the *in situ* and grafting onto method show higher MNP due to MNP assisted crosslinking, providing greater retention than the blending method (Liu, et al., 2020). Even under increased swelling, Alveroğlu et al. (2013) observed that magnetic hydrogels prepared *via in situ* methods maintained MNP retention. Similarly, application of external magnetic fields can cause MNPs within hydrogels to migrate towards the field, ultimately leeching out the hydrogel. Filippi et al. (2019) observed this effect under

application of a constant SMF (50 mT) over 7 days in PEG hydrogels with 15 nm MNPs (1 mg/mL). This highlights a limitation to prolonged magnetic stimulation, as nanoparticle migration may compromise hydrogel stability, and limit long term functionality of the magnetic hydrogel.

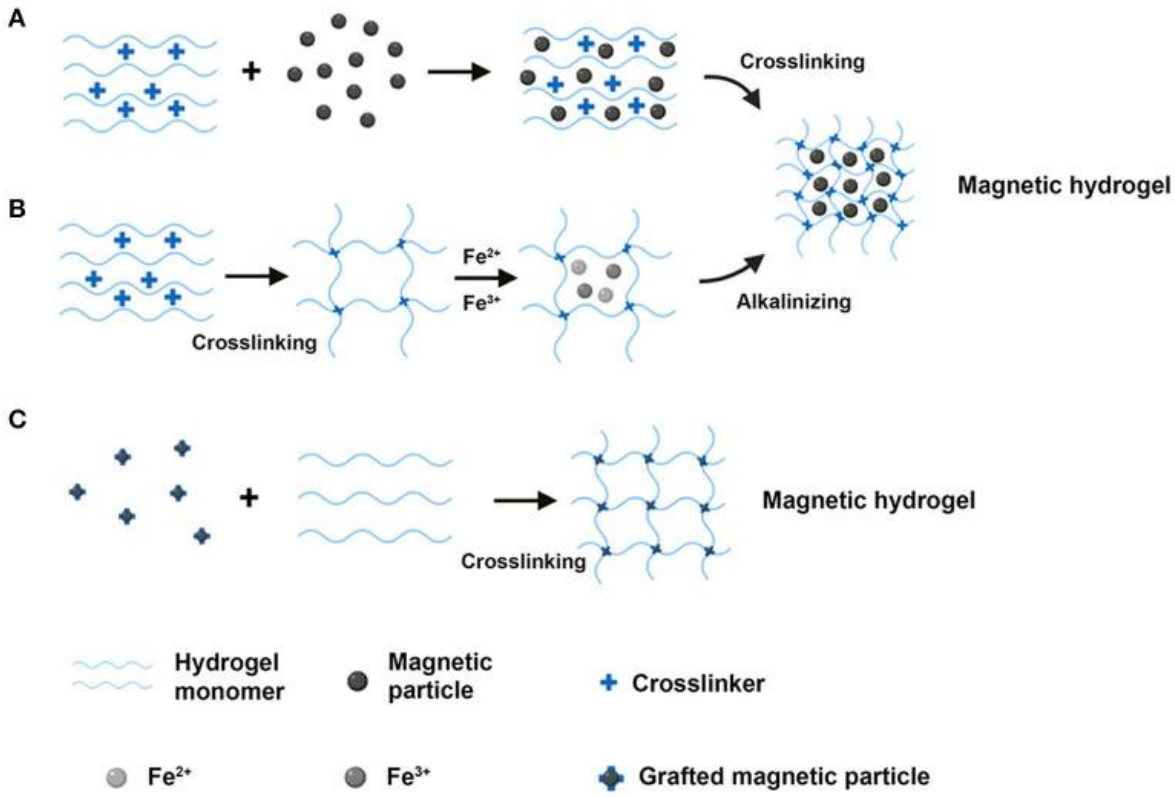

Figure 1-11: Schematic of the three main approaches used to fabricate magnetic hydrogels

Magnetic hydrogels are fabricated using three methods: [A] blending, which mixes a pre-made hydrogel and magnetic nanoparticles (MNPs); [B] *in situ* precipitation, where MNPs are formed directly within the hydrogel; and [C] the grafting onto method, in which MNPs are chemically bonded to polymer chains. Figure reproduced from Liu, et al., 2020.

The benefits of both hydrogels and MNPs can be combined, generating magnetic hydrogels. Magnetic hydrogels are composed of a matrix hydrogel with an additional magnetic component, and magnetic actuation is applied using an external field. The combination of a matrix hydrogel, internal and external magnetic components are more effective at enhancing osteogenesis than each component used in isolation (Yuan, et al., 2018). The preparation method of magnetic hydrogels can influence the responsiveness of MNPs. Zhang et al. (2015) utilised the *in situ* precipitation method to incorporate MNPs into a collagen type II-HA-PEG hydrogel, however the resulting MNPs exhibited paramagnetic behaviour. This is possibly related to particle (~15 nm) aggregation within the hydrogel (Zhang, et al., 2015).

Therefore, preparation method must be carefully selected, as they direct MNP dispersion and influence magnetic behaviour of, which in turn can influence the effectiveness of magnetic actuation.

Commitment to an osteogenic lineage has been confirmed in multiple studies utilising magnetic hydrogels. A study by Paun et al., (2018), showed that incorporation of MNPs into a 3D biometric structure, within a collagen matrix, accelerated cell differentiation of MG-63 osteoblasts *in vitro* after 30 days of magnetic stimulation. The study used MNPs synthesised through co-precipitation, with particle dimensions between 4-20 nm, and SMF stimulation between 100 and 250 mT. Embedded cells began to proliferate and differentiate faster in the 250 mT sample group in comparison to the lower magnetic field groups. A SMF of 250 mT showed an increase in production of ALP, which is secreted when the osteoblasts begin ECM development (Paun, et al., 2018). Similarly, Ma et al. (2022), developed a silk firoin based magnetic hydrogel, which showed upregulation of osteogenic genes and mineralisation in MSCs under a SMF over 21 days. While these studies highlight the upregulation of osteogenic markers, they fail to measure and identify any mechanical changes to the hydrogel which can influence cell behaviour and lineage commitment.

Mechanical effects were addressed by Abdeen et al., (2016) who developed a magnetic hydrogel, by embedding carbonyl iron (CI) nanoparticles within a polyacrylamide hydrogel. Using an increasing range of magnetic actuation, 100 mT-750 mT, they recorded an increase in hydrogel elasticity. The increase was attributed to the magnetic actuation, and was reversible upon decrease of external stimulation, allowing for tuneable modulation of elasticity (Abdeen, et al., 2016). This study also investigated RUNX2 expression by embedded MSCs, demonstrating that osteogenic gene expression could be upregulated in hydrogels with adjustable mechanical properties. However, the experimental design included only SMF controls and lacked non-magnetic hydrogel or MNP only controls. As a result, the individual contributions of MNPs, SMF exposure and mechanically induced stiffness changes cannot be fully distinguished, limiting interpretation of the mechanisms driving the osteogenic response. This represents a common limitation across magnetic hydrogel studies, where incomplete control conditions make it difficult to fully interpret magnetic and material driven effects on cell behaviour.

Bone tissue is highly vascularised and often studies fail to examine if their systems can support vascularisation in the developing tissue. Filippi et al., (2019) developed a magnetic hydrogel composed of PEG and PEG coated MNPs (15 nm, 1 mg/mL). In combination with

a SMF, they examined the potential of stomal vascular fraction to promote vascularisation within the tissue. The study found that SMF actuation promoted vasculogenic properties by increasing endothelial cell proliferation, indicating the potential of magnetic stimulation to support vascular development. Importantly the study also demonstrated its parallel osteogenic response under the same magnetic regime. Upregulation of key osteogenic markers and mineralisation was observed after 7 days 50 mT SMF exposure compared to non-stimulated controls (Filippi, et al., 2019). Together these findings suggest that magnetic hydrogels can support both osteogenic differentiation and early vascularisation, a critical requirement for effective bone tissue engineering.

Not all MSK tissues share the same biological requirements. In contrast to bone, cartilage and tendon are largely avascular and rely heavily on spatially graded mechanical cues to maintain function. As such, magnetic hydrogels have also been explored as tools to generate systems exhibiting phenotypic gradients characteristic of cartilage and tendon tissue, fields associated with BTE. Brady et al., (2015), developed a three-layered nanocomposite magnetic hydrogel in which agarose gels seeded with chondrocytes and dextran coated MNPs were exposed to a 500 mT SMF. This system successfully mimicked the biochemical gradients and depth dependent strain of articular cartilage while maintaining cell viability (Brady, et al., 2015); however, this study did not investigate the osteogenic potential of the hydrogels, instead focusing on chondrogenic outcomes. Similarly, Siliva et al. (2018) investigated a dual hydrogel system aimed at tendon to bone interface engineering using human tendon derived cells and human adipose derived stem cells. A magnetically responsive hydrogel composed of methacrylated chondroitin sulphate (MA-CS) and platelet lysate (PL), incorporating MNPs, was exposed to an oscillated magnetic field at 350 mT. This approach enabled the formation of a phenotypic gradient of the tendon to bone interface using a magnetic hydrogel, supported with the SMF (Silva, et al., 2018). While early osteogenic markers such as RUNX2 were not assessed, upregulation of the later osteogenic marker OPN was observed. Although this does not definitively confirm osteogenic differentiation due to OPNs dual role in both tendon and bone remodelling, the system demonstrates potential as a multifunctional platform relevant to bone tissue engineering.

Hydrogels have attracted attention in clinical applications due to their ability to serve as injectable, biocompatible scaffolds, while MNPs are widely used for their responsiveness to remote magnetic stimulation (Mandal, et al., 2020; Singh, et al., 2015). Combining these components, magnetic hydrogels enable minimally invasive delivery and conformal filling of complex defects, supporting osteogenic differentiation. However, translation to clinical

use faces challenges including nonuniform distribution of MNPs in some magnetic hydrogels preparations, limited load bearing capacity of hydrogels, and potential cytotoxicity or immune responses related to MNPs (Londhe, et al., 2025; Sharma, et al., 2015). Notably current clinical trials involving magnetic or hydrogel-based systems primarily target cancer therapies rather than MSK tissue engineering (Londhe, et al., 2025), highlighting a gap between experimental studies and clinical translation.

While magnetic hydrogels have demonstrated promising potential to enhance osteogenesis, promote mechanotransduction, and support vascularisation *in vitro*, these studies rely on continuous static magnetic stimulation or complex dynamic systems, which may be impractical for clinical applications. Additionally, previous studies have investigated multiple outcomes, including mechanical properties, osteogenic differentiation and vascularisation, however the effects of magnetic actuation on paracrine signalling, particularly EV production and cargo, remain largely unexplored.

This project addresses these gaps by developing magnetic GelMA hydrogels and investigating whether intermittent SMF actuation applied for short periods daily can achieve similar or enhanced effects compared to continuous static field exposure and dynamic magnetic field stimulation. In addition, we aim to elucidate effects of each component by including a range of controls covering effects of MNPs, SMFs and hydrogel models. By combining assessments of MSC proliferation, differentiation, mechanotransducive signalling and EV profiles under both static and dynamic magnetic fields, this work aims to provide insights into how each magnetic actuation field type may influence MSC behaviour and to inform the design of magnetic hydrogel systems for BTE applications.

If MSCs respond favourably to the applied regimes, magnetic stimulation could potentially be used as a preconditioning strategy to prime MSCs or hydrogels prior to implantation, reducing the need for sustained *in vivo* magnetic exposure. Wu et al. (2021), highlighted the potential of magnetic fields and MNPs to precondition MSCs promoting pro-regenerative paracrine signalling profiles that subsequently enhanced bone regeneration and wound healing. In combination with the injectable potential of hydrogels, this approach could allow preconditioned scaffolds to be delivered directly to defect sites.

1.5 Project Aims

This project is funded by the Engineering and Physical Sciences Research Council *via* the EPSRC-SFI Joint Centre for Doctoral Training in Engineered Tissues for Discovery, Industry and Medicine (lifETIME CDT).

In line with lifETIME CDT themes, this project aims to generate magnetic hydrogels for bone tissue engineering. In combination with external magnetic fields, these hydrogels are expected to accelerate osteogenic differentiation in bone marrow-derived MSCs. The aims and objectives of this project include:

- **Investigating MSC response to magnetic fields (Chapter 3)**
    - Assess MSC behaviour (proliferation, viability, cell cycle dynamics and migration) in response to static and dynamic magnetic fields to understand underlying mechanisms.
    - Examine early osteogenic commitment and potential key signalling pathways following magnetic activation
    - Investigate mechanotransduction-related intracellular responses, including YAP signalling and nuclear morphology.
    - Characterise changes in MSC-derived extracellular vesicle (EV) profiles, including EV size distribution and cytokine cargo, under magnetic stimulation.

- **Developing and characterising magnetic GelMA hydrogels (Chapter 4)**
    - Characterise fluidMAG-Dx nanoparticle morphology and magnetic properties
    - Incorporate magnetic nanoparticles (MNPs) into GelMA hydrogels and determine the optimal concentration that maintains mechanical stability and integrity.
    - Integrate MSCs into GelMA hydrogels (both as dispersed cells and spheroids) to assess biocompatibility
    - Evaluate the bioprinting potential of magnetic GelMA hydrogels and compare their mechanical properties with hand-cast gels

- **Investigating the effects of static magnetic stimulation in on MSCs within GelMA hydrogels (Chapter 5)**

- Assess early mechanical changes in GelMA hydrogels containing MNPs and MSCs (dispersed or spheroids) following exposure to a constant static magnetic field (SMF), to determine short term effects on hydrogel stiffness and viscoelasticity.
- Investigate osteogenic commitment of MSCs within GelMA hydrogels under an intermittent SMF (1 hour/day for 28 days) by:
  - Analysing expression of early and late osteogenic markers
  - Evaluating stem cell maintenance through stemness marker expression
  - Assessing calcium mineralisation within hydrogels *via* Alizarin Red S staining
- Characterise long term mechanical remodelling of magnetic hydrogels by MSCs under an intermittent SMF (1 hour/day for 28 days) through rheological analysis.

- **Investigating MSCs response to a dynamic magnetic field (Chapter 6)**
  - Prepare and characterise magnetic GelMA hydrogels using available crosslinking methods and equipment in host institute.
  - Integrate MSCs into the hydrogels and assess their biocompatibility.
  - Investigate the osteogenic response of MSCs embedded in magnetic GelMA hydrogels when exposed to dynamic magnetic fields.

Chapter 2: Materials and Methods

This chapter details the materials, techniques and core experimental procedures throughout the thesis. Variations specific to individual experiments are described within the relevant chapters. Information on biological and technical replicates is provided alongside the respective results to ensure clarity and reproducibility.

2.1 Cell Culture

This project utilises human mesenchymal stromal cells (MSCs) to investigate the effects of magnetic fields on osteogenic differentiation. All cell culture reagents and procedures are described below.

2.1.1 Mesenchymal Stromal Cell Culture: Cells and Reagents

Bone marrow-derived MSCs from multiple donors were used in the experiments described in subsequent chapters. An overview of donor information is provided in **Table 2-1**. Cells were cultured in standard mesenchymal stromal cell growth medium composed of Dulbecco's Modified Eagle Medium (DMEM) supplemented with 10% v/v foetal bovine serum (FBS) and additional supplements as detailed in **Tables 2-2** and **2-3**. All cell culture and cell incubation steps were carried out in a humidified incubator at 37°C with 5% CO_2, unless otherwise specified.

Cell	Donor Ref	Source	Donor Age / Sex / Ethnicity	Catalogue Number	Lot Number
MSC-BM-c	1	Bone Marrow / Femoral Head	80 / Male / Caucasian	C-12974	503Z017.1
	2	Bone Marrow / Femoral Head	64 / Female / Caucasian	C-12974	498Z010.2
	3	Bone Marrow / Femoral Head	80 / Male / Caucasian	C-12974	479Z025

Table 2-1: Overview of mesenchymal stromal cells used in this study

Details the source and donor information of mesenchymal stromal cells (MSCs) used throughout the study. MSCs were obtained from PromoCell GmbH (Germany) and used at passages 3-5 unless otherwise specified.

All experiments primarily used MSCs from Donor 1. Donors 2 and 3 were used in selected experiments to increase the number of biological replicates, as specified in the relevant sections. Unless otherwise stated, MSCs were utilised for experiments at passage 3 to 4 (counted from start of cell expansion).

Media Type	Component	Manufacturer, Catalogue Number	Volume/ Concentration
MSC Expansion 10% DMEM	Dulbecco's Modified Eagles Medium (DMEM)	Sigma-Aldrich, UK Cat No: D5671-500 mL	430 mL
	Foetal Bovine Serum (FBS)	Sigma-Aldrich, UK Cat No: F9665-500 mL	50 mL – 10% v/v
	Antibiotic Solution	Prepared in house (see Table 2-3)	5 mL – 1% v/v (see Table 2-3 for component concentrations)
	L-glutamine*	Sigma-Aldrich, UK Cat No: G7513-100 mL	5 mL – 2mM
	Sodium Pyruvate*	Sigma-Aldrich, UK Cat No: S8636-100 mL	5 mL – 1mM
	10X Minimum Essential Medium Non-essential Amino Acids (MEM-NEAA)	Gibco, UK Cat No: 11140-035	5 mL – 1X
EV Collection Media (10% DMEM-EV)	Dulbecco's Modified Eagles Medium (DMEM)	Sigma-Aldrich, UK Cat No: D5671-500 mL	430 mL
	Foetal Bovine Serum (FBS), exosome-depleted	Thermo Fisher, UK Cat No: A2720801	50 mL – 10% v/v
	Antibiotic Solution	Prepared in house (see Table 2-3)	5 mL – 1% v/v (see Table 2-3 for component concentrations)
	L-glutamine*	Sigma-Aldrich, UK Cat No: G7513-100 mL	5 mL – 2mM
	Sodium Pyruvate*	Sigma-Aldrich, UK Cat No: S8636-100 mL	5 mL – 1mM
	10X Minimum Essential Medium Non-essential Amino Acids (MEM-NEAA)	Gibco, UK Cat No: 11140-035	5 mL – 1X

Promocell Growth Media	MSC Growth Medium (PromoCell, Germany)	PromoCell, Germany Cat No: C-28009	10 - 20% v/v in MSC Expansion 10% DMEM
Osteogenic Media	MSC Expansion 10% DMEM	Prepared in house	473.5 mL
	Dexamethasone 21-phosphate disodium salt	Sigma-Aldrich, Spain Cat No: D1159	500 ul – 1.1µM
	L-Ascorbic acid 2-phosphate sesquimagnesium salt hydrate	Sigma-Aldrich, Spain Cat No: A8960-5G	1 mL – 0.11mM
	β-Glycerophosphate disodium salt hydrate	Sigma-Aldrich, Spain Cat No: G9422-10G	25 mL – 52.8mM

Table 2-2: Composition of mesenchymal stromal cell culture media

Details the formulations used for (i) mesenchymal stromal cell expansion media, (ii) extracellular vesicle collection medium with specific serum conditions detailed (iii) Promocell Growth Media for further expansion and (iv) osteogenic media for positive differentiation control. *Supplements were only added if basal DMEM formulation lacked L-glutamine or sodium pyruvate.

Reagent	Component	Manufacturer, Catalogue Number	Volume/ Concentration
Trypsin/PBS Solution	Trypsin/EDTA Solution	Sigma-Aldrich, UK Cat No: T4049	2 mL – 10% v/v
	Dulbecco's Phosphate-Buffer Solution (PBS) without Ca^{++}/Mg^{++}	Gibco, UK Cat No: 12559069	18 mL – 90% v/v
Cell Freezing Suspension	Foetal Bovine Serum (FBS)	Sigma-Aldrich, UK Cat No: F9665-500 mL	90% v/v
	Dimethyl sulfoxide (DMSO)	Fisher Scientific, UK Cat No:	10% v/v
Antibiotic Solution	Penicillin-Streptomycin	Sigma-Aldrich, UK Cat Not: P0781-100 mL	89 units/mL, / 89 µg/mL
	Amphotericin B	Gibco, UK Cat No: 15290-026	0.27 µg/mL
Buffer Solution	Dulbecco's Phosphate Buffer Solution (PBS) without Ca^{++}/Mg^{++}	Gibco, UK Cat No: 12559069	1X

Table 2-3: Cell culture reagents and buffer solutions

Summarises key reagents, media supplements and buffer compositions used throughout the study during all stages of cell culture.

2.1.2 Mesenchymal Stromal Cell Culture: Thawing, Expansion and Freezing

PromoCell MSCs were stored at -150°C upon delivery. For use, cryovials were rapidly thawed in 37°C water bath, and cell freezing suspension was diluted with 1 mL of 10% DMEM before transfer to a 20 mL universal containing pre-warmed media. Cells were then centrifuged at 350 g for 5 minutes at room temperature to pellet. The supernatant was aspirated, and the pellet resuspended in antibiotic free media and seeded into T75 or T150 tissue culture flasks, then incubated at 37°C and 5% CO_2. Thawed cells were cultured for 24 hours post thawing in antibiotic free media to identify any underlying cell infections prior to freezing. Following 24 hours of incubation, the culture media was inspected for signs of contamination. Cultures confirmed to be free of contamination were subsequently transferred to 10% DMEM supplemented with antibiotics.

Cells were then initially expanded by using PromoCell Growth Media (PromoCell, Germany), following by MSC expansion media until 80-90% confluency before passaging. For both passaging and freezing, expanded cells were detached by incubating with trypsin/phosphate-buffered solution (PBS) (**Table 2-3**) at 37°C for 3 minutes, pelleted by centrifugation, and resuspended in fresh media for culture, or in 1 mL of cell freezing suspension for cryopreservation. Cryovials were frozen at -80°C overnight using a controlled-rate freeing container, and transferred to -150°C for long term storage

2.1.3 Spheroid Formation of MSCs

MSC spheroids were generated using AggreWell™ 400 24-well microwell confinement plates (StemCell Technologies, UK). Prior to seeding, microwell plates were prepared according to the manufacturer's instructions by washing with anti-adherence rinsing solution (StemCell Technologies, UK) to prevent cell attachment. Cells were seeded at a density of 3.6 x 10^5 cells per well (approximately 300 cells per microwell) in 10% DMEM without FBS to promote spheroid formation. Plates were incubated at 37°C in 5% CO_2 for 24 - 48 hours to allow spheroid formation, confirmed with light microscopy. For collection, spheroids were gently harvested using P1000 pipette tips cut approximately 5 mm from the distal end. Prior to use, pipette tips were coated with 10% FBS v/v in PBS to minimise cell attachment and spheroid disruption during transfer. Spheroids were then concentrated by filtration using a 60 µm pluriStrainer (pluriSelect, Germany) and counted manually under light microscopy before use in downstream assays.

2.2 Cell Analysis

2.2.1 Cell Viability Assay

MSC viability was evaluated using the LIVE/DEAD™ Viability/Cytotoxicity Kit (Invitrogen, L3224) which enables the simultaneous detection of live and dead cells through dual fluorescent staining. The kit employs two fluorogenic dyes: Calcein AM, a non-fluorescent, cell permeant compound that is hydrolysed by intracellular esterases into a green, fluorescent signal in viable cells; and Ethidium homodimer-1 (EthD-1), which can only penetrate compromised cell membranes, binding to nucleic acids to produce a red fluorescent signal in dead cells. Monolayer cells, cells and spheroids encapsulated in hydrogels were incubated in 10% DMEM containing 2 µM Calcein AM and 4 µM EthD-1 at 37°C for 20 minutes prior to imaging.

Following incubations, fluorescence imaging was performed using an EVOS™ M7000 imaging system with Green Fluorescent Protein (GFP) and Texas Red filter cubes to detect green and red fluorescent, respectively (**Table 2-4**). Acquired images were analysed using ImageJ software (version 1.54) following a thresholding-based protocol to distinguish and count live and dead cells. Cell viability was quantified as the percentage of live cells relative to total number of cells across multiple fields of view. For spheroid analysis, three-dimensional image stacks (z-stacks) were acquired to assess spatial distribution of viable and non-viable cells within the spheroid structure. Cross sectional fluorescence intensity profiles of green and red fluorescence were extracted to evaluate cell viability gradients, with particular focus on the identification and characterisation of necrotic core formation.

Light Cube	Colour	Excitation	Emission	Cat Number
GPF	Green	482/25 nm	524/24 nm	AMEP4951
Texas Red	Red	585/29 nm	628/32 nm	AMEP4955
DAPI	Blue	357/44 nm	447/60 nm	AMEP4950

Table 2-4: Fluorescence filter cubes and specifications for EVOS M7000 imaging system

Outlines the fluorescent light/filter cubes used for imaging cell samples with the EVOS M700 fluorescent microscopy system

2.2.2 Immunofluorescence

To investigate Yes-associated protein (YAP) subcellular localisation and nuclear morphology, MSCs were seeded into 96 well plates at density a of 1.56 x 10^4 cells/cm^2. The

four experimental conditions were applied, and cell samples were collected at time points: 2, 6, 24, 48 and 72 hours.

At the designated endpoints, cells were washed with PBS and fixed with 3.7-4.1% v/v formaldehyde in 2% w/v sucrose/PBS for 15 minutes at 37°C. Immunofluorescence staining was performed on cultures to visualise nuclear, cytoskeletal and intracellular proteins.

Following fixation, samples were incubated with 20 mM Glycine for 5 minutes to remove residual fixative and washed three times with PBS. Cells were then permeabilised for 5 minutes at 4°C using 0.5% v/v Triton in PBS, then blocked with 1% w/v bovine serum albumin (BSA) in PBS to minimise non-specific antibody binding. The primary antibody, a mouse monoclonal (IgG1) anti-YAP (Proteintech), was diluted 1:1600 in 1% w/v BSA/PBS and applied to samples, incubated for 1 hour at 37°C, then washed three times with 1% w/v BSA/PBS. Secondary staining was performed using a conjugated donkey anti-mouse secondary (IgG, H+L) (ThermoFisher) at dilution 1:1000 in 1% w/v BSA/PBS for 30 minutes at 37°C. Simultaneously, conjugated phalloidin-488 (Proteintech) was applied at 1:500 for F-actin visualisation. Following incubation, samples were washed three times with 1% w/v BSA/PBS and nuclei were counterstained with one drop of Hoechst for 15 minutes at room temperature, followed by a final PBS wash. Mounting media (60% v/v Glycerol/PBS) was applied prior to imaging.

Fluorescence imaging was performed using an EVOS™ M7000 imaging system equipped with GFP, DAPI, Texas-Red filter cubes to detect green, blue and red fluorescent, respectively (**Table 2-4**). Acquired images were analysed with Image J software. Nuclear morphology was assessed using DAPI-channel images, with measurements of nuclear circularity and area. YAP localisation was evaluated using Texas-Red (YAP) and DAPI (nuclear) channels. The total YAP fluorescence per cell and nuclear YAP fluorescence were quantified, and nuclear translocation of YAP was calculated as the ratio of nuclear to total YAP signal.

Step	Reagent	Supplier	Catalogue Number	Concentration/ Volume
Fixation	Dulbecco's Phosphate Buffer Solution (PBS) without Ca^{++}/Mg^{++}	Gibco, UK	12559069	1X
	Formaldehyde (Methanol Free)	ThermoFisher, UK	28906	4% w/v in PBS
	Glycine	Gibco, UK	12559069	20 mM in PBS
Permeabilisation	Dulbecco's Phosphate Buffer Solution (PBS) without Ca^{++}/Mg^{++}	Gibco, UK	12559069	1X
	Triton X-100	Sigma Aldrich, UK	T9284-100 mL	0.5% in PBS
Blocking & Wash	Dulbecco's Phosphate Buffer Solution (PBS) without Ca^{++}/Mg^{++}	Gibco, UK	12559069	1X
	Bovine Serum Albumin	Sigma Aldich, UK	A7906-100G	1% w/v in PBS
Antibodies	YAP1 Monoclonal antibody (Mouse / IgG1)	Proteintech, UK	66900-1-Ig	1:1600
	AlexaFluore, 594 anti-mouse (Donkey/IgG)	ThermoFisher, UK	A32744	1:1000 in 1% w/v BSA/PBS
	CoraLite Plus 488- Phalloidin (green)	Proteintech, UK	PF00001	1:500 in 1% w/v BSA/PBS
Nuclear Stain	Hoechst, NucBlue™ Live Cell Stain ReadyProbes™ reagent	Invitrogen, UK	R37605	1X
Mounting Medium	Dulbecco's Phosphate Buffer Solution (PBS) no calcium, no magnesium	Gibco, UK	12559069	1X
	Glycerol	Fisher Scientific, UK	10795711	200mM in PBS

Table 2-5: Immunofluorescence reagents used in this study

Lists the antibodies, stains and reagents used for immunofluorescence procedures throughout the study

2.2.3 Wound Healing (Scratch Assay)

To assess the migratory capacity of MSCs, a wound healing (scratch) assay was performed. MSCs were seeded onto 6 well culture plates at a density of 3.13 x 10^4 cells/cm^2 and cultured over 48-72 hours to full confluency. Mechanical wounding was performed using a P200

pipette tip to create six intersecting linear wounds per well, three horizontal lines and three vertical lines, across the monolayer surface **(Figure 2-1)**. Plates were then subjected to one of four experimental conditions.

At predetermined time points (2, 6, 24, 48 and 72 hours) five wells per were harvested for MSC gene expression analysis. For RNA extraction, 350 µL of Buffer RLT (Qiagen, UK) was added directly to each well, and cells were gently detached using a sterile cell scraper to ensure complete lysis. The resulting cell lysate was transferred to sterile Eppendorf tubes and immediately stored at -80°C until RNA extraction and isolation.

The remaining well was reserved for visualisation of MSC migration. At each timepoint, the well was fixed and stained with crystal violet, and images of the wound area were captured. An additional 0-hour reference image was acquired immediately following scratch formation to facilitate comparative scratch analysis of wound closure over time.

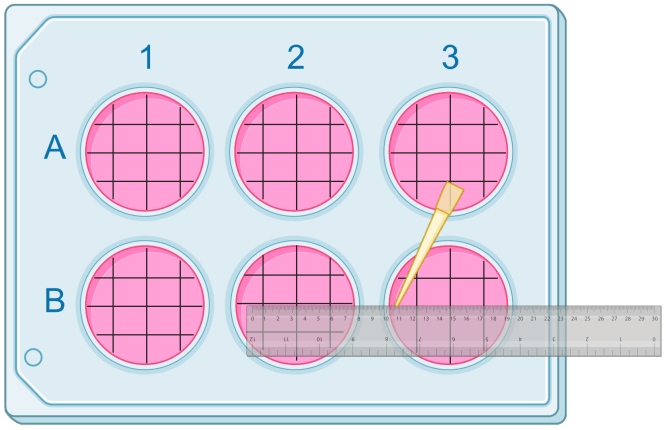

Figure 2-1: Schematic of scratch assay experimental layout

Schematic of the scratch assay technique used in 6 well plates. The diagram illustrates the typical orientation and distribution of scratches within each well. Created with Biorender.com

2.2.4 Crystal Violet Staining and Wound Healing Analysis

Following RNA lysis of designated wells, cell culture media was aspirated from the remaining wells and the monolayers washed gently with PBS. Crystal violet staining solution (Sigma-Aldrich) (~500 µL per well) was added to fully cover the surface of standard 6-well plates and samples were incubated with the stain for 30 minutes at room temperature. After incubation the stain was removed, and wells were repeatedly washed in dH_20 to remove residual stain and then airdried overnight at room temperature.

Imaging of the scratch area and cell migration was performed using the EVOS™ M7000 imaging system under brightfield mode. Acquired images were analysed with ImageJ software (version 1.54) employing the "MRI Wound Healing" macro (sourced from GitHub). Wound area at each timepoint was quantified and expressed as a percentage of the initial scratch area.

2.2.5 RNA Extraction and Isolation (Monolayer and Hydrogels)

Total RNA was extracted from the MSC monolayers and hydrogel encapsulated MSCs using the RNeasy Micro kit (Qiagen, UK) following the manufacturers protocol. Monolayer cells were prepared for RNA extraction using Buffer RLT (Qiagen) while hydrogel-encapsulated cells were processed using TRIZOL reagent (Invitrogen). For monolayer samples, 350 µL of 70% v/v ethanol was added to the lysate. For TRIzol-processed samples an equal volume of 70% v/v ethanol was added to the aqueous phase obtained following chloroform induced phase separation. Each sample was then transferred to RNeasy spin columns and centrifuged to allow RNA binding to the membrane; the flow through was discarded. Columns were then washed with 350 µL of Buffer RW1 and centrifuged. To eliminate genomic deoxyribonucleic acid (DNA) contamination, 80 µL of DNase I solution (prepared as a 1:8 dilution in Buffer RDD) was applied directly to the membrane. Samples were incubated at room temperature for 15 minutes. Following DNase digestion, columns were washed with buffer RW1 and centrifuged.

At this stage, collection tubes were discarded and columns placed into new collection tubes and buffer RPE was added, and columns were centrifuged. The flow through was discarded, and 500 µL of 80% v/v ethanol was added to each column, followed by another centrifuge step. Columns were placed into new collection tubes, lids were opened, and columns were centrifuged at full speed for 5 minutes to dry the membrane. Subsequently, columns were transferred to new RNase-free collection tubes, and the RNA was eluted by adding 14 µL of RNase free water to the column membrane and centrifuging. RNA concentration and purity was assessed using a NanoDrop™ spectrophotometer (Thermo Fisher Scientific). All samples were normalised to equal RNA input concentrations prior to reverse transcription and stored at -80°C prior to complementary DNA (cDNA) synthesis.

2.2.6 Reverse Transcription

cDNA synthesis was performed using the QuantiTect Reverse Transcription Kit (Qiagen) following the manufacturer's protocol. All reagents, including RNA samples, were thawed and kept on ice throughout processing. RNA samples were first diluted with RNase-free water to a predetermined concentration, normalised across all samples. To remove residual genomic DNA, 2 µL of genomic DNA wipe out buffer was added to each reaction. Samples were incubated at 42°C for 2 minutes to eliminate any residual genomic DNA, then immediately transferred to ice.

The reverse transcription mix was prepared by adding 1 µL of Quantiscript Reverse Transcriptase, 4 µL of Quantiscript RT Buffer, and 1 µL of RT Buffer Mix to each RNA sample bringing the reaction volume to 20 µL. Reverse transcription was carried out at 42°C for 15 minutes to synthesise cDNA, followed by 95°C for 3 minutes to inactive the reverse transcriptase. Synthesised cDNA was stored at -20°C prior to qPCR.

2.2.7 Real-Time Quantitative Polymerase Chain Reaction

Real-time quantitative reverse transcription polymerase chain reaction (RT-qPCR) was performed using the 7500 Real-Time PCR Systems (Applied Biosystems, UK). Reactions were carried out in a final volume of 20 µL, comprising 10 µL SYBR Green Master Mix (Applied Biosystems, UK), 0.1 µL forward primer (50 nM), 0.1 µL reverse primer (50 nM), 7.8 µL RNase free H_20 and 2 µL of template containing 4 ng of total cDNA. Cycling parameters and primer sequences used are found in **Tables 2-6** and **2-7** respectively.

Stage	Temperature (°C)	Time	Cycles
Hold	95	20 seconds	1
Cycling	95	3 seconds	40
	60	30 seconds	
Melt Curve	95	15 seconds	1
	60	60 seconds	
	95	15 seconds	
	60	15 seconds	

Table 2-6: RT-qPCR cycling conditions

Details the thermal cycling conditions used for fast RT-qPCR on the Applied Biosystems 7500 system including each stage of the protocol and its parameters

Gene	Forward	Reverse
ALCAM	TTCCAGTCCCTCTACTCAGAGC	TTCCAGTCCCTCTACTCAGAGC
ALP	ACCACCACGAGAGTGAACCA	CGTTGTCTGAGTACCAGTCCC
GAPDH*	TCCAAAATCAAGTGGGGCGA	AAATGAGCCCCAGCCTTCTC
MMP-2	AGCGAGTGGATGCCGCCTTTAA	CATTCCAGGCATCTGCGATGAG
MMP-9	GCCACTACTGTGCCTTTGAGTC	CCCTCAGAGAATCGCCAGTACT
Nestin	GGGATGGCTGGAGTGGAAAA	CTGCTCTACCACCTCCTCCT
Osteocalcin	CACTCCTCGCCCTATTGGC	CCCTCCTGCTTGGACACAAAG
Osteopontin	GAAGTTTCGCAGACCTGACAT	GTATGCACCATTCAACTCCTCG
RhoA	TCTGTCCCAACGTGCCCATCAT	CTGCCTTCTTCAGGTTTCACCG
Rac1	CGGTGAATCTGGGCTTATGGGA	GGAGGTTATATCCTTACCGTACG
RUNX2	CCCAGTATGAGAGTAGGTGTCC	GGGTAAGACTGGTCATAGGACC

Table 2-7: RT-qPCR gene primers and sequences

Lists the genes and their corresponding forward and reverse primers used for RT-qPCR. *Denotes housekeeping gene

Quantitative gene expression was determined using the comparative Ct (ΔΔCt) method. Ct values for each target gene were first normalised (ΔCt) to the Ct value of the housekeeping gene, used as an internal control. The relative expression levels were then calculated by comparing the ΔCt of treated samples to the corresponding ΔCt of the control group to obtain ΔΔCt values. Relative gene expression was expressed as $\log_{10}$ fold change, calculated as $\log_{10}(2^{-\Delta\Delta Ct})$, equivalent to $-\Delta\Delta Ct \times \log_{10}2$.

All primer pairs were obtained from the research centre's validated primer pool, which have been previously tested for specificity and amplification efficiency. These efficiencies are sufficiently similar to allow the use of the ΔΔCt for relative quantification, which assumes that target and reference genes amplify at comparable rates to produce accurate fold change measurements (Livak & Schmittgen, 2001).

2.2.8 Fluidigm RT-qPCR

MSCs were seeded into T75 cell culture flasks at a density of 1.33×10^4 cells/cm^2 and cultured to full confluency over 24-72 hours. Flasks were then subjected to one of four experimental conditions for three time points (day 1, day 3, and day 7). At each end point, cells were lysed using Buffer RLT (Qiagen) and processed through RNA extraction and cDNA synthesis as previously described.

Samples were subsequently prepared for Fluidigm™, a microfluidic high throughput RT-qPCR platform, following the manufacturers protocol. The preparation included the following steps:

1. Specific Target Amplification (STA)
2. Exonuclease I Treatment
3. Preparing Sample Pre-mix and Samples
4. Preparing Assay Mix
5. Priming and Loading of the 96:96 Dynamic Array Integrated Fluidic Circuit (IFC)

2.2.8.1 Specific Target Amplification (STA)

In an RNase-free Eppendorf, 1 µL of each forward and reverse primer was pooled (96 primer pairs; 192 primers), with DNA suspension buffer to create a primer mixture. For each sample, the STA reaction was prepared in a final volume of 5 µL, consisting of 2.5 µL TaqMan™ PreAmp Master Mix, 0.5 µL primer mixture (final concentration 500 nM), 0.75 µL RNA-free H_20 and 1.25 µL of cDNA sample. The reaction was vortexed, centrifuged and processed using a thermal cycler under the conditions outlined in Table 2-10. This step enhances the expression of specific target genes for improved detection from low-input cDNA.

Condition	**Hold**	**Cycles (10-14)**		**Hold**
Temperature (°C)	95	95	60	4
Time	10 minutes	15 seconds	4 minutes	∞

Table 2-8: Thermal cycling protocol for specific target amplification using the Fluidigm technique

Details the amplification parameters used in the Fluidigm protocol for specific target pre-amplification

2.2.8.2 Exonuclease I Treatment

To remove any unincorporated primers, 2 µL of exonuclease reaction mix was added to each sample. The reaction mix consisted of 1.4 µL RNase-free H_20, 0.2 µL Exonuclease I reaction buffer, and 0.4 µL of Exonuclease I (final concentration 4 U/µL). Samples were vortexed and centrifuged and incubated in thermal cycler under the conditions described in Table 2-11. Following treatment, samples were diluted 1:5 with TE buffer (TEKnova) and stored at -20°C until loading onto the array.

Condition	Digest	Inactive	Hold
Temperature (°C)	37	80	4
Time	30 minutes	15 minutes	∞

Table 2-9: Thermal cycling protocol for Exonuclease I treatment, Fluidigm

Outlines the thermal cycling steps used for exonuclease digestion in the Fluidigm protocol

2.2.8.3 Preparing Sample Pre-mix and Samples

To prepare samples for loading, 2.25 µL of each STA and Exonuclease I treated sample was combined with 2.75 µL of Sample Pre-Mix to a final volume of 5 µL. The Sample Pre-Mix consisted of 2.5 µL of 2X SsoFast EvaGreen Supermix with Low Rox, and 0.25 µL of DNA binding Dye Sample Loading Reagent. Each 5 µL sample mix solution was vortexed for at least 20 seconds, briefly centrifuged and storing on ice until loading onto the array.

2.2.8.4 Preparing Assay Mix

For each gene, a combined forward and reverse primer mix (100 µM) was diluted to a working concentration of 5 µM. Each 5µL assay mix was prepared by combining 0.25 µL of the primer, 2.25 µL of 1X DNA Suspension Buffer, and 2.5 µL 2X Assay Loading Reagent. The primer assay mix was vortexed, centrifuged and kept on ice while the chip was being primed.

2.2.8.5 Priming and Loading of the 96:96 Dynamic Array IFC

Priming: To prepare the 96:96 Dynamic Array IFC, control line fluid was injected into each accumulator on the chip. The chip was then placed into the IFC Controller HX and primed using the Prime (136x) script, according to the manufacturer's instructions.

Loading: Following priming, 5 µL of each prepared assay mix was loaded into the designated assay inlets, and 5 µL of each sample mix was loaded into the sample inlets (**Figure 2-2**).

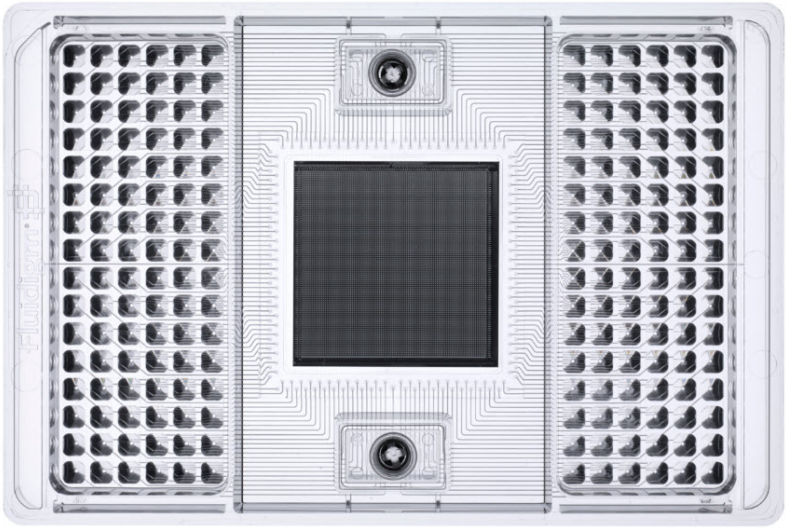

Figure 2-2: Fluidigm, 96:96 Dynamic array integrated fluidic circuit

The 96:96 dynamic array was utilised in this study. The assay inlets are on the left, sample inlets on the right.

The array was run in the BioMark HD system following the protocol for the following cycling parameters in **Table 2-10**.

Type	Temperature (°C)	Duration (seconds)	BioMark HD Ramp Rate (°C/s)
Thermal Mix	70	2400	5.5
	60	30	5.5
Hot Start	95	60	5.5
PCR (30 cycles)	96	5	5.5
	60	20	5.5
Melting Curve	60	3	1
	60-95	3	1

Table 2-10: Cycling parameters for 96:96 Fluidigm Dynamic Array

Details the thermal cycling protocol used for RT-qPCR on the Fluidigm platform for the 96:96 dynamic array

2.2.9 Cytokine Array

MSCs were seeded into T75 cell culture flasks at a density of 1.33 x 10^4 cells/cm^2 and cultured to full confluency over 24-72 hours. Flasks were then subjected to one of four experimental conditions for three time points - day 1 (24 hours), day 3 (72 hours) and day 7. At 24 hours prior to end point, cell culture media was replaced with 10% DMEM -EV. At end timepoints, the conditioned media was collected into low protein binding falcon tubes

and stored at -80°C until further processing for cytokine array analysis. A media only control (DMEM-EV) was also collected to account for background signal and media derived cytokines.

The Proteome Profiler™ Human XL Cytokine Array Kit (Biotechne, UK) was used to evaluate relative cytokine expression levels in the conditioned media. Each Human XL Cytokine Array membrane was first incubated with 2 mL of Array Buffer 6 (blocking buffer) for 1 hour on a rocking platform shaker using the supplied 4 well membrane dish. All subsequent incubations and washes were held on rocking platform shakers at room temperature unless otherwise specified. One membrane was used per sample. For each sample, 500 µL of conditioned media was mixed with 1000 µL of Array Buffer and incubated overnight at 4°C.

Following incubation, membranes were placed into Petri dishes and washed three times with 1X wash buffer, each lasting 10 minutes. Membranes were then transferred back to cleaned membrane wells and incubated with 30 µL of Detection Antibody Cocktail diluted in 1.5 mL of 1X Array Buffer 4/6 for 1 hour. After incubation, membranes were again washed three times and then incubated with 2 mL of 1X Streptavidin-HRP solution for 30 minutes. A final set of three washes was performed.

Each membrane was transferred to a plastic sheet protector, and 1 mL of Chemi Reagent Mix was applied evenly across the membrane surface. Bubbles were carefully smoothed out, and membranes incubated with the reagent for 1 minute before removing excess liquid. Membranes were then completely sealed and exposed to X-ray film using a Li-Cor imaging system for 10 minutes to visualise chemiluminescent signal.

2.2.10 Micro BCA Protein Assay

To quantify the protein content of cell supernatants or within extracellular vesicle preparations, the Micro BCA™ Protein Assay Kit (Thermo Fisher, UK) was used. A standard curve was prepared using serial dilutions of BSA. Working reagent was freshly prepared by combining Reagents MA, MB and MC in a 25:24:1 ratio immediately prior to use. BSA standards and experimental samples were plated in triplicate and mixed with the working reagent. Plates were incubated at 37°C for 2 hours, then cooled to room temperature. Absorbance was measured at 562 nm using a plate reader, and protein concentrations were calculated from the standard curve.

2.2.11 MSC Extracellular Vesicles

MSCs were seeded into T75 cell culture flasks at a density of 1.33 x 10^4 cells/cm^2 and cultured to near confluency using 10% DMEM-EV. Flasks were then subjected to one of four experimental conditions for a duration of 8 days. Conditioned media (15 mL) was collected from six flasks at 48 hour intervals into low protein binding falcon tubes and stored at -80°C until EV isolation. EV isolation and characterisation were carried out with the support of PhD students Justine Clarke and Eva Bochti from within the Berry group; with a grateful acknowledgement that the following EV protocols were developed and optimised by both Justine and Eva.

2.2.11.1 EV Isolation

Once media collection for all conditions was completed, conditioned media was processed using differential centrifugation. Conditioned media was centrifuged at 300 g for 5 minutes, and decanted into new falcon tubes, the resultant pellet was discarded. Further centrifugation was completed at 2000 g for 20 mins, after which the pellet was discarded and media decanted into a new low protein binding falcon.

EVs were then concentrated from ~400 mL media using Tangential Flow Filtration (TFF), an ultrafiltration method, using the MasterFlex L/S pump system (Cole-Parmer). TFF was set up utilising a VivaFlow 50R TFF Cassettes (Sartorius, Germany) as a filter. The pump system was set up at 200 rpm, and the cassette was flushed with water to remove residual reagents from cassette storage. The cassette was drained, and filtration was began using conditioned media. A first diafiltration was completed to remove residual proteins in the conditioned media. Sample was then concentrated until ~20 mL remained. To retrieve any residual/remaining EVs from the membrane, an equal volume of PBS was added to the filtrate and concentrated to 20 mL. After filtration, the remaining solution ~20 mL was centrifuged in ultrafiltration 100kDa columns at 5000 g for 10-30 minutes at 4°C to until sample was concentrated sample to 500 µL.

Following concentration, EV samples (500 µL) were further purified using size exclusion chromatography (SEC) with the Automatic Fraction Collector (AFC) (IZON, New Zealand). This method separates particles in the approximate range of 30-350 nm, enabling enrichment of exosome-sized vesicles while removing contaminating proteins. The column (qEV Original Gen 2 35 nm) was pre-equilibrated by flushing with 17 mL of sterile PBS prior to sample application. The entire concentrated sample (500 µL) was then applied to the column,

following by topping with PBS to initiate elution. Eluted fractions of 0.5 mL were automatically collected using the AFC, with a void volume of approximately 2.9 mL. Fractions 1 to 4, corresponding to the expected EV size range, were pooled, yielding a final volume of approximately 2 mL. Purified EV samples were then transferred to low protein binding Eppendorf's and stored at 4°C until EV characterisation.

2.2.11.2 EV Characterisation

Nanoparticle tracking analysis (NTA) was used to characterise EVs using Zetaview (Particle Metrix, Germany). NTA is a widely used technique that enables measurements of the size distribution and concentration of nanoparticles in suspension by tracking their Brownian motion. The movement of individual particles is tracked and recorded using a laser light scattering microscope and video camera, and analysed using the Stokes-Einstein equation, relating particle diffusion to size. From this, key parameters such as particle area, concentration and distribution profile can be derived. For EV analysis, samples were diluted in filtered PBS to concentration range between 10^6-10^9 particles/mL. Measurements were completed three times for each condition

Tuneable resistive pulse sensing (TRPS) was completed using the Exoid TRPS instrument (Izon, New Zealand). Utilising a combination of pressure and voltage, it drives particles through a nanopore with specified diameter. Each particle is detected passing through the pore, causing blockade signal – the magnitude of which is directly proportional to the particle size. Concentration of the sample is correlated from the frequency of the blockade. Calibration beads of known sizes and concentrations are measured after the sample for precision in measurements. For analysis, EV samples were diluted in PBS to final concentrations between 7.5×10^7 - 1.1×10^8 for TRPS.

2.3 Magnetic Fields

Magnetic fields, both static and dynamic, were used as external stimuli in this study to modulate MSC behaviour. The following sections detail the two magnetic systems employed: a static magnetic field system based on permanent magnetic arrays, and a dynamic magnetic field bioreactor based on mechanical displacement of system of neodymium iron boron magnets (*via* a research collaboration). All magnetic exposures were applied at 37 °C, 5% CO_2; the bioreactor was employed in a non-humidified incubator.

2.3.1 Static Magnetic Field

A static magnetic field (SMF) was applied by using neodymium iron boron (NdFeB) magnets arranged in 24 well and 96 well formats, with alternating north and south polarities. The magnetic plates (MagnetoFACTOR-24 /-96) were sourced from Chemicell, Germany (**Figure 2-3**). SMF exposure was achieved by placing the magnetic plates beneath tissue culture well plates; the 24 well array was specifically used for 24 well culture plates, while the 96 well array was recommended for all other culture plate layouts (6, 12, 48 or 96 wells) as well as T75 flasks. The magnetic field strength at the surface of standard tissue culture plastic was measured using a transverse probe HIRST GM08 Gaussmeter and determined to be approximately 370 mT. SMF exposure was applied either intermittently (Int SMF) for 1 hour per day, or constantly (Con SMF) for the full duration of the experiments.

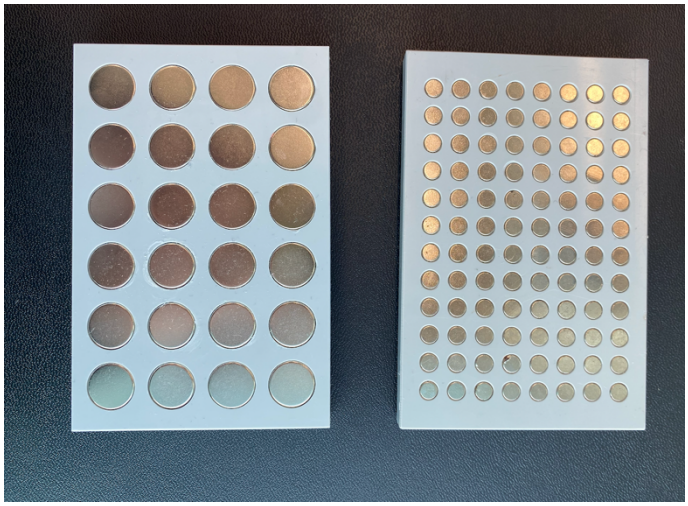

Figure 2-3: MagnetoFACTOR plates for static magnetic field applications

MagnetoFACTOR plates-24/-96 (left and right, respectively) were sourced from Chemicell, Germany. These plates were utilised for static magnetic field applications

2.3.2 Dynamic Magnetic Field Bioreactor

A dynamic magnetic field (DMF) was applied using a custom bioreactor from the Centro de Biomateriales e Ingeniería Tisular, Universitat Politècnica de València, in collaboration with Dr Gloria Gallego Ferrer, Dr Jose Luis Aparicio Collado, and Dr Arantxa Martínez Férriz. The DMF bioreactor, developed by BCMaterials (Basque Country, Spain), consists of a 48well NbFeB magnet array and applies displacement of the array beneath stationary tissue culture plates/flasks. Culture plates were position in a designated holder above the magnet array (**Figure 2-4, A**).

Magnetic stimulation was applied as follows:

- **Displacement**: The magnetic array oscillated horizontally back and forth over a 10 mm path along a single plane below the culture plates. This oscillatory motion occurred continuously during each 5-minute active stimulation period.
- **Field strength**: The magnetic field strength varied from 0 mT (space between magnets) and 23 mT (directly above magnets). As the magnet array displaced, cells experienced a dynamically changing field from 0-23 mT.
- **Exposure schedule**: Stimulation was applied intermittently in 30 minute cycles with 5 minutes of oscillating magnetic field followed by 25 minutes of rest, repeated over a 16 hour daily active period. Following this was an 8-hour period of no stimulation (**Figure 2-4, B**).
- **Control of parameters:** All displacement cycles and timing were controlled *via* the bioreactor software, allowing specification of displacement (mm), cycle duration (min), active/rest timing and oscillation direction.

[A]

[B]

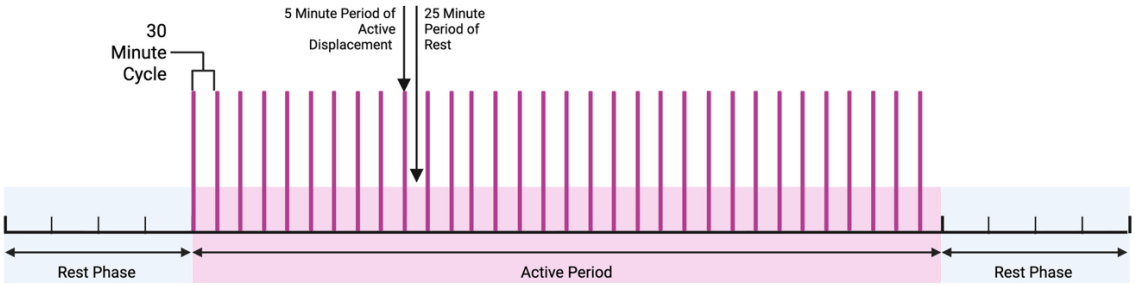

Figure 2-4: Dynamic magnetic field bioreactor for application of oscillating magnetic field

An oscillating dynamic magnetic field was applied utilising a custom built dynamic field bioreactor. [A] The bioreactor contained a 48 well NbFeB magnetic plate that was displaced below cell culture plates/flaks. [B] The applied regime consisted of a 16-hour active period, followed by an 8-hour rest phase. During the active period, the bioreactor operated 30-minute cycles, each comprising 5 minutes of magnetic displacement, and 25 minutes of rest. This pattern was repeated continuously throughout the experimental duration. Created with Biorender.com

2.3.3 Experimental Conditions

The following experimental conditions were assessed throughout this study, using magnetic arrays described in Sections 2.3.1 and 2.3.2:

- **Control** – standard conditions without magnetic field exposure
- **Intermittent static magnetic field** (**Int SMF**) – magnetic field (370 mT) applied for 1 hour per day using the NdFeB magnetic arrays
- **Constant static magnetic field** (**Con SMF**) – magnetic field (370 mT) applied continuously for full duration of the experiment using the NdFeB magnetic arrays
- **Dynamic magnetic field** (**DMF**) – alternating magnetic field (0-23 mT) applied for 16 hours daily, followed by 8 hour static exposure (~23 mT)

2.4 Magnetic Nanoparticle Characterisation

Dextran coated iron oxide MNPs (FluidMAG-Dx) were sourced from Chemicell (Germany) for use in this study. MNPs were analysed to determine their morphology, size distribution, and magnetic properties. A combination of electron microscopy, image-based size analysis and super conducting quantum interference device (SQUID) magnetometry was employed for comprehensive characterisation.

2.4.1 Transmission Electron Microscopy of MNPs

MNPs were suspended in deionised water at a concentration of 25 mg/mL and sonicated for 5 minutes to minimise aggregation. A small volume (3-5 µL) of the suspension was then pipetted onto carbon-coated copper-TEM grids (400 mesh; AGAR Scientific Ltd). Prior to sample loading, the grids were glow-discharged using a Quorum Q150TES high vacuum coater to enhance particle adherence to the carbon surface. After air drying, the grids were imaged using a JEOL 1400 FLASH TEM (JEOL Ltd, Japan) operated at an accelerating voltage of 80 kV. Images were acquired using the JEOL TEM Centre software (version 1.7.26.3016) and a JEOL inbuilt CCD camera. Representative micrographs were captured at magnifications of x25,000 and x120,000 to assess particle morphological and size.

2.4.2 Size Distribution

The hydrodynamic size distribution of MNPs was measured in collaboration with Liquid Research Ltd (UK) using a Malvern Zetasizer (version 7.03). Measurements were conducted at 25°C using disposable sizing cuvettes with MNPs dispersed in deionised water.

Instrument parameters were set with dispersant refractive index of 1.330, viscosity of 0.8872 cP, and material refractive index of 1.59.

2.4.3 Super Conducting Quantum Interference Device

Magnetic measurements were performed by Ethan Lowe (PhD Student) in collaboration with the Murrie Research Group (School of Chemistry, University of Glasgow) using a Quantum Design Magnetic Property Measurement System SQUID magnetometer. Neat samples of the MNPs (25 mg/mL in deionised water) were loaded into the instrument for magnetisation studies. Magnetic hysteresis loops were acquired by sweeping the magnetic field from +1.5 T to -1.5 T and back to +1.5 T at a rate of 0.35 mT/s (3.5Oe/s) at 300K (26.85°C). Additional field sweeps were conducted up to 0.4 T at the same temperature. Variable temperature measurements were also performed between 273K (-0°C) and 300K (26.85°C) to assess dynamic magnetic behaviour in response to an oscillating field.

2.5 Magnetic Hydrogel

A naturally derived gelatin methacryloyl (GelMA) based hydrogel embedded with magnetic nanoparticles (MNPs) was employed to enable magnetic actuation. This section details the key materials used for hydrogel synthesis, the fabrication protocol for magnetic hydrogels and the enzymatic digestion process for RNA isolation from cell-laden hydrogels.

2.5.1 Magnetic Hydrogel: Components

The key materials used for magnetic hydrogel synthesis and subsequent enzymatic digestion are summarised in **Tables 2-11** and **2-12** respectively. **Table 2-11** lists the components and materials required to prepare GelMA hydrogels, with embedded MSCs. **Table 2-12** details the reagents and solutions for hydrogel digestion and the removal of MNPs from the final digested suspension.

Hydrogel Fabrication Component	Manufacturer	Catalogue Number
Gelatin Methacryloyl (GelMA) – Porcine Skin	Gelomics, Australia (*via* Swift Analytical, UK)	SASKU0010
Lithium phenyl-2,4,6-trimethylbenzoylphosphinate (LAP)	Sigma-Aldrich	900889-5G
fluidMAG-DX	Chemicell, Germany	4104-1
Polydimethylsiloxane (PDMS)	ConRo Electronics, UK	1673921
Dulbecco's Phosphate Buffer Solution (PBS) without Ca^{++}/Mg^{++}	Gibco, UK	12559069

Table 2-11: Components used for magnetic hydrogel fabrication

Summarises the hydrogel components, and materials employed in the synthesis of GelMA-based magnetic hydrogels.

Hydrogel Digestion Component	Manufacturer	Catalogue Number
Collagenase D from *Clostridium histolyticum*	Merck Life Science UK Limited, UK	11088866001
Ethylenediaminetetraacetic acid (EDTA)	Invitrogen by Thermo Fisher, UK	15575020
TRIzol™	Thermo Fisher, UK	15596026
Chloroform (≧99.8%)	Fisher Scientific, UK	C/4960/17

Table 2-12: Reagents used for enzymatic digestion of hydrogels

Details the components employed in the breakdown of GelMA hydrogels and subsequent removal of magnetic nanoparticles and other inorganic residues.

2.5.2 Magnetic Hydrogel: Fabrication

A stock solution of unpolymerised GelMA was prepared by dissolving lyophilised GelMA in sterile PBS and incubating at 37°C for 12-16 hours until fully dissolved. The 20% w/v GelMA stock solution was further diluted with PBS to final concentrations of 5%, 7.5% and 10% w/v for hydrogel fabrication.

MNPs (fluidMAG-DX) were dispersed throughout GelMA hydrogels at final concentrations ranging from 0.25 mg/mL to 1 mg/mL prior to crosslinking. This range was chosen based on previous studies, which have reported effective use of MNPs in hydrogels at concentrations from 0.2 mg/mL to 10 mg/mL (Liu, et al., 2020; Wang, et al., 2024). A lower, gradually increasing range was used in this study to systematically assess the effect of MNP

concentration on hydrogel mechanical properties while minimising potential cytotoxic or aggregation effects at higher concentrations. MNP dispersal in stock suspension was achieved by sonication to ensure homogenous distribution. When required, a suspension of dispersed cells or cell spheroids was incorporated into the GelMA-MNP hydrogels prior to crosslinking **(Figure 2-5)**.

Lithium phenyl-2,4,6-trimethylbenzoylphosphinate (LAP) was prepared at 40 mM in deionised water and added to the hydrogels at a final concentration of 0.05% v/v immediately prior to crosslinking. After addition of the crosslinker, hydrogels were pipetted into polydimethylsiloxane (PDMS) cylindrical moulds (13 mm in diameter and 2 mm in height) and exposed to ultraviolet (UV) light (~7 mW/cm^2) for 5 minutes at room temperature to initiate polymerisation. Following polymerisation, hydrogels were incubated in DMEM at 37°C until further use.

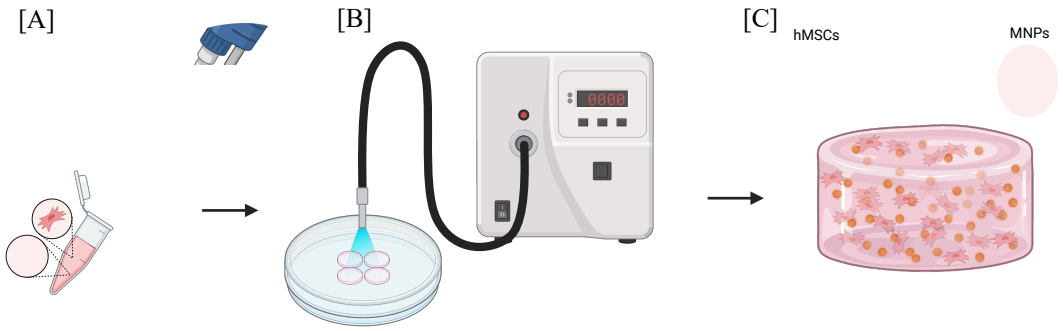

Figure 2-5: Schematic of magnetic GelMA hydrogel fabrication

Magnetic GelMA hydrogels were fabricated using the blending method [A] mesenchymal stromal cells (MSCs) and magnetic nanoparticles (MNPs) were homogeneously dispersed within unpolymerised GelMA prepolymer solution. [B] Following the addition of photoinitiator the mixture was exposed to ultraviolet light to initiate photo crosslinking and form a stable hydrogel network. [C] This process allowed for simultaneous encapsulation of MSCs and uniform distribution of MNPs throughout the GelMA matrix. Created with Biorender.com

2.5.3 Magnetic Hydrogel: Digestion and RNA Retrieval

Cells were extracted from hydrogels by enzymatic digestion using collagenase D, diluted to 2.5 mg/mL in sterile PBS and filtered through a 0.22 µm filter. Following removal of cell culture media, an equal volume of collagenase solution was added to each well and incubated at 37°C for 90 minutes. To aid digestion, the solution was gently aspirated and dispensed using a pipetted every 30 minutes to mechanically agitate and break up partially digested

hydrogel fragments. After digestion, collagenase activity was neutralised by adding an equal volume of 10 mM Ethylenediaminetetraacetic acid (EDTA). The resulting solution was then transferred to a universal, and cells along with MNPs were pelleted by centrifugation.

The pellet was resuspended in 1 mL of TRIzol reagent and homogenised thoroughly and incubated at toom temperature for 5 minutes to allow complete dissociation of nucleoprotein complexes. Chloroform (0.2 mL per sample) was added, and samples were gently aspirated and incubated for 2-3 minutes at room temperature. Samples were centrifuged at 12,000 g for 15 minutes at 4°C to separate the mixture into a lower phenol-chloroform phase, an interphase and an upper aqueous phase. The aqueous (RNA containing) phase was recovered into a sterile RNase-free Eppendorf and stored at -80°C for subsequent RNA extraction and isolation. This process also facilitated the separation of cellular material from residual inorganic components following hydrogel digestion.

2.6 Hydrogel Analysis

A range of mechanical, structural and surface characterisation techniques was employed to evaluate the physical properties of the hydrogels. The following subsections describe the methods used for assessing mechanical profiling, strength testing, contraction, wettability, internal structure and staining.

2.6.1 Rheology

A 20% w/v stock solution of unpolymerised GelMA was prepared as previously described (section 2.5.2). Final GelMA concentrations of 5%, 7.5% and 10% w/v were prepared with 0.5% w/v LAP photoinitiator and pipetted into the PDMS cylindrical moulds (13 mm diameter, 2 mm height). Samples were polymerised under UV light (~7 mW/cm^2) for 5 minutes and incubated in DMEM at 37°C prior to testing. Rheological measurements were conducted using an Anton Paar MCR 302 rheometer, equipped with an 8 mm measuring plate. The slightly smaller measuring plate diameter (8 mm) relative to the same size (~13 mm) was used to minimise edge effects, prevent slippage at the sample boundary and ensure uniform shear is applied to the central region of the hydrogel (Ricarte & Shanbhag, 2024). The gap was set by maintaining a contact force below 0.1 N. All tests were performed at 37°C. Storage modulus (G′) and loss modulus (G″) were measured over a strain range of 0.01% to 0.1% to ensure measurements were within the linear viscoelastic region. Measurements were taken immediately after polymerisation, as well as 24, 48 and 72 hours

post polymerisations for all GelMA concentrations. Any minor shrinkage of the hydrogel over time was accommodated by the 8mm plate, ensuring consistent coverage of the central sample region during measurements. To assess the effect of MNPs on GelMA mechanics, hydrogels at 5%, 7.5% and 10% w/v GelMA concentrations were prepared with increasing MNP concentrations (0.25, 0.5, 0.75 and 1 mg/mL) crosslinked with LAP and tested at 72 hours post polymerisation using the same rheological protocol.

2.6.2 Compression of Hydrogels

Hydrogels (7.5% w/v GelMA) were prepared and polymerised as previously described. Immediately after polymerisation, sterile weights of 12 g, 25 g or 50 g were placed on top of each hydrogel sample for 5 minutes. During compression, sterile swabs were used to absorb fluid displacement from the hydrogel surface beneath a filter layer. Following compression, hydrogels were incubated in DMEM at 37°C. Rheological measurements (G′ and G″) were completed at 24, 48 and 72 hours post polymerisation using the same Anton Parr MCR 302 Rheometer setup and conditions as previously described.

2.6.3 Contraction

To assess contraction behaviour, 7.5% and 10% w/v GelMA hydrogels were prepared and polymerised as previously described. Four experimental conditions were tested for each GelMA concentration: GelMA only, GelMA with cells, GelMA with MNPs and GelMA containing both cells and MNPs. MSCs were encapsulated at a density of 1 x 10^6 cells/mL. MNPs were incorporated at a concentration of 0.25 mg/mL. Following polymerisation, hydrogels were suspended in DMEM and incubated at 37°C. Hydrogel diameter was measured using a digital calliper at hourly intervals for the first 12 hours post-polymerisation, followed by measurements at 24 and 48 hours. Three measurements were taken per hydrogel at angles shown in **Figure 2-6**.

Figure 2-6: Measurement of contracting hydrogels

Schematic representation of measurements taken during contraction study. Hydrogels were measured with a digital calliper, at three angles, 0°, 45° and 90°. Created with Biorender.com

2.6.4 Water Contact Angle

To further investigate the biological compatibility of GelMA hydrogels, surface wettability was assessed *via* water contact angle measurements. GelMA hydrogels (7.5% and 10% w/v) containing 0.25 mg/mL and 0.5 mg/mL MNPs, as well as control hydrogels without MNPS, were prepared and polymerised. Measurements were performed 72 hours post-polymerisation.

Contact angles were measured using an optical tensiometer (Attension, Biolin Scientific). Prior to measurement, hydrogels were dried under ambient lab conditions for 5 minutes to improve consistency. The tensiometer was set for live analysis using contact angle (Young-Laplace). Images were recorded for 30 seconds at 20 frames per second and droplet rate was set at 2 µL/s. A 3 µL droplet of deionised water was dropped onto the surface of each hydrogel, and contact angle was recorded. Both wet and dried hydrogel samples were initially tested; however, measurements were more reproducible with dried samples, so this method was used for further testing. Each hydrogel was measured in triplicate, and re-dried between replicate measurements.

2.6.5 Freezing Hydrogels

To prepare hydrogels for micro-computed tomography (Micro-CT) and scanning electron microscopy (SEM), hydrogels were flash frozen by full immersion in liquid nitrogen and subsequently freeze-dried overnight using a freeze dryer (FreeZone, Labconco), using the settings in **Table 2-13**. After freeze drying, samples were stored in parafilm sealed cell culture plates at room temperature until imaging.

Step	Ramp Rate	Shelf Temp (°C)	Time	Vacuum (mbar)
1	0.1	-10	2 hours	0
2	0.1	0	2 hours	0
3	0.1	5	∞	0

Table 2-13: FreeZone settings used for removal of fluid and drying hydrogels

Details the settings used on the FreeZone system for freeze drying of GelMA hydrogels

2.6.6 Micro Computed Tomography

Micro-CT imaging was performed in collaboration with Dr Jonathan Williams at the University of Strathclyde. Samples were scanned using a Skyscan 1172 (Bruker). Micro-CT scanning was performed with tube voltage at 43 kVp and tube current at 100 µA. Scans were acquired at a voxel resolution of 2.5 µm with a 0.3° rotation step over 180°, and exposure time of 1000 ms per frame. No metal filter was applied, and frame averaging was set to 2. Reconstruction software NRecon (version 1.6.9.18) was utilised to generate 8-bit greyscale images, which were subsequently used for morphometric analysis in CTAn (version 1.20.8). Each hydrogel sample was analysed using three representative cubic sub volumes of interest (subVOIs) with side lengths of 0.8 mm. Quantitative morphometric parameters were extracted included porosity, pore thickness, gel thickness and connectivity density providing insight into the microstructural characteristics of the hydrogels.

2.6.7 Electron Microscopy

SEM was performed at the Glasgow Imaging Facility using a JEOL IT-100 SEM (JEOL Ltd, Japan). Freeze dried hydrogel samples were mounted on aluminium pin stubs (AGAR Scientific Ltd, UK) using conductive double-sided carbon tape (AGAR Scientific Ltd, UK). Samples were then sputter coated with a 20 nm layer of gold-palladium using a Quorum Q150TES high vacuum coater to improve surface conductivity. Imaging was conducted under high vacuum at an accelerated voltage of 10 kV to examine both surface morphology and internal structure. TIFF-format images were acquired using JEOL InTouch Scope software.

TEM was also performed on freeze dried hydrogel samples to attempt identification and assessment of MNP dispersal and morphology within the hydrogels. Images were acquired using the JEOL TEM Centre software (version 1.7.26.3016) and a JEOL inbuilt CCD camera. Representative micrographs were captured at magnifications of x15,000, x25,000 and x100,000 to assess particle morphological and location.

2.6.8 Histology

Hydrogels were fixed in 3.7-4.1% v/v formaldehyde at room temperature for 30 minutes, then washed and stored in phosphate-buffered saline at 4°C until further processing. Fixed samples were embedded in optimal cutting temperature compound, frozen and cryosectioned. Tissue sections approximately 15 µm were obtained using a LEICA CM1860 UV cryostat, mounted onto glass slides and air-dried to remove residual OCT. Alizarin Red S stained was used for detection of calcium deposition, serving as an indicator of mineralisation. Alizarin Red S detects calcium through a pH dependent chelation mechanism, forming an insoluble red-orange complex with calcium salts, enabling visualisation of mineral deposition. Alizarin red S staining was completed using the reagents described in **Table 2-14**.

A 2% w/v Alizarin Red S solution was freshly prepared prior to staining by dissolving Alizarin Red S in distilled water (2 g in 100 mL) and the pH was adjusted to 4.1-4.3. Cryosection hydrogel samples were rinsed briefly in chilled 100% acetone to dehydrate the sections. Samples were transferred to a 1:1 acetone/xylene for 2 minutes to remove lipids and prepare the sections for clearing. Sections were incubated in freshly prepared 2% w/v Alizarin Red S Solution for 5 minutes, followed by a brief dip in 100% acetone to reduce background staining. Slides were then cleared in 100% xylene for 5 minutes. Slides were air dried and images were acquired using EVOS M7000 under brightfield settings.

Staining Component	Supplier	Catalogue Number
Alizarin Red S Solution	Sigma-Aldrich, UK	A5533-25G
Acetone	Sigma-Aldrich, UK	179124
Xylene	CellPath	EGZ-0800-25A

Table 2-14: Reagents used for Alizarin Red S histology staining

Lists the reagents and solutions used in Alizarin Red S staining used for assessing mineralisation in cell-laden hydrogels

2.6.9 Laser Doppler Vibrometry

To quantify the mechanical displacement of magnetic hydrogels in response to applied magnetic fields, laser doppler vibrometry (laser interferometry) was performed, in collaboration with Dr Jonathan Williams at the University of Strathclyde. The application of magnetic fields limits the use of conventional optical imaging as the magnetic field source

is positioned beneath the hydrogel preventing direct optical imaging through the material. Displacement measurements were conducted using a laser interferometer (Model SP-S SIOS Meßtechnik GmbH, Germany) which provides non-contract, high resolution detection of surface vibrations and nanoscale displacements. The interferometer was mounted vertically above the sample, with the laser directed downward at the surface of the hydrogel. To ensure consistent reflection of the laser signal, a small square of prismatic self-adhesive reflective tape was fixed directly to the top surface of each hydrogel. The set up enabled precise tracking of the hydrogel surface motion, without physical contact or interference with the material's mechanical properties. Measurements were completed on 7.5% w/v GelMA hydrogels with 0.25 mg/mL MNPs. Control measurements were taken on hydrogels in the absence of a field, and under application of a SMF to identify displacement with field application.

The system captures displacement by analysing the interference pattern generated between the reflected laser beam and internal reference signal. The time domain interference data was recorded and processed using the INFAS software (SIOS), which applies a fast Fourier transform (FFT) to convert the signal in the frequency domain. This allowed for accurate extraction of displacement amplitude and frequency components resulting from magnetic field application.

2.7 Bioprinting

Magnetic GelMA hydrogels were printed using a CELLINK 3D bioprinter. The printing parameters are detailed in **Table 2-15.** Hydrogels composed of 7.5% w/v GelMA, either alone or with incorporated MNPs (0.25 mg/mL) were prepared using 0.5% w/v LAP. Unpolymerised GelMA mixtures were printed as 8 mm cylinder with 22 gauge nozzle, with a layer height of 0.410 mm and final height of 1.5 mm. A cross hatch pattern was used and fill density was set to 75%. Printed hydrogels were subsequently crosslinked *in situ* using the CELLINK bioprinters integrated UV light source (405 nm for 30 seconds).

Following fabrication, the hydrogels were evaluated for surface wettability and mechanical properties using water contact angle measurements and rheological analysis, respectively, as previously described in sections 2.6.1 and 2.6.4. Rheological properties were assessed at day 1, day 3, and day 7 post printing to evaluate changes in mechanical integrity over time. Water contact angle measurements were conducted at 72 hours to assess surface wettability on grid printed hydrogels.

Parameter	7.5% w/v GelMA Only	7.5% w/v GelMA+ 0.25 mg/mL MNPs
Thermal Print Head Temperature	22°C	21.5°
Pressure	50 kPa	50 kPa
Print Speed	4.0 mm/s	5.0 mm/s
Pre-flow Delay	-500 ms	-500 ms

Table 2-15: CELLINK bioprinting parameters used for GelMA hydrogels

Summarises the key bioprinting settings used with CELLINK system for fabricating GelMA hydrogels

2.8 Statistical Analysis

All data sets were initially recorded in Microsoft Excel and subsequently analysed using GraphPad Prism (v 10.2.0). Prism was used to identify outliers (ROUT method, Q = 1%), perform normality testing (Shapiro-Wilk test), and apply the subsequent appropriate parametric or non-parametric statistical test. Specific tests, and post hoc tests, used for each dataset are reported in the corresponding figure legend or results section. A significance threshold of $p < 0.05$ was applied throughout the study. Biological replicates were defined as independently prepared hydrogel batches or repeated experiments with a new cell source (**Table 2-1**), capturing natural variability between preparations. Technical replicates consisted of repeated measurements on the same hydrogel batch or cell source to account for measurement variability.

Chapter 3: The Effect of Static and Dynamic Magnetic Fields on Mesenchymal Stromal Cells in Monolayer

3.1 Introduction

MSCs are multipotent stem cells with the ability for self-renewal and differentiation into a number of diverse mesenchymal lineages including osteogenic, chondrogenic, adipogenic and myogenic tissues (Sheng, 2015; Steward & Kelly, 2014). MSCs are easily isolated and cultured making them a key resource in tissue engineering and regenerative medicine. In bone tissue engineering, MSCs are an established source of osteoprogenitor cells, and play a critical role in the formation, repair and remodelling of bone (Liu, et al., 2022).

MSC behaviour is regulated and influenced by biochemical and biophysical cues within their microenvironment, both *in vivo* and *in vitro* (Liu, et al., 2022). Biophysical cues encompass a range of mechanical and structural factors from muscle contractions and arterial flow to substrate stiffness, topography and mechanical loading (Gasiorowski, et al., 2013). Among these, magnetic fields have emerged as a tuneable and non-invasive biophysical stimulus with significant potential in bone regeneration (Shuai, et al., 2018; Yuan, et al., 2018).

In biomedical applications, magnetic fields are classified as static or dynamic magnetic fields. SMFs maintain a consistent strength and fixed polarity, while a dynamic field can be modified for strength, frequency and orientation (Fan, et al., 2020). Magnetic fields have been observed to influence proliferation, differentiation, migration, cytoskeleton reorganisation, morphology and gene expression (Paun, et al., 2018; Yuan, et al., 2018). Magnetic fields have been used to drive MSC differentiation, particularly with the goal of enhancing bone tissue engineering strategies (Paun, et al., 2018). However, the mechanisms underlying how magnetic fields can influence MSCs requires further research.

Mechanotransduction is a process where cells experience a physical force that leads to the induction of biochemical reactions which influences cell behaviour (Steward & Kelly, 2014). Several signalling pathways show response to magnetic fields, producing intracellular and extracellular responses. Signalling pathways such as BMP, Wnt/β-Catenin, and SHH are known to regulate linage commitment and have been observed to show modulation under mechanical stimuli (Li, et al., 2014; Rahman, et al., 2015; Sun, et al., 2022).

In addition, MSCs exert therapeutic effects *via* paracrine signalling, primarily through their secretion of cytokines, including EVs. EVs carry bioactive cargo which may influence the behaviour of neighbouring cells, modulating tissue repair (Presen, et al., 2019). Mechanotransduction has been demonstrated to influence paracrine signalling in osteoprogenitor cells, including changes to the composition of secreted factors that regulate migration, proliferation and differentiation (Brady, et al., 2015). Therefore, analysis of cell secretome may provide some insight into MSC response to external stimulation.

3.1.1. Chapter Aims

This chapter aims to investigate and compare MSC response to both static and dynamic magnetic fields. The following objectives were set:

- Assess MSC behaviour, including proliferation, viability, cell cycle dynamics and migration in response to a magnetic field
- Examine early osteogenic commitment with magnetic activation, and modulation in key signalling pathways
- Investigate mechanotransduction intracellular responses including YAP signalling, nuclear morphology and intracellular calcium flux.
- Characterise changes in MSC-derived EV profiles, including EV size distribution and cytokine profile under a magnetic field

3.2 Methods

The following experiments were completed with the material and methods outlined in Chapter 2. Cell culture was completed as outlined in 2.1 Cell Culture.

The following magnetic conditions were used:

- **Control** – standard conditions without magnetic field exposure
- **Intermittent static magnetic field** (**Int SMF**) – magnetic field (370 mT) applied for 1 hour per day using the NdFeB magnetic arrays
- **Constant static magnetic field** (**Con SMF**) – magnetic field (370 mT) applied continuously for full duration of the experiment using the NdFeB magnetic arrays
- **Dynamic magnetic field** (**DMF**) – alternating magnetic field (0-23 mT) applied for 16 hours daily, followed by 8 hour static exposure (~23 mT)

The subsequent sections using the following methods:

- Cell Response to Static and Dynamic Magnetic Fields: 2.2.1 Cell Viability Assay, 2.2.3 Wound Healing (Scratch Assay), 2.2.4 Crystal Violet Staining and Wound Healing Analysis, 2.2.5 RNA Extraction and Isolation, 2.2.6 Reverse Transcription, 2.2.7 Real-Time Quantitative Polymerase Chain Reaction, 2.2.8 Fluidigm
- Early Osteogenic Differentiation Under Static and Dynamic Magnetic Fields: 2.2.5 RNA Extraction and Isolation, 2.2.6 Reverse Transcription, 2.2.7 Real-Time Quantitative Polymerase Chain Reaction, 2.2.8 Fluidigm
- Early Molecular Responses to Magnetic Stimulation: 2.2.5 RNA Extraction and Isolation, 2.2.6 Reverse Transcription, 2.2.7 Real-Time Quantitative Polymerase Chain Reaction, 2.2.8 Fluidigm
- Mechanotransduction: 2.2.2 Immunofluorescence, 2.2.5 RNA Extraction and Isolation, 2.2.6 Reverse Transcription, 2.2.8 Fluidigm
- Paracrine Signalling Under Static and Dynamic Magnetic Fields: 2.2.9 Cytokine Array, 2.2.10 Micro BCA Protein Assay, 2.2.11 MSC Extracellular Vesicles

3.3 MSC Response to Static and Dynamic Magnetic Fields

3.3.1 MSC Viability Fluorescent Staining

To assess the potential cytotoxic effects of magnetic fields on MSCs, a viability assay was employed after application of magnetic fields to MSCs over 7 days. Previous studies suggest that the effects of magnetic fields on MSCs are dependent on field strength, with constant exposure (500 mT) promoting cell survival in some reports, while fields of 18 mT inducing cell death in others (Marędziak, et al., 2017; Sadri, et al., 2017). In the present study, a field strength of 370 mT was applied, and we hypothesise this field strength would act similar to the 500 mT field, and maintain MSC viability compared to unexposed controls.

MSC viability was investigated to determine cell response to static and dynamic magnetic fields after 7 days exposure. Live cells were stained green with Calcein AM, and dead cells stained red with Ethidium homodimer-1 **(Figure 3-1, A)**. Viability was measured as a percentage of Calcein stained cells to total cells stained.

Across 7 days, no significant changes in cell viability were identified with magnetic conditions, in comparison to control, 86.3% (±6.0%). In addition, no significant changes were identified between the various magnetic field regimens – Intermittent or Constant SMF,

or DMF conditions, 85.4% (±1.0%), 89.6% (±1.9%) and 88.4% (±0.2%) respectively. **(Figure 3-1, B)**.

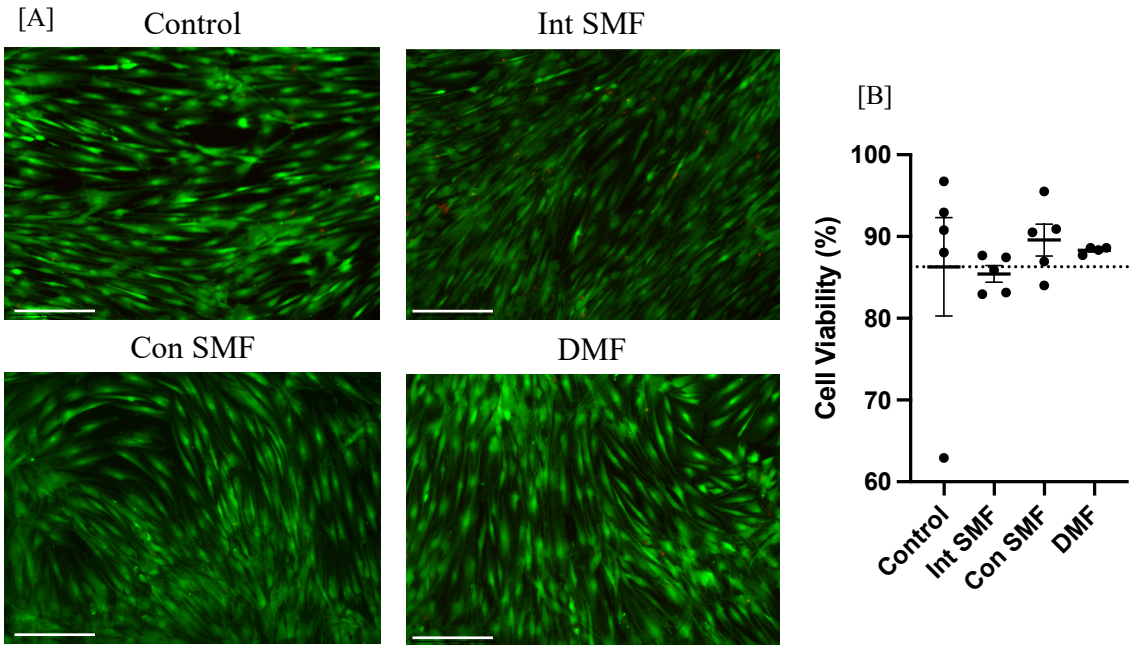

Figure 3-1: Cell viability is maintained under magnetic field exposure

Viability of mesenchymal stromal cells (MSCs) (passage 5) was assessed using LIVE/DEAD staining [A] Representative Live/Dead fluorescence microscopy of MSCs stained Calcein AM (live cells, green) and Ethidium homodimer-1 (dead cells, red) at day 7, captured with EVOS fluorescent microscopy; scale bar shows 275 µm. [hB] Quantification of cell viability (% live cells) calculated from fluorescence images (n=1, five images were collected per flask). Error bars represent mean ± SEM; dotted line represents mean for control (86.3%). A one-way ANOVA and post hoc Tukey test was performed to identify significance between conditions.

3.3.2 Cell Cycle Regulation

Magnetic fields have been reported to influence MSC proliferation and function, potentially by modulating the cell cycle (Marędziak, et al., 2017). With viability data indicating that magnetic fields do not compromise MSC survival, it remained unclear if these fields could affect proliferation dynamics. Based on previous literature, we expected the applied regimes to produce field dependent effects on cell cycle promoters and regulators, reflecting the variability reported in earlier studies (Boda, et al., 2015; Buemi, et al., 2001; Manjua, et al., 2021; Zheng, et al., 2018).

Cell cycle regulation in response to both static and dynamic magnetic fields was investigated over 7 days, at time points day(s) 1, 3 and 7. Cells were lysed and processed for Fluidigm

RT-qPCR. Gene expression of cell cycle markers were measured and compared to control. **(Figure 3-2)**.

Cell Cycle Promotors: Expression of CDK4 was mostly upregulated, with intermittent and constant SMF showing an early increase, a decline by day 3 then a recovery at day 7. DMF exposure induced upregulation that gradually declined over time. CDK2 expression was initially downregulated but increased by day 3 under all conditions; intermittent SMF exposure showed a continued increase at day 7, constant SMF exposure returned to control levels by day 7 and DMF decreased back to baseline by day 7. CDK1 expression showed an early upregulation under most conditions, peaking at day 3. Exposure to an intermittent SMF caused CDK1 levels to decease by day 7, while constant SMF remained elevated and CDK1 expression peaked under a DMF at day 3. Expression of CCND1 (Cyclin D) was downregulated at day 1 in all conditions, then slightly upregulated at day 3. At day 7 an intermittent SMF maintained an upregulation, whilst a constant SMF and DMF resulted in decrease in expression (**Figure 3-2**). Overall magnetic field exposure modulated cell cycle promoter gene expression, with an intermittent SMF promoting more sustained cell cycle activity compared to the transient effects observed with a constant SMF and DMF.

Cell Cycle Inhibitors: Expression of inhibitor p16, was upregulated at day 1 in all conditions, followed by a downregulation at day 3, most notably under a DMF. By day 7 it remained suppressed under both SMF conditions but began returning to baseline with DMF exposure. Expression of p21 was also trending towards a downregulation under both intermittent and constant SMF across all timepoints. Exposure to a DMF induced a transient increase at day 3, but expression decreased again by day 7. Expression of inhibitor p27 showed a delayed upregulation under both SMF conditions, increasing gradually to peak at day 7. Exposure to a DMF induced an early upregulation, peaking at day 3 (**Figure 3-2**). Overall magnetic fields also modulated expression of cell cycle inhibitors. Inhibitors, p16 and p21 were generally downregulated over time under both SMF conditions, suggesting reduced inhibitory signalling. In contrast, p27 showed delayed upregulation, indicating a potential compensatory response under all fields.

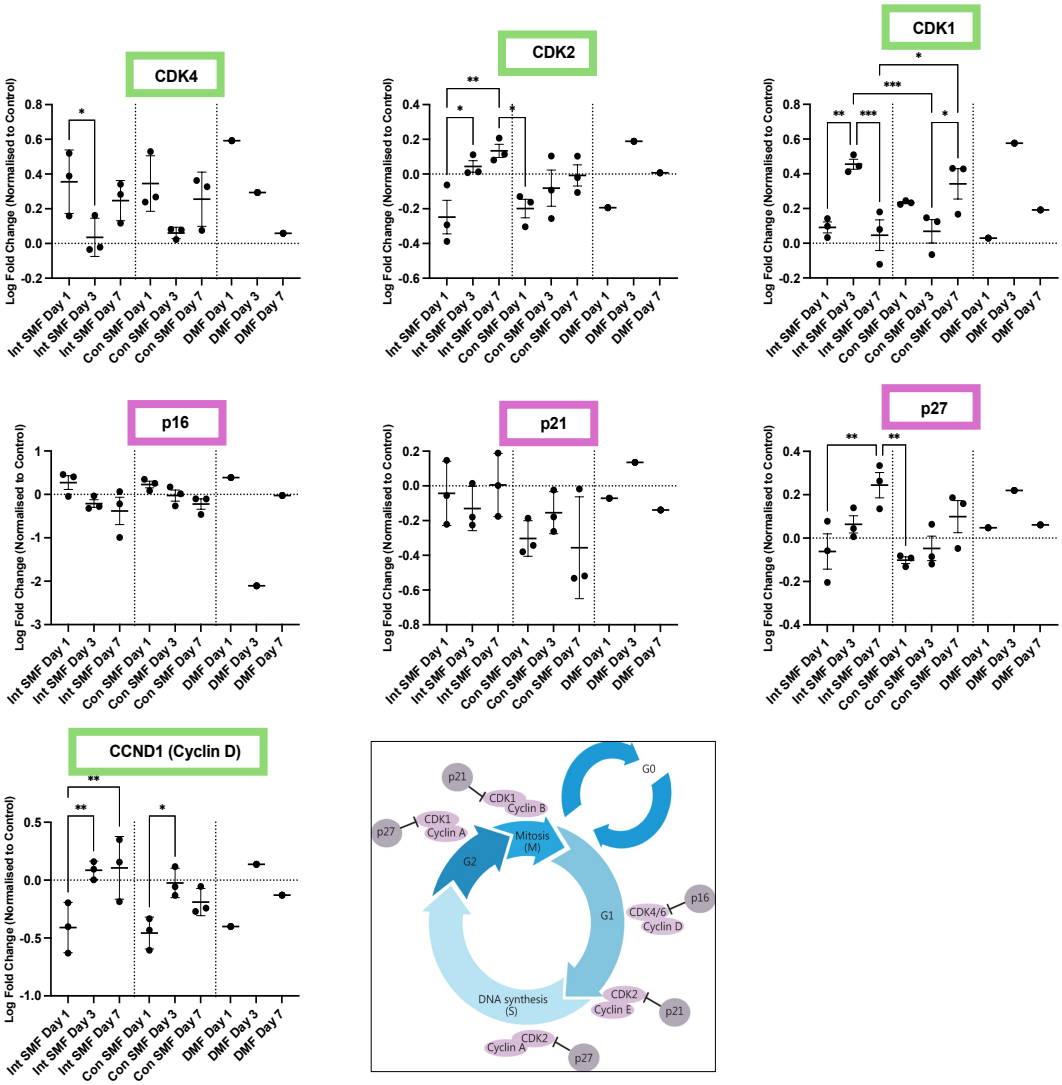

Figure 3-2: Magnetic field exposure modulates regulation of cell cycle promoters and inhibitors

Insert illustrates cell cycle stages with associated regulatory genes (Bai, et al., 2017). Green boxes highlight cell cycle promoters, while pink boxes highlight cell cycle inhibitors. Log fold change was normalised to control; dotted line shows control value. Error bars represent mean ± SEM. A one-way ANOVA and post hoc Tukey test was performed to identify significance between conditions. Data represents 3 technical replicates for both SMF conditions and 1 technical replicate for DMF (n=1). Due to limited measurements, DMF was excluded from statistical analysis

3.3.3 MSC Proliferation

To determine whether the observed changes in cell cycle gene expression translated into altered MSC proliferation, Ki67 gene expression was assessed over the same 7-day period. Ki67 is a nuclear protein expressed in actively cycling cells and widely used as a marker of cell proliferation (Sun & Kaufman, 2018). Application of magnetic fields have been observed to have varying effects on cell proliferation, with some reports showing increased proliferation, and some reporting an inhibition of proliferation under similar regimes (Manjua, et al., 2021; Zheng, et al., 2018). Based on these studies, we hypothesis magnetic fields to have field dependent effects on cell proliferation. Proliferation, *via* Ki67 gene expression, was measured in response to static and dynamic magnetic fields over 7 days, at timepoints: day(s) 1, 3 and 7.

Across all magnetic conditions, MSC proliferation was mainly influenced by the intermittent SMF, where a significant increase in Ki67 expression was noted at after 3 days of exposure, reducing back to control levels by day 7. A similar trend was noted in DMF. In contrast, the constant field did not influence MSC proliferation at the times points assessed **(Figure 3-3)**.

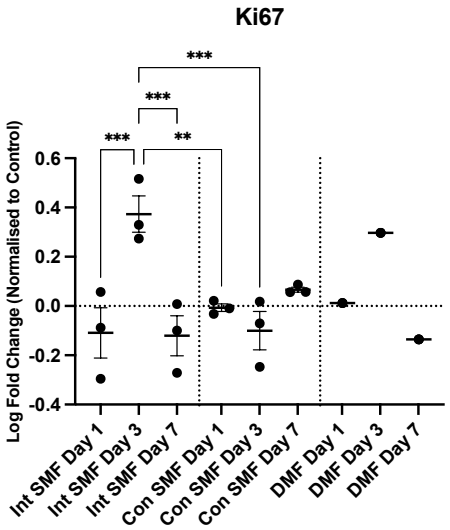

Figure 3-3: Magnetic field exposure modulates cell proliferation via Ki67 expression

Gene expression under magnetic fields over 7 days. Log fold change was normalised to control; dotted line shows control. Error bars represent mean ± SEM. A one-way ANOVA and post hoc Tukey test was performed to identify significance between conditions. Data represents 3 technical replicates for both SMF conditions and 1 technical replicate for DMF (n=1). Due to limited measurements, DMF was excluded from statistical analysis

3.3.4 Cell Migration Scratch Assay

Magnetic fields have been reported to influence MSC migration and regenerative behaviour, which are critical for tissue repair applications (Paun, et al., 2018; Yuan, et al., 2018). To investigate the effect of static and dynamic fields on MSC motility, a scratch assay was employed. As with cell proliferation, magnetic fields are expected to have field and duration dependent effects on cell migration, with potentially improved migration under a SMF (Sun, et al., 2023). MSCs cultured as a monolayer were mechanically scratched to create a wound area, allowing investigation of cell migration during wound closure. Monolayer cultures were mechanically scratched, and magnetic field regimes were applied to observe their effect on MSC motility and migration.

Due to method of application of both static and dynamic fields, time lapse imaging was not feasible for these conditions, so wound closure data was analysed from fixed cell images **(Figure 3-4)** and cells were lysed at the same timepoints (2, 6, 24, 48 and 72 hours) for gene analysis of Ras-related C3 botulinum toxin substrate 1 (Rac1), RhoA, MMP-2 and MMP-9 (**Figure 3-5**).

Using the crystal violet images, the scratch area was measured, and progression of scratch closure was recorded as percentage of initial scratch area (**Figure 3-4, 3-5**). To monitor wound closure, images were captured at four distinct regions along the scratch wound separately by roughly 90°, evenly distributed to cover the wound area and avoid the overlap of scratches, ensuring consistent sampling each time. Minimal changes were observed in wound area after 2 hours across all groups, though DMF showed a slightly greater reduction (~12%). At 6 hours the scratch areas had unexpectedly increased in the control and intermittent SMF groups; ~118% and ~116% of initial wound in control and intermittent SMF respectively. Under a constant SMF the wound area remained unchanged, and application of a DMF showed continued reduction to 82% of the initial wound. At 24 hours, active wound closure was evident, with the control group showing the greatest reduction (~70% of initial wound), compared to intermittent (~44%) and constant SMF (~41%). The DMF exposure group showed the least closure (~28%). By 48 hours, wounds in both control and intermittent SMF groups were nearly closed, while a constant SMF lagged with only ~70% closed, and DMF remaining significantly delayed (~23% closed). At the final timepoint, 72 hours, control and intermittent SMF groups had nearly complete wound closure (~96% and ~87% wound closure respectively). In contrast, constant SMF and DMF

showed limited closure (~67% and ~47%) with the DMF group performing significantly worse **(Figure 3-5)**.

Expression of Rac1 increased steadily across all magnetic field conditions, with upregulation beginning around 6 hours, and generally peaking by 24 hours, suggesting enhanced migratory signalling. Expression of RhoA peaked early (6 hours) under both constant SMF and DMF exposure, followed by a general decline over time. An intermittent SMF did not show this early increased but instead showed a delayed upregulation after 48 hours. MMP-2 expression showed a consistent trend of upregulation under all magnetic field conditions, peaking around 24 hours, before dipping slightly or stabilising by 72 hours. In contrast MMP-9 showed more variable expression with no clear consistent trend across conditions. While there was occasional upregulation at later time points (72 hours), the overall pattern was scattered. Taken together these results suggest magnetic field exposure does stimulate MSC migration, particularly through effects on Rac1 and MMP-2 **(Figure 3-6)**.

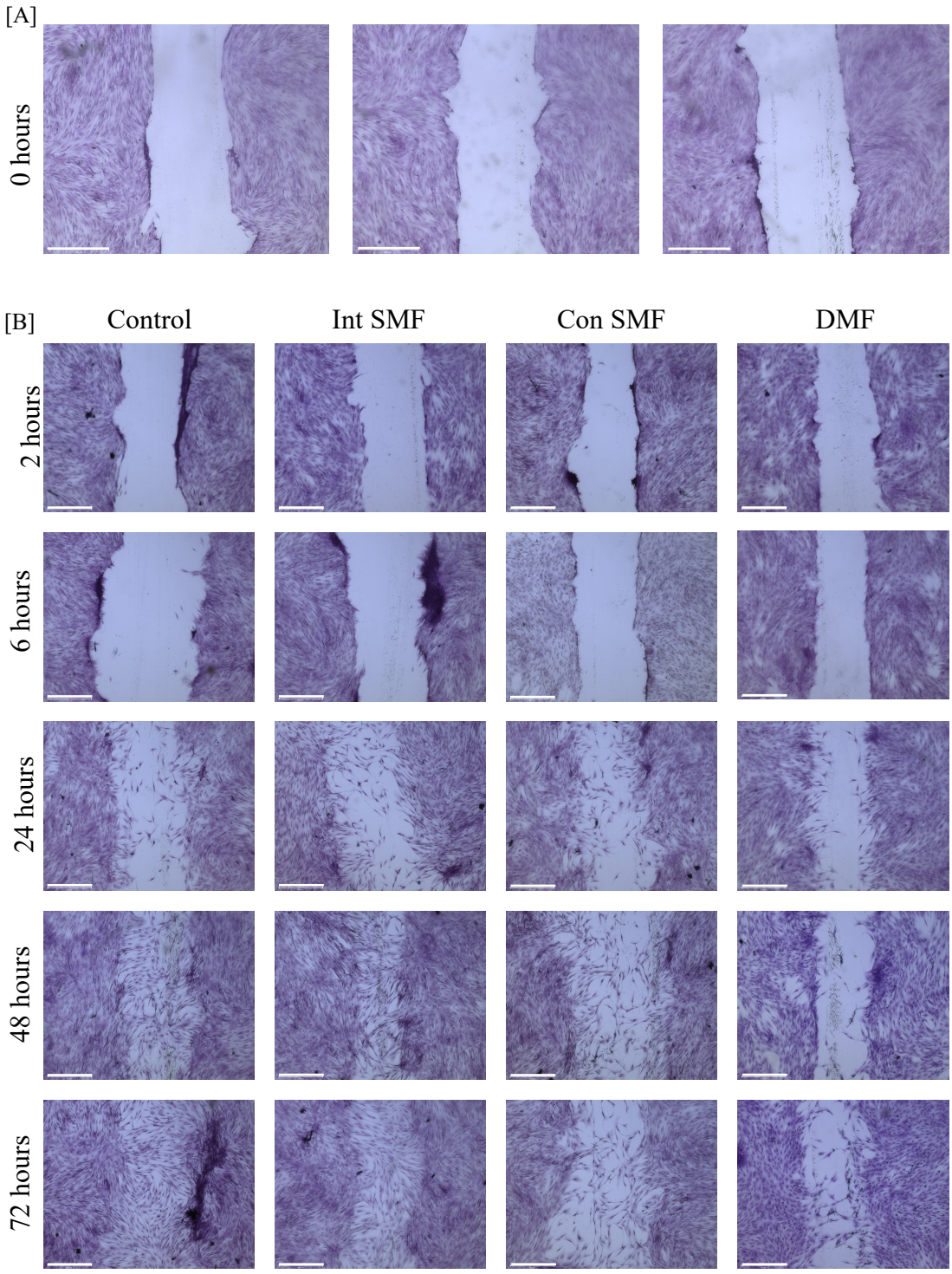

Figure 3-4: Magnetic field exposure influences cell proliferation in wound healing scratch assay

Confluent mesenchymal stromal cell (MSC) cultures were scratched with a p200 pipette tip, cells were fixed and stained with crystal violet at time points to observe cell migration and wound closure (n=1). Images were captured with light microscopy setting on EVOS; scale bars show 650 µm [A] 0 hours showing cells immediately post scratch, illustrating the clear cell margins [B] A collection of images taken at 2, 6, 24, 48 and 72 hours post scratch.

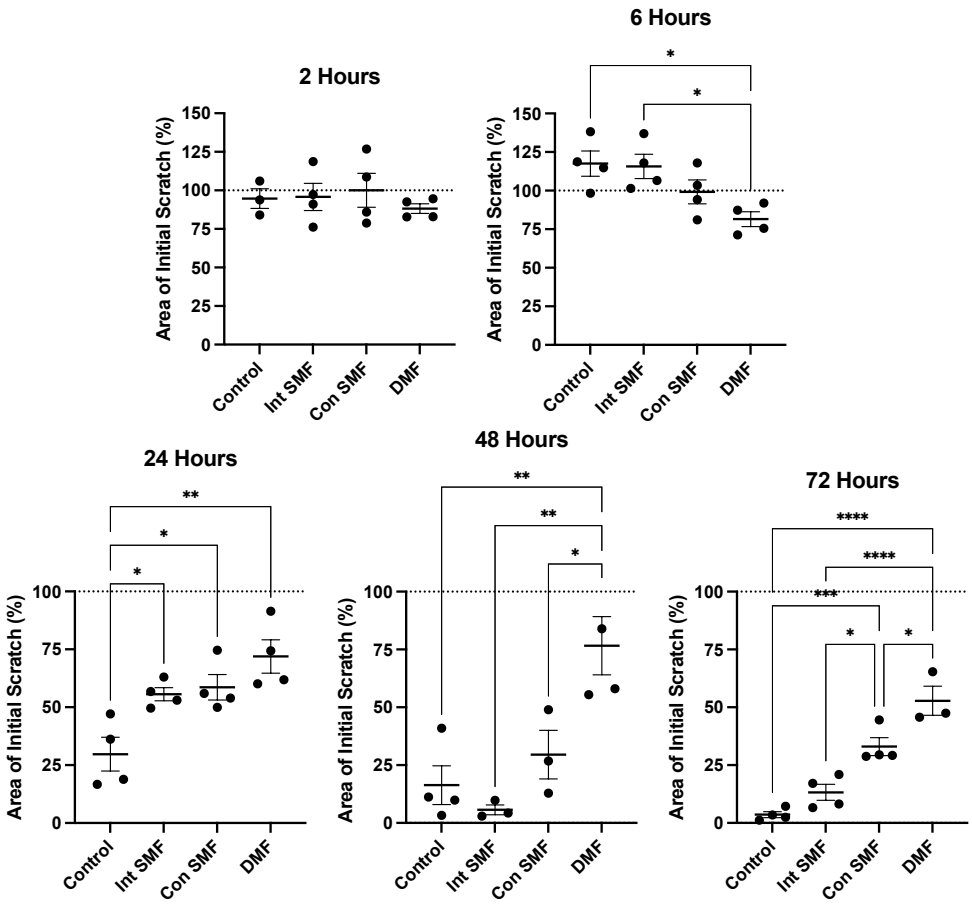

Figure 3-5: Magnetic fields influence rate of wound closure during scratch assay

Area of initial scratch measured over time was generated using the crystal violet images; the scratch area was measured, and progression of scratch closure was recorded as percentage of initial scratch area. One well per condition was imaged, with four images from each well collected (n=1). Error bars represent mean ± SEM. A one-way ANOVA and post hoc Tukey test was performed between conditions at each time point to identify significance between conditions.

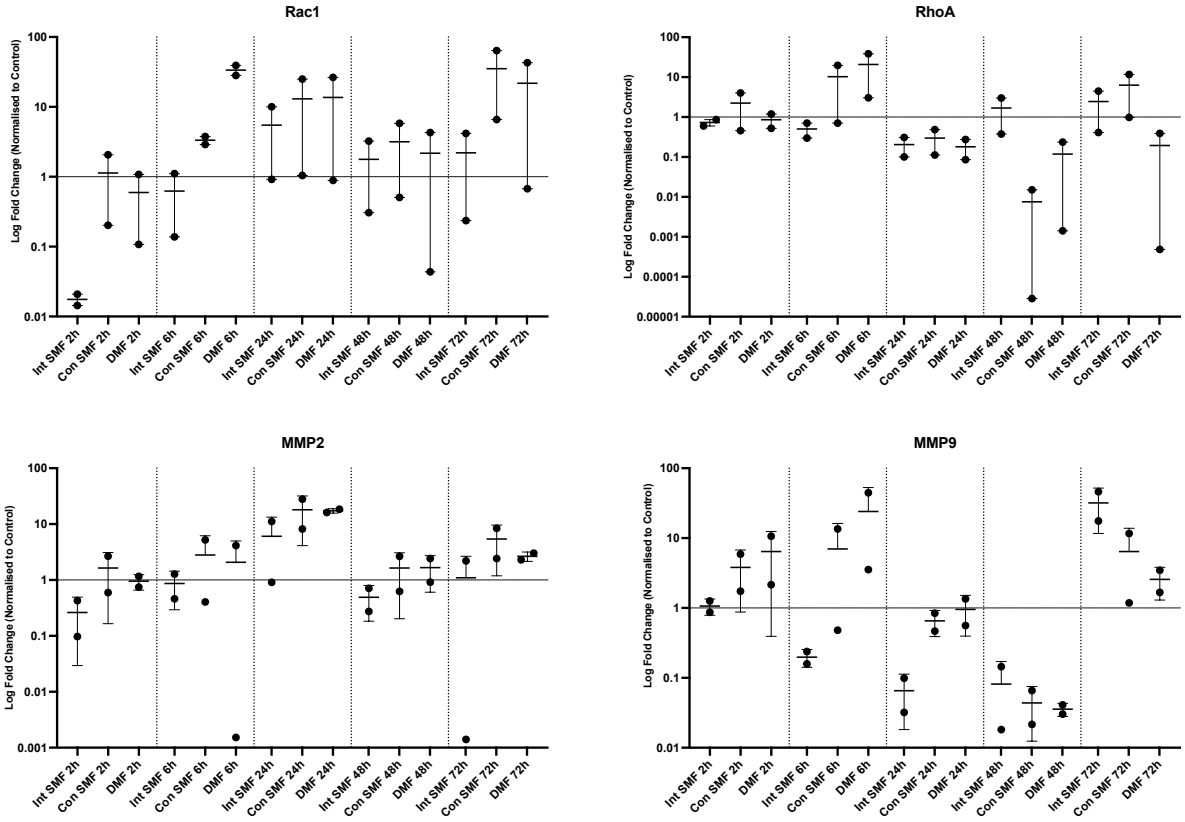

Figure 3-6: Magnetic fields modulate motility related gene expression

Gene expression under magnetic fields over 72 hours. Fold change was normalised to control; dotted line shows control. Error bars represent mean ± SEM. Due to limited replicates, statistical analysis was not completed. Data represents 2 technical replicates only (n=1).

3.4 Early Osteogenic Differentiation Under Static and Dynamic Magnetic Fields

3.4.1 Commitment to Osteogenic Pathway

MSCs possess the ability to differentiate into multiple lineages, including osteoblasts, which are critical for bone formation and regenerative therapies. Magnetic fields have been observed to promote osteogenic lineages over other differentiation pathways (Zhang, et al., 2018). Based on varying reports in previous literature, the applied regimes were expected to promote commitment to an osteogenic pathway and produce field dependent effects on osteogenic differentiation, enhancing both early and late osteogenic markers.

Osteogenic commitment in MSCs was examined under magnetic fields over 7 days, at time points: day(s) 1, 3 and 7. Cells were lysed and processed for Fluidigm RT-qPCR. **Figure 3-7, A** illustrates the various genes assessed during early commitment from MSC to

osteoprogenitor and then to pre-osteoblast/osteoblast over the 7 days, following MSC progression down an osteogenic lineage (Liu, et al., 2023).

Initially, commitment to other MSC lineages was examined, including myogenesis, chondrogenesis, and adipogenesis (**Figure 3-7, B**). Chondrogenic commitment was investigated through expression of SOX 9 for chondrogenesis, MyoD for myogenesis and PPARγ for adipogenesis (**Figure 3-7, A**). Expression of MyoD and PPARγ were undetectable *via* qPCR suggesting absent expression in MSCs exposed to magnetic fields. Meanwhile, a marked downregulation of SOX9 expression was observed in all magnetic conditions at day 1. At day 3, expression of SOX9 was downregulated for constant SMF, with small upregulation visible in intermittent SMF and DMF conditions compared to control measurements. By day 7, SOX9 expression was again downregulated in all conditions **(Figure 3-7, B).**

Early MSC commitment to osteogenic differentiation was examined over 7 days, *via* expression of RUNX2, MSX2, FOXP1 and MAF (**Figure 3-7, A**). In general, all genes indicated increased expression when stimulated with a magnetic field, as reflected in the heatmap (**Figure 3-7, B**). Exposure to an intermittent SMF stimulated significant increases over time in all four osteogenic genes. The most pronounced upregulation was observed for RUNX2, MSX2 and MAF, with FOXP1 also showing a steading increase from day 1 through day 7. Constant SMF exposure showed trends of increasing expression for most genes, though the changes were less consistent and only MAF reached statistical significance by day 7. RUNX2 and MSX2 showed moderate or stable expression, while FOXP1 was downregulated over time. DMF exposure generally induced early upregulation of all genes at days 1 and 3, followed by decreased expression by day 7. FOXP1 expression was downregulated by day 7, while other genes retained upregulation or levels similar to control (**Figure 3-8**).

MSC proliferation to pre-/osteoblasts was examined, and an intermittent SMF generally stimulated increased expression of osteogenic genes over time despite some initial downregulation. Expression of RUNX2 under magnetic fields has previously been reported. Notably SP7/Osterix, β-Catenin, ATF4 and ALP showed marked upregulation by day 7. Col1A1 initially increased but gradually decreased by day 7, through it remained elevated relative to control. Exposure to constant SMF was less stimulatory overall, trending toward decreased gene expression across most genes. Exceptions included SP7/Osterix and ATF4, which increased significantly at day 7, and Col1A1, which was consistently increased at all

time points. However, β-Catenin and ALP were downregulated under constant SMF. DMF exposure increased some gene expression early on, with β-Catenin and Col1A1 initially upregulated. However, these genes decreased by day 7, while expression of ALP and SP7/Osterix increased over 7 days (**Figure 3-9**).

Overall, these results indicate that magnetic field exposure, particularly an intermittent SMF, promotes osteogenic commitment and differentiation in MSCs over 7 days, with distinct gene expression patters suggesting enhanced progression toward the osteoblast linage.

[A]

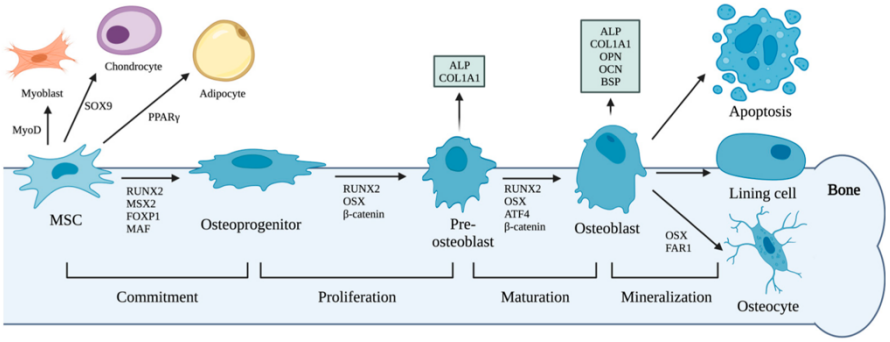

[B]

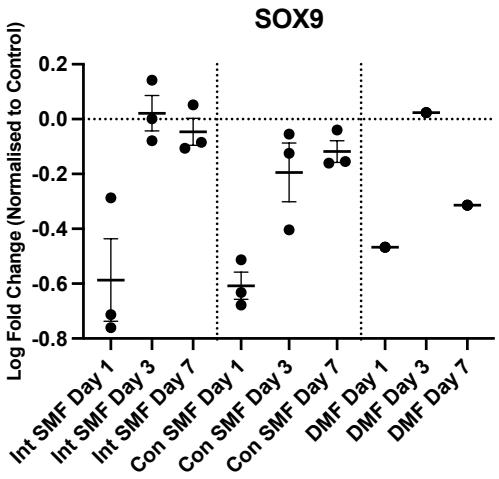

Figure 3-7: Exposure to magnetic fields over 7 days supresses chondrogenic differentiation via downregulated SOX9 expression

Mesenchymal stromal cell (MSC) commitment to potential lineages was investigated [A] Schematic of MSC commitment to osteogenic cells. Figure reproduced from Liu, et al., 2023. [B] Gene expression under magnetic fields over 7 days. Log fold change was normalised to control; dotted line shows control. Error bars represent mean ± SEM. A one-way ANOVA and post hoc Tukey test was performed to identify significance between conditions. Data represents 3 technical replicates for both SMF conditions and 1 technical replicate for DMF (n=1). Due to limited measurements, DMF was excluded from statistical analysis

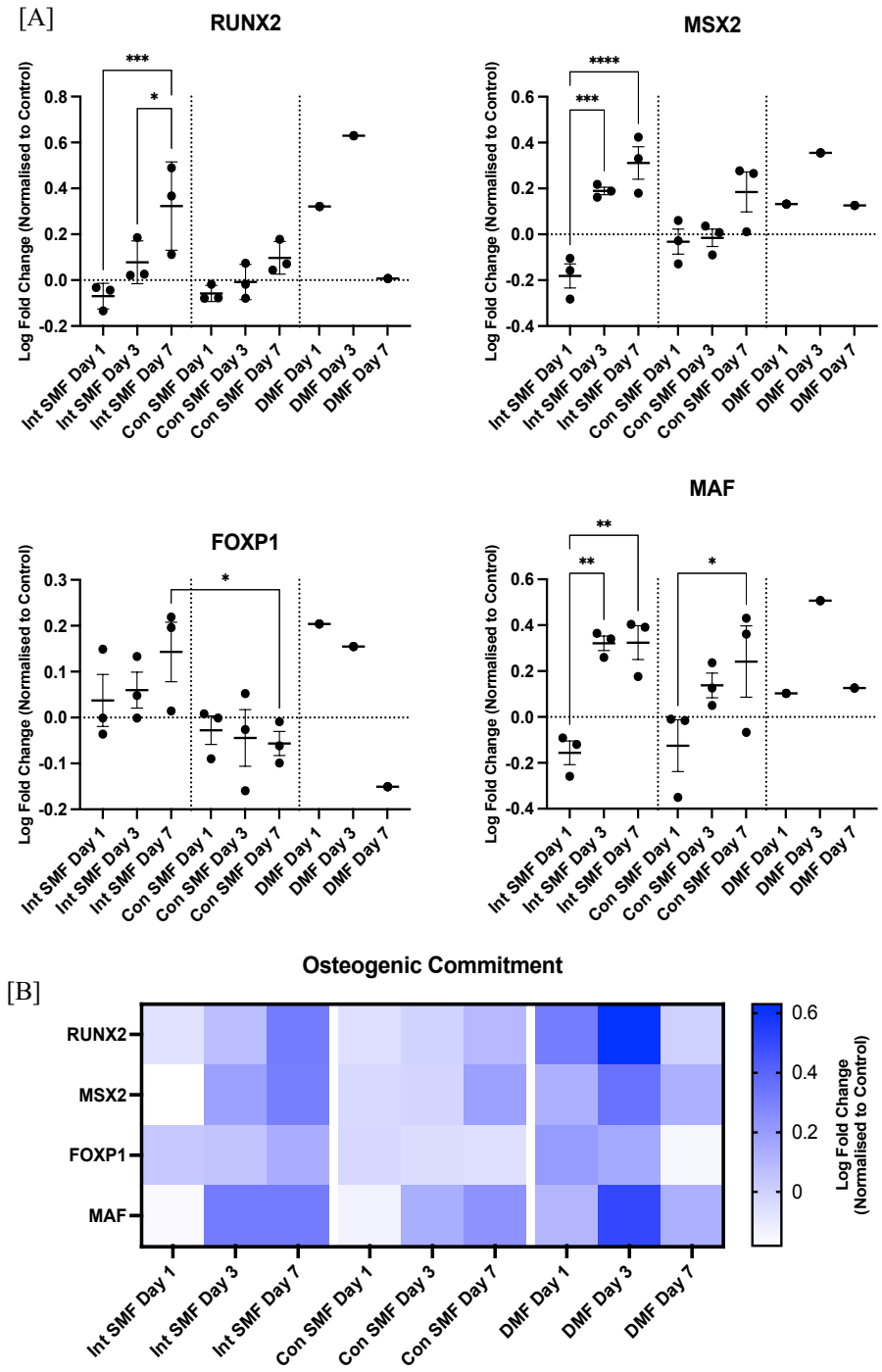

Figure 3-8: Exposure to magnetic fields over 7 days promotes MSC commitment to osteoprogenitor cells

The first stage of osteogenesis was investigated, commitment to osteoprogenitor cells [A] Gene expression under magnetic fields over 7 days. Log fold change was normalised to control; dotted line shows control. Error bars represent SEM. A one-way ANOVA and post hoc Tukey test was performed to identify significance between conditions. Data represents 3 technical replicates for SMF and 1 technical replicate for DMF (n=1). Due to limited measurements, DMF was excluded from statistical analysis [B] Gene expression in heat map.

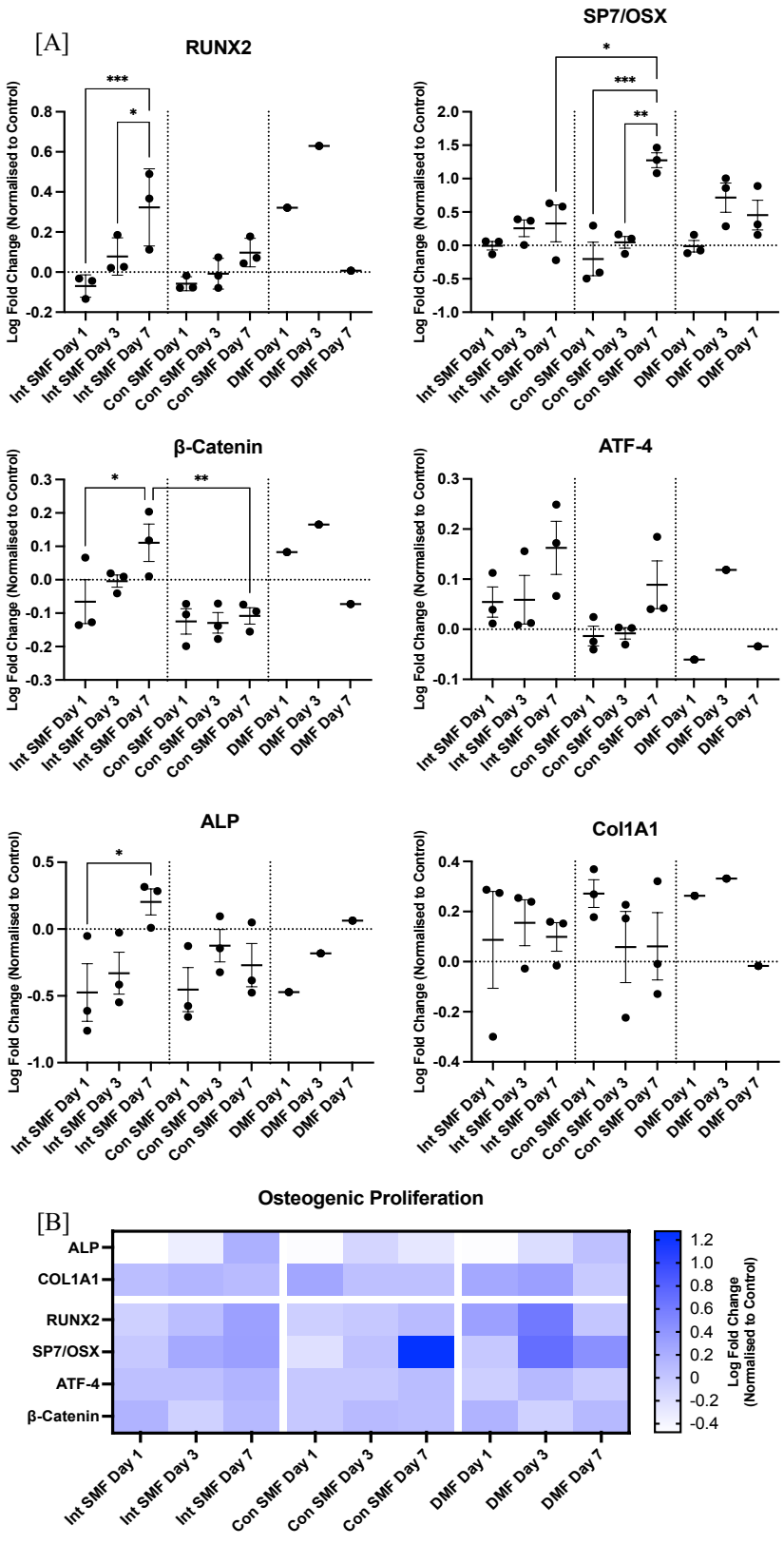

Figure 3-9: Exposure to magnetic fields over 7 days promotes MSC profileration and maturation to preosteoblasts

The second and third stages of osteogenesis were investigated, proliferation of osteoprogenitor cells and maturation to pre-/osteoblasts [A] Gene expression under magnetic fields over 7 days. Log fold change was normalised to control; dotted line shows control. Error bars represent mean ± SEM. A one-way ANOVA and post hoc Tukey test was performed to identify significance between conditions. Data

represents 3 technical replicates for SMF and 1 technical replicate for DMF (with exception of SP7/OSX which has 3 technical replicates for DMF) (n=1). Due to limited measurements, DMF was excluded from statistical analysis [B] Gene expression in heat map.

3.5 Early Molecular Responses to Magnetic Stimulation

MSC differentiation down an osteogenic lineage is regulated by several different pathways, including BMP, Wnt/β-Catenin, SHH and Groucho pathways. Previous studies suggest that magnetic field effects on these pathways are dependent on field strength and duration, with different static and dynamic regimens preferentially activating specific signalling cascades (Kim, et al., 2015; Li, et al., 2020). We therefore investigated multiple pathways to identify the effect of each regime on these pathways, given that the effects are expected to be dependent on field strength and duration.

This section investigated the gene expression of several key genes from each of these pathways during early commitment and differentiation in MSCs under magnetic stimulation over 7 days (day(s) 1, 3 and 7). Cells were lysed and processed for Fluidigm RT-qPCR as previously. Due to limited measurements, DMF was excluded from statistical analysis unless otherwise stated.

3.5.1 Modulation of the BMP Signalling Pathway

BMP2, a ligand that initiates BMP signalling, and two inhibitors of DNA binding (ID1 and ID2) were assessed under magnetic field stimulation. Both ID1 & ID2 are reported as being increased early targets of osteogenic BMP2 (Kulterer, et al., 2007).

Under intermittent SMF, BMP2 expression started lower than control but significantly increased by day 3. Although expression declined by day 7 it remained elevated compared to day 1. Both ID1 and ID2 were initially upregulated but showed a gradual decline over time, with ID1 significantly downregulated by day 7. Exposure to a constant SMF showed a similar pattern, BMP2 was significantly upregulated by day 7, while ID1 and ID2 were initially increased, followed by a return to control levels. In response to a DMF, BMP2 was significantly upregulated at both day 3 and day 7, while ID1 expression remained low or undetectable. ID2 expression decreased from day 1 to 3 but showed a marked increase by day 7 (**Figure 3-10**). Taken together these findings suggest that magnetic fields, particularly

intermittent and constant SMFs may activate BMP signalling pathways during early osteogenic differentiation in MSCs.

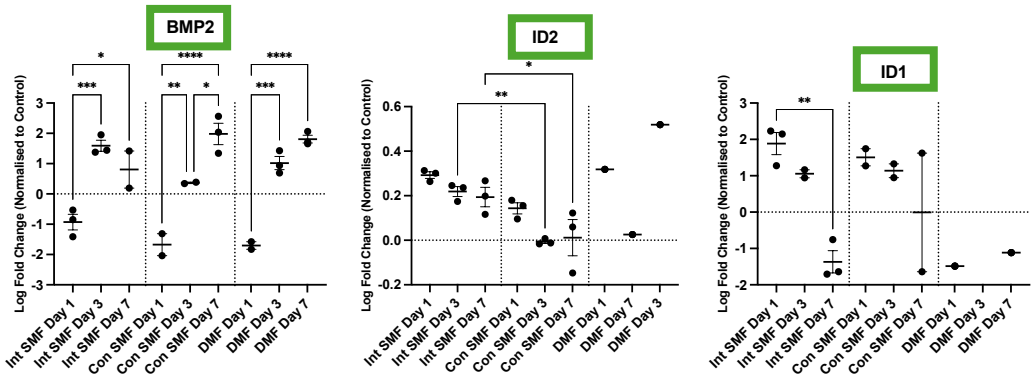

Figure 3-10: Exposure to magnetic fields over 7 days promotes activation of BMP signalling pathway in MSCs

Green boxes denote promoters of osteogenesis. Gene expression under magnetic fields over 7 days. Log fold change was normalised to control; dotted line shows control. Error bars represent mean ± SEM. A one-way ANOVA and post hoc Tukey test was performed to identify significance between conditions Data represents 3 technical replicates for SMF and 1 technical replicate for DMF (with exception of BMP2 which has 3 technical replicates for DMF) (n=1). Due to limited measurements, DMF was excluded from statistical analysis in ID1 and ID2.

3.5.2 Activation of Wnt/β-Catenin Signalling Pathway

Various genes linked to the Wnt pathways (canonical β-Catenin dependent and non-canonical), which are involved in osteogenesis, were assessed in response to magnetic field stimulation, namely Wnt3a, key transcription factors including members of the T cell factor family (TCF3, 4 & 7), and lymphoid enhancer binding factor (LEF1) alongside two Wnt inhibitors – Dickkoph-1 (DKK1) and secreted frizzled-related protein 1 (SFRP1).

Stimulation with an intermittent SMF generally enhanced expression of genes positively associated with Wnt signalling. Notably, LEF1 and TCF3 showed significant upregulation by day 7, alongside a moderate increase in β-Catenin (**Figure 3-9**). Inhibitory regulators DKK1 and SFRP1 were either unchanged or slightly downregulated by day 7. While Wnt3a and TCF7 were mildly upregulated (**Figure 3-11**), Wnt5a remain unaffected. RhoA, a non-canonical Wnt target, showed a clear and significant increase over time, supporting possible non-canonical pathway activation (**Figure 3-12**). Under a constant SMF, gene expression was more variable. While Wnt3a and TCF3 increased over time, only DKK1 reached significant upregulation. SFRP1 and TCF7 trended downward (**Figure 3-11**), and β-Catenin

remained downregulated throughout (**Figure 3-9**). Expression of Wnt3a and RhoA fluctuated but trended slightly upward by day 7 (**Figure 3-12**). In contrast, DMF stimulation produced inconsistent gene responses across time. Early increases were observed for some positive regulators (LEF1, TCF3) but most genes including TCF7 and β-Catenin were downregulated by day 7. Inhibitors such as DKK1 and SFRP1 also showed varied expression and no clear activation of RhoA was observed (**Figure 3-9, 3-11, 3-12**).

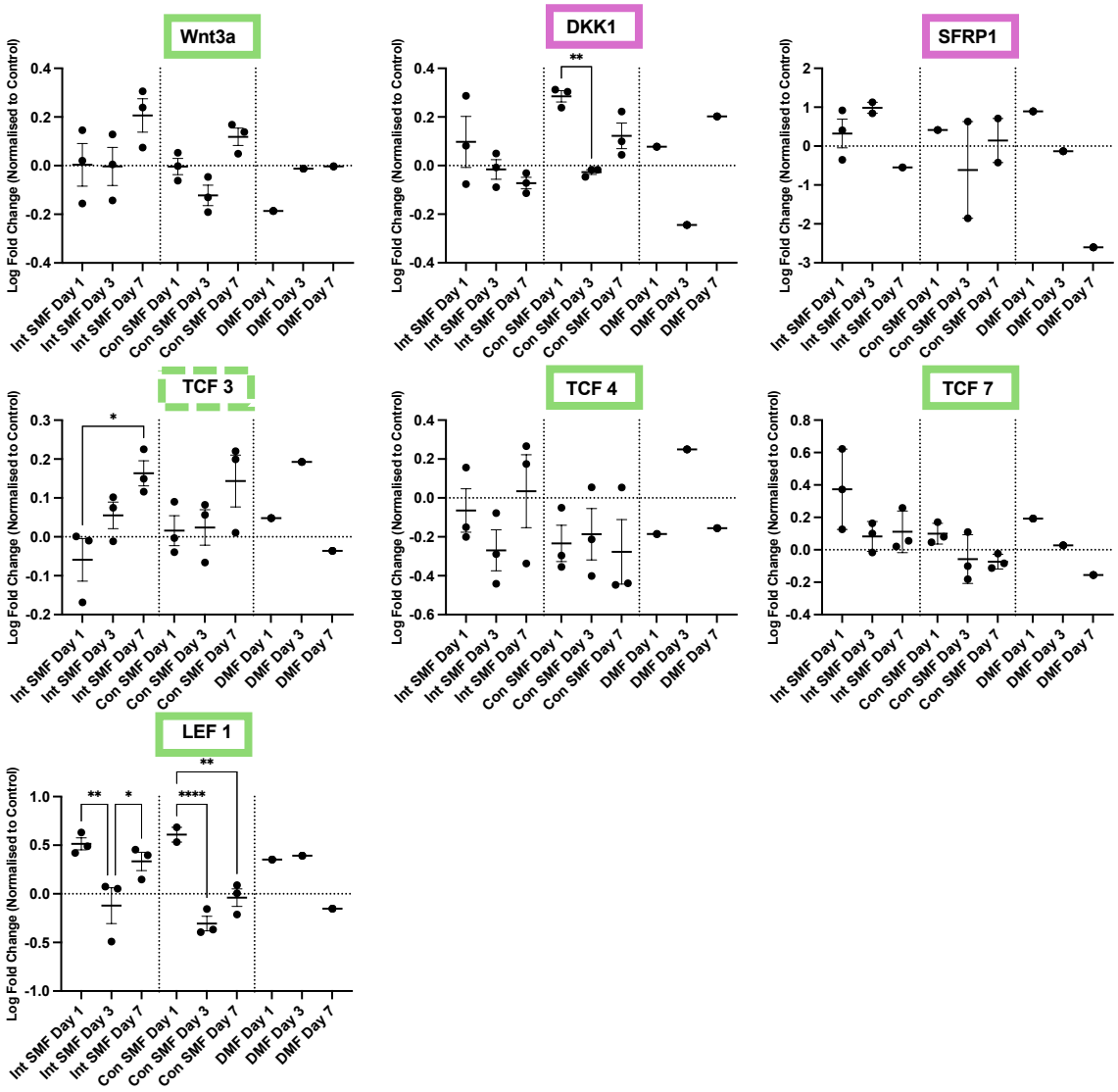

Figure 3-11: Exposure to magnetic fields over 7 days modulates activity of canonical Wnt signalling pathway in MSCs

Green boxes denote promoters of osteogenesis; dashed green denotes promoter if combined with β-Catenin; pink boxes denote inhibitors of Wnt (osteogenesis). Gene expression under magnetic fields over 7 days. Log fold change was normalised to control; dotted line shows control. Error bars represent mean ± SEM. A one-way ANOVA and post hoc Tukey test was performed to identify significance between conditions. Data represents 3 technical replicates for SMF and 1 technical replicate for DMF (n=1). Due to limited measurements, DMF was excluded from statistical analysis.

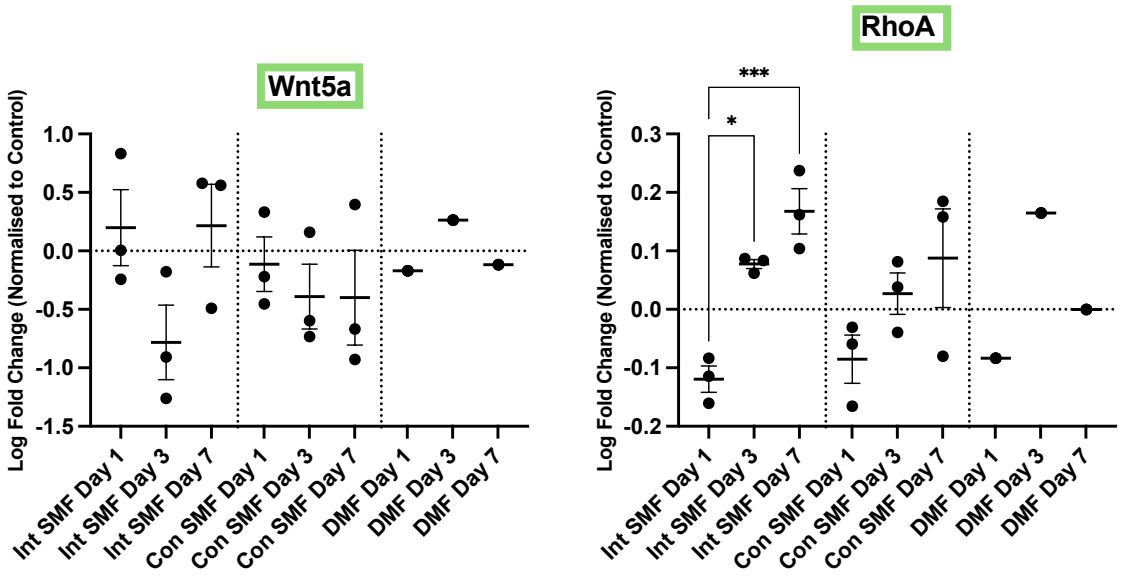

Figure 3-12: Exposure to magnetic fields over 7 days modulates activity of non-canonical Wnt signalling pathway in MSCs

Green boxes denote promoters of osteogenesis. Gene expression under magnetic fields over 7 days. Log fold change was normalised to control; dotted line shows control. Error bars represent mean ± SEM. A one-way ANOVA and post hoc Tukey test was performed to identify significance between conditions. Data represents 3 technical replicates for SMF and 1 technical replicate for DMF (n=1). Due to limited measurements, DMF was excluded from statistical analysis

3.5.3 Sonic Hedgehog and Groucho/TLE Axis in Signal Regulation

To investigate the involvement of the SHH pathway, several members of the Glioma-associated oncogene homolog 1 family were assessed: GLI1, GLI2 and GLI3. These genes play a critical role in hedgehog signalling, which is essential for osteogenic regulation. Alongside these, several members of the Groucho/TLE family of proteins, which are intimately involved in regulating pathways such as Wnt and Notch for osteogenesis, including TLE1, 2, 3 & 4.

Stimulation with an intermittent SMF led to a general downregulation of GLI transcription factors. While GLI1 and GLI2 were downregulated from day 3 onward, GLI3 showed a notable increase at days 3 and 7. Among the TLE co-repressors, most were initially downregulated, however TLE1, TLE3 and TLE4 showed upregulation by day 7, suggesting a mild late phase activation in response to intermittent SMF. Under a constant SMF, expression of all GLI genes remained similar to or below control levels across time. GLI2 had a brief upregulation at day 3, but GLI1 and GLI3 remained largely downregulated.

Similarly, TLE gene expression was mostly reduced, with the exception of TLE1, which trended upward toward control levels by day 7. Overall, the constant SMF appeared to have a limited stimulate effect on the SHH or Groucho/TLE pathways. In contrast, DMF exposure produced more variable gene response. For the GLI factors, expression shifted from early upregulation (notably GLI1 and GLI3 at day 3) to downregulation by day 7. Among TLE genes, expression patterns fluctuated across time points: for example, TLE3 and TLE4 were upregulated at day 3 but decreased again by day 7 (**Figure 3-13**). In summary, these findings suggest that magnetic actuation does not consistently activate the SHH or Groucho/TLE pathways during MSC osteogenesis. While there are some transient gene expression changes, particularly under DMF and intermittent SMF, overall involvement appears limited.

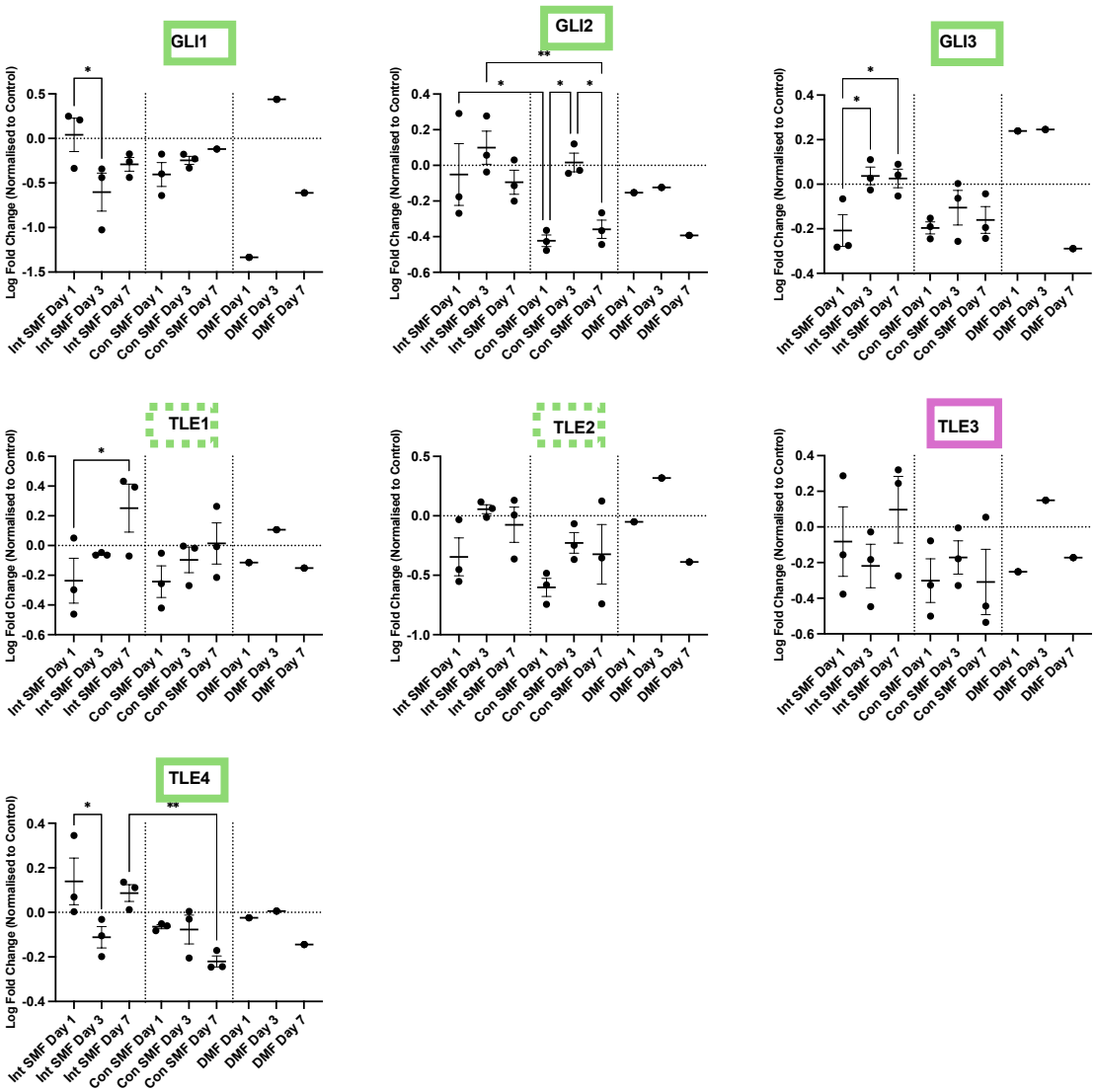

Figure 3-13: Exposure to magnetic fields over 7 days modulates activity of Sonic Hedgehog and Groucho/TLE signalling pathway in MSCs

Green boxes denote promoters of osteogenesis (dotted line represents conflicting evidence); pink boxes denote inhibitors of osteogenesis. Gene expression under magnetic fields over 7 days. Log fold change

was normalised to control; dotted line shows control. Error bars represent mean ± SEM. A one-way ANOVA and post hoc Tukey test was performed to identify significance between conditions. Data represents 3 technical replicates for SMF and 1 technical replicate for DMF (n=1). Due to limited measurements, DMF was excluded from statistical analysis.

3.5.4 Induction of Angiogenesis

Angiogenesis (blood vessel formation) and osteogenesis are linked processes that are essential for bone repair and regeneration. To complement the investigations of signalling pathways affected by magnetic field exposure, key hypoxic and angiogenic markers were also examined. Angiogenic signalling is closely associated with osteogenesis, as vascularisation supports bone formation and tissue remodelling (Grosso, et al., 2017). Based on the established relationship between osteogenesis and vascularisation we hypothesised that an intermittent SMF would lead to upregulation of both angiogenic and hypoxic markers.

Transcription factors to cell adaptation to low oxygen, hypoxia-inducible factors 1 and 2 (HIF1A and HIF2A) were examined, alongside VEGF, angiopoietin 1 (ANG-1), FGF-2 and IL-6. Intermittent SMF exposure led to a progressive increase in both HIF1A and HIF2A expression over time. While HIF1 was briefly downregulated at day 3, it showed a significant upregulation by day 7. Similarly, HIF2A increased from day 3 and remained elevated through day 7. In contrast, a constant SMF had minimal effect on hypoxia gene expression. HIF1A showed a transient rise at day 3, returning to baseline by day 7, while HIF2A expression increased slightly at day 3 but remained close to control levels overall. The response to a DMF was more variable, HIF1A was consistently upregulated peaking at day 3, whereas HIF2A remained downregulated across all time points showing a steady decline (**Figure 3-14**). In summary, MSCs induce a slight hypoxic response when exposed to an intermittent SMF.

Exposure to an intermittent SMF induced an initial downregulation of VEGF expression, which progressively increased to a significant upregulation by day 7, and ANG-1 expression was maintained slightly above control levels over 7 days. Similarly, IL-6 expression peaked significantly at day 3, before returning to baseline by day 7, while FGF-2 showed a biphasic response, with upregulation observed at days 1 and 7, with a significant downregulation at day 3. In contrast, constant SMF exposure consistently downregulated VEGF expression, with a modest increase at day 3, followed by further decline at day 7, while FGF-2 remained

consistently downregulated at all time points. ANG-1 expression under a constant SMF was similar to control, with little variation over 7 days. IL-6 exhibited a slight upregulation initially but trended downward over time, approaching control levels by day 7. DMF exposure resulted in a downregulation of both VEGF and FGF-2 at day 1; VEGF expression then peaked at day 3, returning to a downregulation by day 7. ANG-1 and IL-6 were consistently upregulated from days 1-3 but trended downwards by day 7, with IL-6 showed marked downregulation (**Figure 3-14**). Collectively these findings indicate that an intermittent SMF most strongly stimulates angiogenic and inflammatory signalling over time. In comparison, a constant SMF and DMF showed more variable or transient angiogenic responses.

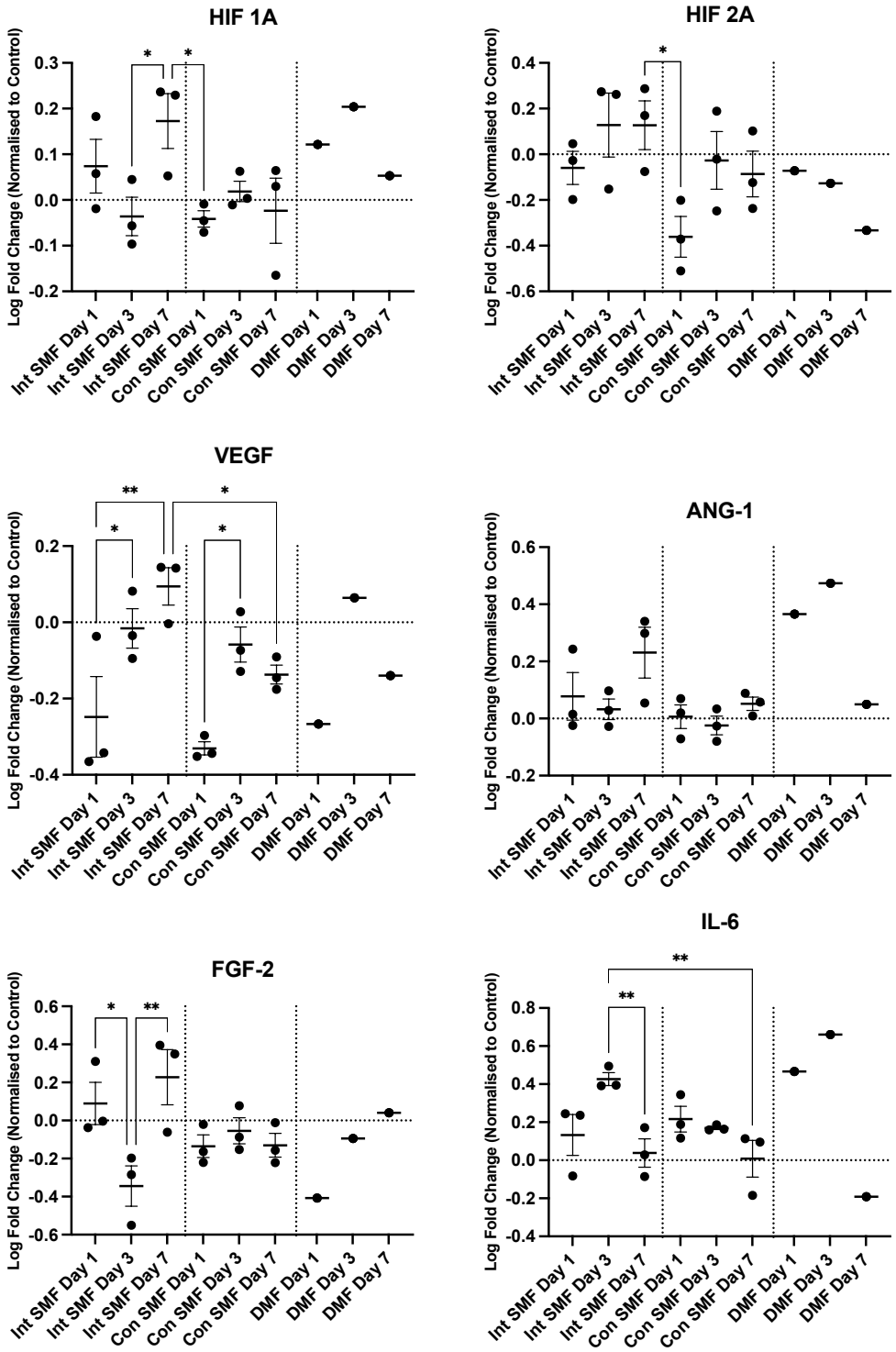

Figure 3-14: Exposure to magnetic fields over 7 days promotes upregulation of hypoxic markers and induction of angiogenesis

Gene expression under magnetic fields over 7 days. Log fold change was normalised to control; dotted line shows control. Error bars represent mean ± SEM. A one-way ANOVA and post hoc Tukey test was performed to identify significance between conditions. Data represents 3 technical replicates for SMF and 1 technical replicate for DMF (n=1). Due to limited measurements, DMF was excluded from statistical analysis

3.6 Mechanotransduction

3.6.1 YAP Gene Expression

MSCs are highly responsive to mechanical cues in their microenvironment, converting these physical signals into biochemical responses through a process known as mechanotransduction – a key driver of their fate and function, particularly during osteogenesis. YAP signalling is a central mechanotransducive pathway that translocates to the nucleus in response to mechanical stimuli. Magnetic fields can generate biophysical cues that influence MSC mechanosensing and downstream YAP activity (Yang, et al., 2016). Given the relationship between YAP signalling and osteogenic commitment (Sun, et al., 2022), an intermittent SMF is expected to promote YAP translocation in line with its observed effect on enhancing osteogenic commitment.

To investigate how magnetic fields influence mechanotransduction, the activity of YAP and TAZ, transcriptional co-activators, were examined in MSCs over 7 days using Fluidigm RT-qPCR **(Figure 3-15)**.

In MSCs exposed to an intermittent SMF, YAP expression trended towards slight upregulation throughout the 7 day period, whereas TAZ expression remained similar to control. Under a constant SMF, YAP expression was initially trending higher than control values, but decreased with time in culture, whilst TAZ expression trended to down regulation, gradually increasing over 7 days to control levels. In MSCs exposed to a DMF, YAP expression varied around control values, with TAZ expression increased early on, coming back to control values by day 7 **(Figure 3-15)**.

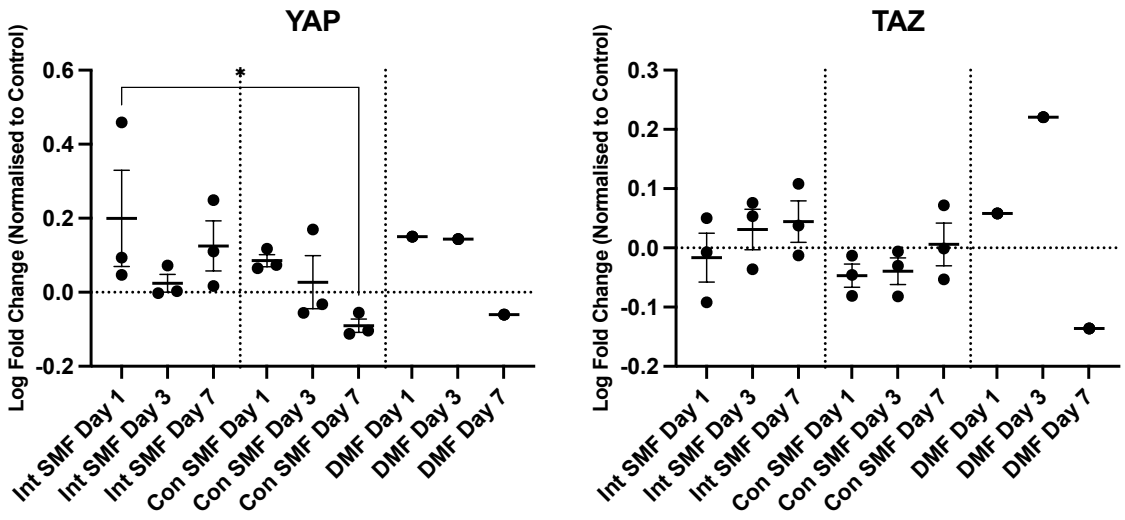

Figure 3-15: Exposure to magnetic fields over 7 days regulates YAP/TAZ expression in MSCs

Gene expression under magnetic fields over 7 days. Log fold change was normalised to control; dotted line shows control. Error bars represent mean ± SEM.A one-way ANOVA and post hoc Tukey test was performed to identify significance between conditions. Data represents 3 technical replicates for SMF and 1 technical replicate for DMF (n=1). Due to limited measurements, DMF was excluded from statistical analysis

3.6.2 YAP Nuclear Translocation

Upon mechanical activation, YAP translocates from the cytoplasm to the nucleus, where it interacts with transcription factors to regulate gene expression, particularly genes associated with osteogenesis (Lin, et al., 2025). Nuclear localisation of YAP is therefore a key indicator of MSC mechanotransduction and osteogenic potential. Magnetic fields can provide biophysical cues that mimic aspects of mechanical stimulation, potentially modulating YAP translocation in a field-dependent manner (Zheng, et al., 2018). Nuclear translocation of YAP is expected in response to the applied magnetic fields, reflecting their influence mechanotransducive pathways. In this study, MSCs were exposed to magnetic regimes and nuclear YAP localisation was assessed. Fluorescent MSC imaging of cells allowed for quantification of nuclear translocation over 72 hours **(Figure 3-16, A)**.

Following quantification of YAP staining in the cytoplasm and nucleus, the ratio of nuclear to total YAP was measured and expressed as a percentage (**Figure 3-16, B**). In control cells, nuclear YAP gradually decreased over time in culture from ~2.4% at 2 hours to ~1.6% at 72 hours. In contrast, all magnetic field stimulations caused an early increase in YAP at 2 and 6 hours, suggesting an acute cellular response to the magnetic environment. While levels

began to decline after 24 hours, they generally remained above or close to control values until eventually decreasing to similar levels by 72 hours **(Figure 3-16, B)**. This pattern suggests that MSCs may interpret magnetic field stimulation as a mechanical input, leading to transient YAP nuclear translocation consistent with activation of mechanotransducive pathways.

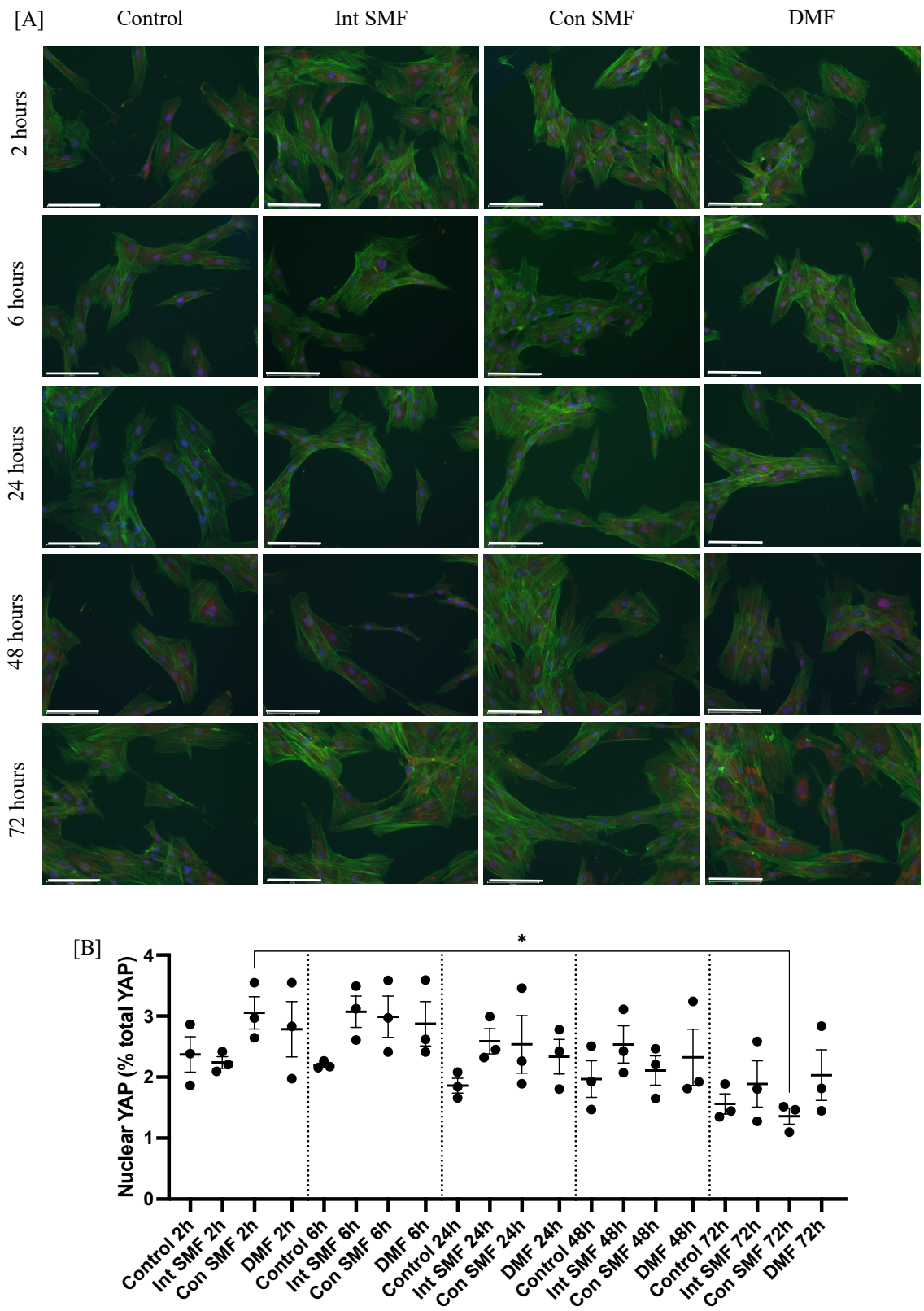

Figure 3-16: Exposure to magnetic fields over 7 days promotes translocation of YAP to nucleus

Immunofluorescent staining was utilised to investigate translocation of Yes-associated protein 1 (YAP) to nucleus under magnetic actuation. Images were captured with fluorescent microscopy on EVOS; scale bars show 150 µm [A] Images taken of timepoints 2, 6, 24, 48 and 72 hours. Green= F-actin (cytoskeleton); Red=YAP and Blue= DAPI stained nucleus [B] Quantification of nuclear YAP as

percentage of total YAP expression over time. Using acquired imaging, three technical replicates used, with five non-overlapping images per well. Images were analysed using ImageJ, and total YAP expression was quantified by measuring the YAP expression, while nuclear YAP was calculated as YAP overlapping with nuclear staining. Error bars represent mean ± SEM. A one-way ANOVA and post hoc Tukey test was performed to identify significance between conditions.

3.6.3 Nuclear Morphology

Nuclear morphology can adapt depending on the mechanical input from the surrounding microenvironment. Typically, high cell tensions will deform the nucleus and flatten or elongate it, which is usually related to increased nuclear YAP. Therefore, in addition to YAP translocation, fluorescent images **(Figure 3-16, A)** were used to examine changes to nuclear area and circularity under application of magnetic fields. Changes in nuclear morphology are expected in response to applied magnetic fields, reflecting the effects of mechanotransducive channels.

In the control, nuclear area showed a gradual small decrease over time. Under an intermittent SMF, at 2 hours nuclear area was significantly reduced compared to control. By 6 hours, there was a slight non-significant increase above control. At 24 and 48 hours, nuclear area remained slightly reduced but not significantly different. By 72 hours, there was a further reduction in nuclear area, though not statistically significant. Magnetic actuation with a constant SMF significantly reduced nuclear area at 2 and 6 hours in comparison to control and all other conditions. At 24 hours, the reduction persisted but was not significant. At 48 hours, nuclear area significantly increased compared to all other group. By 72 hours, nuclear area decreased significantly below control levels. DMF exposure also resulted in a significantly reduced nuclear area at 2 hours in comparison to control, but larger than nuclei under constant SMF exposure. At 6 hours, nuclear area was similar to control but statistically different due to data variability. At 24 and 48 hours, nuclear area showed slight, non-significant reductions. At 72 hours nuclear area was significantly reduced compared to control (**Figure 3-17**). In summary, nuclear area decreased at 2 hours in all magnetic field conditions compared to control. Over time, intermittent SMF exposure showed minor fluctuations with no significant long-term changes, constant SMF exposure caused a significant early reduction and a spike at 48 hours, and DMF exposure showed variable but generally decreased nuclear area by 72 hours.

In parallel with nuclear area, circularity was analysed as an additional indicator of mechanical response, with increased circularity typically reflecting reduced cytoskeletal

tension and lower mechanical strain on the nucleus (Dahl, et al., 2008). Nuclear circularity increased significantly at 2 hours across all magnetic field conditions compared to control, indicating early nuclear shape changes. Over time, intermittent SMF showed an initial rise in circularity followed by a gradual decline, with significantly reduced circularity at 24 hours. Values returned closer to control levels at 48 hours and increased slightly again at 72 hours, though not significantly. Exposure to a constant SMF consistently showed elevated circularity across nearly all time points. Significant increases were observed at most time points (excluding 48 hours), suggesting a more sustained morphology effect on the nucleus. In contrast, DMF exposure produced more variable results. After an initial increase at 2 hours, circularity significantly dropped at 6 and 24 hours. By 72 hours, circularity was again significantly elevated, similar to constant SMF but distinct from both control and intermittent SMF (**Figure 3-18**). These findings suggest that magnetic stimulation, particularity under a constant SMF induces sustained changes in nuclear morphology, potentially reflecting altered mechanical signalling within MSCs.

Together this data suggests that magnetic field stimulation, regardless of type, induces a rapid mechanical response in MSCs, marked by increased nuclear YAP, reduced nuclear area and more rounded nuclear morphology. This pattern is consistent with early mechanotransduction events, where cells may perceive magnetic fields as a form of mechanical input, prompting cytoskeletal tension and nuclear adaption.

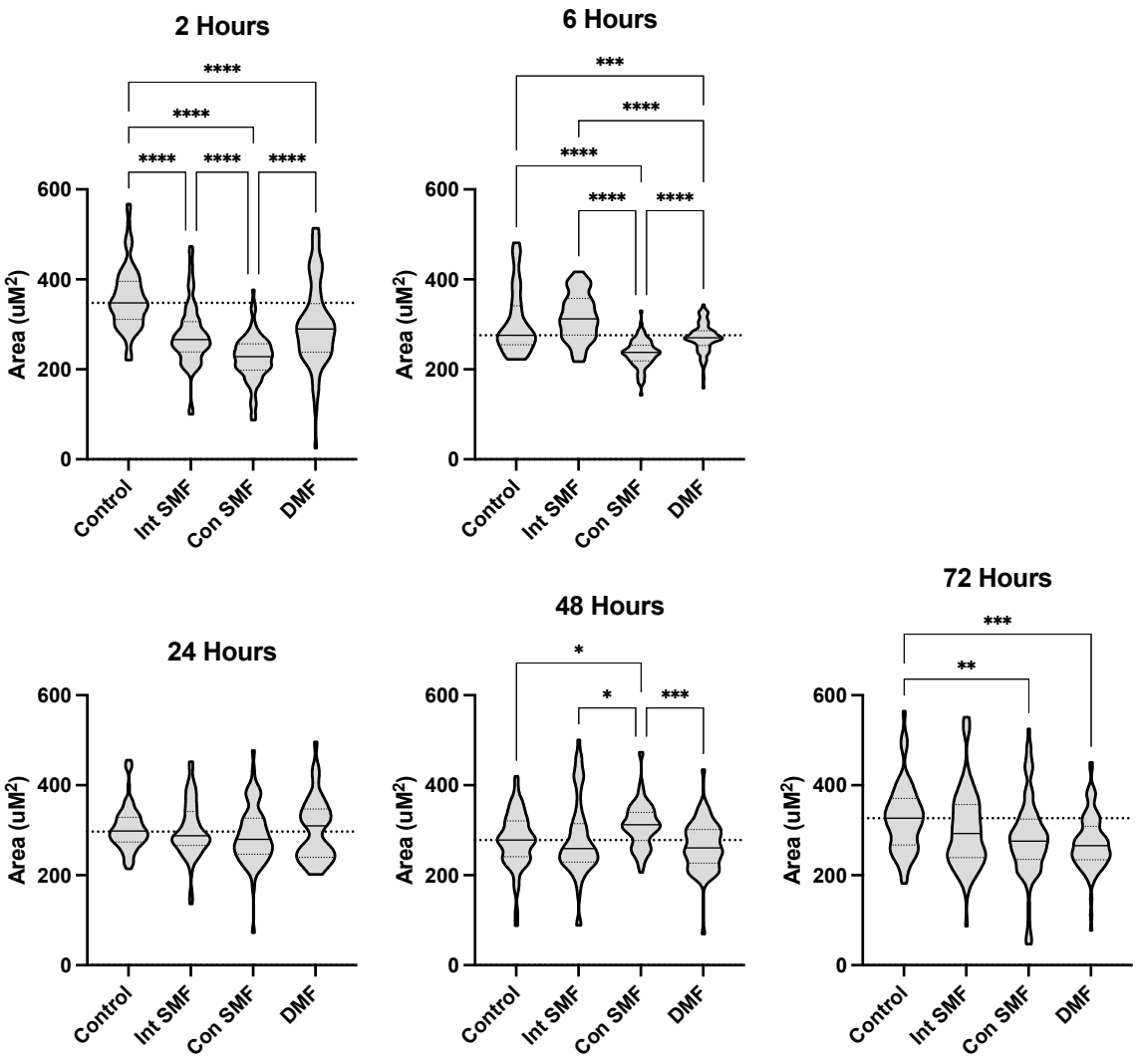

Figure 3-17: Exposure to magnetic fields reduces nuclear area in MSCs

Mesenchymal stromal cells were imaged using EVOS fluorescent microscopy. Nuclear area was quantified using DAPI staining with ImageJ software. Truncated violin plots show the distribution of nuclear circularity measurements with median (solid line) and interquartile range (dashed lines), and dotted line shows median of control group. For each condition, 3 wells were imaged with 5 non-overlapping fields per well (n=1). A one-way ANOVA and post hoc Tukey test was performed to identify significance between conditions.

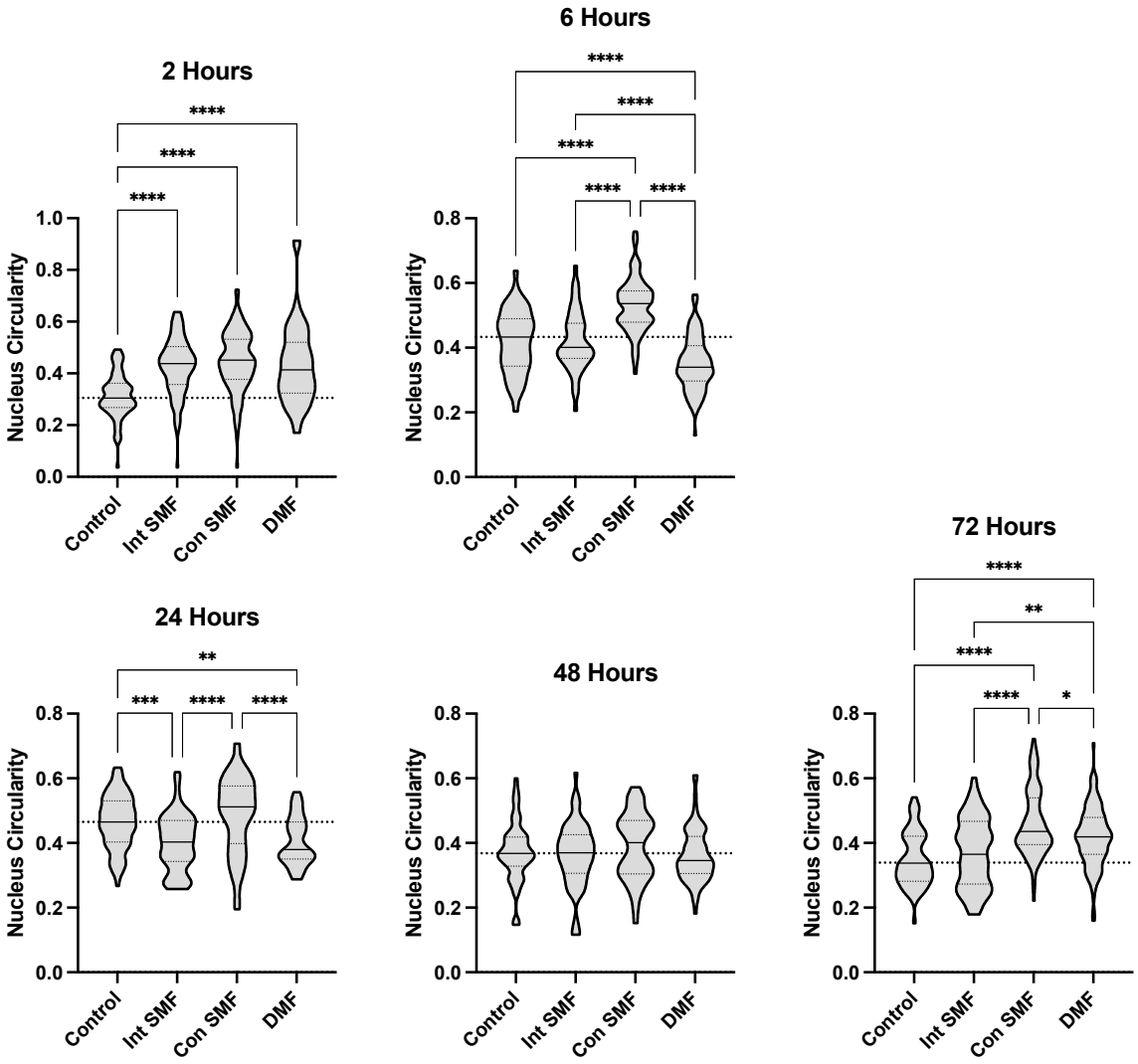

Figure 3-18: Exposure to magnetic fields modulates nuclear circularity

Mesenchymal stromal cells were imaged using EVOS fluorescent microscopy. For each condition, 3 wells were imaged with 5 non-overlapping fields per well. Nuclear outlines for circularity analysis were determined using DAPI staining, and quantification was performed with ImageJ software. Truncated violin plots show the distribution of nuclear circularity measurements with median (solid line) and interquartile range (dashed lines), and dotted line shows median of control group. For each condition, 3 wells were imaged with 5 non-overlapping fields per well (n=1). A one-way ANOVA and post hoc Tukey test was performed to identify significance between conditions.

3.7 Paracrine Signalling Under Static and Dynamic Magnetic Fields

Paracrine signalling is crucially important for the therapeutic effects of MSCs. MSCs release a mix of growth factors, cytokines, chemokines and EVs. These act to modulate inflammation, promote cell proliferation and differentiation and assist in tissue remodelling - therefore are important in bone tissue engineering

3.7.1 Cytokine Section in Cell Supernatant

Paracrine signalling, *via* cytokines, is recognised as a major contributor the therapeutic potential of MSCs. MSCs secret a diverse range of cytokines, dynamically adapting these profiles in response to external cues to modulate their therapeutic effects, for example inducing a wound healing profile in response to tissue injury. Magnetic fields, as a form of biophysical stimulation, may influence MSC paracrine activity, potentially enhancing secretion of regenerative or angiogenic factors (Manjua, et al., 2021; Wu, et al., 2021; Zhang, et al., 2023). In this study MSCs were exposed to magnetic field regimes, and the levels and profiles of secreted cytokines were assessed. Cytokine secretion profiles are expected to be influenced by the applied magnetic fields, although the specific profiles remain to be determined.

Cell suspension was collected from cells exposed to magnetic fields over 7 days for identification of cytokine expression on day(s) 1, 3 and 7. Protein concentration was measured prior to cytokine analysis **(Figure 3-19, A)**. In addition to cell conditions, a negative control using only cell culture media was run to determine any cytokines secreted by MSCs into the media **(Figure 3-19, B)**.

Protein expression from the collected MSC conditioned media in all conditions was examined prior to cytokine analysis, with protein concentration was maintained between 7 and 12 mg/mL for most conditions. Protein concentration was not normalised prior to cytokine analysis, as no significant differences between samples were observed, and consistent volumes of cell suspension were collected for analysis **(Figure 3-19, A)**. To determine any background cytokine expression present in cell media, a fresh culture media negative control was analysed, showing only reference points on negative control, confirming absence of background cytokines present in cell media **(Figure 3-19, B)**.

The cytokine expression was then determined, mapping positive hits from the membrane blots onto the list of cytokines supplied in the kit **(Supplementary Figure S 1)**. Utilising reference points, expression was quantified to create profile for each condition. Generally, the cytokine levels were highest on day 1, reducing on days 3 and 7 in all conditions **(Figure 3-19, C).**

On day 1, nineteen cytokines were detected, with nine prominently secreted by control MSCs, including Serpin E1, IGFBP-3, IL-8, Chitinase 3-like 1, IL-6 and MCP-1, while

Pentraxin 3, Thrombospondin and VCAM- showed lower levels. All magnetic field conditions enhanced cytokine secretion compared to control, especially IFGBP-3, IL-8, Serpin E1, MCP-1 and Chitinase 3-like 1. Additional cytokines such as Angiogenin, DKK1, ENA78 and FGF-19 were only detected under magnetic simulation. Among these, intermittent SMF induced the least secretion, while constant SMF uniquely promoted Cystatin C, ENA-78, SDFα, and VCAM-1 secretion. By day 3, fewer cytokines (fifteen total) were identified with generally lower expression. The control profile was similar to day 1 with mild increases in DKK1, ENA-78 and GROα. Magnetic field exposed MSCs maintained a cytokine profile similar to day 1. At day 7 cytokine numbers and expression further decreased across all conditions, with only four cytokines consistently detected in both control and magnetic field samples: Chitinase 3-like 1, DKK1, IL-8 and Serpin E1 **(Figure 3-19, C).**

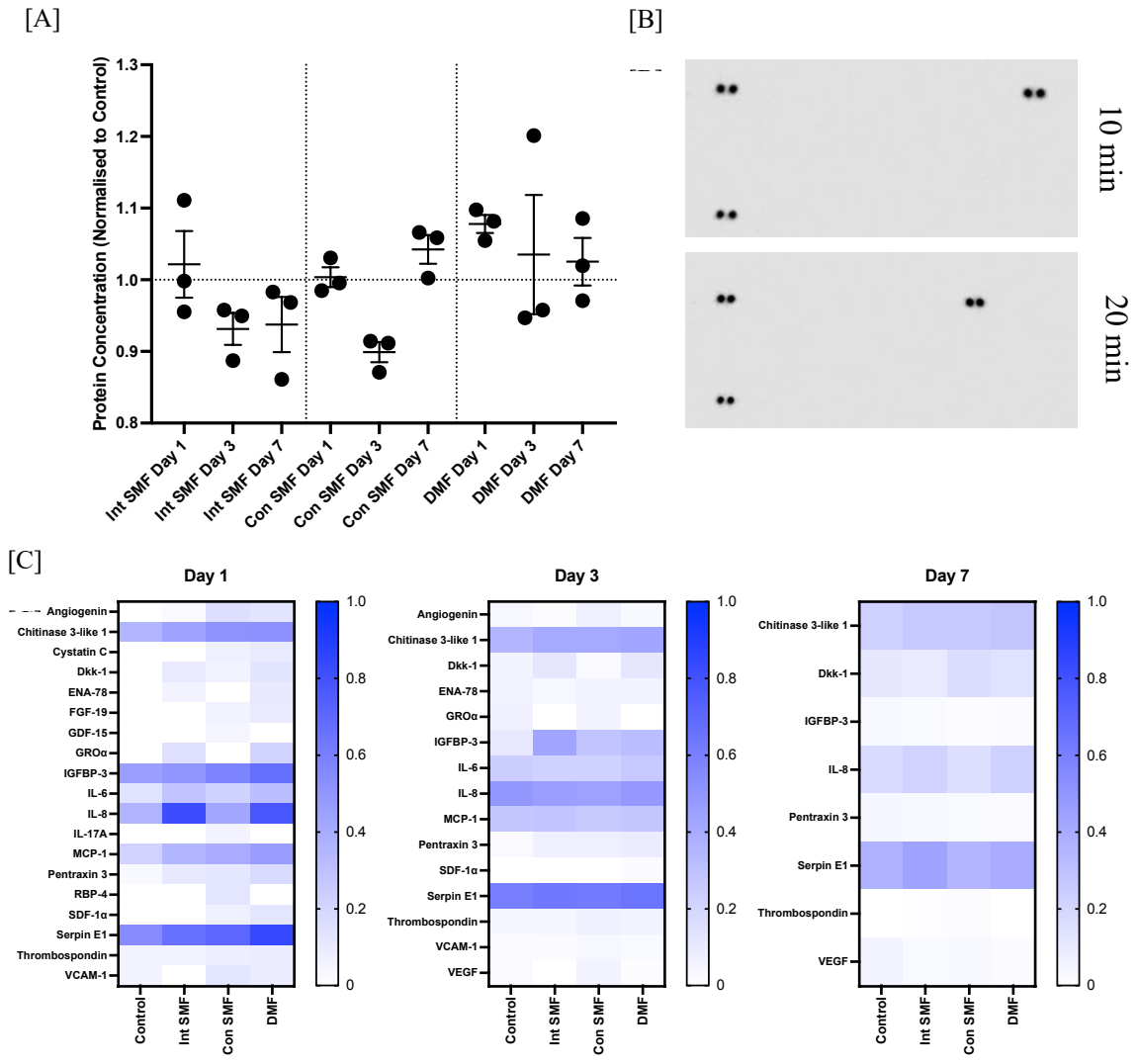

Figure 3-19: Exposure to magnetic fields alters MSC cytokine profiles

Conditioned media from mesenchymal stromal cells (MSCs) was collected at days 1, 3 and 7 and analysed using the Human Cytokine Array immunoblot [A] Protein concentration of MSC conditions media. Error bars represent mean ± SEM. A one-way ANOVA and post hoc Tukey test was performed to identify significance between conditions. [B] The media only negative control blot, demonstrating the reference points, with no detectable cytokines from the media (with 10 and 20 minute exposure time) [C] Cytokine profiles MSC conditioned media at days 1, 3 and 7, normalised to reference points (n=1)

3.7.2 Extracellular Vesicle Collection, Isolation and Characterisation

In addition to cytokines, EVs play a key role in MSC paracrine signalling, carrying bioactive molecules such as proteins, RNAs and lipids that can influence target cells and modulate tissue regeneration. To investigate whether how magnetic regimes influence broader paracrine function *via* EVs, MSC-derived EVs were collected and isolated from 2D MSC cultures under magnetic fields. EV characteristics were analysed using ZetaView nanoparticle tracking analysis (NTA) and tuneable resistive pulse sensing (TRPS). Based on the adaptions to MSC cytokine profiles under magnetic field exposure we anticipated the applied magnetic regimes would similarly influence broader paracrine signalling, including EV production and characteristics.

EV concentration was measured against particle size, showing similar peaks in concentration between 130-160 nm EV size for all magnetic field conditions, suggesting isolated EVs were a mix of both exosomes and microvesicles. **Figure 3-20** shows the NTA data. The EV concentration collected for MSC cultures was highest in control cells and those stimulated with an intermittent SMF (7.99 x 10^6 per mL and 9.50 x 10^6 per mL respectively), whilst cells exposed to a constant SMF and DMF conditions showed a noticeable reduction in their peak concentration (1.47 x 10^6 per mL and 1.0 x 10^6 per mL respectively). The total concentration of control EVs was lowest (1.7-1.8 x 10^8 per mL) with cells exposed to magnetic fields generating higher concentrations of EVs overall: 2.0-2.2 x 10^8 per mL (intermittent SMF); 2.5-2.7 x 10^7 per mL (constant SMF) and 2.5-3.6 x 10^7 per mL (DMF).

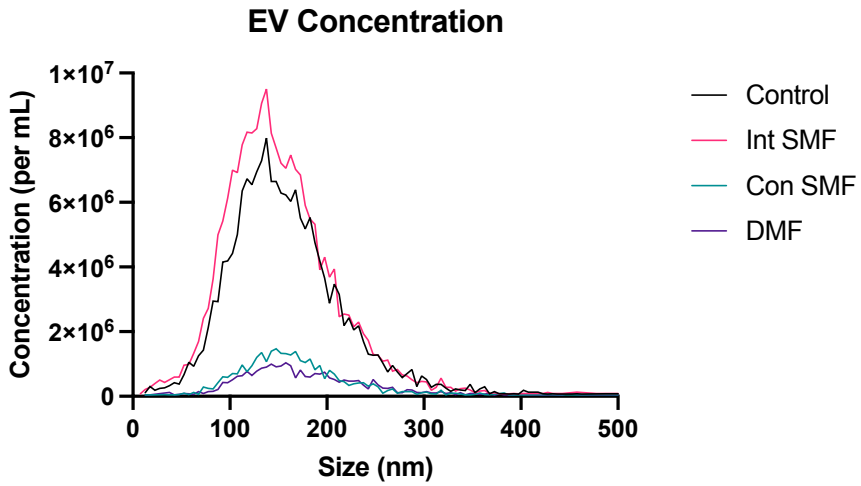

Figure 3-20: Exposure to magnetic fields alters MSC EV concentration and size

Extracellular vesicles (EVs) were isolated from mesenchymal stromal cells cultured under magnetic field regimes for 8 days. Collected EVs were isolated and analysed using nanoparticle tracking analysis for EV concentration against size (n=1).

EV concentration and size was also analysed using TRPS. Interestingly, an increased concentration of SMF EVs was detected for both intermittent and constant SMF conditions, with both showing increased concentrations compared to control, and DMF showing a marked reduction in concentration. In control condition, overall EV concentration was identified at 2.62 x 10^9 per mL, with peak concentration of 4.32 x 10^8 at for particles size ~107 nm. Exposure to an intermittent SMF increased overall EV concentration to 5.42 x 10^9, with peak of EV size seen at 133 nm with highest concentration of 9.34 x 10^7 per mL. Interestingly, with TRPS a high concentration of EVs was identified from exposure to a constant SMF at 4.69 x 10^9 per mL. A clear peak in concentration was identified with EVs around 142 nm, with a concentration of 1.00 x 10^9 mL. Under a DMF, EV concentration showed a marked reduction to 5.7 x 10^7 per mL, with a peak in concentration observed at 115 nm, with a concentration of 1.15 x 10^8 **(Figure 3-21, A)**. In addition, mean (± SD) particle diameter was measured using TPRS. Diameter for control EVs was 175 nm (±73.4 nm). Under an intermittent SMF mean EV diameter increased to 184 nm (±72.2 nm) while a Con SMF showed similar measurements to control at 175 nm (±73.4 nm). Exposure to a DMF reduced particle size to 141 nm (±49.4 nm) **(Figure 3-21, B).** Data from both the NTA and TRPS analyses are summarised in **Table 3-1**.

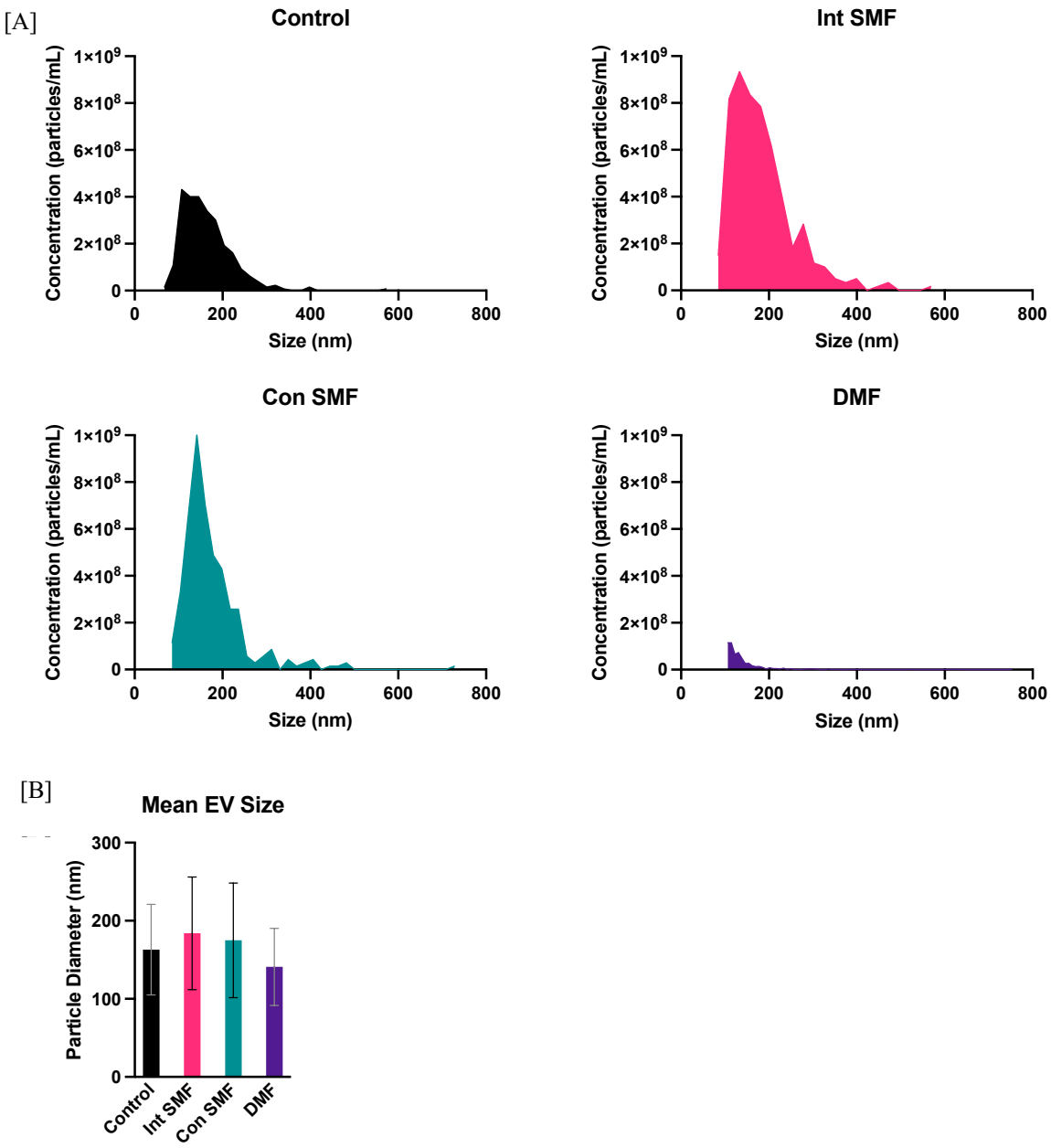

Figure 3-21: Exposure to magnetic fields alters MSC EV concentration and diameter

Extracellular vesicles (EVs) were isolated from mesenchymal stromal cells cultured under magnetic field regimes for 8 days. Collected EVs were isolated and analysed using tuneable resistive pulse sensing [A] Histograms of concentrations against size [B] Mean EV particle size, error bars represent SD (n=1).

Condition	NTA		TRPS	
	Concentration (Particles/mL)	Size (nm)	Concentration (Particles/mL)	Size (nm)
Control	1.7 - 1.8 x 10^8	143 -150	7.5 x 10^7	163 (±58)
Int SMF	2.0 - 2.2 x 10^8	139 - 144	1.1 x 10^8	184 (±72)
Con SMF	2.5 - 3.6 x 10^7	155 - 158	9.8 x 10^7	175 (±73)
DMF	2.5 - 2.7 x 10^7	160 - 168	5.7 x 10^8	141 (±49)

Table 3-1: Extracellular vesicle characterisation by nanoparticle tracking analysis and tuneable resistive pulse sensing

Extracellular vesicles (EVs) were isolated from mesenchymal stromal cells cultured under magnetic field regimes for 8 days. Collected EVs were isolated and analysed using nanoparticle tracking analysis (NTA) and tuneable resistive pulse sensing (TRPS). For NTA, the table shows the range of EV concentration and size measured across three technical replicates. For TRPS, average EV concentration and size are reported (n=1).

3.7.3 Extracellular Vesicle Cytokine Cargo Characterisation

In addition to assessing overall MSC cytokine secretion, the cargo of isolated EVs was investigated to determine which signalling molecules were selectively packaged and potentially delivered to target cells. MSCs are known to alter EV cargo in response to mechanical and biophysical cues, selectively packing signalling molecules to adapt their paracrine output to the microenvironment (Kou, et al., 2022). Based on the observed changes to MSC cytokine profiles under magnetic fields (**Figure 3-19**) EV cargo is expected to display distinct field dependent profiles, with pro-regenerative and anti-inflammatory expression dominating these profiles. EVs collected from MSCs exposed to magnetic fields were examined to characterise how magnetic stimulation influences this adaptive packaging, providing insight into field dependent.

As previously for the MSC conditioned media, protein concentration was measured; here, the DMF has significantly less protein content than all other conditions (**Figure 3-22, A**). EV concentration was normalised prior to cytokine analysis, with control and both SMF conditions at 5 x 10^9. Due to the significantly reduced protein concentration from the DMF samples, an EV concentration of 1 x 10^9 was ultimately used for this condition. Expression was divided into two heat maps to identify changes between high- and low-level expression profiles.

In control, intermittent and constant SMFs, the EV cytokine cargo consistently included Chitinase 3-like 1, EMMPRIN, Endoglin, IGFBP-3, Pentraxin 3, Serpin E1 and Thrombospondin. In contrast the DMF condition exhibited a highly restricted cytokine profile, with detectible expression limited to only Pentraxin 3 and Thrombospondin. Among the detected proteins, Serpin E1 showed the strongest expression across control and both SMF conditions. IGFBP-2 was notable expressed in both control and intermitted SMF samples, while Chitinase 3-like 1 was present across all conditions but most prominent under a constant SMF **(Figure 3-22, C)**.

In addition to strongly expressed cytokines, eighteen other cytokines were detected at lower expression levels across conditions. Notably, FGF-7 was detected in both control and intermittent SMF samples, while HGF showed a progressive increase in expression corresponding to increasing magnetic field exposure time. VCAM-1 was also consistently observed at low levels across magnetic field conditions.

The MSC-EV cytokine profile differed from the MSC conditioned media profile, illustrating the differences in paracrine signalling between soluble secreted factors and those packaged into EVs. Several cytokines were uniquely detected in EVs but not in conditioned media, indicating selective packaging. Among these EMMPRIN and Endoglin showed particularly high expression in EVs. Additional cytokines present only in EV cargo at low levels included Angiopoietin-1, DPPIV, FGF-7, HGF, Lipocalin-2, M-CSF, MMP-9, Osteopontin, Resistin and uPAR. Conversely some cytokines presented in the conditioned media were notably absent from the EV cytokine profile, including Angiogenin, Cystatin-C, DKK1, ENA-78, FGF-19, GROα and RBP-4. These findings indicate that EV cargo does not merely reflect the soluble secretome but represents a distinct and selectively enriched subset of cytokines, potentially tailored for targeted intercellular signalling.

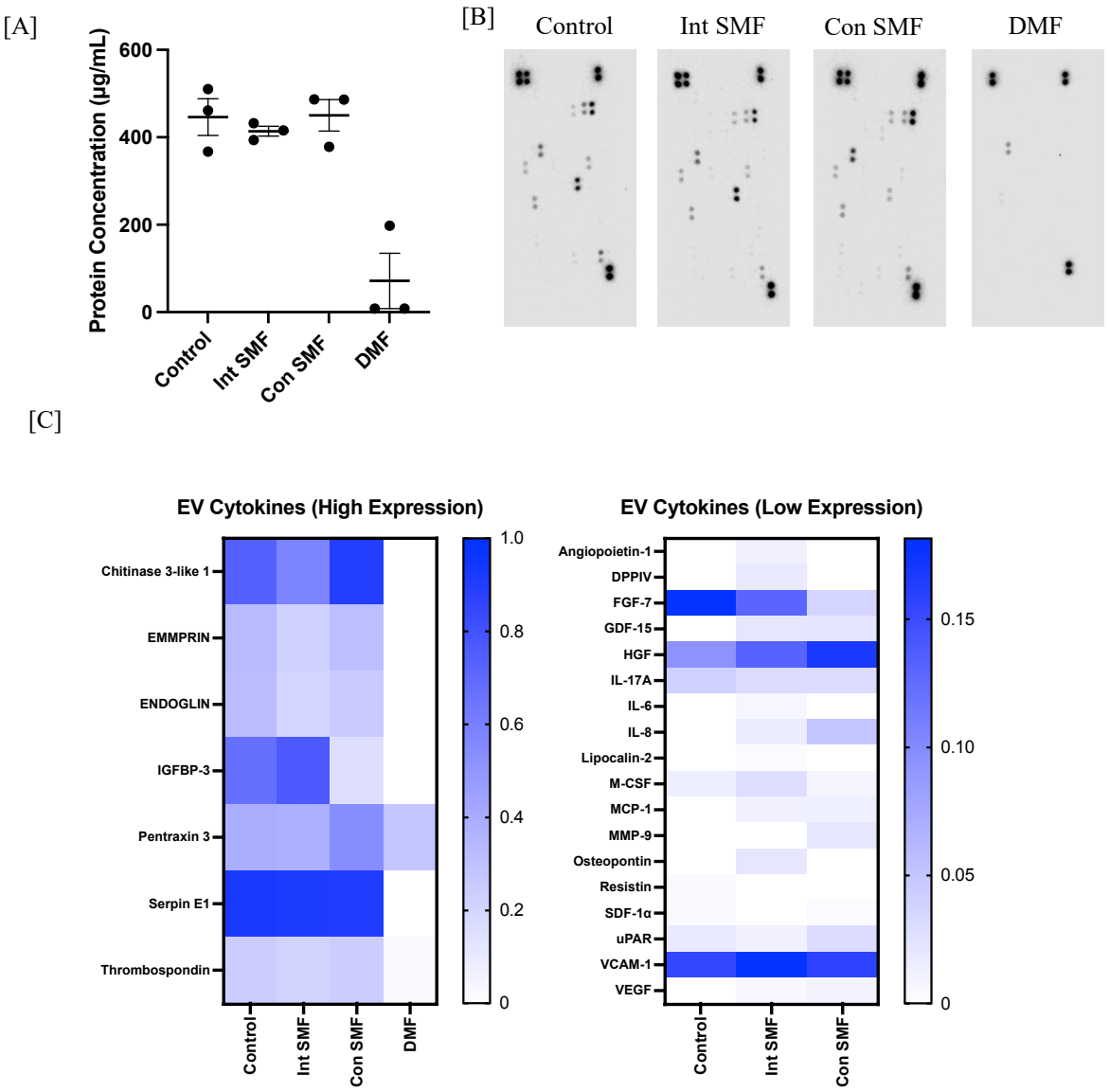

Figure 3-22: Exposure to magnetic fields alters contents of MSC EVs

Extracellular vesicles (EVs) were collected over 8 days from mesenchymal stromal cells (MSCs) under magnetic regimes, and their cargo analysed using the Human Cytokine Array immunoblot [A] Protein concentration of EV collections from each condition. Error bars represent mean ± SEM. A one-way ANOVA and post hoc Tukey test was performed to identify significance between conditions. [B] Cytokine expression detected on nitrocellulose membranes arrays, showing protein cargo present across magnetic field conditions [C] Cytokine profiles for EVs for each condition presented as two heat maps, separated by expression intensity. High expression was defined as ≥0.2 (arbitrary units), and low expression as <0.2, except from thrombospondin under the DMF condition, which was included in the high expression group due to high expression in other conditions. The DMF condition was excluded from the low-expression heatmap as no cytokines were detected within this range (n=1).

3.8 Discussion

3.8.1 An Intermittent Magnetic Field Stimulates MSC Proliferation

A key objective of tissue engineering is to develop strategies that influence cell behaviour, particularly by modulating the cell cycle to promote proliferation and tissue regeneration. Proper regulation of the cell cycle is essential to ensure balanced cell growth, maintain stem cell function and prevent premature aging or abnormal cell proliferation, all of which are critical for effective tissue engineering (Shaikh, et al., 2023).

MSC proliferation was assessed by measuring the expression of the proliferation marker Ki67, over 7 days under SMF and DMF actuation. Application of an intermittent SMF significantly increased Ki67 expression at day 3, which then returned to control levels at 7 (**Figure 3-23**). A similar, though less pronounced, trend was observed with DMF exposure. In contrast, application of a constant SMF did not significantly affect MSC proliferation.

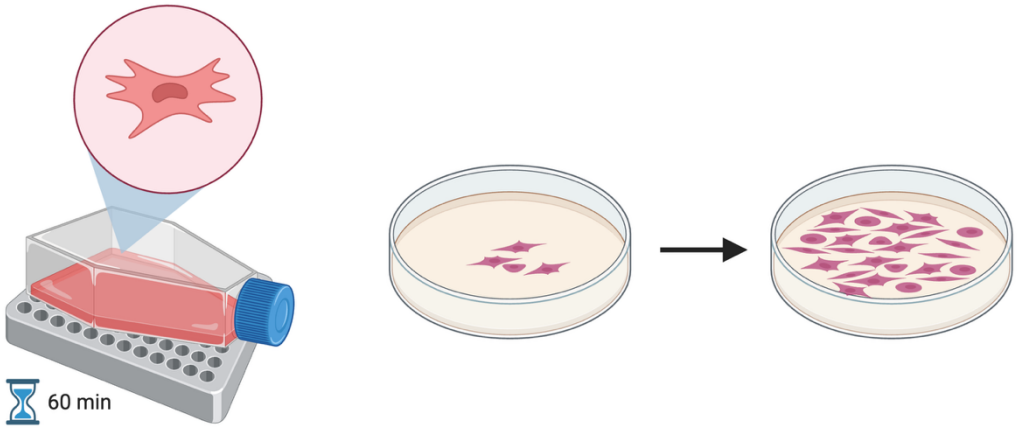

Figure 3-23: Intermittent static magnetic field increases mesenchymal stromal cell proliferation

Exposure to an intermittent static magnetic field (1 hour per day) increases mesenchymal stromal cell proliferation, observed *via* significantly increased Ki67 activity. Created with Biorender.com

Further analysis of cell cycle regulation revealed that intermittent SMF promoted upregulation of cell cycle promoters such as CDK4, CDK3 and CCND1 over time, suggesting enhanced cell cycle activity. In contrast, both constant SMF and DMF induced short-lived effects. Cell cycle inhibitors, including p16 and p21 were generally downregulated over time under both SMF conditions, indicating suppression of inhibitory signalling, whereas expression of inhibitor p27 showed upregulation. These findings indicate that intermittent SMF exposure may stimulate MSC proliferation by increasing the

expression of key cell cycle promoters, while selectively modulating cell cycle inhibitors. However, these observations are based on gene expression analysis alone, and future work could incorporate direct proliferation assays such as Ki67 immunostaining and functional cell cycle analyses to validate these preliminary findings.

Previous studies have reported varying effects of magnetic fields on MSC proliferation, often depending on field strength, duration, frequency and cell type (**Table 3-2**). Marędziak et al., (2015) demonstrated that 500 mT constant SMF exposure over 7 days enhanced MSC proliferation and reduced apoptosis, accompanied by downregulation of p21, p53 and Bax (a pro-apoptotic protein) expression. These changes were linked to increased AKT pathway signalling and upregulation of integrins which mediate mechanotransduction and cell survive (Marędziak, et al., 2017). Similarly, Zhang, et al, (2023) reported that exposure to a constant SMF (320 mT) for 24 hours promoted proliferation of periodontal ligament stem cells (PDLSCs) *via* activation of AKT signalling (Zhang, et al., 2023). AKT, also known as kinase B, is a key regulator of cell cycle and proliferation (Marędziak, et al., 2017).

Likewise, Wu et al., (2022) also demonstrated that a 140 mT SMF applied constantly over 72 hours significantly promoted MSC proliferation by over 20% compared to control cells (Wu, et al., 2022). Field strength appears to be a critical parameter; Zheng et al., (2018) observed *via* a CCK-8 assay that a weak SMF (1 mT) significantly promoted proliferation in DPSCs, whereas increasing the field strength to 2 mT and 4 mT resulted in no further improvement (Zheng, et al., 2018).

Conversely, Sadri et al, (2017) found that continuous exposure to a constant 18 mT SMF reduced MSC proliferation by prolonging G1 phase, with shifts observed in cell cycle distribution (G1 and S phases). They also reported reductions in cell viability after 36 hours of constant SMF exposure with recovery by 72 hours (Sadri, et al., 2017). In contrast to Sadri et al, we detected no significant impact of MSC viability under any magnetic field condition; however, our measurements were conducted at day 7, beyond their observed effect window. Potential early cytotoxicity may have resolved by this time, or the magnetic stimulation within our study remained within a non-cytotoxic range. This is further supported by our observation of sustained expression of G1 phase promoter, inducing that G1 progression was not impacted under magnetic actuation in our system. Boda, et al., developed magnetised substrate, delivering constant SMF (100 mT) exposure to MSCs up to 7 days in culture, and observed SMF exposure induced G0/G1 arrest, impacting the transition from proliferation to differentiation, and reducing the duration of S and G2/M phases. Some MSCs also

exhibited partial cell cycle arrest, underscoring complex effects of SMF on cell cycle regulation (Boda, et al., 2015).

Cell Type	Field Type	Field Strength	Field Duration	Cell Proliferation	Reference
MSCs	Int SMF	370 mT	1 hour / day for 72 hours	Increased	Figure 3-3
MSCs	Con SMF	370 mT	72 hours	No change	Figure 3-3
MSCs	DMF	23 mT, 0.3 Hz	16 hour cycle (5 min active, 25 min rest), 8 hour rest	Increased	Figure 3-3
MSCs	Con SMF	500 mT	7 days	Increased	(Marędziak, et al., 2017)
PDLSCs	Con SMF	320 mT	24 hours	Increased	(Zhang, et al., 2023)
MSCs	Con SMF	140 mT	72 hours	Increased	(Wu, et al., 2022)
DPSCs	Con SMF	1 mT	24 hours	Increased	(Zheng, et al., 2018)
		2 mT		No change	
		4 mT		No change	
MSC	Con SMF	18 mT	36 hours	Decreased	(Sadri, et al., 2017)
MSCs	Con SMF	100 mT	7 days	Decreased	(Boda, et al., 2015)
MSCs	Con SMF	450 mT	24 hours	Increased	(Manjua, et al., 2021)
	DMF	450 mT, 0.25 mHz		Decreased	
		450 mT, 17 mHz		No change	
MSCs	DMF	2 mT, 50 Hz	24 hours	Increased	(Singh, et al., 2023)
MSCs	DMF	1 mT, Range of frequencies (7.5, 15, 30, 50, 75 Hz)	24 hours	No change	(Zhang, et al., 2018)
Vero Kidney Cells	Con SMF	50 mT	6 days	Decreased	(Buemi, et al., 2001)
ccRCC	DMF	4.5mT, 50 Hz	72 hours	Decreased	(Cios, et al., 2021)
HEK293				No change	

Table 3-2: Summary of magnetic fields on cell proliferation

Summary of the effects of magnetic fields on cells, including the range of cell types studied, magnetic field types, field strengths, exposure durations and observed effects on cell proliferation.

Manjua et al., (2021) investigated both constant static and dynamic magnetic stimulation (up to 0.45T, over 24 hours) on MSCs, reporting that SMFs promoted proliferation and were more stable. For dynamic fields, they tested low frequency (0.26 mHz) dynamic magnetic stimulation, which caused cellular stress leading to reduced cell numbers, while higher frequency (17 mHz) dynamic stimulation preserved cell numbers without similar detrimental effects (Manjua, et al., 2021). In our study, the DMF was applied at 0.3 Hz, with an intensity of 23 mT, delivered intermittently for 16 hours per day using 5 minute on/25 minute off cycles. Using this pulsed, low frequency regime, and lower field strength, we observed enhanced MSC proliferation without negative impacts on viability. This suggests that the duty cycle and intermittent nature of the stimulation may play a role in mitigating stress responses observe with continuous low frequency dynamic fields.

In regard to a DMF, Singh et al, (2023) applied a nearly constant DMF at 2 mT and 50 Hz frequency in combination with a conductive nanofiber matrix. They observed significantly enhanced MSC proliferation and lineage specification, with increased Ki67 expression and activation of proliferation related genes, highlighting the synergistic effects of combined biophysical cues (Singh, et al., 2023). In contrast, Zhang, et al. (2018) observed no significant change in PDLSC proliferation with an increasing frequency from 7.5-75 Hz /1 mT constant DMF exposure using MTT assay. Responses to magnetic fields can also vary significantly between cell types. Buemi et al., (2021) reported that a constant 50 mT SMF applied over 6 days to Vero kidney cells reduced both apoptotic and proliferating cell numbers, while increasing necrotic cells, indicating a cell type specific cytotoxicity (Buemi, et al., 2001). Cois et al., (2021) observed application of a DMF (4.5 mT, 50 Hz) over 72 hours on healthy kidney cells, HEK293, and 3 renal carcinoma lines (ccRCC). They observed cell cycle arrest in the ccRCC lines at G1, while HEK293 cells were unaffected under the same magnetic regime (Cios, et al., 2021).

Together these findings underscore the critical importance of carefully tuning magnetic field parameters, including strength, frequency, during and duty cycle, as well as considering cell specific responses. Our results suggest that a 370 mT SMF applied intermittently for short periods (1 hour / day) most effectively promotes MSC proliferation, while maintaining healthy cell cycle dynamics.

3.8.2 MSC Migration Depends on the Type of Magnetic Field Stimulation

To explore the effects of magnetic field exposure on MSC migration and regeneration potential, a scratch assay was performed to assess wound closure over 72 hours. Distinct migratory behaviours emerged under the differing magnetic field conditions. While the control and an intermittent SMF exposure supported progressive wound closure, a constant SMF slowed this process and DMF exposure markedly impaired wound closure. These differences became more pronounced over time, with intermittent SMF producing wound closure levels comparable to the control (**Figure 3-24**).

Gene expression analysis also showed that MSCs responded differently depending on the magnetic field applied. Rac1, a key regulator of cytoskeletal dynamics and cell motility, was consistently upregulated across all conditions, supporting its central role in migration. In contrast, RhoA expression peaked early in the constant and DMF groups, decreasing over time, suggesting a short-lived increase in cytoskeletal tension. Interestingly, an intermittent SMF led to a delayed RhoA response, which could reflect a different mode of mechanosensing or delayed tension response. Matrix remodelling genes also showed field dependent regulation. MMP-2, a key protease involved in ECM degradation during migration, was upregulated across all groups, peaking at 24 hours. This aligns with its known role in enabling cell movement through tissue (Caley, et al., 2015). However, MMP-9 expression showed no consistent trend, suggesting it may not be the primary driver of magnetic field induced migration under these conditions.

Constant SMF and DMF application showed impaired wound healing in MSCs over 72 hours, despite upregulation of Rac1 (motility) and MMP-2 (ECM remodelling), particularly at 6, 24 and 72 hours. This discrepancy suggests that increased gene expression does not necessarily translate into enhanced cell migration. It is possible that post transcriptional regulation alters MMP-2 protein activity (Poliseno, et al., 2024), and in addition MMP-2 upregulation may not result in faster migration, however, may still support ECM remodelling (Yu, et al., 2017). MMPs are tightly regulated by TIMPs and in hindsight, assessing TIMP-2 expression, a key inhibitor of MMP-2, may have provided additional insight in MMP-2 dynamics (Philip, et al., 2004).

Supporting evidence for reduced motility can be observed within nuclear circularity measurements at 72 hours, which revealed nuclei in cells under a constant SMF and DMF had a more rounded nuclear morphology in comparison to control cells, indicating reduced

polarisation and motility (Dahl, et al., 2008). Furthermore, nuclear YAP levels were significantly lower at 72 hours under constant SMF compared to 2 hours, suggesting diminished mechanotransduction and migration associated signalling with prolonged exposure (Yang, et al., 2016). A limitation of the qPCR data is that it was based on only two technical repeats, and in some cases one repeat showed upregulation while the other showed downregulation. Therefore, the observed gene expression changes should be interpreted cautiously as they may not represent the functional status of the proteins or their impact on migration.

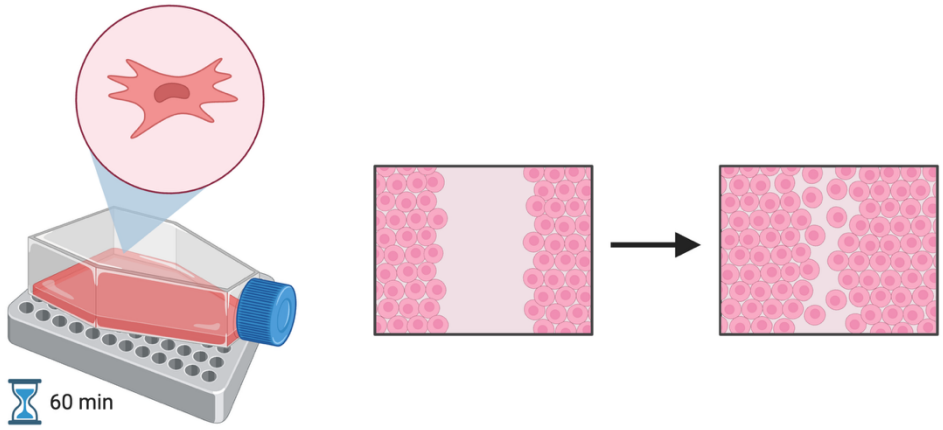

Figure 3-24: Intermittent static magnetic field exposure maintains mesenchymal stromal cell migration

Exposure to an intermittent static magnetic field (1 hour per day) increases preserves wound healing capacity in scratch assay in mesenchymal stromal cells. Created with Biorender.com

Overall, the data demonstrates that magnetic field exposure modulates MSC migration in a field type specific manner. Constant SMF and DMFs impaired wound closure, despite upregulation of migration associated genes. In contrast, intermittent SMF supported wound closure comparable to control conditions, indicating a potentially different mechanosensing response. These findings underscore the sensitivity of MSC migration to both the type and dynamics of magnetic field exposure and highlight the complexity of interpreting gene expression changes in relation to functional outcomes.

While this data is suggestive of the magnetic field dependent effects on MSC migration, a key limitation is that only one single biological source was used, although live imaging and gene expression analyses was derived from the same cell source. Gene expression was also restricted to a small PCR panel, potentially overlooking other relevant regulators such as TIMP-2. In addition, qPCR measures mRNA rather than protein function and protein activity

cannot be assumed from qPCR data (Poliseno, et al., 2024). Additionally, the 2D migration assay may not fully replicate in vivo migration dynamics. Future studies should incorporate multiple cell sources, expanded gene panels, protein level analyses and more physiologically relevant models to validate these findings.

Several studies have demonstrated that magnetic field exposure enhances stem cell migration, although effects vary depending on the magnetic parameters and experimental models used. Zhang et al., (2023) reported that a constant 320 mT SMF significantly enhanced migration in periodontal ligament stem cells (PDLSCs) in scratch assays at both 12 and 24 hours, compared to control groups (Zhang, et al., 2023). Similarly, Sun et al., (2023) demonstrated that *in vivo* conditioning with a constant 200 mT SMF for 14 days enhanced migration of bone marrow derived MSCs in an osteoarthritic mouse model. When isolated and cultured *in vitro*, these magnetically preconditioned MSCs demonstrated improved wound healing in scratch assays over 24 hours (Sun, et al., 2023).

Zheng et al., (2018) applied a 1 mT constant SMF to dental pulp stem cells (DPSCs), observing increased cell numbers in the wound area after 24 hours. They also reported significant upregulation of MMP-1 and MMP-2 without changes in expression of TMP-1 and TMP-2, highlighting a role for matrix remodelling in magnetically induced migration (Zheng, et al., 2018). In our study we observed increased MMP-2 expression across all magnetic field groups at 24 hours, but no significant trends in MMP-9 expression, suggesting that different MMPs may be selectively activated depending on field characteristics or stem cell type.

In contrast, DMFs can have frequency dependent effects. Zhang et al., (2018) found that MSC migration was significantly enhanced under DMFs with frequency ranging from 7.5-75 Hz per 1 mT DMF, with optimal migration (87% wound closure) observed at 50 Hz/1 mT. This study identified increased intracellular calcium flux under 50 Hz conditions as a potential mechanism driving enhanced migration (Zhang, et al., 2018). Our DMF system operated at a much lower frequency (0.3 Hz) which may account for the reduced capacity to support MSC migration in our system.

Indirect magnetic stimulation has also been explored. Wu et al., (2021) exposed MSCs to a 100 mT SMF consistently for 48 hours and isolated their EVs. These EVs significantly enhanced wound closure in a HUVEC scratch assay, suggesting paracrine effects from magnetically conditioned MSCs (Wu, et al., 2021).

These findings collectively demonstrate that both direct and indirect magnetic actuation can enhance MSC migration, though responses are highly dependent on field strength, frequency and exposure duration. The relatively limited migration observed under DMF in our study, at low frequency, aligns with prior reports that identify higher frequency DMFs or strong DMFs as more effective in promoting MSC motility.

As mentioned previously, application of an intermittent SMF enhanced MSC proliferation; however, wound closure rates in the scratch assay were similar to control. This combination of results implies that while cells are proliferating under an intermittent field, their individual motility may not increase, and overall wound closure likely reflects the combined contribution of proliferation and migration. Due to the process of applying the magnetic fields, live imaging of the wound closure *via* time lapse video recording was not feasible. Live image recording would allow for tracking of individual MSCs trajectories, and quantification of migration speed, direction and trajectory consistency (Dormann & Weijer, 2006). Therefore, while an intermittent SMF appears to enhance MSC proliferation, the relationship to motility in wound healing remains unclear, and further studies which can incorporate live image recording are needed to fully elucidate the dynamics of MSC migration under magnetic stimulation.

3.8.3 An intermittent Magnetic Field Promotes Early Osteogenesis Potentially *via* BMP Signalling

This study explored how different magnetic field types influence early osteogenic commitment in MSCs. Commitment to other lineages (myogenic, adipogenic and chondrogenic) was largely absent or suppressed across all conditions. Osteogenic markers were notably upregulated under magnetic stimulation, especially with intermittent SMF which drove the strongest and most consistent increases over time. **Table 3-3** summaries the pathways and genes investigated and their effect on osteogenesis.

Early osteogenic markers (RUNX2, MSX2, FOXP1 and MAF) were progressively upregulated with intermittent SMF application, alongside later osteogenic genes (SP7-Osterix, ALP and β-Catenin). Although constant SMF and DMF also induced some gene activation, these effects were less robust than those seen under intermittent SMF. Among several signalling pathways investigated, BMP signalling emerged as the most consistently activated and likely primary mechanism driving osteogenic commitment under these magnetic regimes. Our study showed that both SMF and DMFs led to strong upregulation

of BMP2 with SMF conditions showing decrease over time with inhibitors ID1 and ID2, aligning with enhanced osteogenic gene expression. Other pathways, including Wnt, SHH, and Groucho/TLE, showed either mixed or minimal responses, while hypoxia and angiogenic markers were moderately activated, suggesting a broader regenerative response. These findings suggest that BMP signalling may be an important pathway through which intermittent SMF promotes early osteogenesis in MSCs (**Figure 3-25**).

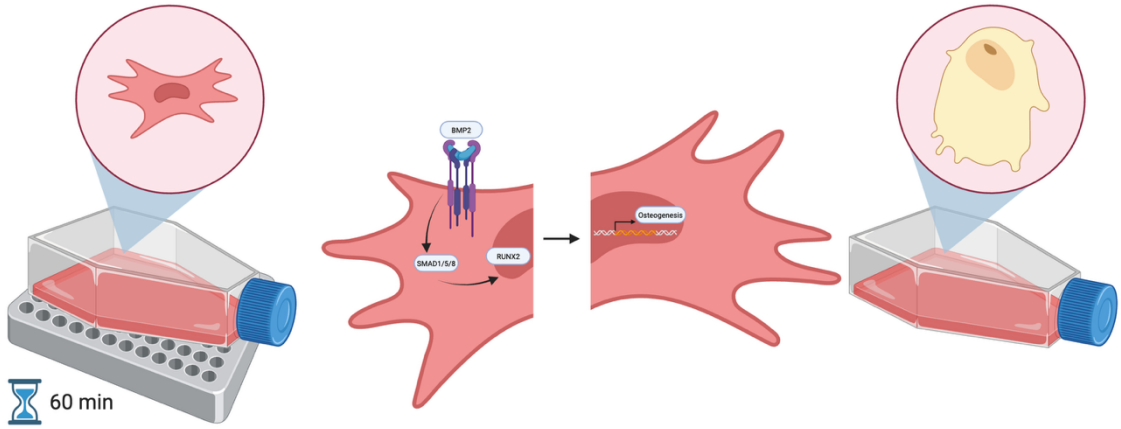

Figure 3-25: Intermittent static magnetic field exposure activates bone morphogenetic protein signalling pathway

Exposure to an intermittent static magnetic field (1 hour per day) appears to activate bone morphogenetic protein (BMP) signalling pathway, which contributes to differentiation of mesenchymal stromal cells into pre-/osteoblasts over 7 days in culture. Created with Biorender.com

Zhang et al., (2023) observed that exposure to a constant 320 mT SMF promoted osteogenesis in PDLSCs. Matrix mineralisation was evident after 14 days of magnetic field stimulation, with upregulation of ALP, RUNX2, and BSP at both day 7 and day 14 (Zhang, et al., 2023). Zheng et al., (2018) observed that exposure to a weak SMF at 1 mT promoted osteogenesis in DPSCs after constant 14 day exposure. This was evidenced by upregulation of ALP, and positive Alizarin Red S staining indicating matrix mineralisation. Interestingly, these effects were not significantly observed under magnetic field strengths of 2 mT or 4 mT, suggesting a dose-dependent response. Notably, the 1 mT condition also promoted nuclear translocation of YAP/TAZ, indicating altered cellular mechanosensing (Zheng, et al., 2018). We observed increased expression of YAP/TAZ (**Figure 3-15**) under intermittent SMF, with slight increase in nuclear YAP over 48 hours (**Figure 3-26**). In contrast, Wang et al., (2016) observed that exposure of MSCs to a 500 mT constantly for 7 days led to the

downregulation of osteogenic marker genes (SSP1, OSX) suggesting a potential inhibitory effect on osteogenic differentiation under a higher SMF field (Wang, et al., 2016)

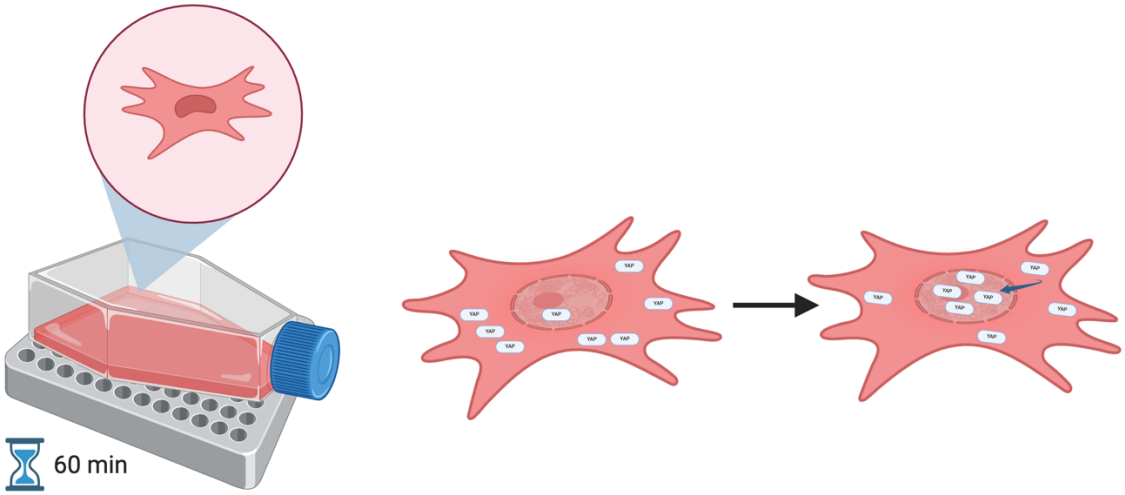

Figure 3-26: Intermittent static magnetic field exposure promotes translocation of Yes-associated 1 to nucleus

Exposure to an intermittent static magnetic field (1 hour per day) promotes Yes-associated protein 1 (YAP) translocation to the nucleus. Created with Biorender.com

Yuan et al., (2018) observed that constant SMF exposure, especially when combined with MNPs, significantly upregulated expression of BMP2 and BMP4 in mG-63 osteoblast-likes cells. This upregulation suggests activation of the BMP signalling pathway, known to promote osteogenesis through downstream effectors like RUNX2. Correspondingly, the study reported enhanced osteogenic differentiation marked by increased ALP activity over 14 days (Yuan, et al., 2018). Similarly, Kim et al., (2014) demonstrated that DMF exposure (1 mT, 45 Hz, 8 hours per day), again combined with MNPs, significantly upregulated BMP2 expression in MSCs, prompting osteogenic differentiation over 7 days. Their study indicates this DMF induced osteogenesis is closely associated with activation of the BMP signalling pathway (Kim, et al., 2015). Building on these findings, Yuan et al., (2023) demonstrated that moderate constant SMF exposure (280 mT) promotes osteogenesis by modulating the FLRT/BMP signalling balance (FLRT=Fibronectin leucine-rich transmembrane protein). Specifically, SMF enhanced BMP2 and SMAD1/5/8 expression while supressing FLRT2, a known regulator of BMP signalling, thereby amplifying osteogenic differentiation (Li, et al., 2020). Yun et al., (2016) combined constant SMF exposure with magnetic scaffolds and observed enhanced osteoblast differentiation over 10 days. They reported significant upregulation of BMP2 expression and activation of the BMP signalling pathway, as

evidenced by increase phosphorylation of SMAD1/5/8 (Yun, et al., 2016). These results reinforce the role of magnetic fields as a modulator of BMP bone formation.

Chen et al., (2019) observed that exposure to a DMF (1 mT, 15 Hz, 4 hours/day) significantly enhanced osteogenic differentiation, marked by increased expression of key osteogenic markers (OPN, RUNX2, COLI and OCN) at both the gene and protein levels. They also detected OCN deposition *via* immunofluorescence, signalling matrix maturation. Their findings suggest that under this magnetic regime, the Wnt signalling pathway plays a significant role in driving osteogenesis (Chen, et al., 2019). Kim et al., (2020) applied a similar DMF (1 mT, 45 Hz) on an osteoblast-like cell line (Saos-2) for 8 hours per day and observed abundant expression of osteogenic genes following magnetic stimulation, further supporting the pro-osteogenic potential of DMFs. Chen et al., (2023) reported that low frequency DMF (6-282 μT, 16 Hz) promoted osteogenic differentiation of SCP-1 cells. Notably, intermittent exposure, 10 mins every 8 hours, proved more effective that continuous exposure. They proposed that upregulation of Piezo1 and increased intracellular calcium flux were key mechanisms triggering activating downstream pathways (including AKT, Wnt and SMAD) (Chen, et al., 2023). Considering other pathways, He et al., (2021) demonstrated that exposure of MSCs to 10-50 mT constant SMFs, combined with magnetic graphene oxide, significantly enhanced osteogenic differentiation, primarily through the activation of the Wnt/β-Catenin signalling pathway (He, et al., 2021).

Petecchia et al, (2015) used a pulsed DMF (2 mT, 75 Hz) for just 10 minutes per day. Interestingly their regime reduced calcium deposition, suggesting that while their DMF promotes differentiation signals, it may inhibit later stages of mineralisation (Petecchia, et al., 2015). Bloise et al., (2018) applied the same pulsed DMF regime used by Petecchia et al., (2015) however MSCs were cultured on a titanium nanostructure under this regime for 28 days. They observed an upregulation of osteogenic genes (RUNX2, ALP, BMP2) alongside increased mineralisation and calcium deposition (Bloise, et al., 2018). Similarly, Boda et al, demonstrated that exposure of MSCs to a constant 100 mT SMF substrate over 14 days enhanced osteogenic differentiation. SMF exposure significantly upregulated the expression of early osteogenic markers (RUNX2, ALP, COL1A1) and late markers (OPN, OCN) indicating both osteoblast commitment and maturation (Boda, et al., 2015). These results suggest that the substrate plays a critical role in mediating the cellular response to a DMF, potentially enhancing the mechanical cues in osteogenic signalling pathways.

Regarding pathway activation, Zhang et al., (2025) investigated the effect of SHH on BMP9 induced osteogenic differentiation in MSCs. SHH expression alone had minimal osteogenic effect, however it significantly enhanced BMP9 induced osteogenic differentiation by increasing ALP activity, mineralisation and osteogenic marker expression. Mechanistically, SHH amplified SMAD signalling *via* GLI1 and GLI2, promoting bone formation (Zhang, et al., 2025).

In their OA mouse model, Sun et al., (2023) observed that exposure to a constant 200 mT SMF for 14 days increased expression of SOX9, a key chondrogenic marker (Sun, et al., 2023). This suggests that certain magnetic field parameters may promote alternative lineages including chondrogenesis. However, we did not observe this effect in our *in vitro* model at 370 mT, likely due to differences in exposure conditions and inherent variability between *in vitro* and *in vivo* systems.

Collectively, our results when considered alongside previous studies suggest that the signalling pathways activated by magnetic fields, and the resultant lineage commitment are highly dependent on field strength, frequency and exposure duration. Our study suggests that intermittent SMF exposure promotes early osteogenic commitment in MSCs by modulating the BMP signalling balance.

Signalling Pathway/ Markers for	Gene		Role in Osteogenesis
Bone Morphogenetic Protein (BMP)	BMP2	Bone morphogenetic protein 2	Promotes expression of RUNX2, SP7, ALP and Col1A1I
	ID1	Inhibitor of DNA binding 1	Early BMP2 target that promotes MSC proliferation and delays differentiation
	ID2	Inhibitor of DNA binding 2	BMP2 responsive gene that supports progenitor maintenance during early osteogenesis
Wnt/ β-Catenin (Canonical)	β-Catenin	Catenin beta 1 (CTNNB1)	Promotes MSC osteogenic differentiation by activating RUNX2, SP7, and ALP
	Wnt3a	Wnt family member 3a	Stabilises β-Catenin for translocation to nucleus
	TCF3	Transcription factor 3	Regulates early MSC differentiation, acting as a transcriptional repressor in osteogenesis
	TCF4	Transcription factor 4	Promotes osteogenic gene activation by partnering with β-Catenin during bone formation
	TCF7	Transcription factor 7	Enhances MSC osteoblast differentiation by activating Wnt target genes involved in bone formation
	LEF1	Lymphoid enhancing binding factor 1	Works with β-Catenin to activate osteogenic genes, promoting bone formation
	DKK1	Dikkopf WNT signalling pathway inhibitor 1	A Wnt pathway inhibitor that supresses osteogenesis by blocking Wnt signalling
	SFRP1	Secreted frizzles related protein 1	A Wnt pathway inhibitor that binds Wnt ligands, reducing osteogenic differentiation

Wnt (non-canonical)	Wnt5a	Wnt family member 5a	Regulates cell movement and polarity, influencing osteogenesis independently of β-Catenin
	RhoA	Ras homolog family member A	Controls cytoskeletal dynamics, promoting MSC migration and osteogenic differentiation
Sonic Hedgehog	GLI1	Glioma-Associated Oncogene Homolog 1	Transcription activator involved in osteogenic regulation
	GLI2	Glioma-Associated Oncogene Homolog 2	Mediates SHH signalling, promoting osteoblast differentiation
	GLI3	Glioma-Associated Oncogene Homolog 3	Can act as activator or repressor in SHH pathway, modulating bone development
Groucho/TLE	TLE1	TLE family member 1, transcriptional corepressor	Transcriptional co-repressor regulating Wnt and Notch pathways in osteogenesis
	TLE2	TLE family member 2, transcriptional corepressor	Similar role to TE1, modulating osteogenic signalling pathways
	TLE3	TLE family member 3, transcriptional corepressor	Regulates gene expression through repression, influencing bone formation
	TLE4	TLE family member 4, transcriptional corepressor	Involved in controlling osteogenic gene transcription *via* co-repression

Hypoxia	HIF1A	Hypoxia inducible factor 1 subunit alpha	Key regulator of cellular response to low oxygen, promotes angiogenesis and osteogenesis
	HIF2A	Hypoxia inducible factor 2 subunit alpha	Supports bone formation and vascularisation under hypoxic conditions
Angiogenesis	VEGF	Vascular endothelial growth factor A	Stimulates blood vessel formation, essential for bone repair and regeneration
	ANG-1	Angiopotenin 1	Maintains vascular stability, supporting bone tissue growth
	FGF-2	Fibroblast growth factor 2	Promotes MSC proliferation and differentiation aiding osteogenesis
	IL-6	Interleukin 6	Inflammatory cytokine that can modulate bone remodelling and repair

Table 3-3: Summary of investigated genes, their pathway/function and role in osteogenesis

3.8.4 Magnetic Field Stimulation Alters Paracrine Signalling in MSCs

Paracrine signalling a critical mechanism by which MSCs exert therapeutic effects in tissue engineering and regenerative medicine. Aside from differentiation, MSCs influence their microenvironment through the secretion of soluble factors and EVs which collectively regulate inflammation, angiogenesis and tissue repair. Understanding how to modulate secretory activity is therefore essential for enhancing the regenerative potential of MSC based therapies. This study investigated the effects of magnetic field exposure on MSC paracrine signalling, focusing on both secretion in both conditioned media and EVs. Cytokine expression was monitored over a 7 day period to assess the magnitude and temporal dynamics of the MSC secretome under various magnetic conditions.

Cytokine profiling of MSC conditioned media revealed a diverse and bioactive secretome, with peak expression occurring on day 1. The control condition reflects a balanced, homeostatic state with moderate inflammatory signalling and active tissue expression. The absence of stress markers suggests minimal activation providing a stable baseline for comparison. Under an intermittent SMF, a strong acute inflammatory profile was observed after 1 day, maintained by day 3 without progression towards angiogenesis or repair. By day

7 this response had subsided returning to a baseline profile with no sustained effects. Application of a constant SMF triggered a broader response at day 1, indicating inflammation, vascular activation and metabolic stress. By day 3, this shifted toward a pro-repair profile, but by day 7, expression had normalised, suggesting transient activation without long term changes. Application of a DMF showed a balanced inflammatory and early regenerative response from day 1, which was maintained through day 3, with controlled angiogenic signalling. As with the other conditions, this resolved by day 3 with no persistent activation.

To further understand MSC communication, we next examined EVs, isolating from conditioned media to explore how their properties might differ under various magnetic field conditions. NTA and TRPS revealed that while EV size distributions were broadly similar across all conditions, intermittent and constant SMF maintained EV concentration and size comparable to control, whereas DMF generally reduced EV size and concentration, indicating distinct effects of magnetic field types on MSC EV release profiles (**Figure 3-27**).

Cytokine profiling of isolated EVs revealed selective enrichment of proteins related to lipid transport and membrane localisation, such as Lipocalin-2, uPAR and EMMPRIN, consistent with EV lipid bilayer properties. Notably, DMF EVs showed minimal cytokine presence, while other conditions exhibited high levels of cytokines present in tissue remodelling, inflammation modulation and ECM regulation, suggesting EVs carry a specialised cargo supporting paracrine functions, distinct from soluble secretome.

While these findings provide a useful insight into how magnetic field exposure may influence MSC paracrine signalling, several limitations should be acknowledged. The cytokine analysis was performed using a semi-quantitative assay which allows for the generation of expression profiles but does not provide absolute quantification and is restricted to the targets included within the assay panel. As such, important signalling molecules out with his panel will not be detected. In addition, both cytokine and EV characterisation were performed with media collected from a single cell source and may not fully capture heterogeneity between donors. Future studies should incorporate larger biological replicates from multiple donors, and complementary quantitative approaches will therefore be important to validate these observations and define how magnetic field exposure modulates MSC secretory function.

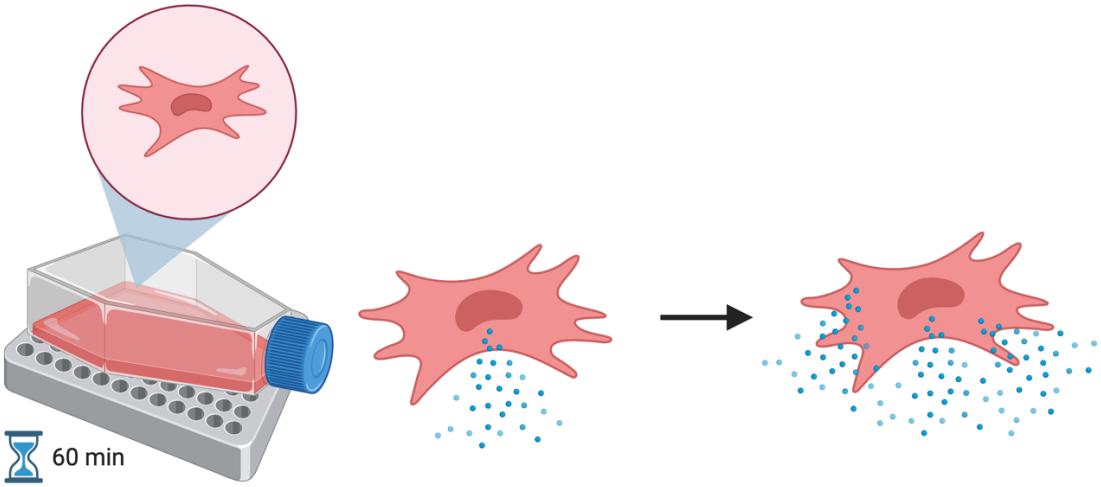

Figure 3-27: Intermittent static magnetic field exposure modulates mesenchymal stromal cell secretome

Exposure to an intermittent static magnetic field (1 hour per day) modulates mesenchymal stromal cell secretome through cytokine release and extracellular vesicle production. Created with Biorender.com

Previous studies have reported varied effects of magnetic fields on MSC paracrine signalling and cytokine expression. Manjuna et al., (2021) observed that VEGF expression was higher in MSCs cultured under SMF conditions compared to DMF conditions (Manjua, et al., 2021). Similarly, Wu et al., (2020), demonstrated that EVs derived from MSCs activated by a 100 mT SMF for 24 hours enhanced protein expression of VEGF, HIF-1α and FGF-2, indicating improved angiogenic potential. Zhang et al., (2023) observed that exposure to a 320 mT SMF for 14 days upregulated proliferation markers PCNA and MCM7, further supporting magnetic field induced cellular activation. In contrast, Wang et al., (2016) found that exposure to a higher SMF (0.5T for 7 days) downregulated key cytokines such as VEGF, IGF-1, TGF-β1 in ASCs.

Wu et al., (2021) applied 100 mT SMF stimulation to MSCs and observed improved osteogenesis, accompanied by increased secretion of miR-1260a, a microRNA that regulates gene expression and promotes bone formation (Wu, et al., 2021). Similarly, Xu et al., (2014) observed that MSCs exposure to a SMF showed enhanced secretion of key microRNAs, including miR-15b-5p, which plays a crucial role in regulating bone remodelling, by supressing Glial Fibrillary Acidic Protein (GFAP) expression, thereby inhibiting osteoclast differentiation and preventing osteoporosis progression (Xu, et al., 2024).

We observed that NTA and TRPS measurements differed in both EV concentration and size distribution, which is consistent with previous reports in the literature (Maas, et al., 2015).

NTA tracks Brownian motion of particles in suspension and calculates size from the diffusion coefficient (Comfort, et al., 2021), while TRPS measures changes in ionic current as particles pass through an increasing size of nanopore (Vogel, et al., 2016). NTA tends to overrepresent larger or more refractive particles and under detect the smaller EVs while TRPS measures particles individually, giving more accurate concentrations, but is sensitive to pore clogging by particles (Maas, et al., 2015). While both methods provide valuable information, TRPS is considered more reliable for absolute EV concentration due to its single particle counting approach (Vogel, et al., 2016). For size distribution NTA may detect a broader range of particle sizes but can be biased by larger particles. Therefore, combining both methods offer complementary insights into EV characteristics.

These studies highlight how magnetic field stimulation can modulate MSC paracrine signalling *via* EV cargo, but comprehensive understanding of these effects, especially how different magnetic fields influence the composition and function of EVs is limited. Further research is needed to elucidate the molecular mechanisms by which magnetic fields regulate EV mediated intercellular communication, which could unlock new regenerative medicine strategies.

3.8.5 Conclusion: Intermittent Static Magnetic Field Positively Stimulates Mesenchymal Stromal Cells

Application of an intermittent SMF appears to positively simulate MSCs by enhancing key regenerative behaviours including proliferation, migration and early osteogenic commitment. These effects appear to be mediated, at least in part through activation of BMP signalling pathways, which are known to play a central role in bone formation, and MSC differentiation. Additionally, there is preliminary evidence suggesting involvement of mechanotransducive mechanisms such as nuclear translocation of YAP, which may help translate mechanical cues into cellular responses. Together these findings suggest that application of an intermittent SMF may represent a promising approach to modulate MSC function and improve their therapeutic potential in tissue engineering applications (**Figure 3-28**).

The decision to apply the SMF intermittently for 1 hour per day in this study was informed by a combination of prior evidence and practical considerations regarding therapeutic relevance. In human foetal lung fibroblasts, application of an intermittent SMF at 370 mT for 1 hour per day, as well as continuously for 24 hour exposure at the same intensity, did

not induce oxidative stress, DNA damage or apoptosis, suggesting that such exposure durations are biologically safe for cells (Romeo, et al., 2016). While the current work does not directly address clinical application, the use of a limited daily exposure period aligns with practical scenarios where prolonged continuous exposure may be less feasible, highlight the potential for an intermittent SMF to be applied safely and effectively in therapeutic contexts.

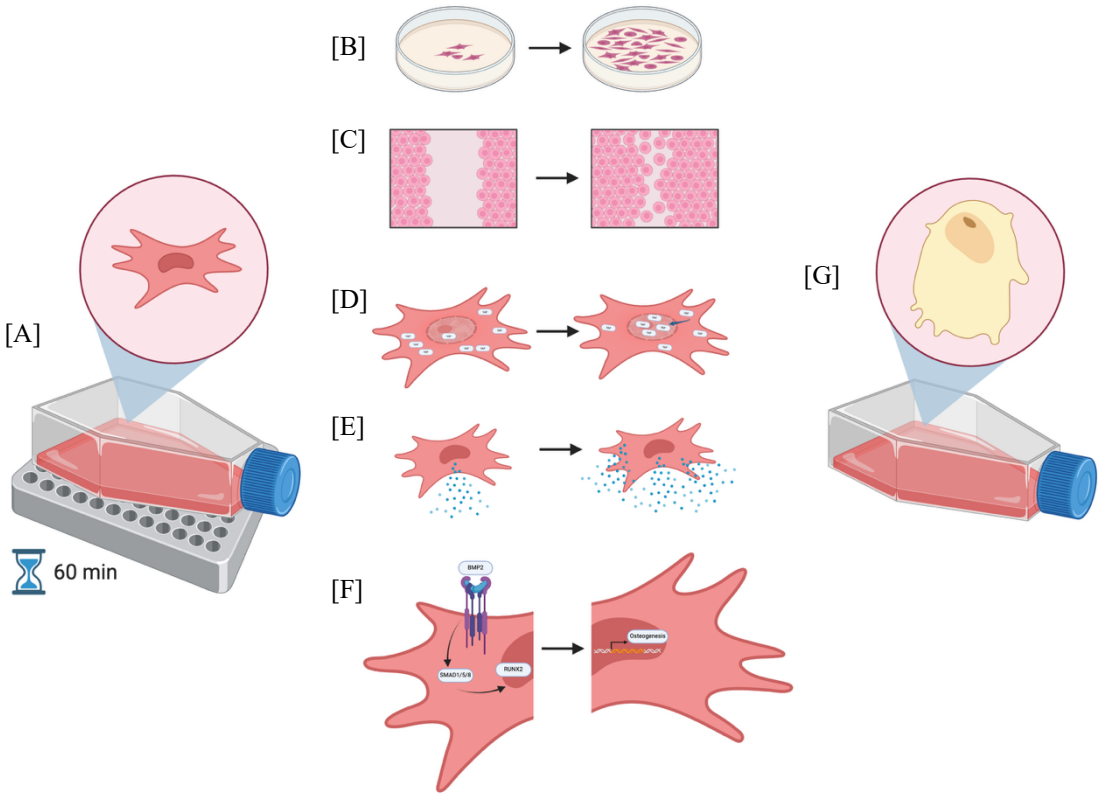

Figure 3-28: Summary of effect of an intermittent static magnetic field on mesenchymal stromal cells

In this study we investigated the effects of intermittent static magnetic fields (SMF) on mesenchymal stromal cells (MSCs) and observed that [A] daily SMF application influenced multiple cellular processes including [B] enhanced proliferation [C] preserving wound healing capacity [D] Yes-associated 1 (YAP) nuclear translocation [E] increased cytokine release and extracellular vesicle production, and [F] activation of the bone morphogenetic protein (BMP) signalling pathway ultimately leading to [G] the development of pre-/osteoblasts over 7 days in culture.

Chapter 4: Development and Characterisation of a 3D Magnetic Hydrogel for Bone Tissue Engineering

4.1 Introduction

Simple bone fractures can often be self-repaired; however, when extensive damage occurs from complex fractures, trauma, tumours or disease, the regenerative capacity of the damaged tissue is impaired (Amini & Lari, 2021). When a significant portion of bone is lost, a critical size defect is formed, leading to a failure of the healthy tissue to heal without intervention (Zhang, et al., 2019). Autograft transplants are the gold standard for the repair of such significantly damaged tissue. The tissue is harvested from a donor site on the patient, usually the iliac crest of the pelvis. Due to this, autografts are biologically relevant grafts, with improved graft biocompatibility, as well as osteogenic capabilities, providing a graft material that is osteoinductive and osteoconductive and has low risk of immune rejection (Oryan, et al., 2017). However, the availability of donor graft tissue is limited. Likewise, tissue harvest surgeries increase patient infection risk, along with donor site weakening and morbidity (Zhang, et al., 2019).

With small to medium defects, an alternative is the use of allografts. In this respect, a range of shapes and sizes can be harvested from either living donors, or cadavers, which are extensively screened, reducing surgical burden on the recipient patient (Turnbull, et al., 2018). However, due to the necessary processing, allografts have diminished osteoinductive capabilities due to the destruction of osteogenic cells; and despite screening they may propose a risk of disease transmission (Amini & Lari, 2021; Turnbull, et al., 2018).

Bone tissue engineering is an area of research that aims to address these challenges, by developing biomaterials that provide a scaffold for relevant cells, such as MSCs which demonstrate osteogenic potential (Perez, et al., 2018). The scaffold should allow MSC growth and subsequent bone tissue repair and regeneration. To provide suitable alternatives to autograft and allograft transplants, these biomaterials must be mechanically suitable and biologically compatible with natural bone tissue (Manzini, et al., 2021; Perez, et al., 2018). Hydrogels, such as gelatin methacryloyl (GelMA), have been explored due to their tuneable mechanical properties sustained biocompatibility, and ability for incorporation of nanomaterials such as MNPs (Mamidi, et al., 2023; Zhou, et al., 2023). MNPs are nanoscopic

particles, which can be incorporated into biomaterials to provide non-invasive remote stimulation in response to an external magnetic field (Ali, et al., 2021).

In this chapter, a magnetic hydrogel was developed by incorporating MNPs into GelMA hydrogels to enhance the applied remote magnetic stimulation. MSCs were also integrated into the model as both dispersed cells and spheroids to evaluate the biological performance of the hydrogel.

4.1.1 Chapter Aims

This chapter aims to develop and characterise a magnetic GelMA hydrogel, for use in subsequent research chapters, as a scaffold to support bone tissue repair. The following objectives were set:

- Characterise the morphology and magnetic properties of MNPs
- Incorporate MNPs into GelMA hydrogels and identify the optimal concentration that maintains mechanical stability and impartibility of hydrogels.
- Investigate magnetic GelMA hydrogel biocompatibility, with addition of MSCs
- Investigate bioprinting potential of magnetic GelMA, and its influence on the hydrogel mechanical properties vs hand cast hydrogels

4.2 Methods

The following experiments were completed with the material and methods outlined in Chapter 2. Hydrogels were fabricated as outlined in 2.5.2 Magnetic Hydrogel Fabrication.

The subsequent sections assessed the hydrogels using the following methods:

- Mechanical Properties of GelMA Hydrogel Model: 2.6.1 Rheology, 2.6.2 Compression of Hydrogels
- Biocompatibility: 2.2.1 Cell Viability Assay, 2.6.3 Contraction, 2.6.4 Water Contact Angle, 2.6.5 Freezing Hydrogels, 2.6.6 Micro-Computed Tomography, 2.6.7 Scanning Electron Microscopy
- Characterisation of MNPs: 2.4.1 Transmission Electron Microscopy of MNPs, 2.4.2 Size Distribution, 2.4.3 Super Conducting Quantum Interference Device
- Bioprinting: 2.6.1 Rheology, 2.6.4 Water Contact Angle, 2.7 Bioprinting

4.3 Characterisation of Magnetic Nanoparticles

For use in the magnetic hydrogel model fluidMAG-Dx MNPs were obtained from Chemicell (Berlin, Germany). The particles are described as superparamagnetic, with an approximate hydrodynamic diameter of 200 nm corresponding to their multi-domain cores (chemicell, 2025). This section examines these reported properties to confirm their suitability for the hydrogel model.

4.3.1 Magnetic Nanoparticle Morphology

To verify the characteristics of the commercially sourced MNPs, their morphology and size were assessed prior to use. MNPs were expected to be 200 nm in diameter and exhibit multidomain structure consistent with manufacturers specifications (chemicell, 2025). TEM and DLS were employed to measure particle morphology, while DLS was used to measure particle size distribution.

TEM was used to capture micrographs of the fluidMAG-Dx MNPs. TEM micrographs confirm fluidMAG-Dx are multidomain particles, with diameters between 100-200 nm **(Figure 4-1, A)**. To determine the hydrodynamic diameter and size distribution of fluidMAG-Dx MNPs, dynamic light scattering measurements were performed in collaboration with Liquid Research Ltd (Bangor, Wales). The intensity-weighted size distribution identified a single peak, with diameter of 225.5 nm (±90.59 nm) **(Figure 4-1, B)**. The Z-Average diameter recorded was 197 nm (±90.59 nm) with a polydispersity index of 0.143, representative of a narrow size distribution. The correlation function intercept (0.932) shows a low signal to noise ratio, indicating good data quality **(Supplementary Figure S 2)**.

In summary, DLS analysis measured a particle diameter with a Z-average of 197 nm and an intensity weighted peak of 225 nm, both consistent with Chemicell's reported 200 nm hydrodynamic core size. DLS analysis was superior to TEM in examining particle size, while TEM revealed MNP surface morphology.

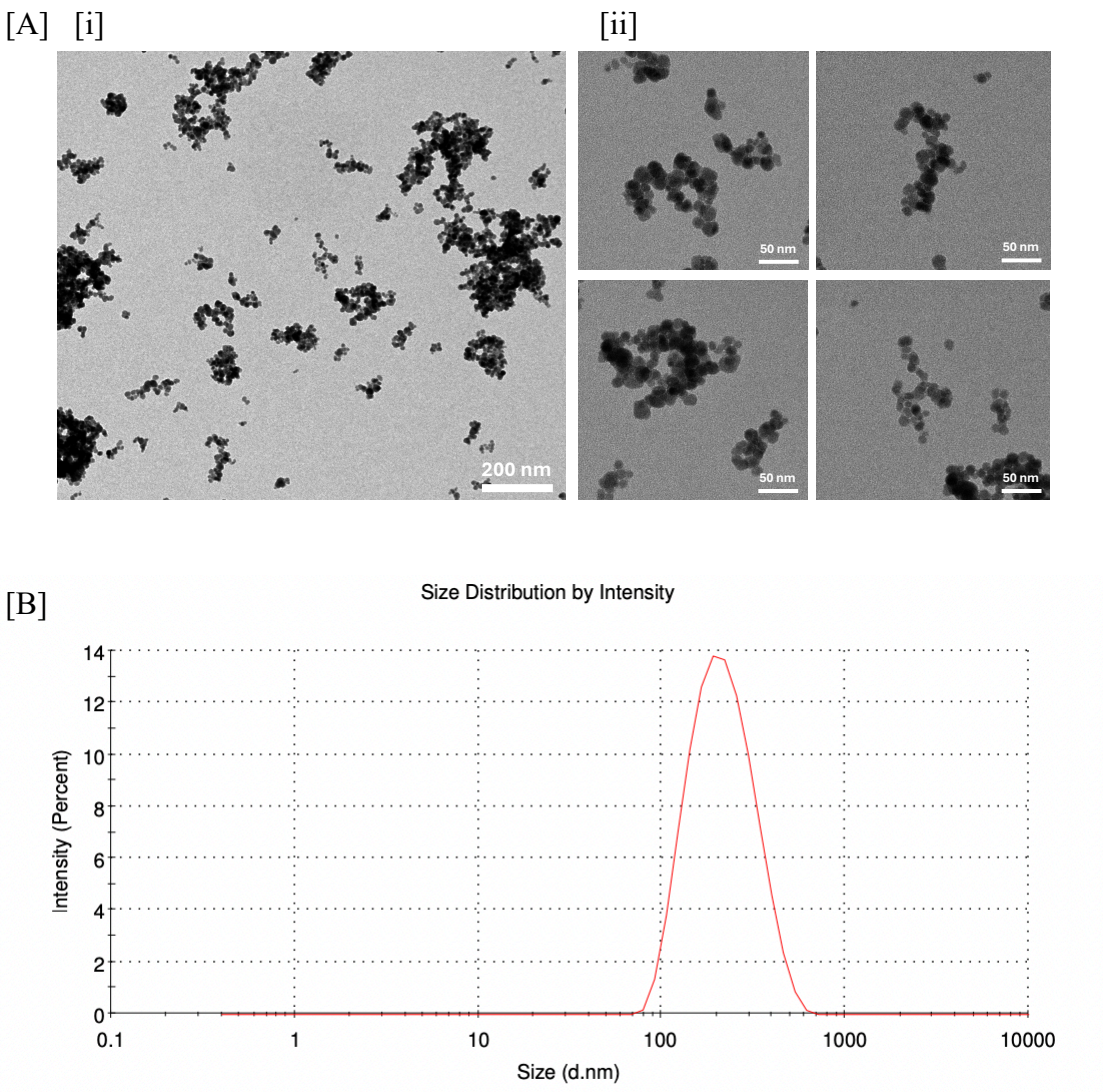

Figure 4-1: FluidMAG-Dx magnetic nanoparticles are multidomain particles around 200nm

Morphology and hydrodynamic size of FluidMAG-Dx particles were investigated [A] Transmission electron microscopy micrographs showing individual and clustered multidomain particles, with core diameters ranging from ~100-200 nm. Scale bar shows (i) 200 nm or (ii) 50 nm. [B] Dynamic light scattering analysis of fluidMAG-Dx particles in suspension, showing a normal distribution, and an intensity weighted peak at 225.5 nm (n=1). Completed in collaboration with Liquid Research Ltd (Bangor, Wales).

4.3.2 Super Conducting Quantum Interference Device

To verify the magnetic properties of the MNPs, SQUID was performed. The MNPs were expected to display superparamagnetic behaviour, based on the manufactures specifications, enabling rapid response to an external field while having negligible remanence once the field

was removed (chemicell, 2025). Confirming superparamagnetism was critical to ensure that the application of magnetic fields could be controlled in subsequent experiments.

In collaboration with the Murrie Research Group (School of Chemistry, University of Glasgow), magnetic measurements of fluidMAG-Dx MNPs were performed using a Quantum Design Magnetic Property Measurement System SQUID magnetometer. Measurements were performed by Ethan Lowe, PhD student. MNPs were magnetised up to 1.5 T, swept back down to -1.5 T and then back up to 1.5 T at 3.5 Oe/s (0.35 mT/s) **(Figure 4-2, A)**. At 0 T, MNPs show a large remnant magnetisation (M_T), 37.3 emu/g, which requires a coercive field (H_C), 63.14 mT, to remove **(Figure 4-2, B)**. MNPs were magnetised with a smaller field sweep from 0.4 T to -0.4 T, and back up to 0.4 T **(Figure 4-2, C)**, resulting in a significantly smaller M_T and H_C **(Figure 4-2, D)**.

The ability of the MNPs to respond to an oscillating magnetic field was examined under reducing temperatures 26.85°C (300K) to -0.15°C (273K). The in-phase molar magnetic susceptibility (χ'M) is the proportion of the MNPs that follow the oscillating field. Between 1 Hz and 600 Hz, χ'M remains relatively constant. As temperature decreases, a small decrease in χ'M follows indicating some degree of magnetic blocking at lower temperatures **(Figure 4-2, E)**. Conversely, the out-of-phase molar magnetic susceptibility, χ''M, is the proportion of MNPs that do not follow the oscillating field **(Figure 4-2, F, G)**. A small fraction of χ'M are χ''M, indicating that almost all magnetic moments follow the oscillating field.

In summary, SQUID analysis revealed that the MNPs exhibit behaviour more consistent with ferromagnetism in response to magnetic fields at 1.5 T, although this ferromagnetic behaviour is markedly reduced under smaller applied fields. Under application of a 0.4 T field, MNPs exhibit superparamagnetic behaviour.

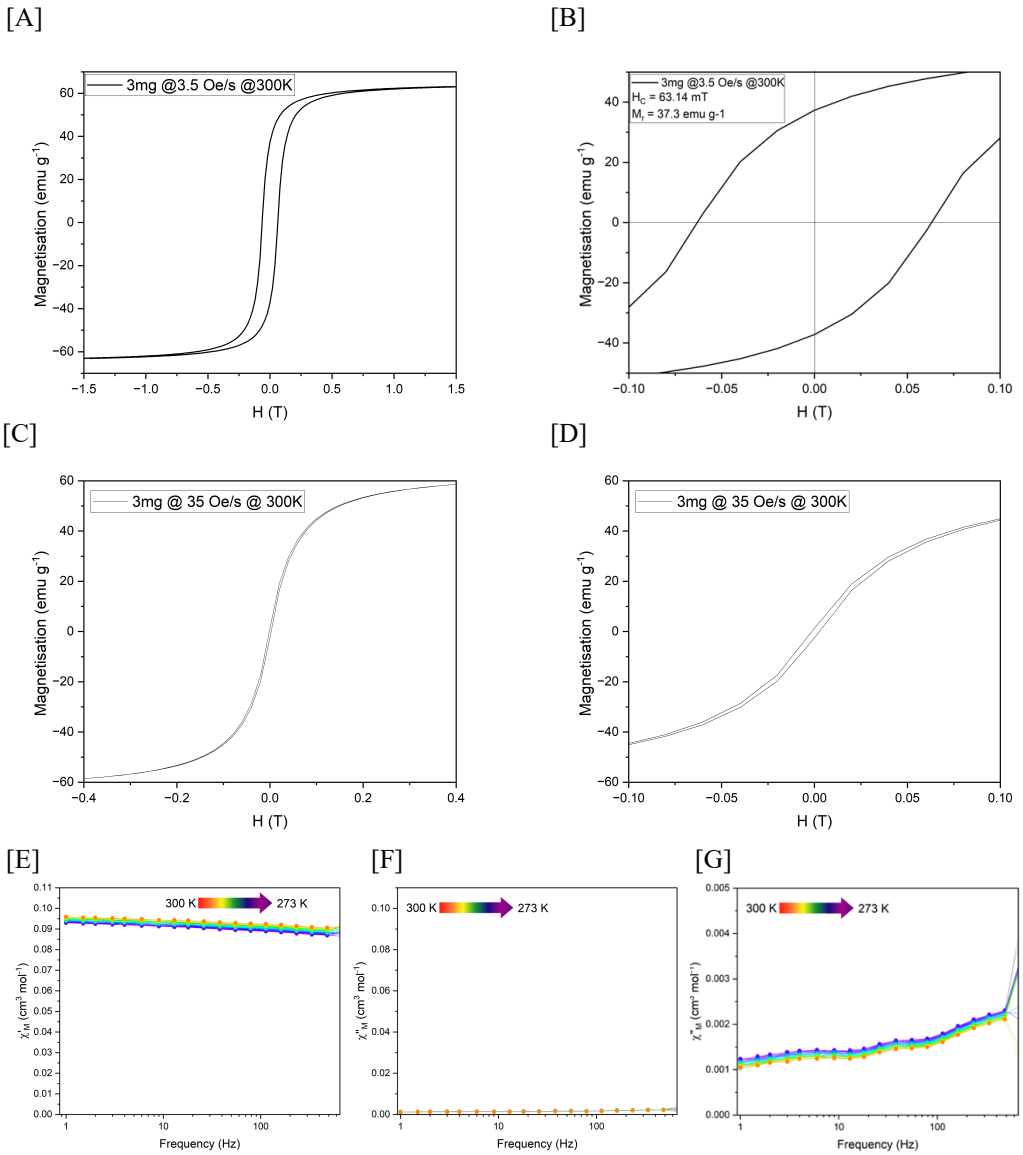

Figure 4-2: FluidMAG-Dx MNPs exhibit superparamagnetic behaviour at 0.4T and ferromagnetic behaviour at 1.5T

Measurements were performed in collaboration with the Murrie Research Group (School of Chemistry, University of Glasgow) [A] Magnetisation curve with a field sweep from 1.5 T to -1.5 T and back at 3.5 Oe/s, showing magnetic response of magnetic nanoparticles (MNPs). [B] Zoom in at hysteresis loop at 0 T from panel A, illustrating remnant magnetisation (M_T) of 37 emu/g, and required coercive field (H_C) to remove remnant magnetism (63.14 mT). [C] Magnetisation curve with smaller field sweep from 0.4 T to -0.4 T and back, showing reduced magnetic response. [D] Corresponding zoom in on hysteresis loop near 0 T for reduced sweep, illustrating decreased M_T and H_C. [E] Temperature dependent in-phase molar magnetic susceptibility (χ'M) measured between 300K and 273K across frequencies from 1-600 Hz, showing slight decrease at lower temperatures indicating magnetic blocking. [F, G] Out-of-phase molar magnetic susceptibility (χ''M) across the same temperature and frequency range, demonstrating the majority of magnetic moments follow the oscillating field.

4.4 Mechanical Properties of GelMA Hydrogel Model

This section evaluates the mechanical and viscoelastic properties of GelMA hydrogels with varying polymer concentrations, both alone and with incorporated MNPs, serving as a model soft hydrogel system.

4.4.1 Mechanical Properties of GelMA

To characterise the mechanical properties of GelMA hydrogels, rheological measurements were performed. GelMA hydrogels with concentrations of 5%, 7.5% and 10% w/v were initially examined using rheology, to provide an understanding of the mechanical properties upon polymerisation and at 24, 48 and 72 hours post polymerisation. Hydrogels are viscoelastic materials, so they have both a storage modulus (G′ – the elastic component) and a loss modulus (G″ – the liquid-like component). Increasing the polymer concentration was expected to enhance the mechanical stiffness of the hydrogels with higher G′ values anticipated for stiffer formulations. Additionally, incorporation of MNPs was expected to influence hydrogel mechanical properties, potentially altering stiffness depending on particle concentration and ease of dispersion within the hydrogel.

With the GelMA hydrogel alone, there was a significant difference for each hydrogel family between timepoints, where generally both G′ and G″ increased with increasing gelatin concentration with changes present over 72 hours (**Figure 4-3, A**). The 5% w/v hydrogels showed median G′ initially increased over 48 hours, but then decreased significantly, back down to 0 hour values. More specifically, the values ranged from 350 Pa (203-765 Pa) at 0 hour to 743 Pa (588-912 Pa) at 24 hours, and to 805 Pa (717-989 Pa) at 48 hours, then down to 300 Pa (275-467 Pa) at 72 hours. G″ also significantly increases between 0 and 24 hours, from 16 Pa (11-19 Pa) to 47 Pa (32-57 Pa) respectively. However, it is significantly reduced between 48 and 72 hours, from 36 Pa (22-46 Pa) to 5 Pa (2-10 Pa) **(Figure 4-3, A)**. These values suggest that the 5% w/v GelMA represents a soft hydrogel, which behaves more as a solid (elastic) hydrogel.

The 7.5% w/v GelMA hydrogel values are higher than the previous 5% w/v hydrogels but follow a similar trend. Here, G′ is recorded at 538 Pa (467-822 Pa) at 0 hours, increasing to 1035 Pa (581-1300 Pa) at 24 hours and to 2320 Pa (1720-2640 Pa) at 48 hours. At 72 hours, no significant change in G′, 1978 Pa (1636-2635 Pa), is recorded. G″ also increases from 26 Pa (17-42 Pa) at 0 hours over 24 and 48 hours, to 130 Pa (104-226 Pa) and 207 Pa (164-226

Pa) respectively; however, it significantly decreases to 42 Pa (20-58 Pa) at 72 hours **(Figure 4-3, A)**. Again, the values are in the expected range for a soft hydrogel.

Finally, the 10% w/v GelMA hydrogels performed very similarly to the 7.5% w/v hydrogels, both in terms of values and trends. Again, G′ increased significantly from 0 hours to 48 hours, from 339 Pa (155-662 Pa) to 751 Pa (526-2495 Pa), and 2020 Pa (1153-2428 Pa) respectively. No significant change was then recorded between 48 hours and 72 hours, with G′ remaining steady at 2000 Pa (1463-3880 Pa), although higher upper limit and quartile measurements were observed at this timepoint. Similarly, G″ steadily increased over time, significantly between 0 and 24 hours, from 30 Pa (23-56 Pa) to 81 Pa (24-158 Pa) and at 107 Pa (65-147 Pa) and 165 Pa (107-252 Pa) for 48 and 72 hours respectively. Again, a wider range of measurements was noted for these measurements **(Figure 4-3, A)**. These values again represent a soft hydrogel.

Tanδ values, calculated from median G′ and G″ are presented in **Table 4-1**. All values are ~0.1 or below, indicating elastic behaviour dominates over viscous behaviour (G′ greater than G″). At 24 hours, tanδ values peak for both 7.5% w/v (0.121) and 10% w/v (0.108) hydrogels, however values decrease notably for all concentrations at 48 and 72 hours suggesting the material becomes more elastic over time.

	Time since polymerisation (hours)			
GelMA Concentration (%, w/v)	**0**	**24**	**48**	**72**
5	0.044	0.064	0.044	0.017
7.5	0.050	0.121	0.089	0.021
10	0.090	0.108	0.053	0.080

Table 4-1: Tanδ values of GelMA hydrogels with increasing GelMA concentration

Tanδ (=G″/G′) values of GelMA hydrogels with increasing GelMA concentration (5%, 7.5% and 10% w/v) at 0, 24, 48 and 72 hours post polymerisation. Tanδ near 0 indicate the material shows more elastic behaviour, while close to 1 indicates viscous behaviour.

Following MNP incorporation, rheology was carried out again, to determine any potential changes in mechanical properties. The 5%, 7.5% and 10% w/v GelMA hydrogels were examined, with increasing MNP concentrations from 0.25 mg/mL - 1 mg/mL (n=3). In general, the mechanical properties were reduced with increasing concentration of MNPs,

with few exceptions in 5% and 7.5% w/v GelMA hydrogels with low concentrations of MNPs. **(Figure 4-3, B)**.

In 5% w/v GelMA hydrogels, G′ initially increases with the addition of 0.25 mg/mL MNPs, 439 Pa (367-642 Pa), in comparison to the control/no MNP hydrogel at 316 Pa (189-566 Pa). However, whilst the addition of 0.5 mg/mL MNPs maintained mechanical properties, 433 Pa (271-562 Pa) above the control measurement, the addition of 0.75 mg/mL and 1 mg/mL MNPs both significantly decreased G′ (48 Pa (128-303 Pa) and 158 Pa (123-179 Pa) respectively). Meanwhile, G″ was significantly decreased across almost all MNP concentrations. The addition of 0.25 mg/mL, 0.5 mg/mL and 1 mg/mL MNPs (15 Pa (8-20 Pa), 14 Pa (7-18 Pa) and 7 Pa (4-12 Pa) respectively) significantly decreased G″ compared to the control, 20 Pa (16-25 Pa), while the addition of 0.75 mg/mL did not appear to significantly affect G″ at 17 Pa (10-13 Pa) **(Figure 4-3, B)**.

The control 7.5% w/v hydrogels, G′ value of 2385 Pa (1715-2648 Pa) is initially maintained with the addition of 0.25 mg/mL and 0.5 mg/mL MNPs at 2287 Pa (2120-2503 Pa) and 1797 Pa (1675-1938 Pa) respectively. However, when the MNP concentration was increased to 0.75 mg/mL, G′ was significantly reduced to 500 Pa (315-647 Pa), in comparison to control. The addition of 1 mg/mL MNPs also significantly reduced G′, 988 Pa (734-1121 Pa), in comparison to control, however it was increased in comparison to 0.75 mg/mL, likely due to the additional time required to polymerise to the hydrogels (additional 2 minutes). Similarly, G″ values were not significantly affected with the addition of 0.25 mg/mL or 0.5 mg/mL MNPs, 217 Pa (163-261 Pa) and 183 Pa (169-202 Pa) respectively, in comparison to control at 207 Pa (176-222 Pa). However, the higher MNP concentrations of 0.75 mg/mL and 1 mg/mL significantly reduces G″, 43 Pa (34-48 Pa) and 43 Pa (28-61 Pa) respectively **(Figure 4-3, B)**.

Following the same trend, the addition of all MNPs concentrations decreased G′ in 10% w/v hydrogels compared to control, 4780 Pa (4258-6343 Pa). The addition of 0.25 mg/mL does not significantly decrease G′ however it does decrease to 3575 Pa. (2235-4633 Pa). The remaining concentrations (0.5 mg/mL, 0.75 mg/mL and 1 mg/mL) of MNPs significantly reduced G′ to 2445 Pa (1788-3228 Pa), 860 Pa (638-946 Pa) and 844 Pa (647-1008 Pa) respectively. As with the 7.5% w/v GelMA, hydrogels containing 1 mg/mL MNPs required an additional 2 minutes of UV polymerisation to support formation of a usable hydrogel, therefore the decrease was less pronounced. G″ was also reduced in all concentrations. The addition of 0.25 mg/mL MNPs did not significantly reduce G″, 352 Pa (332-450 Pa), in

comparison to control, 437 Pa (407-488 Pa). Additions of 0.5 mg/mL, 0.75 mg/mL and 1 mg/mL significantly decreased G″ in comparison to the control: 223 Pa (193-454 Pa), 90 Pa (67-106 Pa) and 83 Pa (69-92 Pa) respectively **(Figure 4-3, B)**.

Again, tanδ values, were calculated from median G′ and G″ in hydrogels with addition of MNPs (**Table 4-2)**. Tanδ values for GelMA with incorporated MNPs remain generally low ~0.1 or below, indicating elastic behaviour is maintained with addition of MNPs. A slight increase above 0.1 is observed in 5% and 10% w/v hydrogels with 0.75 mg/mL MNPs (0.116) and 7.5% w/v hydrogels with 0.5 mg/mL MNPs suggesting a slight increase in viscous behaviour in these conditions. However overall, MNP concentration does not significantly alter the elastic behaviour of the hydrogels, suggesting that they do not impact the hydrogel network.

	Concentration of MNPs (mg/mL)				
GelMA Concentration (%, w/v)	**Control**	**0.25**	**0.5**	**0.75**	**1**
5	0.063	0.035	0.031	0.116	0.042
7.5	0.087	0.095	0.102	0.085	0.043
10	0.091	0.098	0.091	0.105	0.099

Table 4-2: Tanδ values of GelMA hydrogels with increasing concentration of magnetic nanoparticles

Tanδ (=G″/G′) values of GelMA hydrogels (5%, 7.5% and 10% w/v) with increasing magnetic nanoparticle (MNP) concentration (0 – 1 mg/mL) at 72 hours post polymerisation. Tanδ near 0 indicate the material shows more elastic behaviour, while close to 1 indicates viscous behaviour.

Collectively, the data demonstrates that increasing GelMA concentration consistently enhances the mechanical properties of the hydrogels, as evidenced by increasing G′ and G″ moduli. Incorporating MNPs into GelMA hydrogels generally reduces mechanical properties in a dose dependent manner, with some minor exceptions in low MNP concentrations in 5% and 7.5% w/v hydrogels. Despite these changes, all GelMA hydrogels examined exhibit low tanδ values (~0.1 or below), confirming they remain predominately soft and elastic hydrogels.

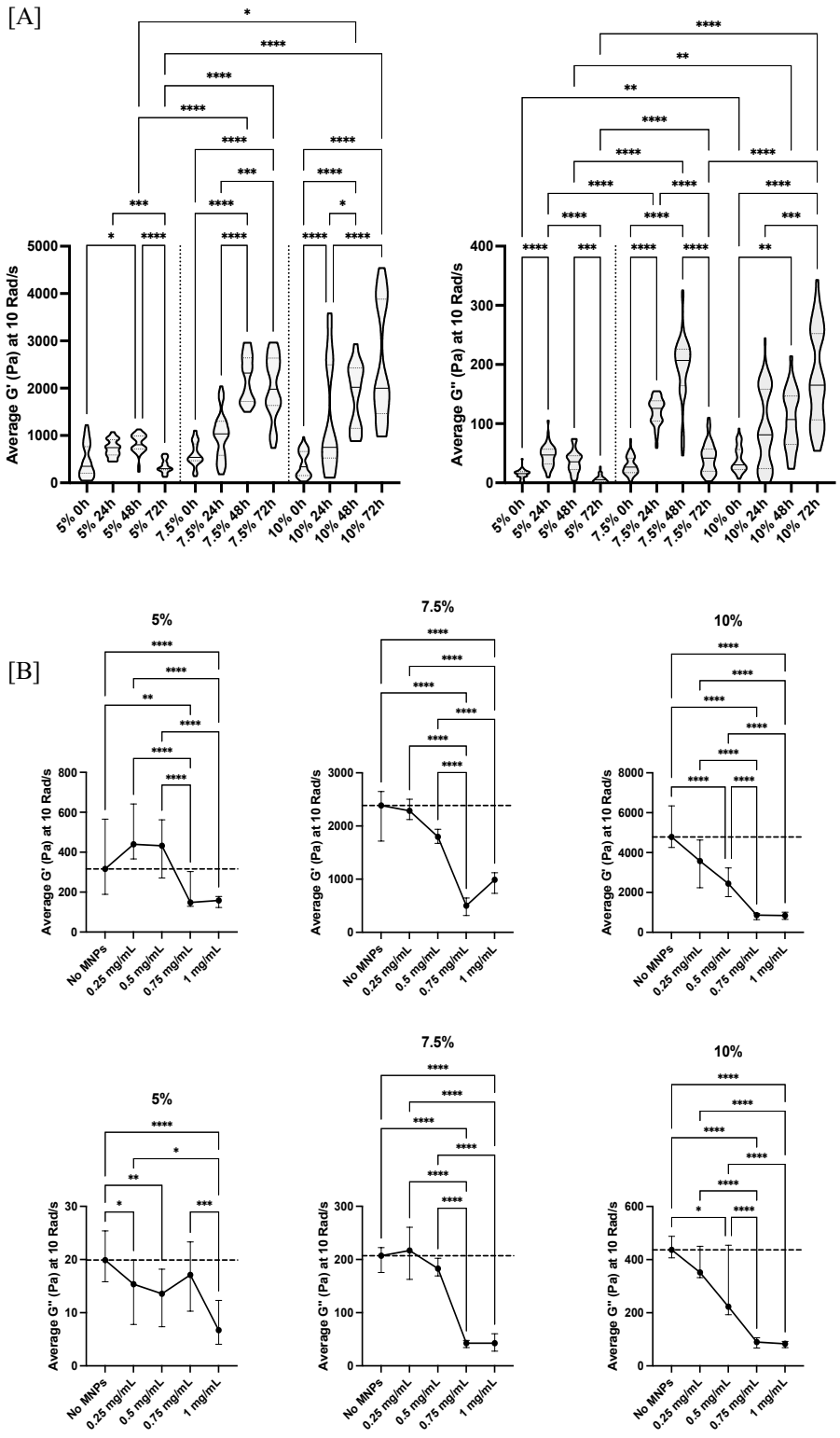

Figure 4-3: Mechanical properties of GelMA hydrogels are influenced by polymer concentration and magnetic nanoparticle content

Storage modulus (G′) and loss modulus (G″) were measured *via* strain sweep tests (0.01-0.1% strain, 1 Hz, 10 Rad/s) for 5%, 7.5% and 10% w/v GelMA hydrogels using an Anton Paar Rheometer [A] Truncated violin plots show distribution of G′ and G″ values with median (solid line) and interquartile range (dashed lines) (n=3). A Kruskal-Wallis test and post hoc Dunn's multiple comparison tests show significance between conditions [B] Median values for G′ and G″ for GelMA hydrogels with increasing

concentration of magnetic nanoparticles (MNPs), from 0.25 - 1 mg/mL; dotted line shows mean of control group (no MNPs). Error bars show median ± IQR (n=3). A Kruskal-Wallis test and post hoc Dunn's multiple comparison tests show significance between conditions

4.4.2 Compression of Hydrogels

Hydrogel compression is an established, simple technique, used to improve a hydrogel's mechanical strength by altering the internal polymer network structure through partial dehydration (Leon-Cecilla, et al., 2023). Hydrogel compression was therefore trialled as a potential approach for enhancing the GelMA hydrogel's mechanical properties, with the expectation that compression immediately post to crosslinking would tighten polymer network and improve hydrogel stiffness. GelMA hydrogels (7.5% w/v GelMA only, no MNPs) were compressed with different weights for 5 minutes immediately after polymerisation and resuspended in cell culture media for 24, 48 and 72 hours prior to measurements. Three weights were used including 12 g, 25 g and 50 g, and a control hydrogel was used. **(Figure 4-4)**.

At 24 hours, a trend was observed with increasing weight correlating to a related decrease in G′. G′ was significantly reduced in hydrogels compressed with 50 g in comparison to the control, 1633 Pa (1470-1919 Pa) and 3025 Pa (2338-3823 Pa) respectively, whereas hydrogels compressed with 12 g and 25 g showed no significant change to mechanical properties in comparison to control, 2408 Pa (1471-2844 Pa) and 1883 Pa (1474-2142 Pa) respectively. The heavier weight (50 g) may have caused the hydrogel network to break down, or structurally rearrange, leading to the observed decrease in stiffness. In contrast the 12 g and 25 g weights may not have been sufficient to alter the mechanical integrity of the hydrogel. No significant change in G″ was observed in with compression. G″ in control hydrogels, 147 Pa (99-171 Pa), was maintained with compression of 12 g, 25 g and 50 g at 142 Pa (76-193 Pa), 171 Pa (126-225 Pa) and 132 Pa (122-233 Pa) respectively **(Figure 4-4)**.

At 48 hours, there was no significant change in G′ for the control, 653 Pa (491-1700 Pa). However 12 g, 25 g and 50 g weights did increased G′ slightly in compressed hydrogels to 1720 Pa (1283-1936 Pa), 1350 Pa (429-1735 Pa) and 850 Pa (628-1162 Pa), respectively. As previously observed, increasing weights for compressed caused reduced G′ in hydrogels. Similar to 24 hours, G″ was unaffected by compression with weights. In comparison to control hydrogels, 118 Pa (68-165 Pa). Hydrogels compressed with 12 g, 25 g and 50 g,

showed no significant change in comparison to control, at 133 Pa (95-161 Pa), 83 Pa (70-102 Pa) and 136 Pa (98-180 Pa) respectively **(Figure 4-4)**.

At the final timepoint, 72 hours, G′ was not significantly affected by compression with weights. With 12 g weights, G′ increased to 2247 Pa (832-2497 Pa) in comparison to control G′ at 1640 Pa (825-2291 Pa). With 25 g and 50 g weights, G′ were closely matched, at 1988 Pa (1579-2785 Pa) and 1972 Pa (1072-2373 Pa) respectively. A significant change in G″ was identified at 72 hours. Hydrogels compressed with 25 g, showed an increase in G″, 225 Pa (190-246 Pa), in comparison to 12 g and 50 g weights, 151 Pa (110-158 Pa) and 141 Pa (113-168 Pa) respectively. No significance was observed between the compressed hydrogels and the control, 168 Pa (120-176 Pa) **(Figure 4-4)**.

Overall, hydrogel compression did not improve the mechanical properties of the 7.5% w/v hydrogels, with little or no difference recorded. Likewise, increasing weight did not seem to make any difference to the overall mechanical properties over time.

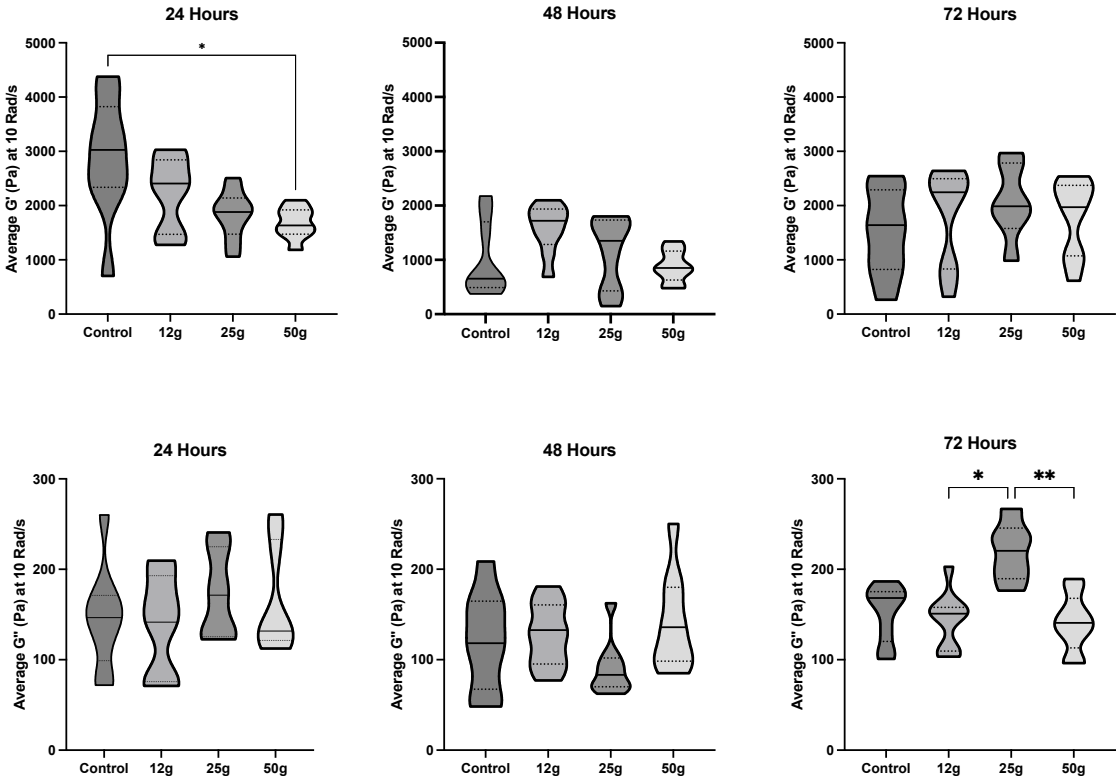

Figure 4-4: Compression does not improve mechanical properties of GelMA hydrogels

GelMA hydrogels were subject to compression immediately post polymerisation under UV light with weights and compared to control hydrogels. Storage modulus (G′) and loss modulus (G″) were measured *via* strain sweep tests (0.01-0.1% strain, 1 Hz, 10 Rad/s) for GelMA hydrogels compressed with 12 g, 25 g and 50 g weights and compared to control hydrogels. Measurements were obtained using an Anton Paar rheometer. Truncated violin plots show distribution of G′ and G″ values with median (solid line) and interquartile range (dashed lines) (n=3). A Kruskal-Wallis test and post hoc Dunn's multiple comparison tests show significance between conditions

Tanδ values, were calculated from median G′ and G″ in compressed hydrogels (**Table 4-3)**. Tanδ values for compressed GelMA generally low ~0.1 or below, indicating elastic behaviour is maintained in compressed hydrogels. A slight increase above 0.1 is observed at 48 hours in 7.5% w/v control hydrogels (0.181) and with 50 g compression weights (0.160), as well as control hydrogels at 72 hours (0.103) and 25 g compressed hydrogels at the same time point (0.111) suggesting a slight increase in viscous behaviour. Overall compression and partial dehydration do not significantly alter the elastic behaviour of the hydrogels.

	Compression Weight (g)			
Time since compression (hours)	**Control**	**12**	**25**	**50**
24	0.048	0.059	0.091	0.081
48	0.181	0.077	0.062	0.160
72	0.103	0.067	0.111	0.071

Table 4-3: Tanδ values of compressed GelMA hydrogels

Tanδ (=G″/G′) values of GelMA hydrogels (7.5% w/v) compressed with increasing weights (12 g, 25 g and 50 g) at 24, 48 and 72 hours post polymerisation. Tanδ near 0 indicate the material shows more elastic behaviour, while close to 1 indicates viscous behaviour.

In summary, compression with weights did not improve mechanical properties in 7.5% w/v GelMA hydrogels. Interestingly there was an trend for compression to reduce hydrogel stiffness, particularly noticeable at 24 hours with comparison of control and 50 g weight compressed hydrogels, but this was not maintained over 72 hours. In addition, tanδ values indicate elastic behaviour is maintained with compression of hydrogels. Overall compression and partial dehydration had minimal effect and therefore was not utilised for further hydrogel preparation.

4.4.3 Final Models Amplitude Sweep

Based on the initial rheological analysis, 7.5% and 10% w/v GelMA hydrogels, with and without 0.25 mg/mL and 0.5 mg/mL MNPs were selected as models for further investigation. These formulations were chosen due to their favourable mechanical properties (2.3 – 4.7 kPa). Although the addition of 0.5 mg/mL MNPs significantly reduced the mechanical stiffness for 10% w/v hydrogels, this concentration was still included to evaluate the impact of a higher MNP concentration in 10% w/v hydrogels. Based on the initial rheological analysis, G′ values of hydrogel containing MNPs remained relatively unchanged compared to controls without MNPs, suggesting that structural integrity and mechanical stiffness were largely maintained. Oscillatory strain sweep tests were therefore employed to evaluate the hydrogels resistance to deformation under increasing strain and to determine the point which they transition from predominantly elastic to viscous behaviour, resulting in hydrogel breakdown. The crossover points, also called the flow point, between G′ and G″ determines the hydrogels viscoelastic limit, which is critical for understanding how these materials might perform under physiological loading conditions.

The amplitude sweeps revealed clear differences in the viscoelastic stability of 7.5% and

10% w/v GelMA hydrogels under increasing strain. For the 7.5% w/v GelMA hydrogel G′ began to decline at 63% strain, while G″ started to increase at 31% strain, with G′ and G″ crossing over at 99% strain, resulting in total hydrogel breakdown. This crossover point indicates the hydrogel models transition from predominately elastic to viscous behaviour, indicating that the 7.5% w/v hydrogels maintain their structural stability under relatively high strain. With addition of 0.25 mg/mL MNPs, strain tolerance was reduced, with G′ beginning to drop at 40% strain, G″ increasing from 22% strain and the crossover occurring at 89% strain. With 0.5 mg/mL MNPs, G′ began to drop at 44% strain, G″ increased from 22% and crossover occurred earlier at 63% strain (**Figure 4-5**).

In contrast, 10% w/v hydrogels showed a decrease in hydrogel strength. In the control 10% w/v hydrogels, G′ began to drop at just 15% strain, G″ increased from 5% strain and complete hydrogel breakdown occurred at 22% strain. With 0.25 mg/mL MNPs G′ declined at just 8% strain, G″ increased from 3% strain and crossover of G′ and G″ was observed under 11% strain. Finally, 0.5 mg/mL MNPs in 10% w/v GelMA further reduced viscoelastic stability as G′ began to decline at 5% strain, G″ increased from 2% strain and crossover occurred as early as 7% (**Figure 4-5**).

While 10% w/v GelMA exhibits higher baseline stiffness, they show a sharp decline in viscoelastic performance under relatively low strain, suggesting weaker hydrogels. In contrast, the 7.5% w/v GelMA retains elastic behaviour over a much broader strain range, indicating a greater structural stability. However, while 7.5% w/v GelMA hydrogels can withstand significant deformation, increasing MNP content reduces their viscoelastic stability under strain. These findings suggest that 7.5% w/v GelMA particularly at low MNP concentrations may offer more robust mechanical performance under dynamic loading conditions.

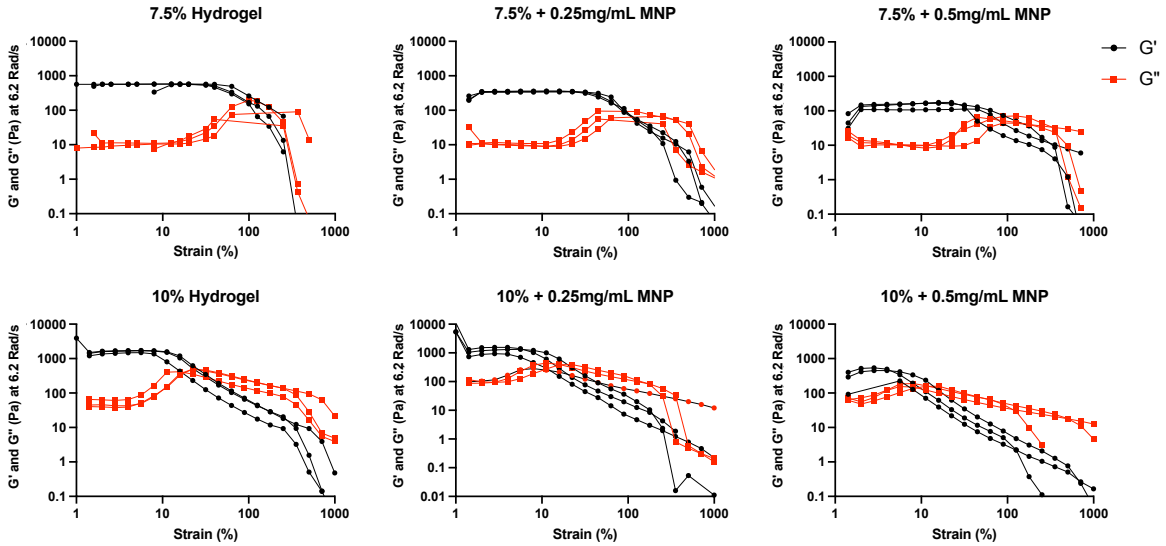

Figure 4-5: Increasing polymer and magnetic nanoparticle concentration reduces viscoelastic stability in GelMA hydrogels

Amplitude sweeps of GelMA hydrogels, 7.5% and 10% w/v, with addition of 0.25 mg/mL and 0.5 mg/mL magnetic nanoparticles (MNPs). Storage modulus (G′ – indicated by black circles) and loss modulus (G″ – indicated by red squares) were measured *via* strain sweep tests (1-1000% strain, 1 Hz, 6.2 Rad/s) for hydrogels 72 hours post polymerisation (n=3). Measurements were obtained using an Anton Paar rheometer.

4.5 Biocompatibility

To evaluate suitability of the developed magnetic hydrogel model for bone tissue engineering applications, biocompatibility was assessed using a range of parameters. This section focuses on the 7.5% and 10% w/v GelMA hydrogels containing 0.25 mg/mL and 0.5 mg/mL dextran coated iron oxide MNPs, which were previously optimised for mechanical properties and magnetic performance. Biocompatibility is a crucial factor in biomaterial application, particularly in tissue engineering where the ultimate goal is integration into host tissue. Biocompatibility determines the materials ability to interact with cells and tissues, promoting cell adherence, differentiation and long term viability. Key characteristics evaluated include hydrogel wettability *via* water contact angle measurements, hydrogel morphology using imaging techniques, contraction behaviour and cell viability assays. These properties together provide a comprehensive picture of how the hydrogel model can support biological interaction with embedded cells.

4.5.1 Wettability

It is important to verify that a hydrogel model is inherently hydrophilic, to ensure a soft, tissue-like environment that is compatible with cells. Magnetic GelMA hydrogels were expected to maintain hydrophilic behaviour. The wettability of GelMA hydrogels was measured using water contact angle (WCA) measurements. Less than 90° corresponds to high wettability (hydrophilic), whereas above 90° signifies low wettability (hydrophobic) **(Figure 4-6)**.

Initially, WCA measurements were obtained from 7.5% w/v GelMA hydrogels only. Wet hydrogels were measured immediately from cell culture media, while dry hydrogels were dried prior to measurements. While both wet and dry 7.5% w/v hydrogels were hydrophilic, 20.4° (±4.4°) and 61.8° (±6.4°) respectively, a significant difference was identified between the conditions **(Figure 4-6, A)**.

WCA measurements of GelMA hydrogels were completed for concentrations 7.5% and 10% w/v both with and without MNPs. Adding MNPs to the 7.5% w/v hydrogel resulted in no significant change to the wettability for both 0.25 mg/mL and 0.5 mg/mL, 70.0° (±1.4°) and 59.1° (±3.0°) respectively, in comparison to the control hydrogel, 61.3° (±5.7°). No significant change was observed in WCA between the 10% w/v control hydrogel, and the addition of 0.25 mg/mL MNPs, 65.2° (±4.5°) and 65.0° (±3.4°) respectively. However, the addition of 0.5 mg/mL MNPs significantly reduced the WCA, 46.2° (±2.0°), in comparison to both control and hydrogels with 0.25 mg/mL MNPs **(Figure 4-6, B)**.

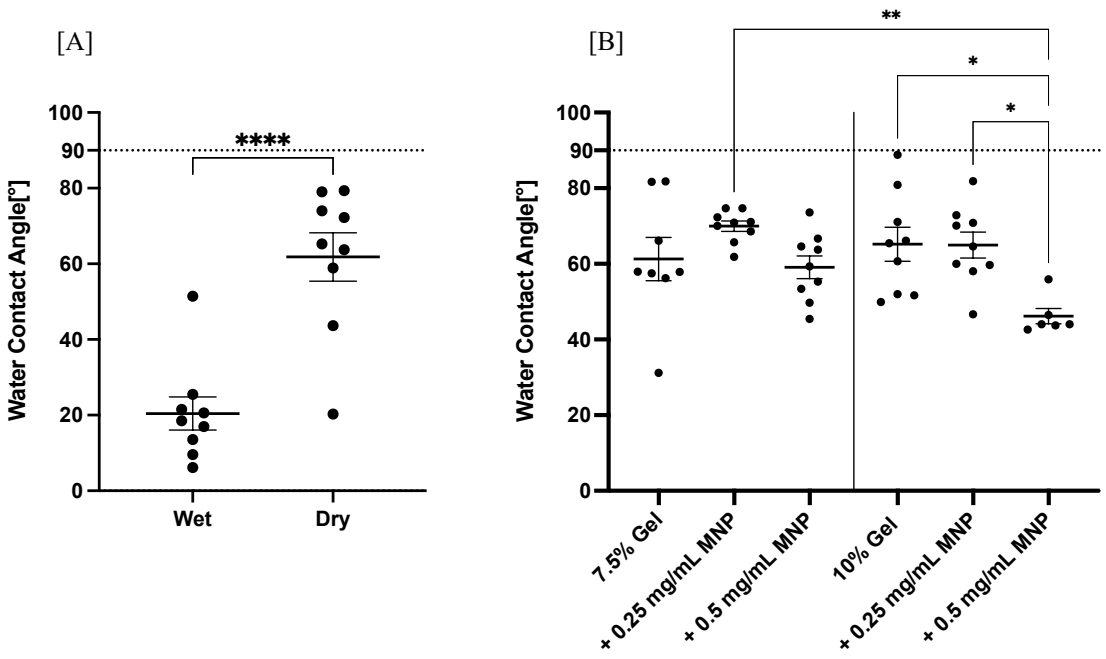

Figure 4-6: Wettability is maintained with increasing polymer and magnetic nanoparticle concentration in GelMA hydrogels

Wettability of GelMA hydrogels was measured using water contact angle (WCA) measurements [A] WCA measurements from 7.5% w/v GelMA hydrogels were obtained with hydrogels immediately removed from culture media (Wet) and after airdrying for 5 minutes (Dry) (n=3). Error bars show mean ± SEM. An unpaired t-test showed significance between conditions. [B] WCA angle measurements obtained from dried hydrogels, 7.5% and 10% w/v, with MNPs at concentrations 0.25 mg/mL and 0.5 mg/mL (n=3). Error bars show mean ± SEM. A one-way ANOVA and post hoc Holm Šídák's tests were performed to identify significance between conditions.

Both 7.5% and 10% w/v GelMA hydrogels are hydrophilic materials, with no significant difference in wettability observed with increasing gelatin concentration. While the addition of MNPs into hydrogels does not generally affect hydrophilicity, a higher concentration of MNPs (0.5 mg/mL) in 10% w/v hydrogels may enhance hydrophilicity as observed with significantly reduced WCA measurements.

4.5.2 Hydrogel Morphology

The internal structure of the 7.5% and 10% w/v GelMA hydrogels were investigated, to identify any changes due to the addition of the MNPs. To achieve this, both SEM and Micro-CT were used, providing information on the pore size, area, circularity and connectivity (Golebiowska & Nukavarapu, 2022). Hydrogel porosity is crucial for tissue engineering applications, as the pores can influence cell behaviour in terms of migration, proliferation

and differentiation, by regulating cell-matrix interactions, nutrient diffusion and mechanical signalling (Annabi, et al., 2010) (Ho, et al., 2022). The incorporation of MNPs was expected to influence the internal pore structure in a concentration dependent manner (Xu, et al., 2012). For bone tissue engineering, larger pores are generally considered favourable (Edwards, et al., 2024). SEM micrographs of GelMA hydrogels were collected for investigation of the hydrogel's internal morphology **(Figure 4-7)**. Pore diameter, area and circularity were measured.

Pore Diameter: The addition of MNPs significantly reduced pore diameter in 7.5% w/v GelMA hydrogels, from 54.7 μm (±3.2 μm) to 34.1 μm (±2.7 μm) and 34.2 μm (±3.9 μm) for 0.25 mg/mL and 0.5 mg/mL concentrations. The diameter of pores within the 7.5% w/v hydrogels were also significantly higher than the 10% w/v GelMA hydrogel at 17 μm (±1.5 μm). Conversely, the addition of 0.25 mg/mL and 0.5 mg/mL MNPs to 10% w/v hydrogels increased diameters to 28.7 μm (±2.8 μm) and 27.8 μm (±3.8 μm) respectively, although these increases were not statistically significant **(Figure 4-7, B)**.

Pore Area: The hydrogel pore areas followed a similar trend. The pore area for the 7.5% hydrogels were significantly higher area than the 10% w/v hydrogels, 2396 μm^2 (±266 μm^2) and 245 μm^2 (±37 μm^2) respectively. The addition of MNPs at both concentrations, 0.25 mg/mL and 0.5 mg/mL, significantly reduced the area in 7.5% w/v hydrogels to 957 μm^2 (±141 μm^2) and 982 μm^2 (±148 μm^2). The pore area in the 10% w/v hydrogels increased with the addition of MNPs, 637 μm^2 (±120 μm^2) and 660 μm^2 (±192 μm^2) for 7.5% and 10% w/v respectively; however, these increases were not statistically significant **(Figure 4-7, C)**.

Pore Circularity: Pore circularity was measured across all conditions, with values ranging from 0.5 to 1, indicating a mixture of pore shapes throughout the hydrogels. A corresponding mixture of pore sizes suggests a heterogenous network, which is beneficial for tissue engineering as it more closely mimics the structural complexity of the natural ECM, particularly bone tissue (Mukasheva, et al., 2024). A significantly increase in circularity was observed from 7.5% to 10% w/v hydrogels, 0.71 (±0.02) and 0.80 (±0.01) respectively, suggesting a shift towards more circular pores with increasing GelMA concentration. The addition of MNPs to the 7.5% w/v hydrogels increased circularity to 0.77 (± 0.01) and 0.77 (±0.02) for 0.25 mg/mL and 0.5 mg/mL respectively. In contrast, the addition of addition of MNPs to 10% w/v hydrogels had no effect on mean circularity values, which remained at 0.81 (±0.01) and 0.79 (±0.02) for 0.25 mg/mL and 0.5 mg/mL respectively **(Figure 4-7, D)**.

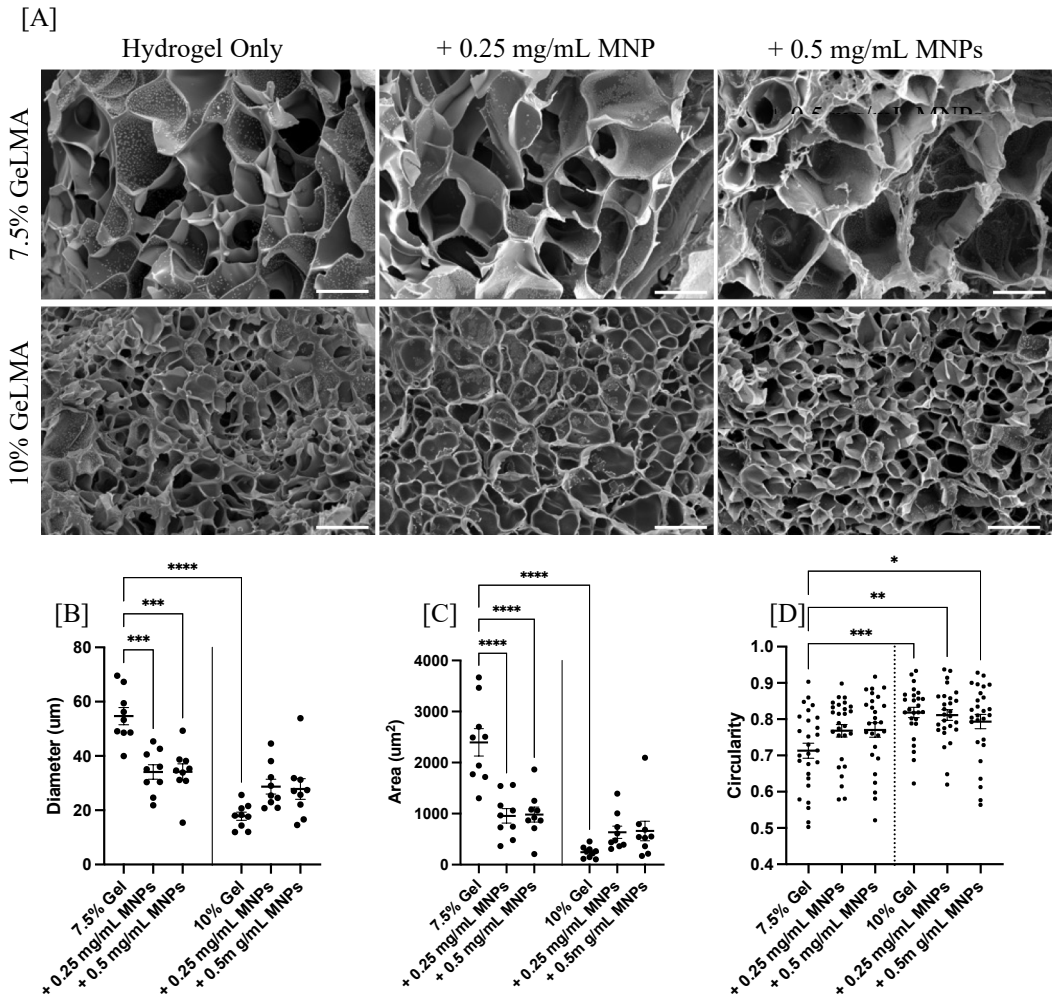

Figure 4-7: Hydrogel morphology is modulated with increasing polymer and magnetic nanoparticle concentration

Freeze dried hydrogels were imaged using scanning electron microscopy (SEM) [A] SEM images of 7.5% and 10% w/v GelMA hydrogels with 0.25 mg/mL and 0.5 mg/mL magnetic nanoparticles (MNPs) (n=3). Scale bar shows 50 µm. [B, C, D] Quantitative analysis of hydrogel morphology including pore diameter, area and circularity derived from SEM micrographs. Error bars show ± SEM. A one-way ANOVA and post hoc Holm Šídák's tests were performed to identify significance between conditions.

In summary, analysis of the internal structure with SEM revealed that adding MNPs reduced pore size and area in 7.5% w/v GelMA hydrogels, while slightly increasing these properties in 10% w/v hydrogels, though not significantly. Pore shapes became more circular with higher GelMA concentration, and MNP addition slightly increased circularity in 7.5% w/v hydrogels but had little effect on 10% w/v hydrogels. These results provide detailed insights into localised pore morphology. Utilising Micro-CT, a more global structural analysis will be completed to identify overall changes and trends in the hydrogel architecture.

Micro-CT images of freeze dried GelMA hydrogels were collected in collaboration with Dr Jonathan Williams at the University of Strathclyde. For an overview of gross hydrogel morphology, measurements of pore thickness, porosity, fibre thickness and connectivity density were collected **(Figure 4-8)**.

Pore Thickness: The hydrogel pore thickness changed depending on GelMA density and MNP concentration. Pore thickness was significantly reduced, by more than half, with increased GelMA concentration from 7.5% to 10% w/v, decreasing from 57.77 μm (±4.86 μm) to 23.33 μm (± 0.54 μm). With regard to the addition of the MNPS, the 7.5% w/v hydrogel pore thickness was reduced significantly when MNPs were introduced, with 0.25 mg/mL MNPs reducing to 30.73 μm (±1.15 μm) and 0.5 mg/mL to 39.42 μm (±3.01 μm). Conversely, in 10% w/v hydrogels, the addition of MNPs seemed to either leave pore thickness unchanged (0.25 mg/mL at 29.56 μm (±1.59 μm)) or increased (0.5 mg/mL to 48.64 μm (±3.55 μm)) **(Figure 4-8, B)**. In summary, this data supports the SEM pore diameter measurements, with a decrease for the 7.5% w/v hydrogels and an increase for the 10% w/v hydrogels.

Hydrogel Porosity: Generally, the porosity of the 7.5% w/v hydrogel was increased, whilst the 10% w/v hydrogel was unchanged following the addition of MNPs. More specifically, the 7.5% w/v hydrogel porosity was 19.5% (±1.9%), but significantly increased with the addition of MNPs at both concentrations (0.25 mg/mL MNPs to 51.5% (±1.1%) and 0.5 mg/mL MNPs to 37.6% (±3.2%)). Meanwhile, the 10% w/v hydrogels had significantly higher porosity than their 7.5% w/v counterparts (66.70% (±1.22%)), but the addition of both 0.25 mg/mL and 0.5 mg/mL MNPs to 10% w/v hydrogels showed no significant change in porosity, 55.37% (±6.60%) and 65.57% (±0.82%) respectively **(Figure 4-8, C)**.

GelMA Fibre Thickness: GelMA Fibre thickness measures the average thickness of the solid hydrogel struts and is an important parameter as thicker struts can hinder the flow of water within the polymer matrix (Jin, et al., 2009). As with porosity, fibre thickness significantly increased with increasing GelMA concentrations, from 22.61 μm (±1.43 μm) in 7.5% w/v hydrogels to more than double, at 57.78 μm (±3.29 μm) in 10% hydrogels. The addition of 0.25 mg/mL MNPs to 7.5% w/v hydrogels significantly increased fibre thickness to 46.58 μm (±1.87 μm), and the addition of 0.5 mg/mL MNPs increases fibre thickness to 35.12 μm (±1.78 μm). The addition of MNPs to 10% w/v hydrogels showed no significant change to fibre thickness for both concentrations, 52.69 μm (±6.02 μm) and 57.11 μm (±2.71 μm), 0.25 mg/mL and 0.5 mg/mL respectively **(Figure 4-8, D)**.

Connectivity: Unlike pore and fibre measurements, no significant change in connectivity density was recorded between 7.5% and 10% w/v hydrogels, 4533 mm^3 (±488 mm^3) and 7488 mm^3 (±585 mm^3) respectively. An increasing trend is visible in connectivity density with the addition of both 0.25 mg/mL and 0.5 mg/mL MNPs to hydrogels, 8401 mm^3 (±1128 mm^3) and 8027 mm^3 (±394 mm^3) respectively, although this was not statistically significant. With 10% w/v hydrogels, the addition of MNPs, at both concentrations 0.25 mg/mL and 0.5 mg/mL, did not impact connectivity density, 7728 mm^3 (±1991 mm^3) and 8085 mm^3 (±655 mm^3) respectively **(Figure 4-8, E)**.

In summary, the SEM and micro-CT analysis provide complementary insights into localised and global structure of GelMA hydrogels. The 7.5% w/v hydrogels generally exhibit larger pore size, diameter and area which was supported by micro-CT data showing greater pore thickness and increased porosity with addition of MNPs. Conversely, 10% w/v GelMA hydrogels display thicker gelatin fibres, and higher overall porosity, resulting in improved connectivity density indicating a more robust and interconnected network. The micro-CT measurements of pore thickness and fibre thickness align well with SEM findings on pore diameter and morphology. Together, these techniques paint a comprehensive picture of how GelMA concentration and MNP incorporation influence hydrogel architecture.

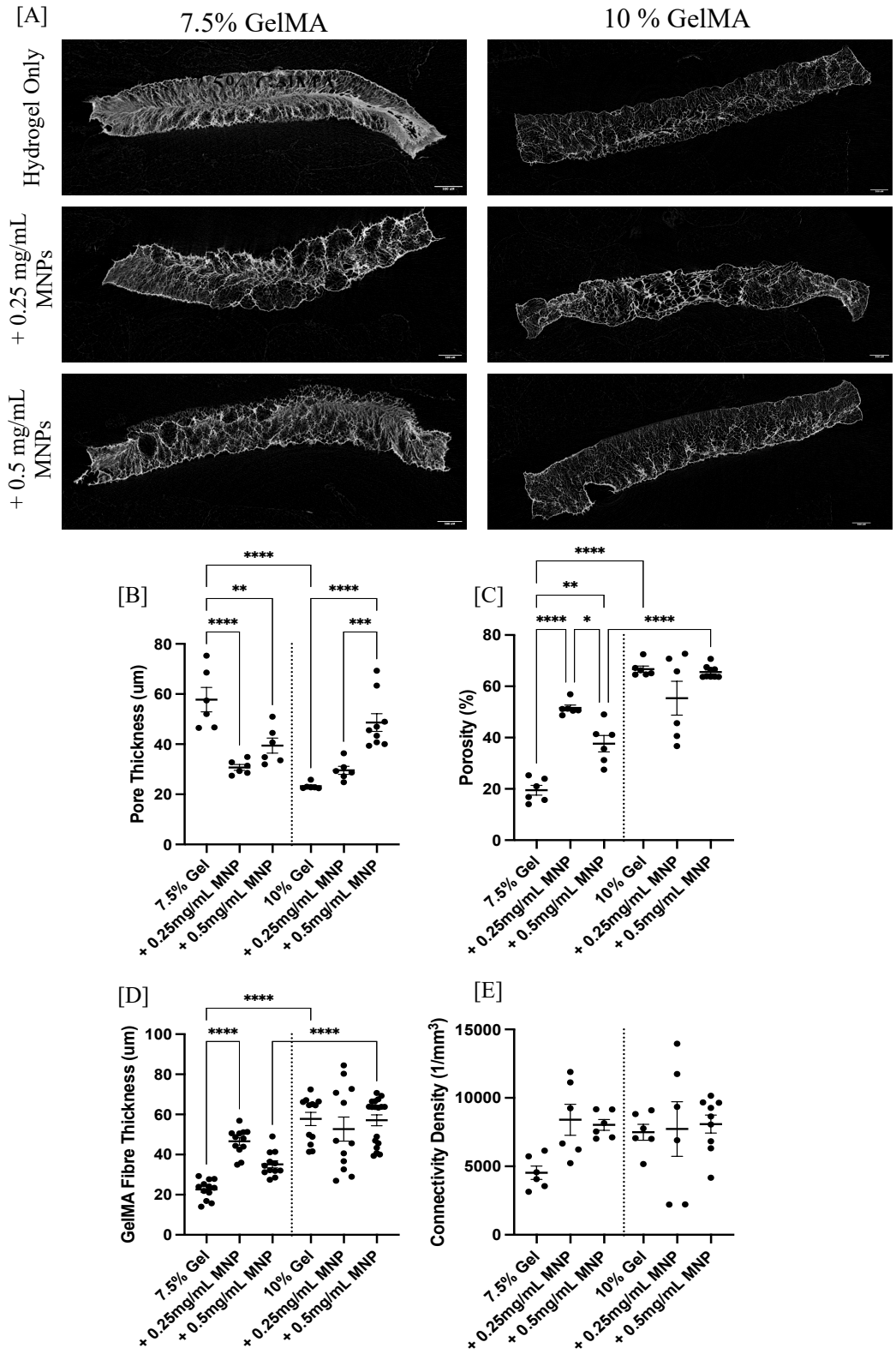

Figure 4-8: Overall hydrogel structure is modulated with increasing polymer and magnetic nanoparticle concentration

Freeze dried hydrogels were imaged using micro-computed tomography (Micro-CT) [A] Micro-CT images of 7.5% and 10% w/v GelMA hydrogels with 0.25 mg/mL and 0.5 mg/mL magnetic nanoparticles (MNPs) (n=3). Scale bar shows 500 μm. [B, C, D, E] Quantitative analysis of hydrogel morphology, including pore thickness, porosity, fibre thickness and connectivity density. Error bars show mean ± SEM

(n=3). A one-way ANOVA and post hoc Holm Šídák's tests were performed to identify significance between conditions.

SEM imaging was employed to observe the overall microstructure of the hydrogels; however, it was unsuitable for visualising the MNPs within the hydrogel matrix. Therefore, TEM imaging was utilised to visualise the MNPs within the hydrogel network. These TEM images demonstrate the presence and interaction of MNPs within the GelMA fibre network (**Figure 4-9**).

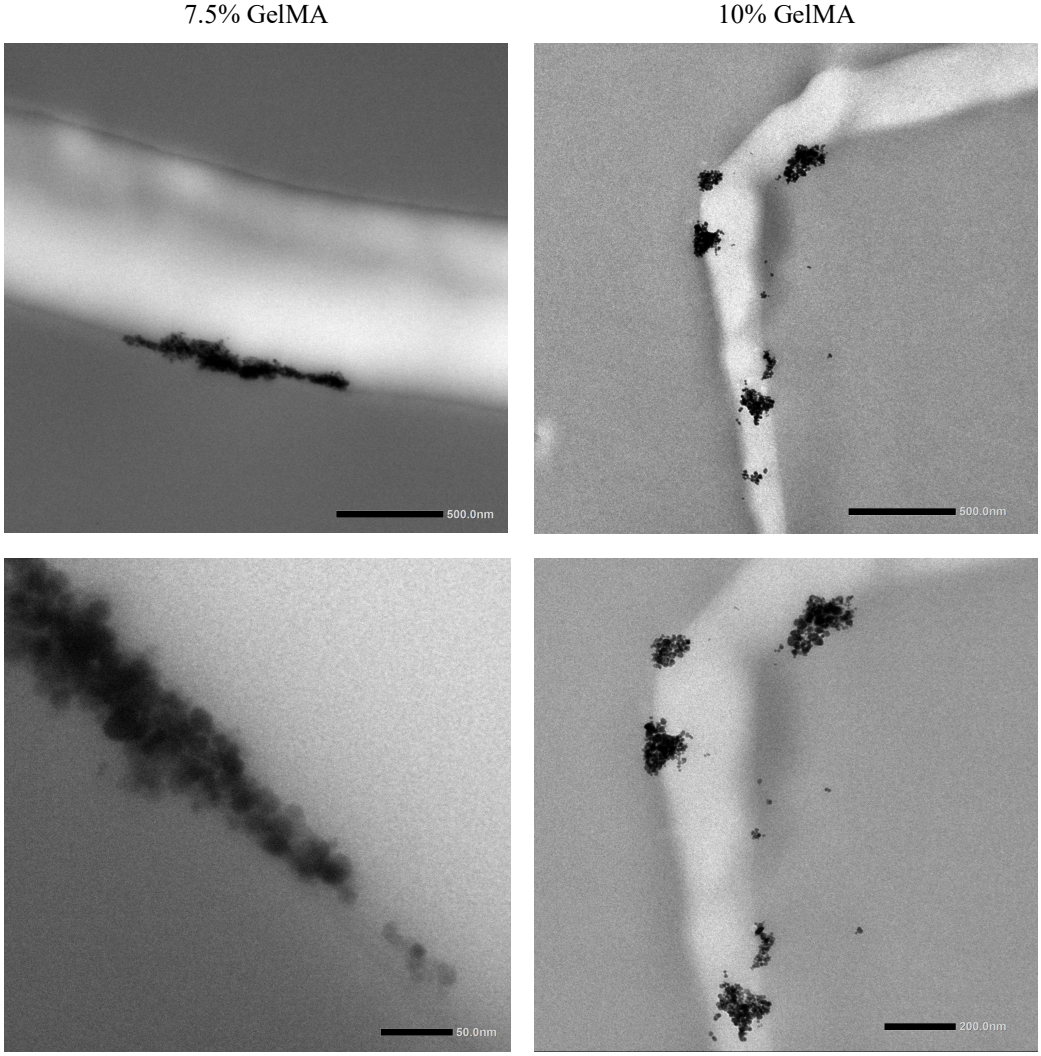

Figure 4-9: FluidMAG-Dx magnetic nanoparticles adhere to GelMA fibres

Freeze dried hydrogels were images using transmission electron microscopy. GelMA hydrogels, 7.5% and 10% w/v, with 0.5 mg/mL magnetic nanoparticles (MNPs) were imaged to identify location of MNPs within hydrogel structure. Representative images show the presence and distribution of MNPs on GelMA fibres. Scale bars represent 500 nm (top row), 50 nm (bottom left) and 200 nm (bottom right).

4.5.3 Swelling and Contraction of Hydrogels

Monitoring hydrogel swelling and contraction over time is important to assess hydrogel ability to absorb water and expand, which is a key factor for their use in regenerative applications. These fluid related changes are closely linked to pore size, and polymer crosslinking interactions (Velasco-Rodriquez, et al., 2021). Hydrogels typically swell upon polymerisation, absorbing water and expanding their structure. However, subsequent contraction can occur as the hydrogel network reorganises, particularly through interaction with cells. This contraction alters the properties of the hydrogel by compressing its inner structure, which can impact cell behaviour, nutrient diffusion and overall scaffold stability. Understanding these changes is crucial for designing hydrogels that maintain their desired properties. The GelMA hydrogels were expected to contract within the initial 24 hours, as contraction was observed during preliminary biocompatibility testing. The extent of hydrogel contraction was quantified over 48 hours to better understand its impact on hydrogel structure. Acellular hydrogels were used as control, to examine the effects of incorporated MNPs and MSCs on contraction time in absence of a magnetic field. Hydrogel diameter was measured at time points over 48 hours to identify contraction rate.

GelMA hydrogels were polymerised in PDMS moulds with a diameter of 12mm and observed over 48 hours (**Figure 4-10).** Essentially, both the 7.5% and the 10% w/v GelMA hydrogels contract over 24 hours, plateauing towards 48 hours.

Across all conditions, a reduction in diameter was observed indicating hydrogel contraction following polymerisation (**Figure 4-10**). The contraction rate varied depending on the presence of MNPs and MSCs. In 7.5% w/v hydrogels, the addition of MNPs or MSCs individually resulted in a slightly reduced contraction rate compared to the control, from -0.113 mm/hr in control hydrogels to -0.093 mm/hr and 0.092 mm/hr for MNPs and MSCs respectively. However, the combination of both MNPs and MSCs led to the greatest contraction rate, -0.138 mm/hr, with a 13.4% reduction in diameter over 12 hours (**Figure 4-10, Table 4-4**).

In 10% w/v hydrogels, a similar trend was observed. The control contracted at -0.119 mm/hr with slightly reduced contraction in the presence of either MNPs or MSCs, 0.088 mm/hr and 0.092 mm/hr respectively. The combination of MNPs and MSCs in 10% w/v hydrogels showed a moderate contraction rate of 0.097 mm/hr. Interestingly while 10% w/v hydrogels

started with a slightly larger average diameter, their overall contraction rates and percentage appear to be comparable to the 7.5% w/v hydrogels (**Figure 4-10, Table 4-4**).

The experiment was repeated with measurements at 0, 24 and 48 hours. Over 24 hours, all conditions for 7.5% w/v hydrogels showed a reduction in diameter from time of polymerisation, which was maintained over 48 hours **(Figure 4.10, B)**. Similarly, over 24 hours, all conditions for 10% w/v hydrogels showed a reduction in diameter within 24 hours, which was maintained at 48 hours **(Figure 4.10, D)**.

Overall, these results indicate that contraction occurs in all hydrogel models, with MNP and MSC content influencing rates and extent of contraction. The presence of both components appears to enhance contraction in 7.5% w/v hydrogels, which is not so pronounced in 10% w/v hydrogels. These results also indicate the hydrogels cease swelling or contracting within a 48 hour window post polymerisation.

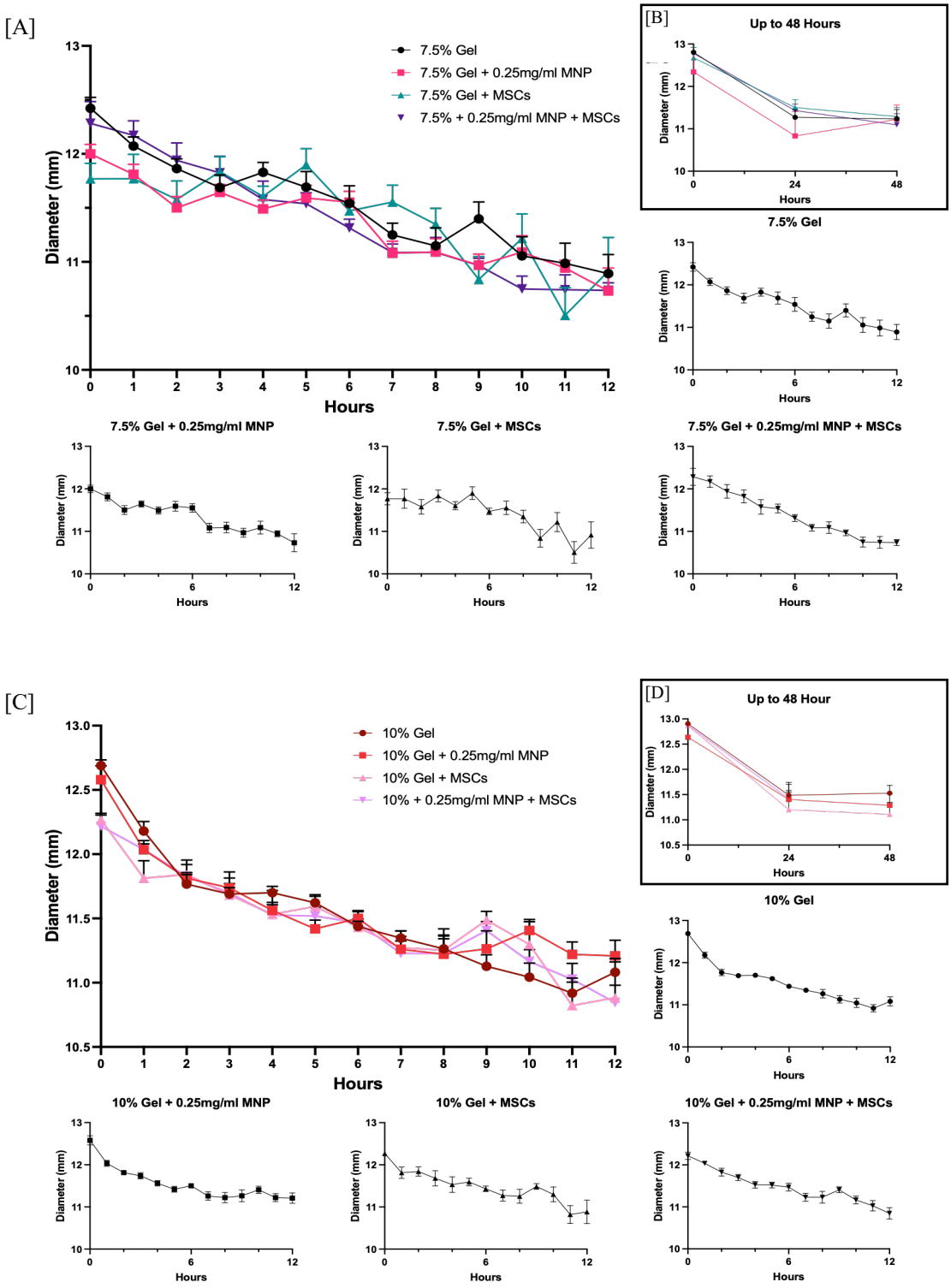

Figure 4-10: GelMA hydrogels undergo contraction independent of cell or magnetic nanoparticle content

Comparison of swelling and contraction of GelMA hydrogels, 7.5% and 10% w/v, with or without mesenchymal stromal cells (MSCs) and/or 0.25 mg/mL magnetic nanoparticles (MNPs). Measurements were collected over [A,C] 12 hours and [B,D] repeated over 48 hours. Data points show mean, error bars represent SEM (n=3)

Condition	Starting Diameter	Contraction Rate (mm/hour)	Total contraction over 12h (mm)	% Contraction
7.5% w/v GelMA	12.316	-0.113	1.354	11.0
7.5% w/v + MNPs	11.997	-0.093	1.116	9.3
7.5% w/v + MSCs	12.025	-0.092	1.104	9.2
7.5% w/v + MNPs + MSCs	12.355	-0.138	1.661	13.4
10% w/v GelMA	12.362	-0.119	1.430	11.6
10% w/v + MNPs	12.178	-0.088	1.067	8.8
10% w/v + MSCs	12.125	-0.092	1.114	9.2
10% w/v + MNPs + MSCs	12.156	-0.097	1.166	9.6

Table 4-4: Summary of selling and contraction of GelMA hydrogels

Contraction rates of GelMA hydrogels, 7.5% and 10% w/v, with or without mesenchymal stromal cells (MSCs) and/or 0.25 mg/mL magnetic nanoparticles (MNPs) over 12 hours. Mean contraction rate was determined from the gradient of the line of best fit (mm/hour), and total contraction over 12 hours was calculated. Percentage contraction was normalised to the initial diameter, measured immediately post polymerisation and prior to swelling in media.

4.5.4 Cell Viability

With a view towards bone tissue engineering, to further investigate biocompatibility, MSCs were encapsulated into 7.5% w/v GelMA hydrogels to measure cell viability over 28 days. Viability was assessed in 7.5% w/v GelMA hydrogels, chosen based on prior experiments with different gelatin concentrations where viability trends were consistent. Light microscopy images of live/dead stained cells were collected at days 1, 3 and 7 for hydrogels with and without MNPs to identify potential toxicity of fluidMAG-Dx MNPs on MSCs. Longer term viability of MSCs was assessed in 7.5% w/v GelMA hydrogels for days 14, 21 and 28 without MNPs. Live cells stained green with Calcein AM, and dead cells stained red with ethidium homodimer **(Figure 4-11, A)**. MSC viability was expected to be maintained throughout the 28 day period, as both GelMA and dextran coated MNPs have previously been demonstrated to be biocompatible (Brady, et al., 2015; Mamidi, et al., 2023; Zhou, et al., 2023).

Across the time course imaging, the MSCs are noted to spread and become elongated within the hydrogel, supporting cell-GelMA interaction. At day 1, cell viability with MNPs was maintained in comparison to control hydrogels, at 98.4% (±1.2%) and 95.2% (0.5%)

respectively. This trend continued at day 3, with viability in control hydrogels at 96.8% (±0.6%) and viability with MNPs at 96.0% (±0.6%). Finally at 7 days, viability was unaffected with addition of MNPs (95.4% (±1.3%)) in comparison to both control (96.1% (±0.2%)) and previous viability measurements at days 1 and 3.

Given viability was unaffected by addition of MNPs, long term viability of MSCs was assessed in GelMA hydrogels only. Viability at day 1 was assessed (viability set to 100%) and subsequent days were normalised to day 1. At days, 14 and 21 viability is maintained above 90%, at 93.7% (±0.8%) and 91.6% (±1.8%) respectively. Cell viability is significantly reduced between 21 and 28 days, to 84.14% (±1.9%). MSCs were also observed to adopt an elongated morphology in hydrogels over 28 days.

In addition, MSC spheroids, around 300 cells per spheroid, were encapsuled into 7.5% w/v GelMA hydrogels, with and without 0.25 mg/mL MNPs. In both conditions, spheroids maintain good viability and shape by day 10 (**Figure 4-12, A**). Measurements of cross section expression of FITC (green fluorescence) and FITC (red fluorescence) were collected to identify cell viability throughout the spheroid, with particular attention to the development of a necrotic core

In control hydrogels, 7.5% w/v GelMA without MNPs, FITC levels were maintained above TRITC, with slight peaks indicating some development of a necrotic core. In hydrogels with incorporated MNPs, some hydrogels showed increasing TRITC expression, while some appeared close to TRITC levels, particularly towards centre of the hydrogels, potentially highlighting earlier development of a necrotic core (**Figure 4-12, B**).

In summary, dispersed MSCs encapsuled into 7.5% w/v GelMA hydrogels maintained high viability and adopted an elongated morphology, indicating good cell to biomaterial interaction. The addition of MNPs did not significantly impact short term viability up to 7 days indicating dextran coated MNPs are non-toxic for encapsuled MSCs. Similarly, MSC spheroids also remained viable, though some signs of earlier necrotic core formation were observed in MNP containing hydrogels. Long term studies showed good viability maintained above 90% over 21 days, with a significant decline to ~84% by day 28. However, viability above 80% is generally well accepted in cell culture applications (Guadix, et al., 2019), indicating the GelMA hydrogel supports good biocompatibility over a four-week period.

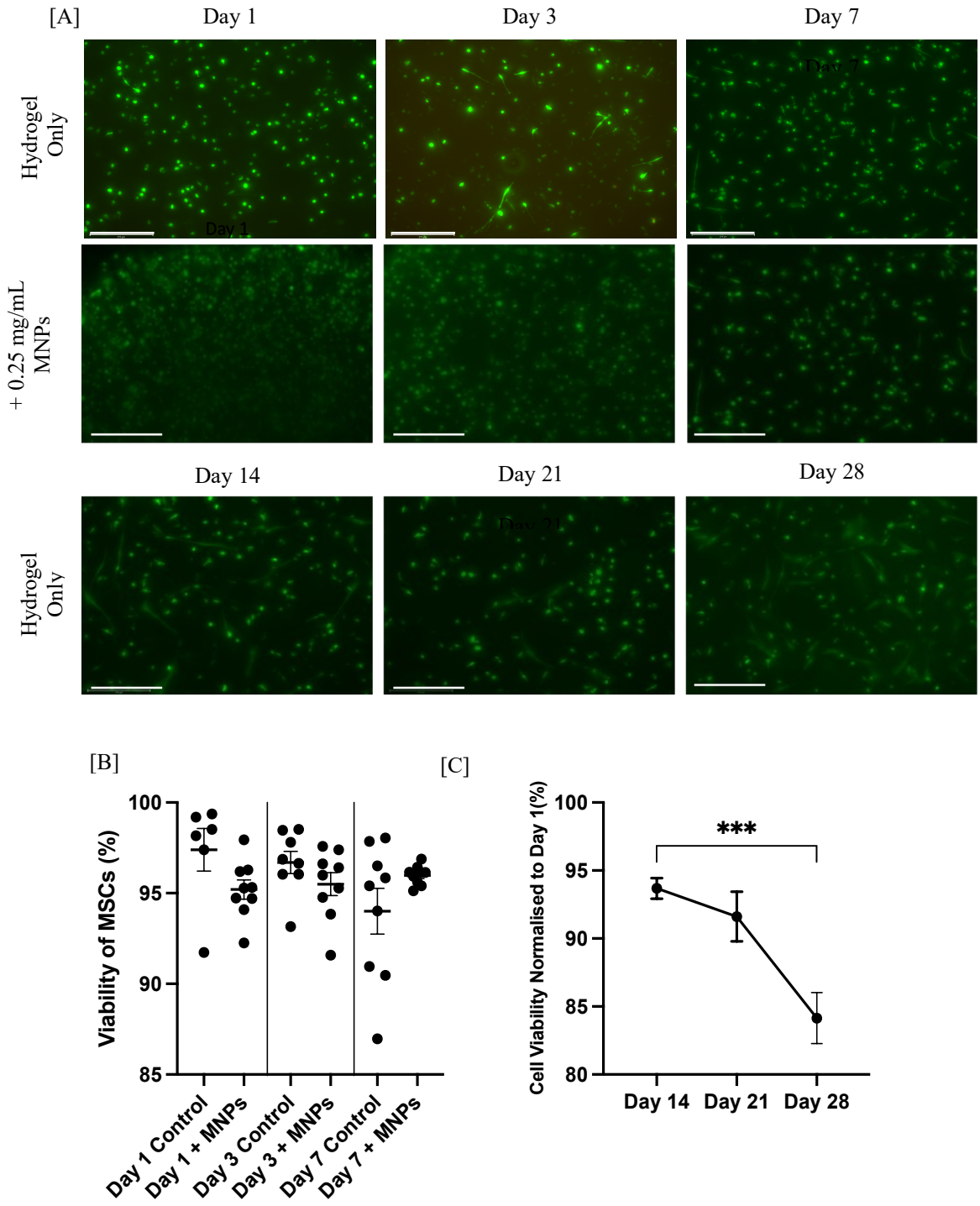

Figure 4- 11: Mesenchymal stromal cell viability is maintained in magnetic GelMA hydrogels over 28 days

Viability of mesenchymal stromal cells (MSCs) in GelMA hydrogels was assessed using LIVE/DEAD staining [A] Representative Live/Dead fluorescence microscopy images of MSCs stained with Calcein AM (live cells, green) and Ethidium homodimer-1 (dead cells, red) captured with EVOS fluorescent microscopy; scale bar shows 275 µm. Top two rows show GelMA MSCs within 7.5% w/v GelMA hydrogels and GelMA hydrogels with 0.25 mg/ml magnetic nanoparticles at day(s) 1, 3 and 7 (n=3). Bottom row shows long term viability in 7.5% w/v GelMA hydrogels only assessed over 28 days (n=3). [B] Quantification of cell viability (% live cells) calculated from fluorescence images. Error bars represent

mean ± SEM. A one-way ANOVA and post hoc Tukey test was performed to identify significance between conditions [C] Quantification of long term cell viability, normalised to day 1, calculated from fluorescence images. Error bars show mean ± SEM. A one-way ANOVA and post hoc Holm Šídák's tests were performed to identify significance between conditions.

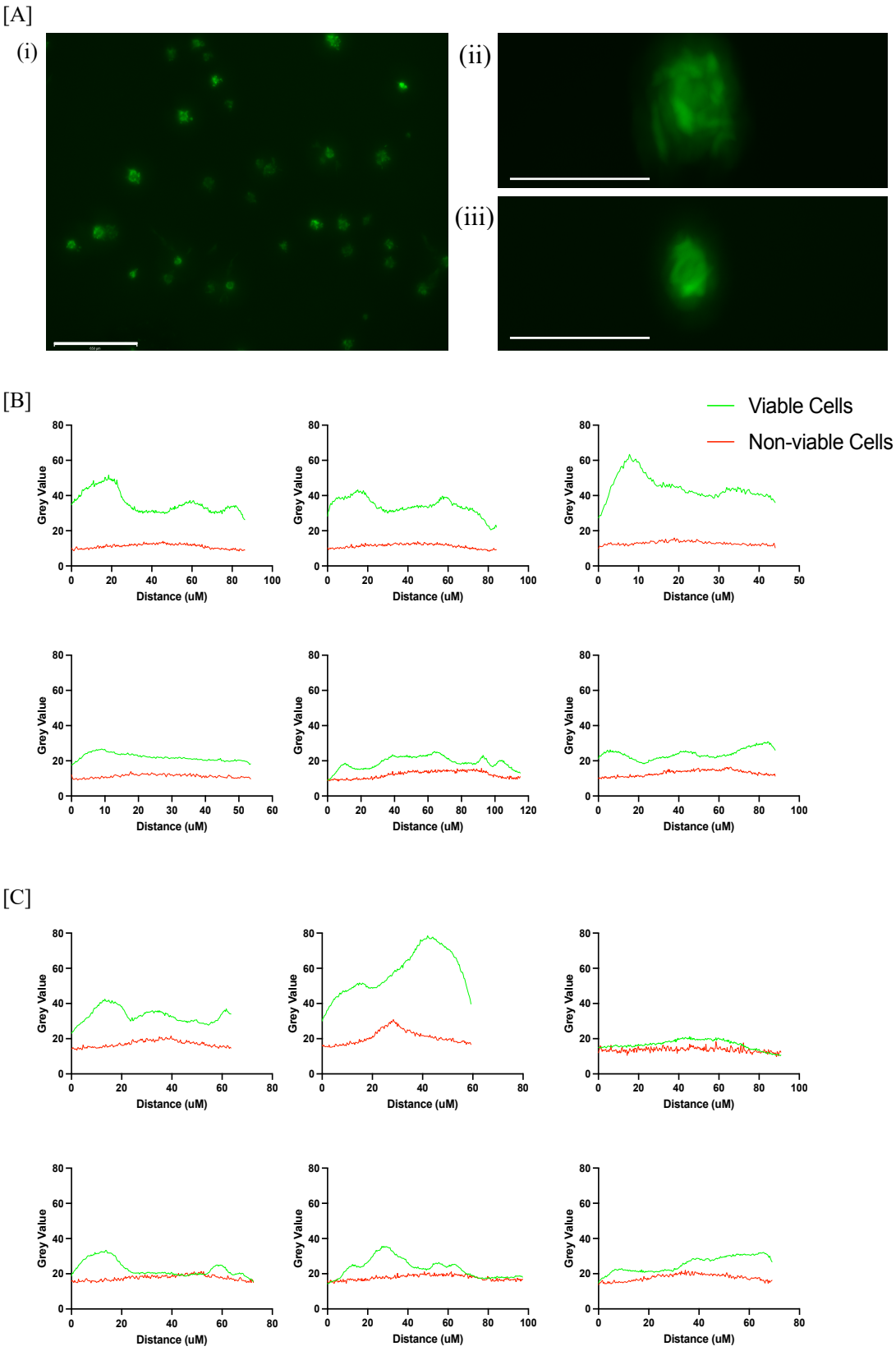

Figure 4-12: MSC Spheroids maintain viability and morphology in GelMA hydrogels

Viability of mesenchymal stromal cell (MSC) spheroids in GelMA hydrogels was assessed using LIVE/DEAD staining [A] Representative Live/Dead fluorescence microscopy images of MSC spheroids within 7.5% w/v GelMA hydrogels with magnetic nanoparticles (MNPs) (iii) and control hydrogels over 10 days (i, ii). Spheroids were stained with Calcein AM (live cell, green) and Ethidium homodimer-1

(dead cells, red) captured with EVOS fluorescent microscopy. Scale bars show (i) 650 µm and (ii, iii) 150 µm [B, C] Cross sectional representation of viable (green) and non-viable (red) fluorescent signal in MSC spheroids encapsuled in [B] 7.5% w/v GelMA hydrogels and [C] 7.5% w/v GelMA hydrogels with 0.25 mg/mL MNPs

4.6 3D Bioprinting

Bioprinting offers significant advantages for bone tissue engineering applications, by enabling rapid fabrication of customised structures with complex geometries. Biomaterials can be deposited in layers, to produce tailored shapes, influencing internal structure such as porosity (Wang, et al., 2020). Here the application of 3D bioprinting was examined for use with the magnetic GelMA model.

GelMA hydrogels were prepared using a CELLINK bioprinter, in collaboration with Dr Eonan Pringle at the Centre for Cellular Microenvironment (University of Glasgow). During the printing process, a technical issue in printing magnetic GelMA hydrogels was identified, related to the print head containing a magnet to allow attachment to the machine. To negate this issue, the MNP hydrogels had to be cooled to room temperature and brought back up to printing temperature to prevent MNP aggregation.

4.6.1 Mechanical Properties of 3D Bioprinted GelMA

To determine stability of printed hydrogels, they were examined using rheological measurements, water contact angle and prepared for SEM imaging. Printed hydrogels were compared to hand cast hydrogels to identify effects of fabrication method on mechanical properties. Printed hydrogels are expected to maintain uniformity and surface integrity comparable to hand cast hydrogels after polymerisation.

Unfortunately, during the freeze-drying process, printed hydrogels demonstrated poor quality to continue for SEM imaging. Printed hydrogels showed diminished uniformity compared to hand cast hydrogels, with printing grid patterns visible after polymerisation. Printed hydrogels also appeared to have grooved surfaces, reminiscent of the printing pattern, while hand cast hydrogels had a uniform shape and flat surface **(Figure 4-13, A)**.

Hydrogels were analysed using rheology at 24 and 72 hours post printing for 3D printed hydrogels, and post polymerisation for hand cast hydrogels. At 24 hours, a significant

increase in G′ was observed in bioprinted 7.5% w/v hydrogels, in comparison to hand cast hydrogels, increasing two fold from 1035 Pa (581-1300 Pa) to 2030 Pa (1690-2260 Pa). At 24 hours, bioprinting appears to increase hydrogel stiffness compared to hand cast hydrogels. A similar trend was observed at 24 hours with addition of MNPs, with G′ increasing from 280 Pa (272-292 Pa) with hand cast hydrogels, to 1140 Pa (1070-1170 Pa) with 3D printed hydrogels. Similarly, despite the preparation method a significant reduction in G′ was observed when MNPs were added, in both bioprinted and hand cast hydrogels. At 72 hours G′ had increased for hand cast hydrogels. In 7.5% w/v GelMA hydrogels, mean G′ was similar for bioprinted and hand cast, 2005 Pa (1940-2093 Pa) and 1978 Pa (1636-2635 Pa) respectively, although a larger range of measurements were observed in hand cast hydrogels. G′ in bioprinted hydrogels with MNPs remained steady from 24 hours, to 1410 Pa (1350-1460 Pa) at 72 hours, however this was significantly reduced compared to hand cast hydrogels at 72 hours, with G′ increasing to 2287 Pa (2120-2503 Pa). This was a significant increase from the same condition at 24 hours (**Figure 4-13, B**).

Similarly, G″ was observed to be impacted by preparation method. At 24 hours G″ of hand cast hydrogels was significantly reduced in comparison to bioprinted hydrogels, 12 Pa (9-15 Pa) and 24 Pa (17-26 Pa) respectively. However, addition of MNPs did not significantly impact G″ in both hand cast (9 Pa (7-13 Pa)) and bioprinted (25 Pa (21-29 Pa)) hydrogels at 24 hours. At 72 hours, hand cast hydrogels showed a significantly reduced G″ compared to bioprinted hydrogels, at 9 Pa (8-14 Pa) and 26 Pa (23-30 Pa) respectively. Interestingly, addition of MNPs in hand cast hydrogels (31 Pa (20-73 Pa)) significantly increased G″ in comparison to bioprinted 32 Pa (26-37 Pa), suggesting that hand casting caused an increase in the hydrogels liquid like properties. While median G″ was not altered by preparation method, but a much wider range of measurements was observed in hand cast hydrogels (**Figure 4-13, B**).

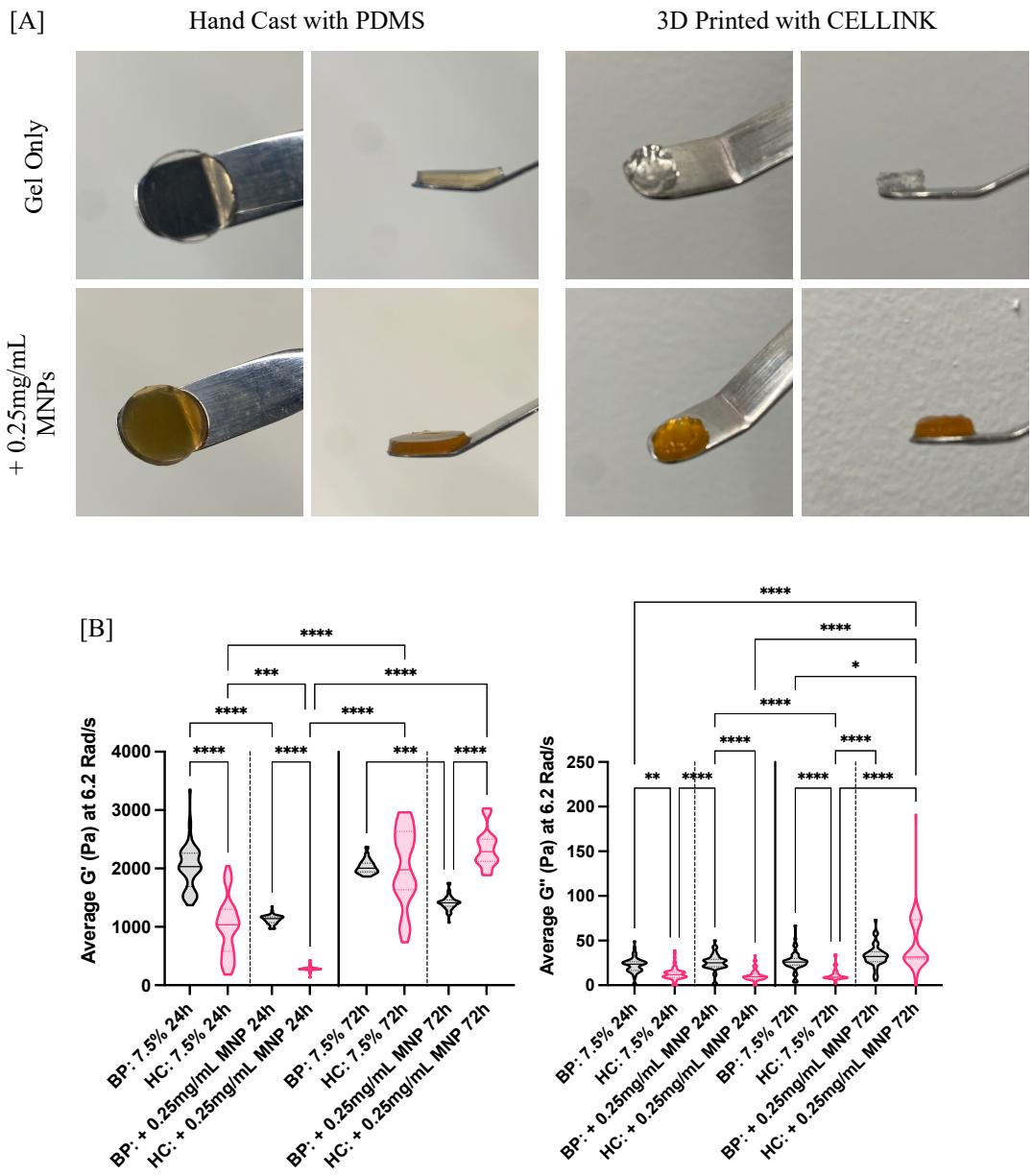

Figure 4-13: GelMA hydrogel mechanical properties are influenced by preparation method

GelMA hydrogels, 7.5% w/v with 0.25 mg/mL magnetic nanoparticles (MNPs) were prepared using CELLINK bioprinter and compared to hand cast [A] Representative images of bioprinted GelMA hydrogels, in comparison to hydrogels hand cast within silicon moulds [B] Storage modulus (G′) and loss modulus (G″) were measured *via* strain sweep tests (0.01-0.1% strain, 1 Hz, 6.2 Rad/s) for GelMA hydrogels. Measurements were obtained using an Anton Paar rheometer. Truncated violin plots show distribution of G′ and G″ values with median (solid line) and interquartile range (dashed lines) (n=3). A Kruskal-Wallis test, and post hoc Dunn's multiple comparison tests, showed significance between conditions.

Tanδ values, calculated from median G′ and G″ are presented in **Table 4-5**. All values are below 0.04, indicating elastic behaviour dominates over viscous behaviour (G′ greater than

G″). At 24 hours, tanδ values remain low across all conditions, indicating predominately elastic behaviour. With additions of MNPs, tanδ values increase in both preparation methods, reflecting the softening effect of MNPs on hydrogel matrix. At 72 hours, tanδ decreased in 7.5% w/v hand cast hydrogels, indicating stiffening over time, while bioprinted hydrogels remained relatively stable. Overall, the hydrogels retained viscoelastic properties, consistent with soft elastic hydrogel behaviour, tanδ <1, with preparation method and time influencing the elastic and viscous response (**Table 4-5**).

	Time Since Polymerisation	
Condition	**24 hours**	**72 hours**
7.5% w/v GelMA, Hand cast	0.011	0.005
7.5% w/v GelMA, Bioprinted	0.012	0.013
7.5% w/v + 0.25 mg/mL MNPs, Hand cast	0.034	0.014
7.5% w/v + 0.25 mg/mL MNPs, Bioprinted	0.022	0.023

Table 4-5: Tanδ values of bioprinted and hand cast GelMA hydrogels

Tanδ (=G″/G′) values of bioprinted and hand cast GelMA hydrogels (7.5% w/v) with magnetic nanoparticles (0.25 mg/mL) at 24 and 72 hours post polymerisation. Tanδ near 0 indicate the material shows more elastic behaviour, while close to 1 indicates viscous behaviour.

4.6.1 Wettability of 3D Bioprinted GelMA

Prior to rheology, at 72 hours, hydrogels were examined using WCA to measure wettability. Bioprinted hydrogels were compared to measurements previously obtained from hand cast hydrogels **(Figure 4-14)**. Printed hydrogels were expected to remain hydrophilic, as the fabrication method should not alter the inherent hydrophilicity of these hydrogels.

Despite previously identified grooves, WCA measurements were able to be obtained from one surface of each hydrogel. Hand cast GelMA hydrogels had a water contact angle 57.9° (±5.7°), increasing to 70.9° (±1.4°) with addition of MNPs although this was not significant. Printed hydrogels retain a similar water contact angle with addition of MNPs, 47.0° (±7.1°) and 45° (±10.1°) respectively. All conditions were measured under 90° and therefore considered hydrophilic.

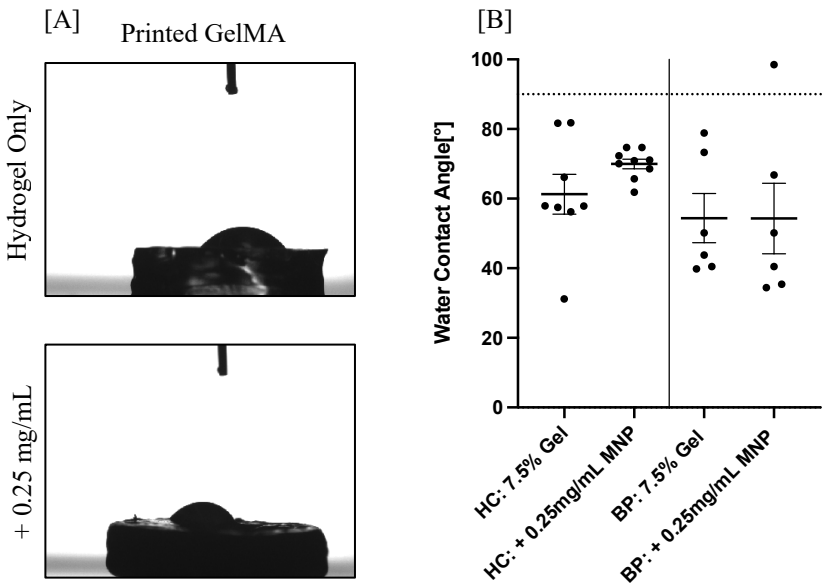

Figure 4-14: Bioprinting GelMA hydrogels maintains wettability

GelMA hydrogels, 7.5% w/v with 0.25 mg/mL magnetic nanoparticles (MNPs) were prepared using CELLINK bioprinter and compared to hand cast. Wettability of GelMA hydrogels was measured using water contact angle (WCA) measurements [A] Images of water droplet with surface contact used for water contact angle (WCA) analysis [B] WCA angle measurements were captured from bioprinted and hand cast hydrogels (n=3). Error bars show mean ± SEM. A one-way ANOVA and post hoc Holm Šídák's tests were performed to identify significance between conditions.

Despite the improved early mechanical properties observed in bioprinted hydrogels, 3D printing was not pursued further due to increased preparation time, cost, technical challenges during printing (particularly with magnetic formulations), and concerns that prolonged handling could negatively impact cell viability.

4.7 Discussion

4.7.1 Magnetic Nanoparticles Demonstrate Tuneable Superparamagnetic Behaviour

The primary goal of incorporating MNPs into hydrogels is to achieve controlled oscillation of particles within the matrix under external magnetic fields. This subtle vibrational movement provides mechanical stimuli to embedded cells, without requiring particle uptake. Therefore, MNP behaviour must support reversable, and non-aggregating responses to external fields, making superparamagnetism a critical property for MNPs within this model.

Characterisation of fluidMAG-Dx MNPs using both TEM and DLS confirmed they are multidomain MNPs with an average hydrodynamic diameter of approximately 200 nm, consistent with the manufacturer's specifications (chemicell, 2025). Nowak et al., (2014), reported similar hydrodynamic sizes (~180 nm) in fluidMAG-D MNPs using comparable methods, though with narrower size distributions compared to our study. Their study also reported an individual particle diameter of 14.9 nm (Nowak, et al., 2014). The broader size distribution observed in our study may result from DLS assumptions of particle sphericity, and inherent particle heterogeneity (Stetfeld, et al., 2016). Importantly this size range has been shown to optimize penetration depth in 3D collagen hydrogels, balancing physical barriers such as pore size and cell density, while maintaining effective responsiveness to magnetic fields (Lewis, et al., 2014).

Magnetic characterisation using SQUID magnetometry revealed that fluidMAG-Dx MNPs exhibit a dual magnetic nature. Under high magnetic fields (±1.5 T), they exhibit ferromagnetic behaviour with clear hysteresis loops, including measurable remanence and coercivity, consistent with magnetic blocking in multidomain particles (Lu, et al., 2007). However, at moderate fields (±0.4 T) the hysteresis loop narrows significantly, indicating a shift towards superparamagnetic behaviour**.** This tuneable response aligns with simulations of 150 nm fluidMAG-D showing that dipole-dipole interactions reduce net magnetic moment at low fields, while broader size distributions enhance it (Schaller, et al., 2009).

The tuneable magnetic response of fluidMAG-Dx MNPs is a critical factor for tissue engineering hydrogel applications. Superparamagnetism is particularly advantageous for magnetic hydrogel systems because, unlike ferromagnetic particles, they do not retain magnetisation after removal of the external field. This prevents particle aggregation and

preserves uniform dispersion in the hydrogel matrix (Eberbeck, et al., 2010). While paramagnetic particles also avoid aggregation, they typically exhibit insufficient magnetic responsiveness to generate meaningful mechanical stimulation (Fan, et al., 2020). In contrast, the superparamagnetic behaviour of fluidMAG-Dx ensures both stability and responsiveness, enabling consistent oscillatory actuation critical for stimulating cell mechanotransduction pathways. Nowak et al., (2014) confirmed superparamagnetic behaviour of fluidMAG-D particles using vibrating sample magnetometer (VSM). They observed that saturation magnetisation, a measure of maximum particle magnetisation, increased with particle size and correlated with hydrodynamic diameter (Nowak, et al., 2014). Similarly, Hong et al. (2008) reported that dextran coated iron oxide MNPs maintain superparamagnetic behaviour across coatings of varying molecular weight, although coating efficiency can influence magnetic properties (Hong, et al., 2008). These findings support the suitability of dextran-coated MNPs for magnetic actuation within hydrogels.

The behaviour of MNPs is influenced not only by the iron oxide core, but also significantly by their surface coating. For *in vitro* applications, fluidMAG-Dx MNPs demonstrate excellent colloidal stability in cell culture media maintaining viability and ECM integration (Eberbeck, et al., 2010). Moreover, studies have shown these coated MNPs exhibit safe biodistribution and no acute toxicity in animal models, supporting their biocompatibility for *in vivo* applications (Hong, et al., 2008). This stability and safety profile reinforces the suitability of dextran coated MNPs for incorporation into cell laden hydrogels.

Alternating current magnetic susceptibility measurements further demonstrate the suitability of fluidMAG-Dx MNPs for oscillating magnetic actuation. The in-phase susceptibility remained relatively stable across the tested temperature range and frequencies, indicating that most magnetic moments effectively follow the applied oscillating field. Corresponding out-of-phase susceptibility values were low, reflecting minimal magnetic lag. This behaviour supports the capacity of fluidMAG-Dx MNPs to rapidly and reversibly reorient in response to external magnetic fields, an essential feature for generating subtle vibrational stimuli within the hydrogel matrix. Additionally, Nowak et al., (2014) reported a strong magnetoviscous effect for 200 nm fluidMAG-D MNPs under applied magnetic fields. While typically observed in fluid suspensions, this effect suggests these particles can exert mechanical forces within a hydrogel matrix when exposed to external magnetic stimulation (Nowak, et al., 2014).

Together these results confirm that fluidMAG-Dx MNPs exhibit field dependent magnetic behaviour that can be harnessed for controlled, non-invasive mechanical stimulation of cultured cells. Their demonstrated ability to oscillate in response to moderate magnetic fields, without becoming magnetically locked or aggregated is crucial for maintaining consistent signalling. Prior studies have shown that magnetic mechanical stimulation enhances osteogenic differentiation of MSCs and supports bone tissue regeneration (Fan, et al., 2020). The reversible, superparamagnetic behaviour demonstrated in this study aligns with these functional requirements, supporting the application of fluidMAG-Dx MNPs in magnetic hydrogel systems for bone tissue engineering.

4.7.2 Magnetic Nanoparticles Incorporate into GelMA to Form a Soft, Elastic Hydrogel Model

4.7.2.1 Hydrogel Models in Bone Tissue Engineering

Hydrogels are widely utilised as biomaterial scaffolds in tissue engineering due to their tuneable mechanical properties. In soft tissue engineering, hydrogel stiffness can be adjusted to mimic the mechanical environment of native tissues (**Table 4-6**).

Tissue Type	**Stiffness**	**Reference**
Bone, Marrow	0.3-10 kPA	(Yang, et al., 2025)
Bone, Cortical	10-100 kPA	(Yang, et al., 2025)
Adipose	2-4 kPA	(Kuss, et al., 2018)
Muscle	8-17 kPa	(Kuss, et al., 2018)
Cartilage, ECM	100 kPa	(Song, et al., 2024)
Cartilage, Pericellular Matrix	20-40 kPa	(Song, et al., 2024)

Table 4-6: Summary of mechanical properties of native tissues

Summary of reported mechanical properties (in kPa) for various native tissues relevant to tissue engineering and biomaterials research

Parekh et al., (2011) observed that MSCs increased commitment to osteogenic differentiation in response to higher stiffness. Their study employed PEG hydrogels with storage moduli ranging from 0.2-59 kPa and demonstrated that observed mechanosenstive behaviour was mediated through integrin dependent cell matrix interactions, highlighting the importance of ECM engagement in linage commitment (Parekh, et al., 2011). Similarly, Park et al., (2011) demonstrated that matrix stiffness influenced MSC differentiation patterns: stiff substrates (>15 kPa) promoted smooth muscle lineage, while softer substrates favoured

chondrogenic or adipogenic differentiation (1-15 kPa). These findings mirror the stiffness values of the corresponding native tissue (Park, et al., 2011). Kuss, et al (2018), further observed that both white and brown adipogenic differentiation occurred in HA and gelatin hydrogels with moduli of 2-4 kPa. Interestingly, brown adipogenesis was favoured in stiffer hydrogels, possibly reflecting the functional association of brown adipose tissue with muscle tissue (Kuss, et al., 2018).

Collectively, these studies highlight that the mechanical properties of hydrogels can be modulated to direct specific cell differentiation outcomes - for example, using stiffer matrices to promote osteogenesis. However, stiffness alone may be insufficient to induce full differentiation, due to overlapping stiffness ranges across tissues, or the need for additional biochemical cues to drive complete lineage commitment (Kuss, et al., 2018; Parekh, et al., 2011; Park, et al., 2011).

4.7.2.2 The Use of Added Factors into Hydrogel Models for Bone Tissue Engineering

Gelatin methacryloyl, GelMA, a naturally derived biomaterial, contains photocrosslinkable methacryloyl groups that allow polymerisation under UV light. GelMA is a viscoelastic biomaterial commonly used in various tissue engineering applications due to its tuneable mechanical properties, and biocompatibility (Yue, et al., 2015).

In this study, a GelMA hydrogel model was developed, and it was observed that increasing gelatin concentration led to increased stiffness (0.3-2 kPa) over 72 hours, with measurements stabilising about 48 hours post polymerisation. Tanδ values indicated that GelMA hydrogels at these concentrations exhibit predominantly elastic behaviour, becoming more elastic over time, likely due to matrix reorganisation. Hydrogel contraction between 0 and 48 hours correlated with increasing stiffness (G′), suggesting mechanical changes result from internal matrix contraction. It is plausible that the observed contraction and corresponding increase in stiffness are partially driven by temperature-induced matrix reorganisation; GelMA crosslinking was initiated at room temperature, and samples were subsequently incubated at 37°C, the shift to physiological temperature may have promoted hydrogel contraction. Luo et al, (2020), demonstrated controllable shrinkage in a chitosan-GelMA hydrogel system. Heating their chitosan-GelMA model from room temperature to physiological temperature induced contraction due to thermal driven physical crosslinks (Lou, et al., 2020). While our GelMA model lacks a thermal responsive co-polymer, their work suggests temperature elevation could contribute to the observed hydrogel changes. All hydrogel conditions were

exposed to the same temperature increase and cultured in cell culture media. While temperature is a likely driver, polymer hydrogels can also respond to pH, ionic strength and media components (Lou, et al., 2020), so these factors cannot be ruled out.

This chapter focused on the development of a magnetic hydrogel by incorporating 200 nm dextran coated, superparamagnetic MNPs into GelMA hydrogels. Homogenous dispersal of MNPs was achieved using a blending method (**Figure 1-11**) (Liu, et al., 2020). MNP incorporation was visually confirmed by a colour change throughout the hydrogel matrix (**Figure 4-13, A**), while maintaining both biocompatibility and mechanical stability. Alveroğlu et al. (2013), developed a magnetic polyacrylamide hydrogel *via in situ* precipitation with incorporated Fe_3O_4 MNPs (12 nm). While this preparation method resulted in similar MNP homogeneity and retention within the hydrogel, the encapsuled MNPs were observed to form aggregates within the hydrogels (Alveroğlu, et al., 2013), which as discussed can impact ability of MNPs to respond to external magnetic fields. (Fan, et al., 2020). Zhang et al. (2015) subsequently utilised the coprecipitation method to incorporate MNPs (15-77 nm) into a collagen type II-HA-PEG (MagGel) hydrogel, achieving uniform nanoparticle distribution without aggregation. However, particle characterisation proved challenging: SEM imaging showed an average diameter of 15 nm, while laser diffraction measured 77 nm, indicating a degree of particle aggregation. This discrepancy may be attributed to the sample preparation for SEM, where particles were dried overnight and ground using mortar and pestle prior to imaging. In addition, the MNPs exhibited weak paramagnetic behaviour in response to an external magnetic field. Composition analysis was inconclusive due to overlapping elemental signals and possible oxidation, limiting accurate determination of composition and long-term behaviour (Zhang, et al., 2015).

The addition of MNPs within the GelMA hydrogels used in this chapter slightly reduced stiffness at higher concentrations; however, the hydrogels remained soft and elastic (2.2-4.8 kPa), making them suitable scaffolds for mimicking the mechanical environment of bone ECM and supporting cell mechanosensing. Similarly, Xuan et al., (2025) developed a polyacrylamide magnetic hydrogel using a blending method, achieving tuneable stiffness by adjusting polymer and Fe_3O_4 nanoparticle concentrations ranging from 0-15% w/v. Stiffness increased with higher polymer content and low MNP concentrations, but excessive MNP loading led to a reduction in stiffness, mirroring trends observed in our GelMA based models at 5% and 7.5% v/v GelMA concentrations (Xuan, et al., 2025). Xuan et al., (2025) used MNPs ranging 10-50 nm, comparable to the MNP size used by Xu et al., (2012) in GelMA

microscale hydrogels at concentrations of 1% and 5%. v/v Xu et al., (2012) reported no significant differences in mechanical properties between controls and MNP hydrogels after 24 hours, suggesting both nanoparticle size and concentration influence the mechanical impact on hydrogel scaffolds (Xu, et al., 2012).

Interestingly Yan et al. (2022), observed that their PAAm magnetic hydrogel increased in stiffness with addition of MNPs when under an external magnetic field, showing a tuneable range of stiffness *via* magnetic actuation which is not something previously considered for this model. Their model relies on magnetic field induced aggregation of MNPs to physically stiffen the hydrogel (Yan, et al., 2021), while our GelMA model exhibited mechanical changes mainly due to network reorganisation during polymerisation. Similarly, Tran et al. (2021), demonstrated that collagen and fibrin hydrogels with MNPs exhibited a reversible increase in stiffness when subjected to an external magnetic field, with the degree of stiffening dependent on both MNP concentration and external magnetic field strength (Tran, et al., 2021) (**Table 4-7**). It is important to note that unlike these studies we did not assess the stiffness of our GelMA hydrogels under an applied field, so potential dynamic stiffening effects through magnetic actuation remain unexplored in our system.

Hydrogel	MNP Composition	MNP Size/ Concentration	Stiffness Range	Reference
GelMA, 7.5% v/v	Dextran coated, Fe_3O_4	197 nm, 0.25 mg/mL	G′: 2-2.5 kPa	Figure 4-3
GelMA, 10% v/v			G′: 2.2-4.6 kPa	
MagGel	Fe_3O_4	15 – 77 nm, 4% w/v	Not defined	(Zhang, et al., 2015)
AM	Fe_3O_4	10 – 50 nm, 13 – 23% w/v	E: 43 – 277 kPa	(Xuan, et al., 2025)
GelMA, 10% v/v	Fe_3O_4	50 nm, 1 -5% w/v	Not defined	(Xu, et al., 2012)
PAAm	Fe_3O_4	20 – 200 nm, 10% w/v	G′: 0.3 – 20 kPa	(Yan, et al., 2021)
Collagen (1-5 mg/mL)	Carboynl iron microparticles	Not defined, 0.1% w/v	G′: 1.5 – 30 kPa	(Tran, et al., 2021)

Table 4-7: Summary of magnetic hydrogel models developed in the literature

Summary of magnetic hydrogel models developed in previous studies including magnetic nanoparticle (MNP) composition, size and concentration in the hydrogel, as well as the reported stiffness range expressed as storage (G′) or Youngs modulus (E), when available.

The structural properties of the hydrogels were examined to determine influence of MNPs. Models with 7.5% w/v GelMA exhibited larger pore diameters and areas compared to 10% w/v GelMA models, supporting enhanced nutrient diffusion and cell infiltration. The addition of MNPs generally decreased pore size in 7.5% w/v hydrogels, likely due to network reorganisation during polymerisation. In contrast, 10% w/v hydrogels showed a slight increase in some pore properties with addition of MNPs, particularly pore thickness, while pore area decreased suggesting different polymer density dynamics (**Figure 4-15**). Porosity increased in the 7.5% w/v GelMA hydrogels with MNPs, facilitating fluid flow and potential cell migration; however, 10% w/v hydrogels already exhibited high porosity, with MNPs causing no significant changes. Interestingly, the addition of MNPs to GelMA hydrogels resulted in reduced pore sizes, which would typically be expected to increase mechanical strength. However, amplitude sweep tests revealed a reduction in stiffness with increasing MNP concentration, particularly at 0.5 mg/mL (**Figure 4-5**). This suggests that, despite the small pores, the presence of MNPs may weaken the hydrogel network under mechanical strain. One possible explanation is the partial aggregation of MNPs within the

matrix, which may interfere with the unform crosslinking or disrupt the network structure. Xu et al., (2012) observed significant aggregation within hydrogel pores *via* SEM, which they associated with reduced pore size. In contrast, SEM imaging of our hydrogel models did not show visible MNP aggregation, suggesting that while some degree of aggregation may occur, it is likely not extensive or structurally dominant in our system.

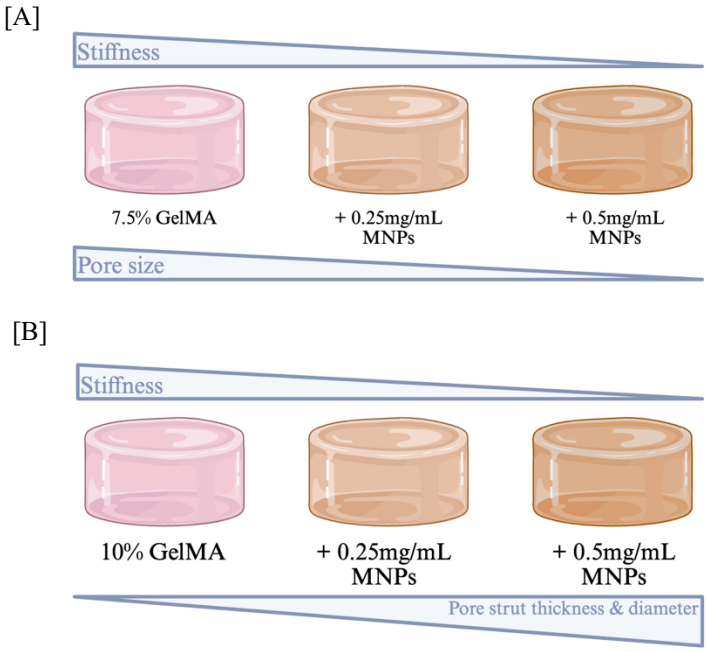

Figure 4-15: Summary of GelMA hydrogel responses to increasing magnetic nanoparticle concentration

In this chapter we developed a tuneable magnetic hydrogel model and observed that [A] with increasing magnetic nanoparticle (MNP) concentration, 7.5% w/v GelMA hydrogels exhibit decrease in stiffness that correlates with decrease in pore size [B] Similarly in 10% w/v GelMA hydrogels, increasing MNP concentration results in reduced stiffness. However, the addition of MNPs increases pore thickness and pore diameter in 10% w/v hydrogels.

Other studies have reported changes in hydrogel structure in response to adding MNPs. Xu et al., (2012) observed aggregation of MNPs within hydrogel pores correlating with increasing nanoparticle concentration and decreasing porosity (Xu, et al., 2012). Yan et al., (2022) reported decreased pore sizes due to MNP chain formation under applied static fields rather than concentration driven network reorganisation. However, their study observed that pore size was inversely related to stiffness (Yan, et al., 2021). Similarly, Haghighattalab et al., (2022) observed incorporating MNPs (20-30 nm) into silk fibroin hydrogels increased both pore size and porosity. Pore size is an important consideration, with porosity ~70% suggested by previous studies for bone tissue engineering (Xiang, et al., 2022). Taken

together, our findings suggest that MNPs can have differential effects on hydrogel microstructure depending on base polymer, MNP/polymer concertation and preparation method, likely reflecting a balance between MNP induced network arrangement and initial matrix density.

The incorporation of MNPs appears to influence the affect the network formation of GelMA hydrogels crosslinked with LAP. Increasing MNP concentrating results in softer hydrogels, and slower gelation; hydrogels with 1 mg/mL MNPs remained partially liquid after standard 5-minute UV exposure. This suggest that MNPs may interfere with the photoinitiated crosslinking of GelMA, possibly by hindering methacryloyl groups or affecting local diffusion thereby modifying the hydrogel network structure. These alternations in network formation are consistent with the observed changes in hydrogel morphology (**Figure 4-15**), such as variations in stiffness, fibre thickness and porosity, highlight MNP incorporation simultaneously influences both the mechanical properties and microstructural organisation of GelMA hydrogels.

While long term retention of the MNPs within the hydrogel network was not directly measured, the characteristic colour of the magnetic hydrogels due to MNP incorporation remained over 28 days, and no obvious changes to overall structure were observed, suggesting likely retention of MNPs. Filippi et al. (2019) reported reduced MNP retention under a SMF, observing MNP migration and accumulation towards the applied magnetic field in their hydrogels, something that was not observed within our model. The preparation method used may influence MNP retention: in this study pre-made hydrogels were blended with MNPs, whereas methods such as grafting MNPs onto polymer chains may enhance retention through chemical bonding (**Figure 1-11**) (Liu, et al., 2020). In addition to retention within the hydrogel, potential interactions between MNPs and cells are relevant for interpretating biological effects. Cellular uptake of multidomain MNPs ~200nm is limited due to their relatively large size and non-uniform shape (Chithrani, et al., 2006; He, et al., 2010). In this study, the average MNPs size was identified as 197 nm with standard deviation of 91 nm (**Supplementary Figure S 2**), meaning that smaller particles within this distribution could potentially be internalised by MSC. Therefore, we cannot exclude the possibility of slow leaching or partial cellular internalisation over a 28 day culture period, and further studies are required to quantify long term nanoparticle retention and uptake. This uncertainty may influence the biological effects observed under MNP conditions, and combined MNP and SMF exposure; if MNPs were partially released or internalised, local

MNP concentrations could vary, potentially modulating cell behaviour and the magnitude of SMF mediated effects.

In this study, initial hydrogel contraction and swelling were evaluated over 48 hours, and no distinct impact of MNPs or cells on these short-term behaviours was observed (**Figure 4-10**). However, long term degradation and remodelling were not directly assessed, and these processes could influence the model over extended culture periods. Biomaterial degradation involves physical, chemical and mechanical changes (Mndlovu, et al., 2024). Hydrogel degradation may alter mechanical properties, porosity and local distribution of MNPs, which in turn could modify the magnitude and spatial pattern of magnetic stimulation experienced by embedded cells (Liu, et al., 2020; Mndlovu, et al., 2024). Since the addition of MNPs was shown to influence some hydrogel properties (**Figure 4-15**), including porosity, their presence could potentially affect degradation kinetics in longer term cultures, modulating both biochemical and magnetic field exposure cues. In addition, application of magnetic fields has been shown to influence the structure and degradation rate of magnetic hydrogels (Liu, et al., 2020). Future studies could explore this degradation and these interactions to better understand how hydrogel remodelling and embedded MNPs collectively impact cellular responses.

In summary, MNPs were successfully incorporated into GelMA hydrogels, without evidence of significant aggregation, preserving both the structural integrity and elastic properties of the hydrogels. Visual analysis using SEM and micro-CT confirmed that MNP addition influenced hydrogel microstructure, particularly in lower GelMA formulations. However, even at higher MNP concentrations, the hydrogels maintained their elastic properties with no evidence of collapse or structural failure.

Soft elastic hydrogels are advantageous in tissue engineering especially for mimicking early-stage bone ECM and supporting mechanosensitive cell responses. The inclusion of MNPs offers the potential for non-invasive mechanical stimulation and dynamic modulation of the matrix environment, features relevant for promoting osteogenesis. Both 7.5% and 10% w/v GelMA hydrogels, with and without MNPs (0.25 mg/mL – 0.5 mg/mL) demonstrated tuneable systems, biocompatible properties and retained sufficient porosity for nutrient diffusion and potential cell infiltration. These findings support the suitability of MNP-GelMA hydrogels as versatile platforms for bone tissue engineering, with the added benefit of magnetic responsiveness for further applications.

4.7.3 Viable Mesenchymal Stromal Cells Integrated in the Magnetic GelMA Model

The integration and viability of MSCs within the developed magnetic GelMA model was evaluated to determine their suitability for bone tissue engineering. To support MSC encapsulation and function, hydrogels must meet several biological and physical criteria.

4.7.3.1 Mechanical Cues Support Cell Viability

As described in previous sections, both 7.5% and 10% w/v hydrogels demonstrated soft, elastic mechanical profiles within the optimal range for soft tissue engineering. Importantly mechanical stability was retained with the incorporation of MNPs. Rheological analysis of 7.5% w/v hydrogels demonstrated stable or increasing G′ values over 72 hours, consistent with time dependent matrix tightening that parallels hydrogel contraction. These mechanical features closely mimic the early ECM environment of developing bone (Yang, et al., 2025) and have been shown to support MSC behaviour and differentiation in other systems**.**

4.7.3.2 Porosity Enables Nutrient Diffusion and Cell Motility

Porosity and wettability are crucial for nutrient exchange, waste removal and cell motility. SEM and micro-CT imaging confirmed both 7.5% and 10% w/v GelMA hydrogels exhibited highly porous structures, with 7.5% w/v models having larger pore diameters and area. The inclusion of MNPs slightly altered pore morphology but did not compromise porosity; in fact, porosity increased in 7.5% w/v models with MNPs potentially enhancing fluid flow and cell migration. WCA measurements confirmed that all hydrogel formulations were hydrophilic. While the addition of MNPs did not significantly alter wettability in 7.5% w/v hydrogels, 10% w/v hydrogels with higher concentrations of MNPs showed enhanced hydrophilicity, which may further promote MSC infiltration and viability. These properties indicate that the developed hydrogels provide a permissive environment for nutrient diffusion and cellular movement.

Manjua et al., (2019) observed surface wettability of magnetic PVA hydrogels could be reversibly modified by applying an external field. Specifically, the application of a magnetic field decreased surface contact angle, indicating increased hydrophilicity. This magnetic stimulation also reduced protein sorption and enhanced protein release at moderate field strengths (0.4 T). These findings indicate the potential of magnetic fields to control diffusion and protein interactions in biomedical applications. (Manjua, et al., 2019)

The imaging techniques utilised in this study required freeze-dried of hydrogels prior to imaging, a process that can alter their natural structure. The removal of water leads to shrinkage, pore collapse or distortion of the hydrogel network due to crystal formation, meaning the observed morphology may differ significantly from the hydrated state (Aigoin, et al., 2025; Franco, et al., 2024). While these changes complicate interpretation, freeze drying still allows for high resolution imaging of internal features (Aigoin, et al., 2025), making it useful for comparisons such as influence of additional components like MNPs on hydrogel structure. Future work should consider utilising techniques, such as laser scanning confocal microscopy, which can visualise hydrogels in natural hydrated state (Podhorská, et al., 2020). When electron microscopy imaging is necessary, alternative preparation methods such as epoxy resin embedding can better preserve the hydrated structure however although these methods are more time consuming than standard freeze-drying methods (Aigoin, et al., 2025).

4.7.3.2 Biological Cues Promote Cell Attachment and Integration

The biological component of GelMA, derived from gelatin, offers cell-adhesive motifs that support MSC adhesion and spreading. Light microscopy of live/dead stained MSCs over 7 days revealed high viability and elongated morphology across all conditions, confirming active cell matrix interaction.

MSC viability was maintained about 95% for MSCs in 7.5% w/v hydrogels, with and without MNPs. The maintenance of viability across these conditions demonstrates that the dextran coated iron oxide MNPs are non-toxic to encapsulated MSCs at concentrations up to 0.25 mg/mL. In our study, long term culture of MSCs in GelMA showed a decline in viability over 28 days to 84%. However, viability above 80% is widely accepted in as a minimum for human MSC expansion an *in vitro* culture (Guadix, et al., 2019).

The literature suggests that cells can tolerate MNP concentrations up a certain limit, which depends on particle aggregation. Li et al., (2019) observed that labelling MSCs with 50 µg/mL uncoated iron oxide MNPs did not impact viability, but concentrations above 50 µg/mL (up to 200 µg/mL) did impact viability due to MNP aggregation. In contrast, polydopamine capped MNPs showed better viability in higher concentrations, by limiting aggregation (Li, et al., 2019). Similarly, Hong et al. (2011), observed concentration to be the main factor impacting cell viability, with iron oxide MNP concentrations below 200 ppm

showing no cytotoxic effect on murine fibroblasts after 24 hours, despite coating or MNP size (10 nm-150 nm). They recommended a concentration of iron oxide MNPs does not exceed 500 ppm to maintain cell viability (Hong, et al., 2011). This correlates to the study by Lewis et al., (2014), who observed varying MNP sizes (100-500 nm) did not affect fibroblast viability over 24 hours when cultured within in collagen hydrogels. In development of a printable GelMA model, Yang et al. (2023) observed that various concentrations of GelMA (3-7.5% w/v) containing iron oxide MNPs all supported C2C12 viability above 90%. They observed good cell adhesion, alignment and elongated morphology, indicating that magnetic GelMA hydrogels are suitable for bioengineering constructs (Yang, et al., 2024).

MSC spheroids were also encapsulated into 7.5% w/v GelMA models with and without 0.25 mg/mL MNPs. Both conditions maintained spheroid shape and general viability over 10 days, with mild necrotic core development which was more pronounced in MNP hydrogels, potentially due to subtle changes in nutrient diffusion. However, spheroids largely maintained structural integrity and overall viability, demonstrating the GelMA model's capacity to support 3D MSC spheroids. These findings are consistent with those reported by Lewis et al., (2014) who also observed high MSC spheroid viability and structural integrity with magnetic levitation methods, demonstrating the trend of sustained spheroid health in MNP based 3D systems.

4.7.4 Conclusion: MSCs Successfully Integrate into the Magnetic GelMA Hydrogel Model

Taken together, the results confirm that our magnetic GelMA hydrogel models (**Figure 4-16**) provide a soft, porous and biologically compatible scaffold for MSC culture. The mechanical integrity of the hydrogels supports cell mechanotransduction, while the pore structure and hydrophilic surface promote nutrient exchange and migration. Importantly, gelatin based GelMA provides natural adhesion sites, enabling high cell viability and elongated morphology indictive of strong cell-material interactions. The incorporation of MNPs did not impair cell viability and offers added potential for magnetic stimulation in future applications.

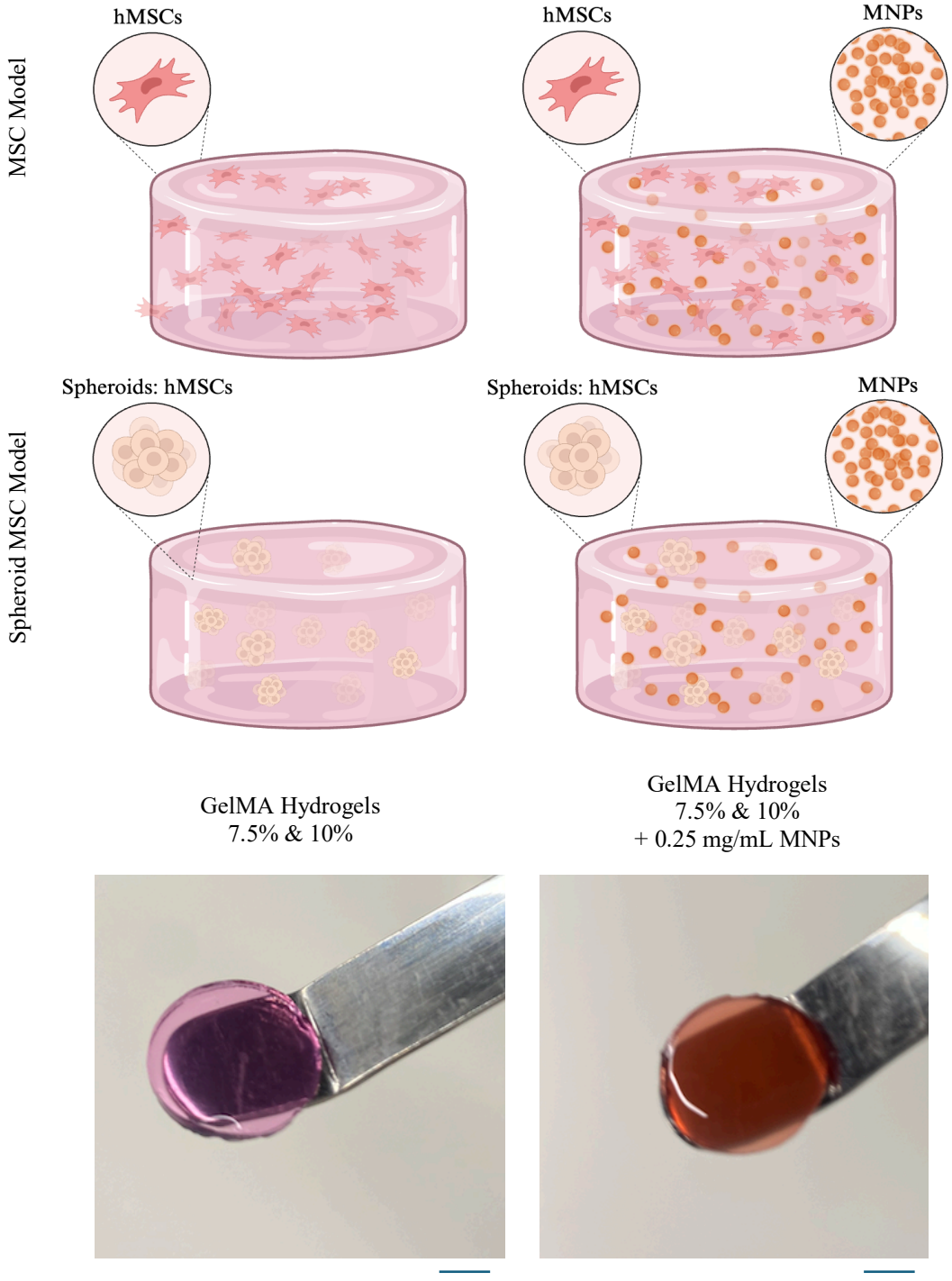

Figure 4-16: Optimised Magnetic GelMA Hydrogel Model

In this chapter we developed a tuneable magnetic hydrogel model (7.5% and 10% w/v, ± 0.25 mg/mL MNPs). This schematic represents of the final models taken forward for magnetic field actuation studies; including 7.5% and 10% w/v GelMA models, with and without 0.25 mg/mL MNPs. The hydrogels incorporated either dispersed MSCs or spheroid MSC models (not to scale). The lower panel is visual representation of hydrogel colour change with addition of MNPs in GelMA post polymerisation (scale bar shows 5 mm). Created with Biorender.com

Chapter 5: The Effect of a Static Magnetic Field on Mesenchymal Stromal Cells in the 3D Magnetic GelMA Model

5.1 Introduction

Bone tissue engineering aims to replace, or regenerate lost and damaged bone tissue, and restore function, as an alternative to traditional bone grafts. A key component of bone tissue engineering are the scaffolds used to maintain a MSC population (Perez, et al., 2018). Typically, these include natural or synthetic derived scaffolds, such as hydrogels to provide both structural and biological support for the embedded cells (Liu, et al., 2020; Markey, et al., 2016). Hydrogels offer scaffolds with high water content, excellent biocompatibility and tuneable properties, making them ideal environments for cell growth and differentiation (Markey, et al., 2016). Gelatin methacryloyl is a natural derived hydrogel that can be crosslinked under UV exposure, forming stable 3D scaffolds (Zhou, et al., 2023).

Prior to crosslinking, MNPs can be incorporated into hydrogels, such as GelMA hydrogels, to create magnetically responsible scaffolds (Yuan, et al., 2018; Zhou, et al., 2023). Incorporation of MNPs allows for scaffolds with potential to respond to an external SMF (Fathi-Achachelouei, et al., 2019). SMFs have a consistent strength and direction (Castro, et al., 2020), providing uniform exposure that has been observed to impact MSC behaviour, by promoting cell proliferation, modulating gene expression and influencing differentiation (osteogenesis) processes (Paun, et al., 2018; Yuan, et al., 2018).

MSCs are an important cell source in bone tissue engineering due to their potential for osteogenic differentiation and responsiveness to biophysical cues (Drake, et al., 2024; Mackie, et al., 2008; Nowlan, et al., 2010). As demonstrated in chapter 3, exposure to a SMFs can promote osteogenic commitment in MSCs. However, cell behaviour in traditional 2D culture does not truly represent the complex dynamics observed in 3D systems, particularly with cell aggregates such as spheroids. Chapter 4 focused on the development and characterisation of a magnetic 3D GelMA hydrogel, embedding MNPs (fluidMAG-Dx, Chemicell) to generate a soft elastic hydrogel model, capable of maintaining a viable MSC population up to 28 days in culture. The magnetic hydrogel platform provides a physiologically relevant 3D bone marrow model to investigate MSC behaviour under magnetic stimulation.

5.1.1 Chapter Aims

The primary aim of this chapter was to combine the knowledge gained from chapters 3 and 4, to investigate whether magnetic stimulation can promote osteogenesis in a 3D bone marrow model using the magnetic GelMA hydrogel platform. To address this, the chapter focused on the following objectives:

- Assess early mechanical changes in 7.5% w/v GelMA hydrogels incorporating MNPs with either dispersed MSCs or MSC spheroids following exposure to a constant SMF to determine short term effects of magnetic stimulation on hydrogel stiffness and viscoelasticity.

- Investigate osteogenic commitment of MSCs within GelMA hydrogels under an intermittent SMF (1 hour day for 28 days)
    - Analysing expression of early and late osteogenic markers
    - Evaluating stem cell maintenance through stemness marker expression
    - Assessing calcium mineralisation within hydrogels *via* Alizarin Red S staining

- Characterise long term mechanical remodelling of the magnetic hydrogels by MSCs under an intermittent SMF (1 hour day for 28 days) through analysis of hydrogel rheological properties

5.2 Methods

The following experiments were completed with the material and methods outlined in Chapter 2. Hydrogels were fabricated as outlined in 2.5.2 (Magnetic Hydrogel Fabrication).

The subsequent sections using the following methods:

- Stability of Magnetic GelMA Hydrogel Model Under Static Magnetic Fields: 2.6.1 Rheology
- Osteogenic Commitment of Mesenchymal Stromal Cells in the Magnetic Hydrogel Model: 2.5.3 Magnetic Hydrogel: Digestion and Cell Retrieval, 2.2.5 RNA Extraction and Isolation, 2.2.6 Reverse Transcription, 2.2.7 Real-Time Quantitative Polymerase Chain Reaction, 2.6.8.1 Alizarin Red S Staining

- Long Term Structural Stability of GelMA Hydrogels Under Static Magnetic Field Exposure: 2.6.1 Rheology

5.2.1 Osteogenic Media Control Differentiation Protocol

As a positive control for osteogenic gene expression, MSCs cultured in monolayer were treated with Osteogenic Media (OGM) (**Table 2-2**) alongside 28 day differentiation of MSCs conducted within GelMA hydrogels. Cells were maintained in OGM for either 14 or 28 days and at endpoints cells were lysed and RNA processed for gene analysis following protocols 2.2.5 RNA Extraction and Isolation, 2.2.6 Reverse Transcription and 2.2.7 Real-Time Quantitative Polymerase Chain Reaction.

5.3 Stability of Magnetic GelMA Hydrogel Model Under Static Magnetic Fields

5.3.1 Rheological Analysis of GelMA Stability Under SMF

Hydrogel mechanical properties play a critical role in regulating cell behaviour; whilst cells are an active participant in shaping and maintaining their environment (Chaudhuri, et al., 2015; Horton, et al., 2020). This dynamic interaction leads to hydrogel remodelling and/or degradation over time, altering the physical properties of the hydrogel. In addition, external magnetic stimulation upon embedded cells has the potential to further influence hydrogel properties through altered cell interactions. To investigate these effects, the magnetic GelMA hydrogel model - 7.5% w/v GelMA, with dispersed MSCs, cell spheroids and MNPs - was exposed to a SMF for 72 hours and rheological measurements were captured and compared to control to examine effects of a constant SMF **(Figure 5-1)**. Based on similar methods in the literature, application of a constant SMF may enhance the mechanical properties of hydrogels containing MNPs (Yan, et al., 2022).

The following conditions were used (as annotated on **Figure 5-1,** +SMF denotes SMF applied):

- 7.5% w/v GelMA only (7.5% GelMA)
- 7.5% w/v GelMA + 0.25 mg/mL MNPs (+ MNPs)
- 7.5% w/v GelMA + dispersed cells (+ MSCs)
- 7.5% w/v GelMA + spheroids (+ spheroids)
- 7.5% w/v GelMA + 0.25 mg/mL MNPs + dispersed cells (+MNPs + MSCs)

- 7.5% w/v GelMA + 0.25 mg/mL MNPs + spheroids (+MNPs + spheroids)

When considering the complete magnetic hydrogel model, incorporating both MSCs and MNPs, the mechanical properties decrease on incorporation of MSCs (dispersed cells or spheroids), but increase when MSCs are combined with MNPs, More specifically, the control 7.5% w/v hydrogel G′ was ~1923 Pa, within a similar range to previously tested samples (**Chapter 4, Figure 4-1, A**), with little change following incorporation of MNPs (~2033 Pa). However, the addition of dispersed MSCs significantly reduced G′ to ~1332 Pa, while the combination of both dispersed MSCs and MNPs reversed this and significantly increased G′ to ~2938 Pa in comparison to control hydrogels. This trend was mirrored when MSC spheroids were incorporated into the model, showing a similar reduction in G′ to ~1587 Pa with a similar increase observed with the combination of spheroids and MNPs to 2274 Pa **(Figure 5-1)**.

The application of a SMF to the various hydrogel models followed a similar trend, but with a greater significant difference to control cells, and being significantly different to their non-stimulated counterparts. Specifically, SMF did not change G′ in the standard 7.5% w/v hydrogels, with G′ observed at ~1652 Pa and ~1940 Pa with addition of MNPs. As without stimulation, hydrogels with dispersed MSCs showed a significant reduction in G′ under a constant SMF, down to almost half that of control values (~862 Pa), as without a SMF. Again, this was reversed and G′ was significantly increased to ~4180 Pa. Conversely, this time MSC spheroids caused a large increase in G′ to ~4175 Pa, in response to a SMF, which was maintained to some degree once MNPs were added to the model (~3000 Pa). **(Figure 5-1)**.

Overall, G″ showed distinct responses depending on the presence of MSCs, MNPs and the application of a SMF, mirroring some of the trends observed in G″. In control hydrogels, the addition of MNPs significantly increased G″ from ~168 Pa to 275 Pa. Similar to G′, the inclusions of dispersed MSCs caused a reduction in G″ to around 49 Pa, however the combination of MSCs and MNPs increased G″ to ~149 Pa. Incorporating MSC spheroids reduced G′ to ~74 Pa, while combining spheroids and MNPs led to an increase to 190 Pa (**Figure 5-1**).

When a constant SMF was applied, G″ significantly deceased to ~82 Pa in the 7.5% w/v GelMA hydrogels but increased with the addition of MNPs to 146 Pa. Hydrogels with dispersed MSCs showed no significant change in G″ under SMF, remaining ~29 Pa, through

the combination of dispersed MSCs and MNPs caused a notable increase to ~175 Pa. For hydrogels containing spheroids, G″ significantly increased to 192 Pa after SMF exposure, while the combination of spheroids and MNPs showed little change from control levels (~201 Pa) (**Figure 5-1**).

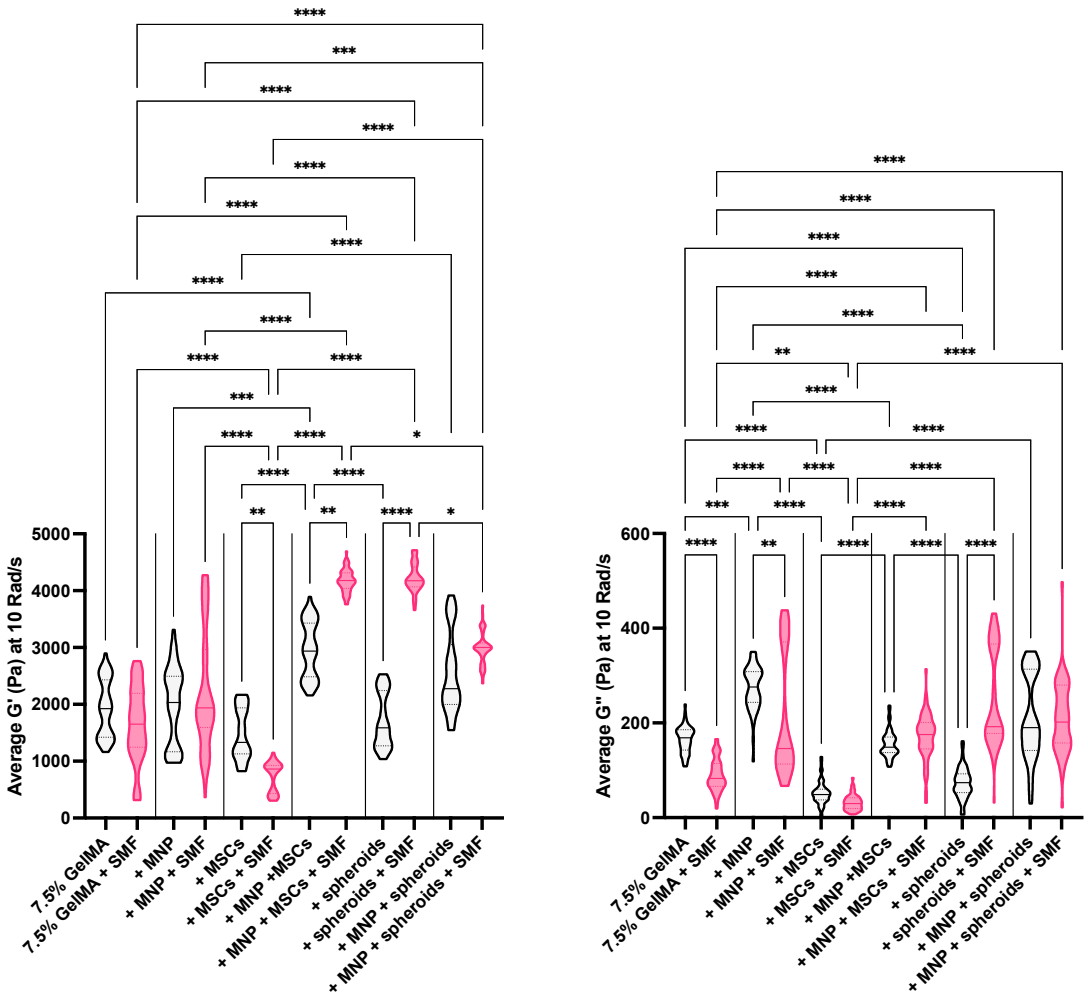

Figure 5-1: Cell incorporation method and application of magnetic field influence hydrogel mechanical properties

GelMA hydrogels were subject to constant static magnetic field (SMF) actuation for 72 hours. Storage modulus (G′) and loss modulus (G″) were measured *via* strain sweep tests (0.01-0.1% strain, 1 Hz, 10 Rad/s) for GelMA hydrogels under SMF and compared to control. Measurements were obtained using an Anton Paar rheometer. Truncated violin plots show distribution of G′ and G″ values with median (solid line) and interquartile range (dashed lines) (n=3). A Kruskal-Wallis test and post hoc Dunn's multiple comparison tests show significance between conditions

Tanδ values, were calculated from median G′ and G″ in hydrogels under a SMF (**Table 5-1**). Tanδ values for GelMA conditions are generally low ~0.1 or below, indicating elastic behaviour is maintained in hydrogels under a SMF in comparison to control. A slight

increase is observed in 7.5% w/v + MNP hydrogels in both control (0.136) and under SMF (0.075) suggesting a slight increase in viscous behaviour with only addition of MNPs. Overall application of a constant SMF does not significantly alter the elastic behaviour of the hydrogels with addition of cells and spheroids.

Overall, the SMF exposure had minimal effect on acellular hydrogels, but did impact the mechanical properties of GelMA hydrogels when they contained dispersed MSCs or MSC spheroids. Considerably stronger hydrogels were derived when the entire model – MSCs and MNPs – were challenged with a SMF, here the hydrogels were on occasion over twice as mechanically strong as control hydrogels without cells or particles. Tanδ values remained low across all conditions indicating that the hydrogels retained elastic behaviour regardless of MNP or cell content. These results suggest that the synergistic effect of MNPs and SMF is pronounced in hydrogels containing MSC.

Condition	**Control**	**Under Constant SMF**
7.5% w/v GelMA	0.088	0.050
7.5% w/v GelMA + MNP	0.136	0.075
7.5% w/v GelMA + MSC	0.037	0.034
7.5% w/v GelMA + MNP + MSC	0.051	0.042
7.5% w/v GelMA + spheroid	0.047	0.046
7.5% w/v GelMA + MNP + spheroid	0.084	0.067

Table 5-1: Tanδ values of GelMA hydrogels after exposure to a constant static magnetic field

Tanδ (=G″/G′) values of 7.5% w/v GelMA hydrogels with 0.25 mg/mL magnetic nanoparticles (MNPs) and/or mesenchymal stromal cells (MSCs) subject to constant static magnetic field (SMF) actuation for 72 hours. Tanδ near 0 indicate the material shows more elastic behaviour, while close to 1 indicates viscous behaviour.

5.3.2 Laser Doppler Vibrometry for Displacement Measurement in GelMA Magnetic Model

Laser doppler vibrometry (LDV) is an established, sensitive and accurate technique to measure the displacement (motion) of samples under applied stimuli (Kranemann, et al., 20). In collaboration with Dr Jonathan Williams, at the University of Strathclyde, laser vibrometry was employed to attempt to determine if hydrogels containing MNPs exhibit any

measurable displacement under application of a constant SMF for the duration of the measurements, which would support a physical response to external magnetic stimulation.

The LDV readouts are represented as an amplitude (nm) vs frequency graph, where peaks indicate the vibrational characteristics of the material being measured. Control hydrogels exhibited a consistent pattern in their amplitude response, characterised with an initial peak at approximately 70 nm at low frequencies, followed by a noticeable peak to ~400 nm at 0.75 Hz. Under exposure to a constant SMF, no significant changes were observed in amplitude when comparison to control hydrogels **(Figure 5-2)**. Therefore, the MNPs did not induce detectable displacement within the hydrogel under the magnetic field. While this does not necessarily indicate the absence of activity, it is suggestive that laser vibrometry may not be sufficiently appropriate to detect the effects of external stimulation within the hydrogels.

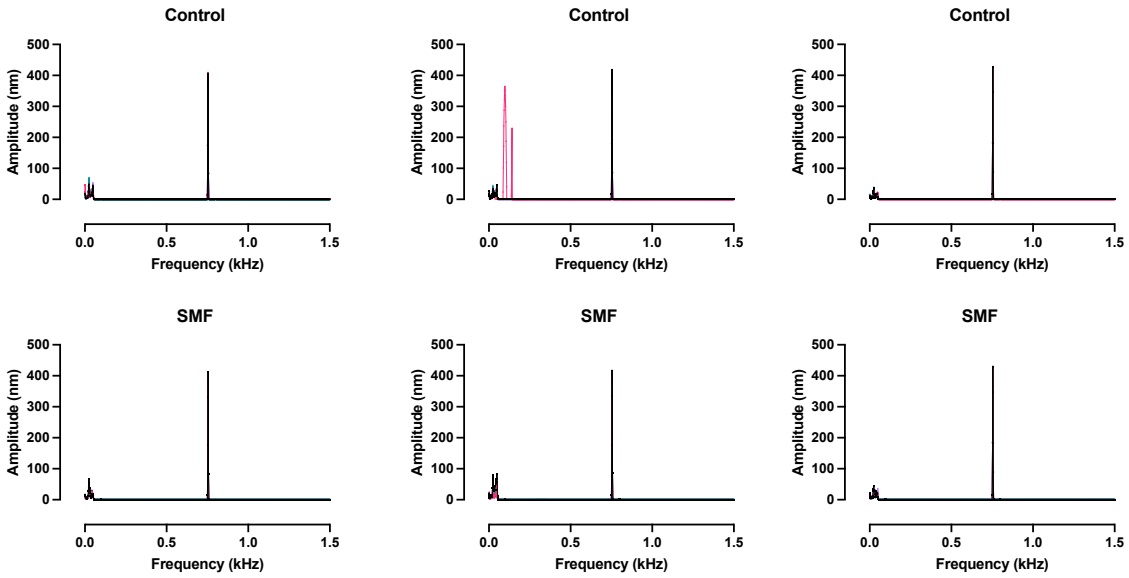

Figure 5-2: Laser doppler vibrometry shows no detectable mechanical movement of hydrogels under a static magnetic field

Analysis of magnetic GelMA hydrogels under the active application of a static magnetic field (SMF) for the duration of measurements. Both data sets represent 7.5% w/v GelMA hydrogels with embedded 0.25 mg/mL magnetic nanoparticles. Hydrogel displacement was measured, amplitude (nm), in response in response to increasing frequency (Hz). Measurements captured Dr Jonathan Williams, University of Strathclyde.

5.4. Osteogenic Commitment of Mesenchymal Stromal Cells in the Magnetic GelMA Hydrogel Model

5.4.1 Gene Expression of Osteogenic Markers and Stemness Markers

This section of work was designed to evaluate whether the optimised magnetic hydrogel platform described in Chapter 4 can promote osteogenesis within a 3D hydrogel environment as a strategy for enhancing osteogenic differentiation. As demonstrated in Chapter 3, osteogenic markers ALP and RUNX2 indicate early osteogenic commitment to pre-osteoblasts, while addition of markers OPN and OCN indicate later commitment to osteoblasts (**Figure 3-7, A**) (Liu, et al., 2023). Stem cell markers, ALCAM and Nestin provide insight into maintenance and self-renewal of the stem cell population (Brinkhof, et al., 2020; Xie, et al., 2015). The expression of these markers was examined in both dispersed MSCs and MSC spheroids within magnetic 7.5% and 10% w/v hydrogels to investigate MSC differentiation in response to magnetic stimulation. Based on the data generated in Chapter 3, the intermittent SMF was selected as the optimal field stimulation to be adopted in this study and was expected to induce an upregulation in osteogenic gene expression on embedded cells over 28 days. Cells were recovered from hydrogels at days 14 and 28 after undergoing exposure to an intermittent SMF, with or without incorporated MNPs. All conditions were normalised to control hydrogels without MNPs and no SMF exposure. Osteogenic media was used as a positive promoter of osteogenesis.

In 7.5% w/v hydrogels with dispersed MSCs, the osteogenic media has indicated a downwards trend for all genes analysed, which was unexpected. The incorporation of MNPs alone does not alter gene expression, apart from a trend to increase RUNX2 at day 28. The use of a SMF alone does appear to partially promote ALP and RUNX2 at early time points (day 14) but has no effect on other genes. Finally, the combined magnetic model – with MNPs and a SMF – demonstrated a small increase in ALP and RUNX at both time points, with potential increase in Osteocalcin and Osteopontin at the later day 28, supporting both early and later osteogenic commitment respectively **(Figure 5-3).**

Conversely, the 7.5% w/v hydrogels with MSC spheroids, generally there were no increases in osteogenic gene expression levels at either time point, with values decreasing compared to control hydrogels. The one exception was Osteocalcin (day 14), which was upregulated in spheroids within magnetic hydrogels exposed to a SMF. The data suggests that an intermittent SMF does not promote osteogenesis in MSC spheroids within a 3D hydrogel.

With regards to a self-renewal phenotype, both ALCAM and Nestin were either similar to control or decreased across all samples at both time points **(Figure 5-4).**

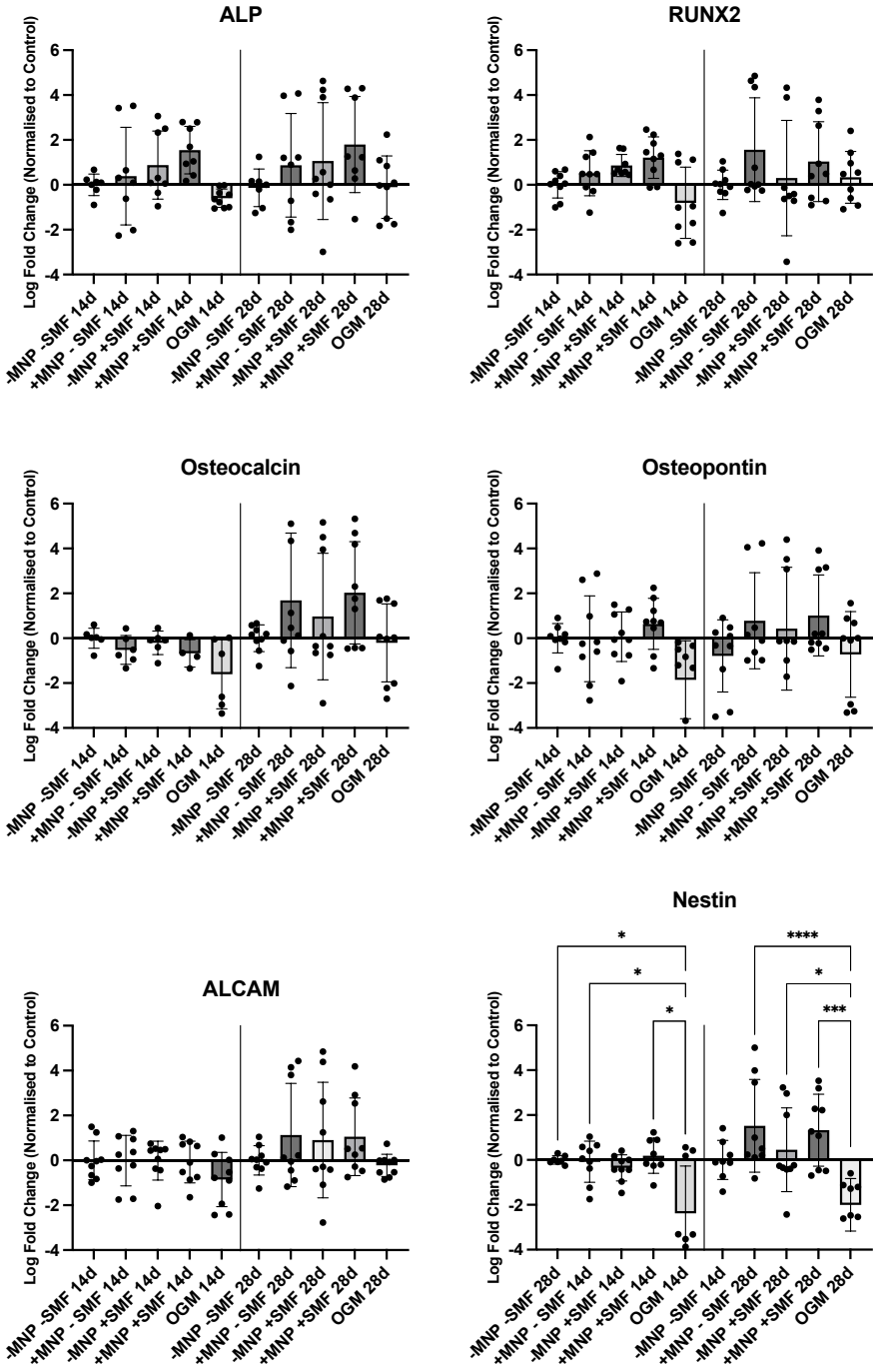

Figure 5-3: Combined magnetic nanoparticle and intermittent static magnetic field exposure modestly promotes osteogenic gene expression in mesenchymal stromal cells in 7.5% w/v GelMA hydrogels

Mesenchymal stromal cell (MSC) commitment to osteogenic lineages, and stem cell maintenance in magnetic GelMA hydrogels was investigated over 28 days under intermittent static magnetic field (SMF) exposure. MSCs were embedded in 7.5% w/v GelMA hydrogels with or without magnetic nanoparticles (MNPs) and exposure to a SMF. Gene expression under magnetic fields over 28 days. Log fold change

was normalised to control. Bars represent mean, error bars represent SEM. A one-way ANOVA and post hoc Tukey test was performed to identify significance between conditions. Data represents 3 biological replicates, each with 3 technical replicates (n=3)

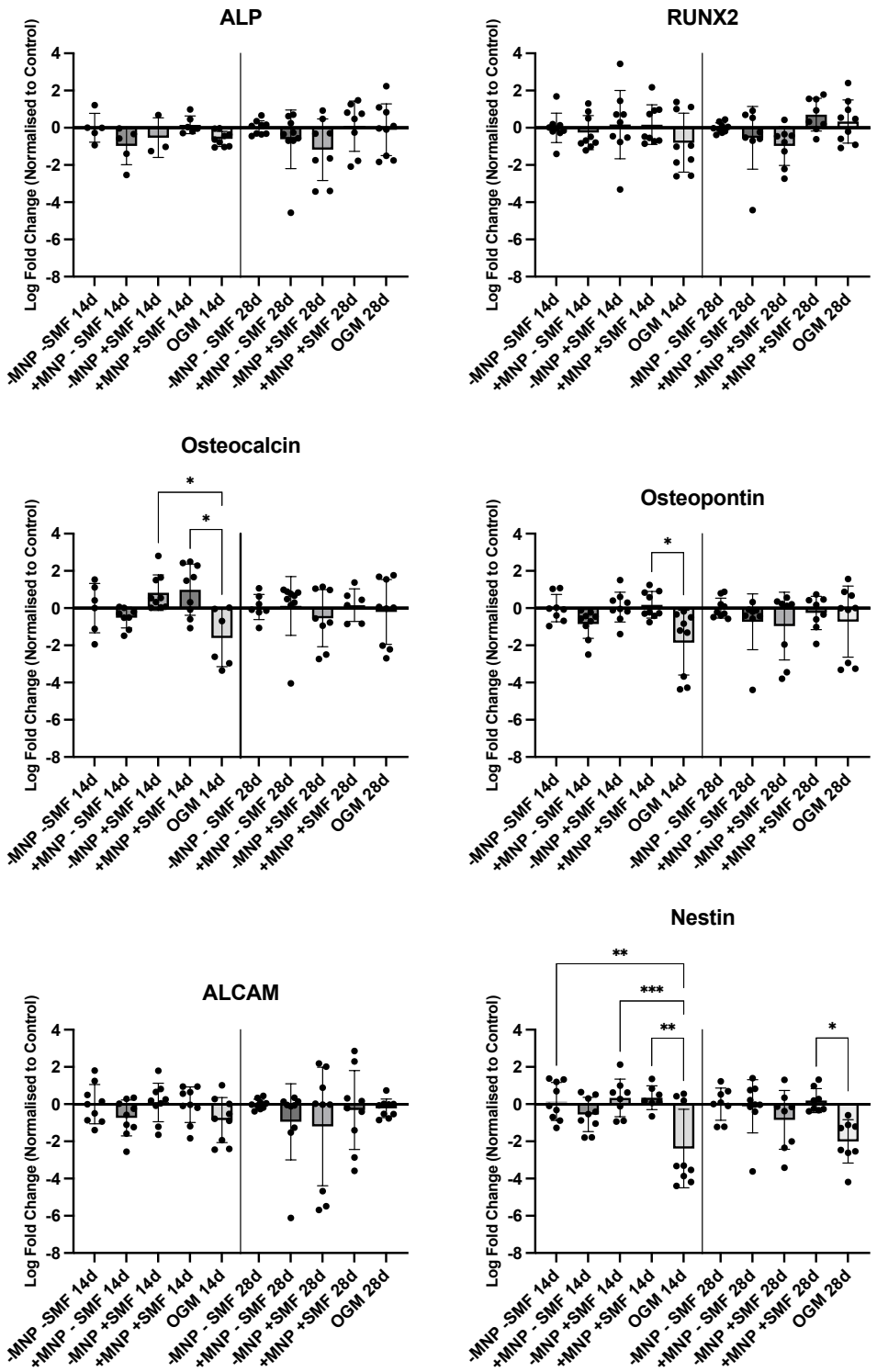

Figure 5-4: Mesenchymal stromal cell spheroids show no osteogenic response to intermittent static magnetic fields in 7.5% w/v GelMA hydrogels

Mesenchymal stromal cell (MSC) spheroid commitment to osteogenic lineages, and stem cell maintenance in magnetic GelMA hydrogels was investigated over 28 days under intermittent static magnetic field (SMF) exposure. MSC spheroids were embedded in 7.5% w/v GelMA hydrogels with or without magnetic nanoparticles (MNPs) and exposure to a SMF. Gene expression under magnetic fields over 28 days. Log fold change was normalised to control. Bars represent mean, error bars represent SEM.

A one-way ANOVA and post hoc Tukey test was performed to identify significance between conditions. Data represents 3 biological replicates, each with 3 technical replicates (n=3)

The same study was carried out in 10% w/v GelMA hydrogels. As with the 7.5% w/v study, again, the osteogenic media seemed to perform worse than the control hydrogels, with down regulation of all osteogenic genes over both time points. However, the incorporation of MNPs or the application of a SMF caused an increase in all osteogenic genes, particularly at the later day 28 timepoint. Combining both the MNPs and a SMF caused a similar increase. There was no change in ALCAM, but an increase in Nestin was observed for all three hydrogel conditions at day 28, suggesting that there was a population of self-renewing MSCs **(Figure 5-5)**.

Again, the study was conducted in 10% w/v hydrogels with MSC spheroids. Osteogenic media generally downregulated ALP, RUNX2, Osteopontin and Osteocalcin at both time points. Incorporation of MNPs and/or application of a SMF showed modest or control level osteogenic expression at day 14. By day 28, most osteogenic markers increased in hydrogels containing MNPs or exposed to SMF. Similarly, combining both MNPs and SMF resulted in tentative upregulation of all osteogenic genes. Stemness markers ALCAM and Nestin were mostly unchanged or slightly reduced, except for a mild increase in ALCAM at day 14 and Nestin under SMF at day 28 **(Figure 5-6)**.

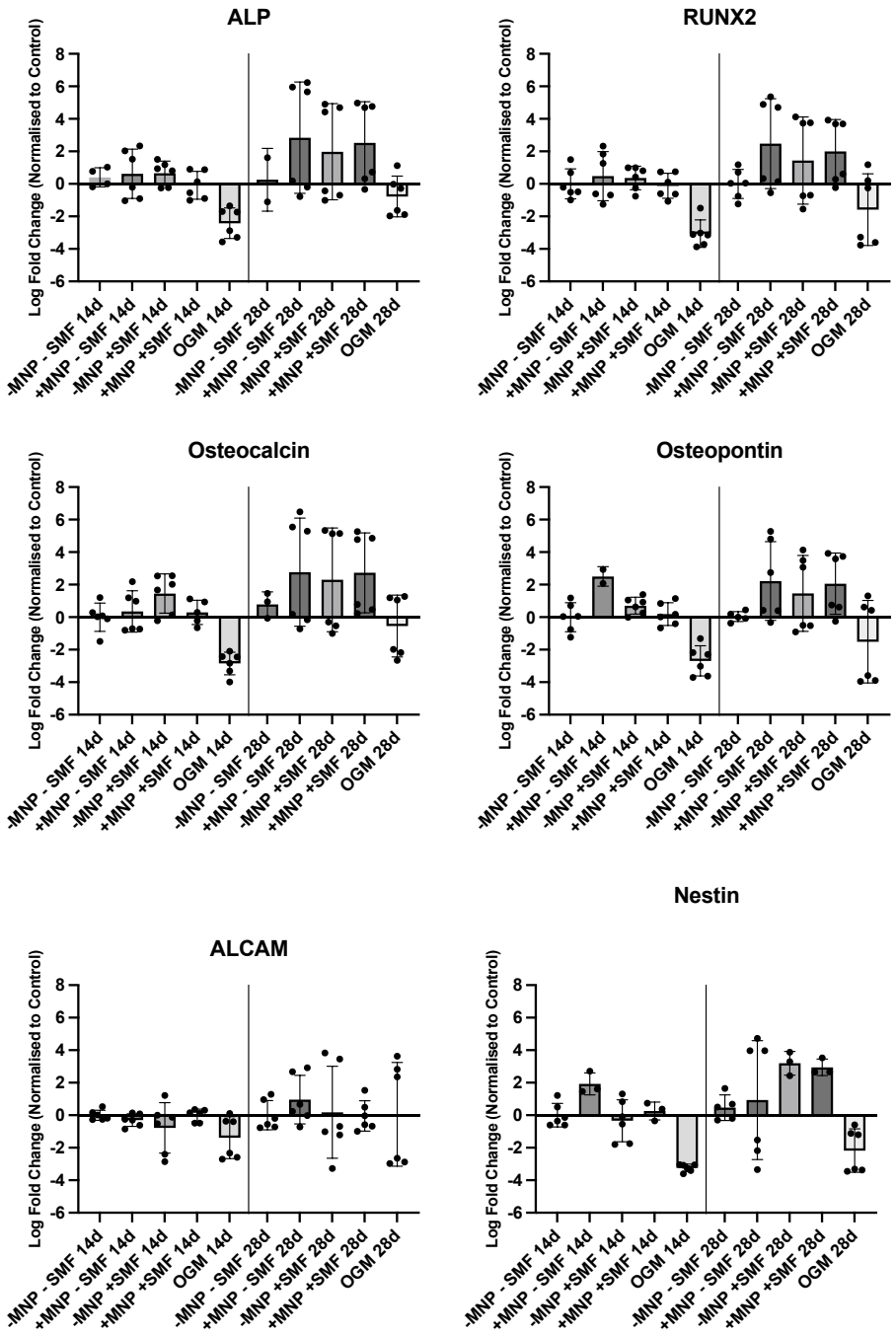

Figure 5-5: Combined magnetic nanoparticle and intermittent static magnetic field exposure modestly promotes osteogenic gene expression in mesenchymal stromal cells in 10% w/v GelMA hydrogels

Mesenchymal stromal cell (MSC) commitment to osteogenic lineages, and stem cell maintenance in magnetic GelMA hydrogels was investigated over 28 days under intermittent static magnetic field (SMF) exposure. MSCs were embedded in 10% w/v GelMA hydrogels with or without magnetic nanoparticles (MNPs) and exposure to a SMF. Gene expression under magnetic fields over 28 days. Log fold change was normalised to control. Bars represent mean, error bars represent SEM. Due to limited replicates, statistical analysis was not completed. Data represents 2 biological replicates, each with 3 technical replicates (n=2)

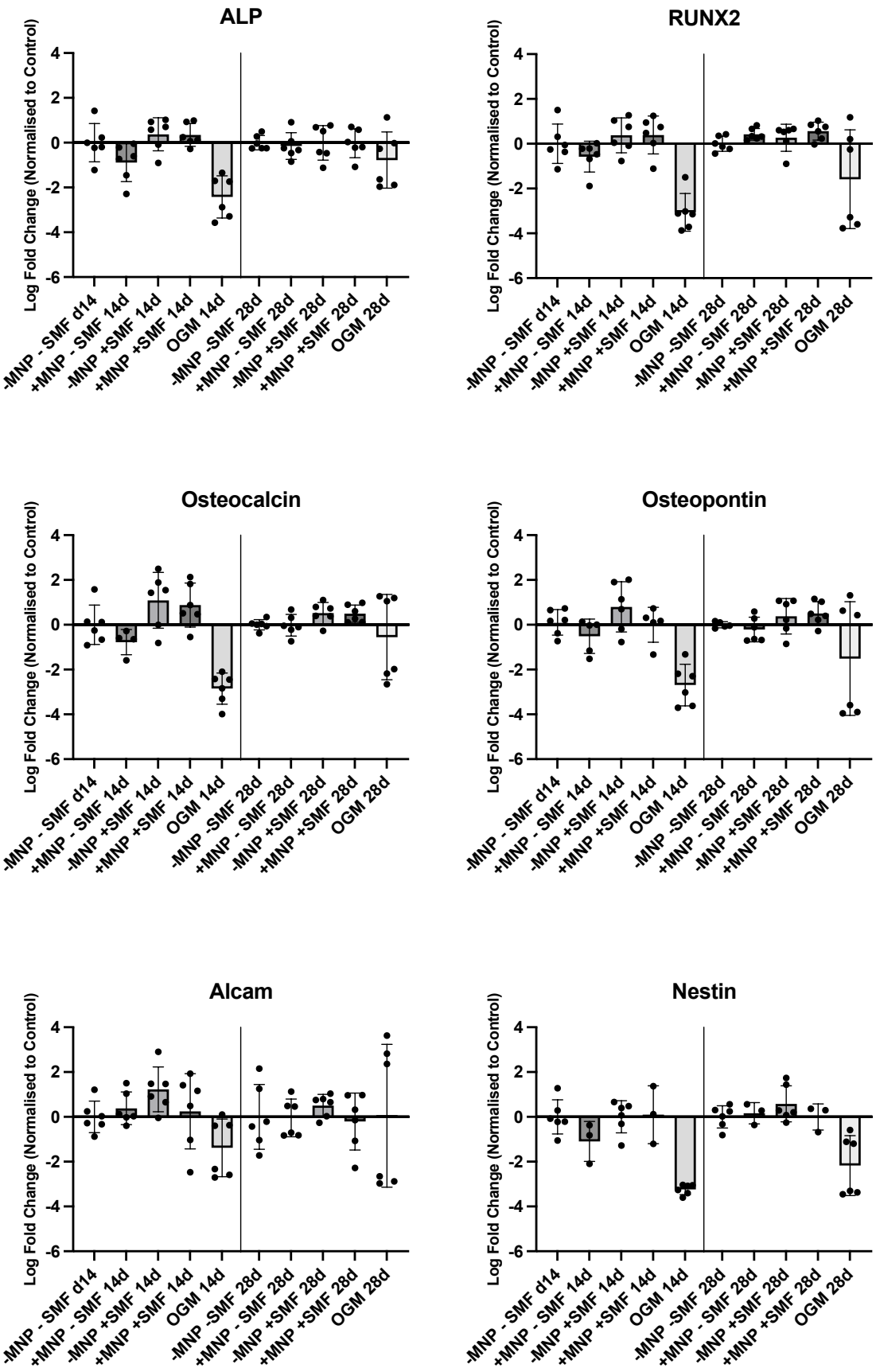

Figure 5-6: Mesenchymal stromal cell spheroids show no osteogenic response to intermittent static magnetic fields in 10% w/v GelMA hydrogels

Mesenchymal stromal cell (MSC) spheroid commitment to osteogenic lineages, and stem cell maintenance in magnetic GelMA hydrogels was investigated over 28 days under intermittent static magnetic field (SMF) exposure. MSC spheroids were embedded in 10% w/v GelMA hydrogels with or without magnetic nanoparticles (MNPs) and exposure to a SMF. Gene expression under magnetic fields over 28 days. Log fold change was normalised to control. Bars represent mean, error bars represent SEM. Due to limited replicates, statistical analysis was not completed. Data represents 2 biological replicates, each with 3 technical replicates (n=2)

Overall gene expression levels can be presented as a heatmap, which better captures the changes and allows for several key observations **(Figure 5-7)**. Firstly, the expression of osteogenic markers was most noticeable within the dispersed MSC models for both 7.5% and 10% w/v GelMA hydrogels, as opposed to the MSC spheroids. Secondly, the osteogenic gene expression increases with time in culture, higher at day 28 than day 14 for dispersed MSCs. Thirdly, the 10% w/v GelMA hydrogel promotes a better osteogenic response than the 7.5% w/v for both dispersed and spheroid MSCs. Fourthly, of the three hydrogel conditions, the MNPs alone or combined MNP/SMF generate the highest osteogenic response. Finally, when investigating self-renewal, whilst ALCAM does not change, Nestin levels are clearly increased in dispersed MSC hydrogel models, under all conditions.

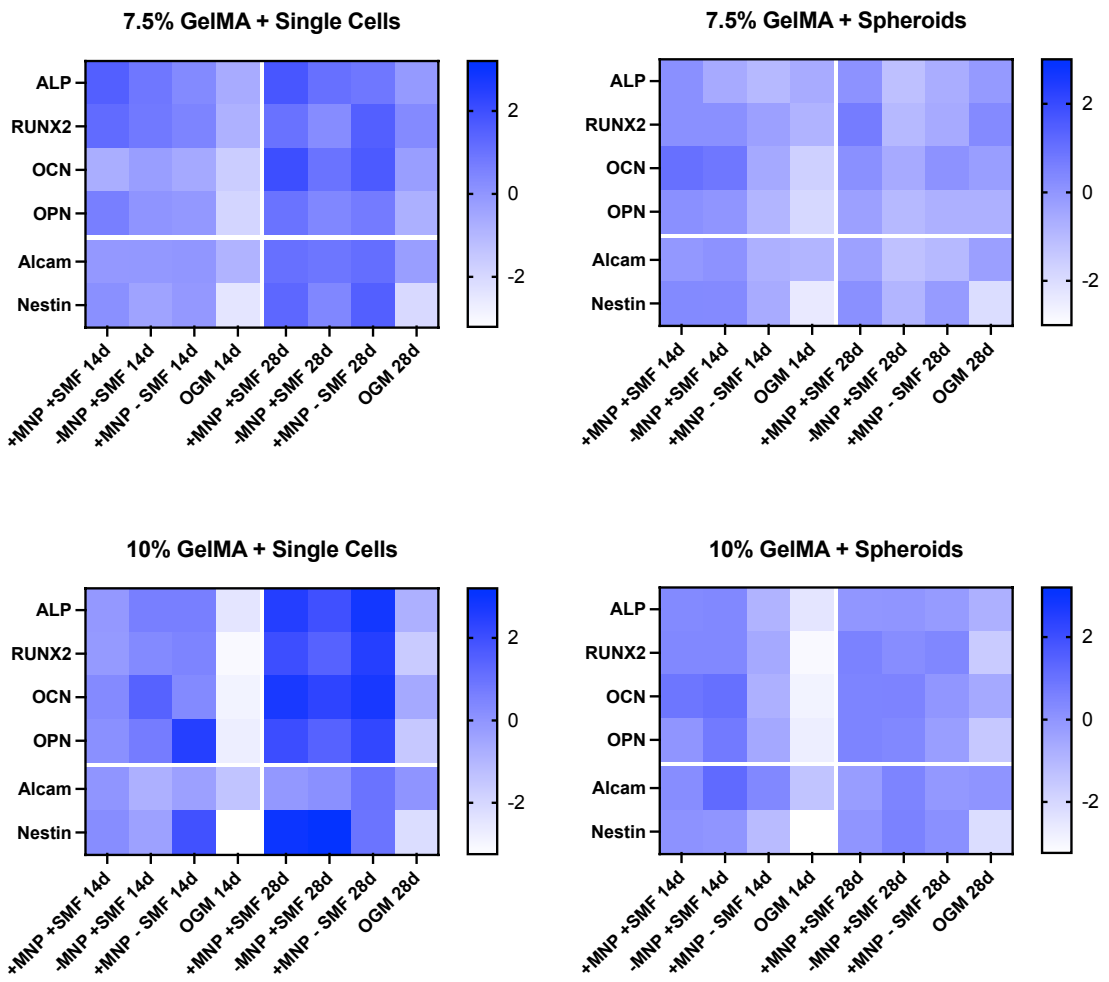

Figure 5-7: Incorporation of magnetic nanoparticles and application of an intermittent static magnetic field shows greater osteogenic potential in dispersed cell model compared to spheroid model

Mesenchymal stromal cell (MSC) spheroid commitment to osteogenic lineages, and stem cell maintenance in magnetic GelMA hydrogels was investigated over 28 days under intermittent static magnetic field (SMF) exposure. Gene summary from 7.5% and 10% w/v GelMA hydrogels, both dispersed MSCs and MSC spheroids.

Collectively, these findings suggest that dispersed MSCs within hydrogels may exhibit greater response to magnetic stimulation, showing trends toward both osteogenic differentiation and maintenance of stemness over time. The MSC spheroid models appeared less responsive across the conditions tested; possibly suggesting the 3D cell organisation affects their ability to differentiate and respond to both internal and external stimuli. Overall, the magnetic hydrogel model combined with dispersed MSCs represents a potentially useful approach for promoting osteogenesis under a SMF.

5.4.2 Mineralisation Assessment *via* Alizarin Red S Staining

As MSCs commit to an osteogenic lineage, they differentiate into osteoblasts, cells responsible for mineralisation of the extracellular matrix. Based on the observed upregulation of osteogenic gene expression, some mineralisation was anticipated to occur by day 28 in hydrogels exposed to an intermittent SMF. Alizarin Red S staining was performed to assess calcium deposition, a key indicator of osteogenic differentiation, in hydrogels containing dispersed MSCs following 28 day exposure to an intermittent SMF. During imaging, residual OCT was observed on some sections and had absorbed the stain contributing to non-specific background staining in certain conditions. As this likely compromised the reliability of quantitative analysis, a qualitative visual assessment was utilised to identify calcium deposition within conditions.

Alizarin Red S staining was present in all conditions; however, the intensity and distribution varied. Some conditions indicated pale pink staining, while other conditions indicated a dense dark red staining. In some images, there was a noticeable background pink hue in pores within the hydrogel, indictive of OCT retention.

In the 7.5% w/v GelMA hydrogels, the control staining was generally light pink, indicating low calcium deposition. Under a SMF, or with the addition of MNPS, the staining was noticeably darker and redder, suggesting enhanced mineralisation. Under a SMF, an orange hue was observed in some imaging, while others show lighter pink hue suggesting heterogeneity in calcium deposition across samples **(Figure 5-8)**.

In the 10% w/v GelMA control hydrogels, that staining was noticeably darker and redder than corresponding 7.5% w/v control hydrogels, suggesting a greater calcium deposition. After exposure to an intermittent SMF, the staining ranged from lighter to dark red, again suggesting some variability in calcium deposition. With addition of MNPs, 10% w/v control hydrogels displayed a lighter pink hue, suggesting low calcium deposition in comparison to hydrogel only. However, application of a SMF resulted in a darker red staining, indicating an increase in calcium deposition **(Figure 5-8)**.

Calcium deposition was observed in all hydrogels, with somewhat greater mineralisation in those containing MNPs and exposed to a SMF. Interestingly, 10% w/v control hydrogels showed relatively strong staining in comparison to 7.5% w/v hydrogels, suggesting these hydrogels alone may contribute to osteogenic activity.

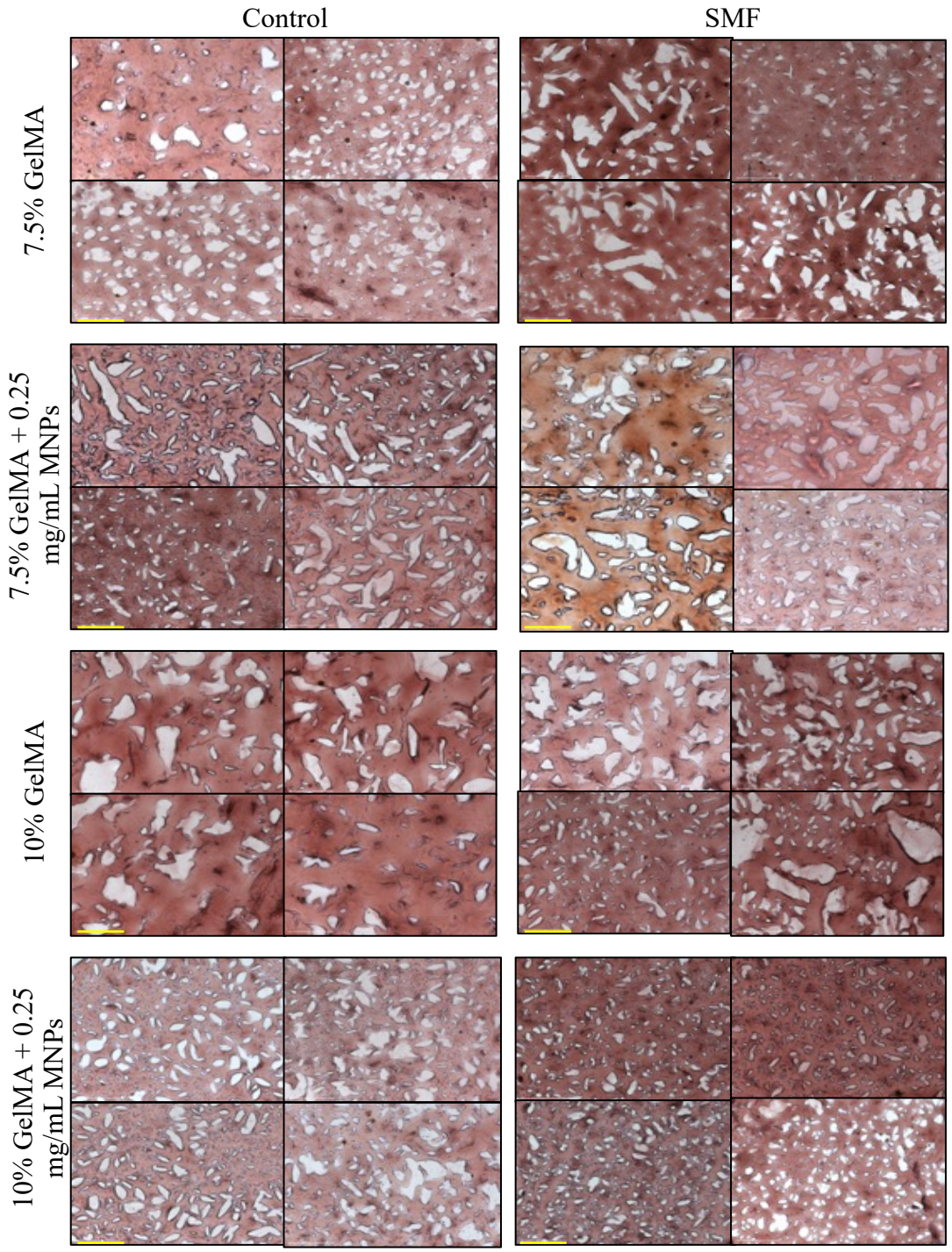

Figure 5-8: Incorporation of magnetic nanoparticles and application of an intermittent static magnetic field increase calcium deposition in GelMA hydrogels

GelMA hydrogels containing dispersed mesenchymal stromal cells, exposed to an intermittent static magnetic field (SMF) for 28 days. Hydrogels were cryosectioned in optimal cutting temperature compound (OCT) and stained with Alizarin Red S to identify calcium deposition. Scale bars show 650 µm. Representative images are shown for each condition (n=3). OCT interference with background staining was observed; therefore, visual analysis was performed in lieu of qualitative measurements.

5.5 Long Term Structural Stability of GelMA Hydrogels Under Static Magnetic Field Exposure

5.5.1 Viscoelastic Behaviour Under an Intermittent SMF

As MSCs have demonstrated osteogenic commitment and calcium mineralisation within the magnetic GelMA hydrogel models, the mechanical properties of the hydrogels were analysed over 28 days to assess the effects of cell behaviour on the mechanical structural stability of the hydrogels. It was anticipated that 10% w/v GelMA hydrogels would exhibit higher stiffness than 7.5% w/v hydrogels, and hydrogels containing MNPs exposured to an intermittent SMF may also enhance mechanical properties potentially due to upregulation of osteogenic gene expression. GelMA hydrogels (both 7.5% and 10% w/v GelMA, with dispersed MSCs, and 0.25 mg/mL MNPs) were exposed to an intermittent SMF for 28 days and rheological measurements were captured and compared to control **(Figure 5-1)**.

The following conditions were used (as annotated on **Figure 5-1,** +SMF denotes intermittent SMF applied):

- 7.5% w/v GelMA + dispersed MSCs (7.5% GelMA)
- 7.5% w/v GelMA + 0.25 mg/mL MNPs + dispersed MSCs (+ 0.25 mg/mL MNPs)
- 10% w/v GelMA + dispersed MSCs (10% GelMA)
- 10% w/v GelMA + 0.25 mg/mL MNPs + dispersed MSCs (+ 0.25 mg/mL MNPs)

Overall, 10% w/v hydrogels were clearly significantly stiffer than the corresponding 7.5% w/v hydrogels, with G′ values ~5060 Pa compared to ~2000 Pa, demonstrating how increasing GelMA concentration leads to a stiffer hydrogel. For the 7.5% w/v hydrogels, the addition of MNPs more than doubled G′ to ~4120 Pa, while the addition of MNPs to 10% w/v hydrogels maintained G′ ~4595 Pa. Under intermittent SMF for 28 days, 7.5% w/v hydrogels showed a further significant increase in G′, reaching ~4670 Pa. Conversely, in 10% w/v hydrogels G′ was maintained with SMF exposure, at ~4810 Pa. With the combination of MNPs and SMF, G′ in 7.5% w/v hydrogels was reduced to ~2920 Pa, while 10% w/v hydrogels observed a similar decrease to ~3620 Pa **(Figure 5-9)**.

Additionally, G″ exhibited dynamic changes over 28 days that varied with hydrogel concentration, MNP incorporation and SMF exposure. In control conditions, G″ in 7.5% w/v hydrogels significantly increased from ~54 Pa to ~304 Pa with MNP incorporation. For 10% w/v hydrogels, G″ was consistently higher, rising to ~628 Pa and further increasing to 885

Pa with addition of MNPs. Under an intermittent SMF, G″ in 7.5% w/v hydrogels increased significantly to ~191 Pa, although the addition of MNPs reduced G″ to ~79 Pa. Similarly, in 10% w/v hydrogels, intermittent SMF exposure caused a marked decrease in G″ to roughly 238 Pa, with further reduction to 517 Pa with addition of MNPs (**Figure 5-9**).

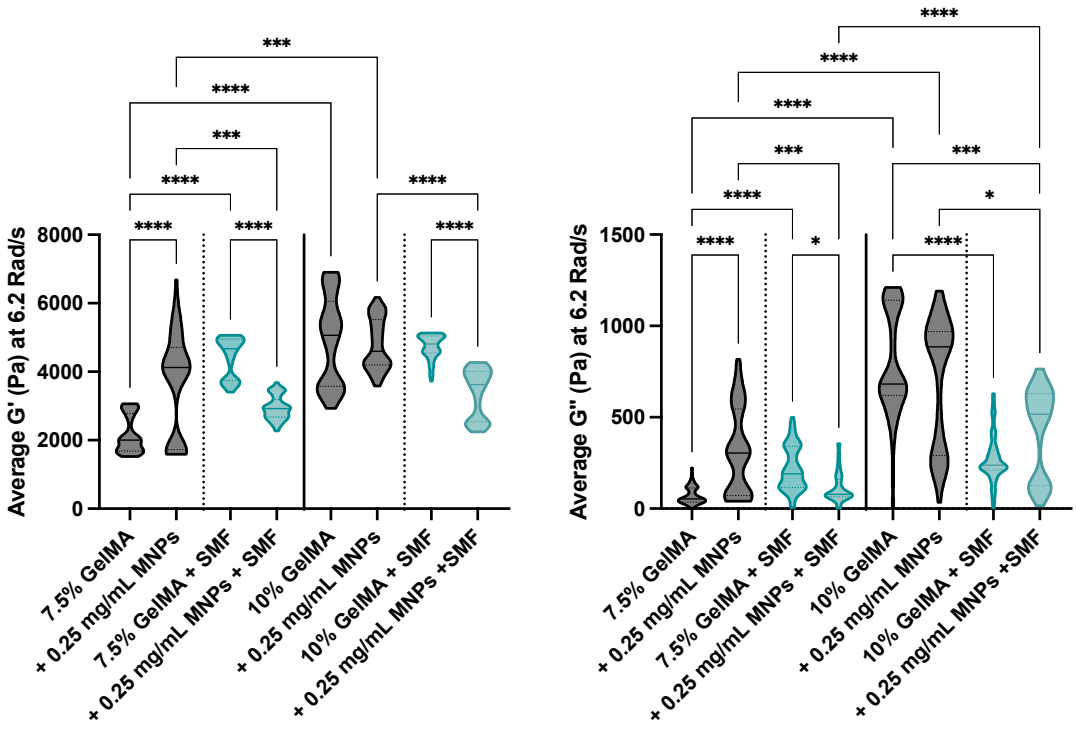

Figure 5-9: Mechanical properties of GelMA hydrogels are influenced by intermittent static magnetic field exposure over 28 days

GelMA hydrogels were subject to intermittent static magnetic field (SMF) actuation for 28 days. Storage modulus (G′) and loss modulus (G″) were measured *via* strain sweep tests (0.01-0.1% strain, 1 Hz, 6.2 Rad/s) for GelMA hydrogels under SMF and compared to control. Measurements were obtained using an Anton Paar rheometer. Truncated violin plots show distribution of G′ and G″ values with median (solid line) and interquartile range (dashed lines) (n=3). A Kruskal-Wallis test and post hoc Dunn's multiple comparison tests show significance between conditions

Tanδ values, were calculated from median G′ and G″ in hydrogels under an intermittent SMF (**Table 5-2**). Tanδ values for GelMA conditions show range from 0.027-0.193, indicating elastic behaviour is maintained with some variation. An increase is observed in 10% w/v control hydrogels including the addition of MNPs, 0.135 and 0.193 respectively indicating an increase in viscous behaviour in 10% w/v hydrogels over 28 days. In addition, 10% w/v hydrogels with MNPs show an increase in Tanδ under an Intermittent SMF for 28 days.

	Control	Intermittent SMF
7.5% w/v GelMA + MSCs	0.027	0.041
7.5% w/v GelMA + MNP + MSCs	0.074	0.027
10% w/v GelMA + MSCs	0.135	0.049
10% w/v GelMA + MNP + MSCs	0.193	0.143

Table 5-2: Tanδ values of GelMA hydrogels after exposure to an intermittent static magnetic field for 28 days

Tanδ (=G″/G′) values of GelMA hydrogels with 0.25 mg/mL magnetic nanoparticles (MNPs) and/or mesenchymal stromal cells (MSCs) subject to intermittent static magnetic field (SMF) actuation for 28 days. Tanδ near 0 indicate the material shows more elastic behaviour, while close to 1 indicates viscous behaviour.

In addition, strain sweeps were conducted to assess the mechanical stability under increasing strain (0.1-1%). All hydrogel conditions maintained their structural integrity within this range, indicating they remain within the linear viscoelastic region. However, differences in the consistency of the measured moduli were observed between conditions. In 7.5% w/v GelMA + MNP, the hydrogels displayed greater variability in measurements in comparison to both 7.5% w/v GelMA and 7.5% w/v GelMA + MNPs + SMF conditions in 10% w/v GelMA hydrogels, most conditions showed some variation with exception of 10% w/v GelMA + SMF which displayed more consistent measurements **(Figure 5-10).**

In summary, over 28 days the mechanical properties of the magnetic hydrogel models were influenced by an intermittent SMF, with results dependent of GelMA concentration. In 7.5% w/v hydrogels, MNPs and magnetic stimulation increase both G′ and G″, while 10% w/v hydrogels exhibit higher baseline stiffness with G′ and G″ reduced in hydrogels only with a combination of MNPs and SMF exposure.

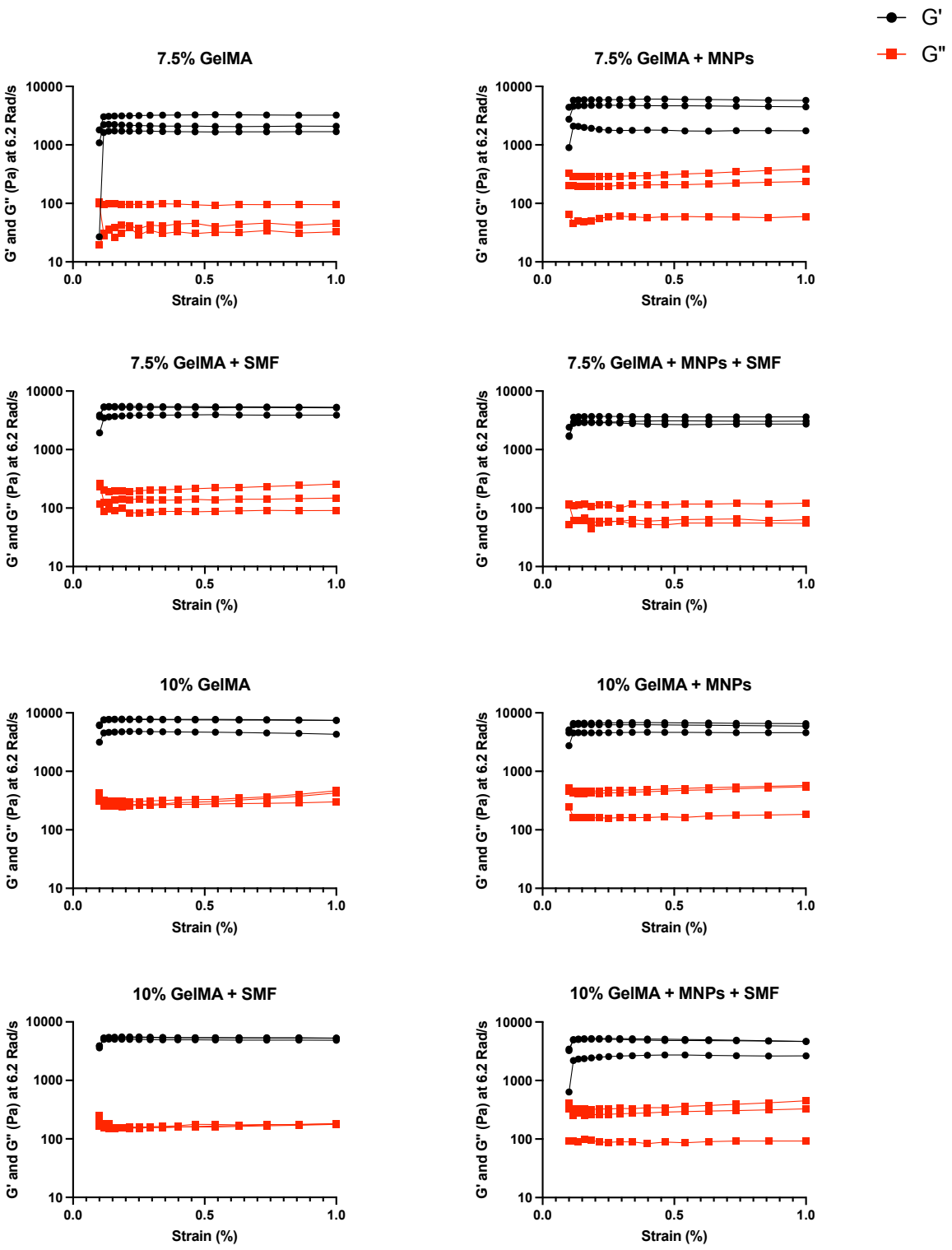

Figure 5-10: Hydrogel mechanical properties depend on GelMA concentration and magnetic field exposure

Amplitude sweeps of GelMA hydrogels, 7.5% and 10% w/v, with addition of 0.25 mg/mL magnetic nanoparticles and mesenchymal stromal cells (MSCs) subject to intermittent static magnetic field (SMF) actuation for 28 days. Storage modulus (G′ – indicated by black circles) and loss modulus (G″ – indicated by red squares) were measured *via* strain sweep tests (0.1-1% strain, 1 Hz, 6.2 Rad/s) for hydrogels 72 hours post polymerisation (n=3). Measurements were obtained using an Anton Paar rheometer.

5.6 Discussion

This chapter integrates previous findings on MSC osteogenic differentiation under SMFs and the magnetic GelMA hydrogel platform to explore how MNPs and SMF application influence hydrogel mechanics and MSC behaviour. By assessing both short term and long-term effects of magnetic stimulation, the study evaluates the capacity of these magnetically responsive hydrogels to provide a dynamic, physiologically relevant scaffold that supports MSC differentiation and mechanical stability. The following sections discuss how the mechanical properties of GelMA hydrogels are modulated by the presence of MSCs (including spheroids), MNPs and SMF exposure. It also evaluates the osteogenic and mineralisation potential of MSCs within these magnetic hydrogels under SMF stimulation.

5.6.1 GelMA Mechanical Properties are Enhanced with MNPs and MSCs

The mechanical properties of 7.5% and 10% w/v GelMA hydrogels are influenced by the presence of MSCs and MNPs, as well as exposure to a SMF. The addition of 0.25 mg/mL MNPs helped to maintain mechanical properties, while combining MSCs (either as dispersed cells or spheroids) with MNPs significantly increasing stiffness. Application of a constant magnetic field (370 mT for 72 hours) further enhances the mechanical strength of hydrogels containing both MSCs and MNPs, while showing minimal impact on acellular hydrogels. Despite alternating conditions, hydrogels predominately exhibit elastic behaviour across all groups.

Higher GelMA concentrations result in stiffer hydrogels, with MNPs and SMF stimulation modulating mechanical properties over time. Zhu et al., (2023) reported that increasing bioprinted GelMA concentration from 3% to 10% w/v enhanced hydrogel stiffness while maintaining scaffold integrity. However, higher concentrations also reduced pore size, limiting long term cell integration and viability (Zhu, et al., 2023). Thus, while increasing GelMA concentration can support mechanical properties, it must be optimised to promote cell integration.

Short term (72 hours) constant SMF exposure in MSC and MNP laden hydrogels notably increased hydrogel stiffness. This effect is likely due to alignment of magnetic nanoparticles within the hydrogel network under the constant field, reinforcing the local polymer matrix, as observed in previous studies where magnetic hydrogels were crosslinked and examined under a magnetic field and exhibited increased stiffness (Tran, et al., 2021; Yan, et al., 2021). GelMA hydrogels also undergo a post-crosslinking equilibrium period (~48-72 hours)

(**Figures 4-3 A, 4-10**), during which contraction and network reorganisation occur, potentially amplifying this stiffening effect in combination with a constant SMF. In contrast, long term intermittent SMF exposure combined with MNPs appears to reduce hydrogel stiffness, despite promoting osteogenesis. This softening may result from cyclic forces applied by the intermittent SMF, which can disrupt or rearrange hydrogel struts over time. Importantly, these forces still seem to provide mechanotransducive effects to the embedded cells, even in the presence of a slightly softer matrix. Minor contributions from hydrogel degradation cannot be excluded as this was not specifically investigated; however, given the apparent maintenance of matrix integrity in hydrogels containing MNPs or exposed to SMF, the dominant effect is likely related to physical restructuring of the polymer network.

As previously discussed, hydrogel stiffness plays a crucial role in regulating MSC differentiation with stiffer matrices generally promoting an osteogenic lineage commitment. Interestingly, Smits et al., (2023) demonstrated a dual photo-crosslinking method to modulate GelMA stiffness. Using a two-step LAP/UV crosslinking method they increased hydrogel stiffness from ~5 kPa to ~40 kPa while preserving hydrogel integrity. This approach could complement our findings by offering a method to counteract the softening effects observed during long term intermittent SMF exposure in magnetic hydrogels, enabling precise tuning of hydrogel mechanics in MSC laden constructs.

While bulk rheological measurements provide valuable insight into the global mechanical properties of the hydrogels, they represent an averaged response and may not capture local stiffness variations introduced by embedded MSCs or spheroids. The incorporation of cells and spheroids can significantly alter the mechanical microenvironment through processes such as cell spreading, contraction and extracellular matrix remodelling, leading to heterogenous stiffness distributions within the hydrogel. Bulk rheology thus potentially masks these spatially localised changes, as it cannot distinguish between the matrix's intrinsic properties and mechanical contributions from cells and spheroids. To better understand these microscale mechanical alterations, complementary techniques should be utilised.

In previous studies, atomic force microscopy (AFM) has enabled spatially resolved stiffness measurements, distinguishing between individual cells and the surrounding matrix. Meng et al., (2021) found that during osteogenic differentiation, MSCs not only altered their mechanical properties, but also remodelled the gelatin substrate, causing local changes in stiffness and surface topography (Meng, et al., 2021). Yen et al., (2020) used AFM to track

MSC stiffness during osteogenic differentiation, showing that Young′s modulus increased over 15 days before plateauing. This cellular change occurred on substrates of varying stiffness, with stiffer substrates promoting MSC stiffening (Yen, et al., 2020). These findings highlight the dynamic, bidirectional mechanical interplay between cells and their microenvironment, which bulk rheological measurement cannot resolve. Therefore, combining bulk and microscale mechanical assessments should be used to provide a more comprehensive understanding of cell-matrix interactions within hydrogels.

In conclusion, GelMA mechanical properties are enhanced with the inclusion of MNPs and MSCs, with short term SMF exposure further increasing stiffness to support osteogenic differentiation. However, long term intermittent SMF can reduce stiffness, highlighting the need to identify the cause of these changes, and explore methods - such as additional crosslinking - to maintain or improve hydrogel mechanics.

5.6.2 The Magnetic Hydrogel Under Intermittent SMF Promotes Osteogenesis

GelMA hydrogels have demonstrated potential for supporting osteogenic differentiation. In our study, 10% w/v GelMA hydrogels generally promoted greater calcium mineralisation than 7.5% w/v hydrogels, even in the absence of MNPs and SMF supporting the idea that a stiffer matrix favours osteogenesis. Similarly, Lee et al., (2020) observed that increasing GelMA concentration from 5% to 15% w/v, which correlates with increased viscosity, led to an increase in ALP activity, calcium deposition and osteogenic gene expression, demonstrating a clear positive correlation between viscoelasticity and osteogenesis (Lee, et al., 2020). Interestingly, Lin et al., (2018) found that while both 7.5% and 10% w/v GelMA hydrogels effectively supported osteogenic differentiation, 10% w/v was optimal, with 15% w/v GelMA showing reduced expression of key markers such as OPN (Lin, et al., 2018). This suggests that although stiffness (altered *via* GelMA concentration) can promote osteogenic differentiation, there may be a threshold beyond which excessive stiffness inhibits osteogenesis, highlighting the need to tune GelMA properties to match the optimal biomechanical window for MSC differentiation.

Incorporation of MNPs (0.25 mg/mL iron oxide) or application of a 370 mT SMF showed increased osteogenic gene expression (ALP, RUNX2, OPN and OCN) particularly at later time points (day 28). Combined MNP and SMF conditions showed more consistent upregulation of osteogenic genes in comparison to other conditions. Calcium deposition was more intense in hydrogels containing MNPs and subject to SMF, indicating enhanced

mineralisation (**Figure 5-11**). Yuan, et al., (2022) observed that a 144 mT SMF combined with iron oxide MNPs and collagen matrix, increased ALP production after 21 days in MG-63 cells, while matrix mineralisation and osteogenic gene expression (RUNX2, Osteonectin, BMP2, BMP4) were upregulated at day 14 (Yuan, et al., 2018). Similarly, Ma, et al, (2022) demonstrated that their silk fibroin based magnetic hydrogel under SMF significantly upregulated osteogenic genes (ALP, Col1) and enhanced collagen mineralisation, during MSCs differentiation into osteoblasts (Ma, et al., 2022). Our findings are consistent with these studies and suggest that combined MNP and SMF stimulation may enhance osteogenic gene expression and mineralisation, although further studies, such as protein-level validation, are needed to confirm the extent of this effect.

Although alizarin red staining is commonly used to indicate mineralised matrix formation and osteoblast activity, it is important to recognise that the observed staining may not exclusively reflect calcium deposition in the ECM. The signal could also result from non-specific deposition of calcium ions or culture media. Alizarin red S staining is not specific for calcium phosphate produced by osteoblasts, and false positives have been reported due to the detection of calcium binding proteins and proteoglycans (Bonewald, et al., 2003). In addition, the method is only moderately sensitive to calcium deposition (Serguienko, et al., 2018). Therefore, while positive staining suggests the presence of calcium it should be interpreted with caution and future work should include complementary assays to confirm osteoblast activity. Complementary staining methods such as Von Kossa should be employed in further studies to distinguish true mineralised matrix from non-specific calcium accumulation (Meinel, et al., 2004).

Filippi et al., (2019) developed magnetically actuated hydrogel constructs containing adipose-derived stromal vascular fraction (SVF) and MNPs. A 50 mT SMF enhanced osteogenic differentiation *via* upregulation of genes (ALP, OCN, Col1 and RUNX2) and activation of BMP2 signalling pathways to promote matrix mineralisation and bone regeneration (Filippi, et al., 2019). In contrast, Tang, et al. (2024) showed that magnetic activation within their magnetic anisotropic hydrogel promoted osteogenic differentiation of MSCs by activating the NOTCH1/2 pathway. This activation was mediated through a signalling cascade, linking the scaffolds magnetic and topographic cues to epigenetic control of osteogenesis (Tang, et al., 2024). These studies demonstrate that magnetic stimulation with MNPs can activate distinct osteogenic signalling pathways, depending on the biomaterial system and cell type.

In our GelMA hydrogel model, where stiffness modulation was observed with combined MNP and SMF treatment, the underlying mechanisms of osteogenesis may involve mechanotransduction pathways sensitive to both substrate stiffness and magnetic forces. For instance, the cytoskeletal tension induced by GelMA stiffening could promote nuclear translocation of YAP/TAZ, which interacts with RUNX2 to drive osteogenic gene expression (Dahl, et al., 2008; Sun, et al., 2022). Additionally magnetic stimulation may influence ion channel activity, leading to activation of MAPK/ERK or BMP2 signalling cascades, which are known to regulate osteogenic commitment (Sun, et al., 2022). Future studies should dissect the relative contributions of these pathways and whether synergistic effects between mechanical cues and magnetic forces are critical for bone formation.

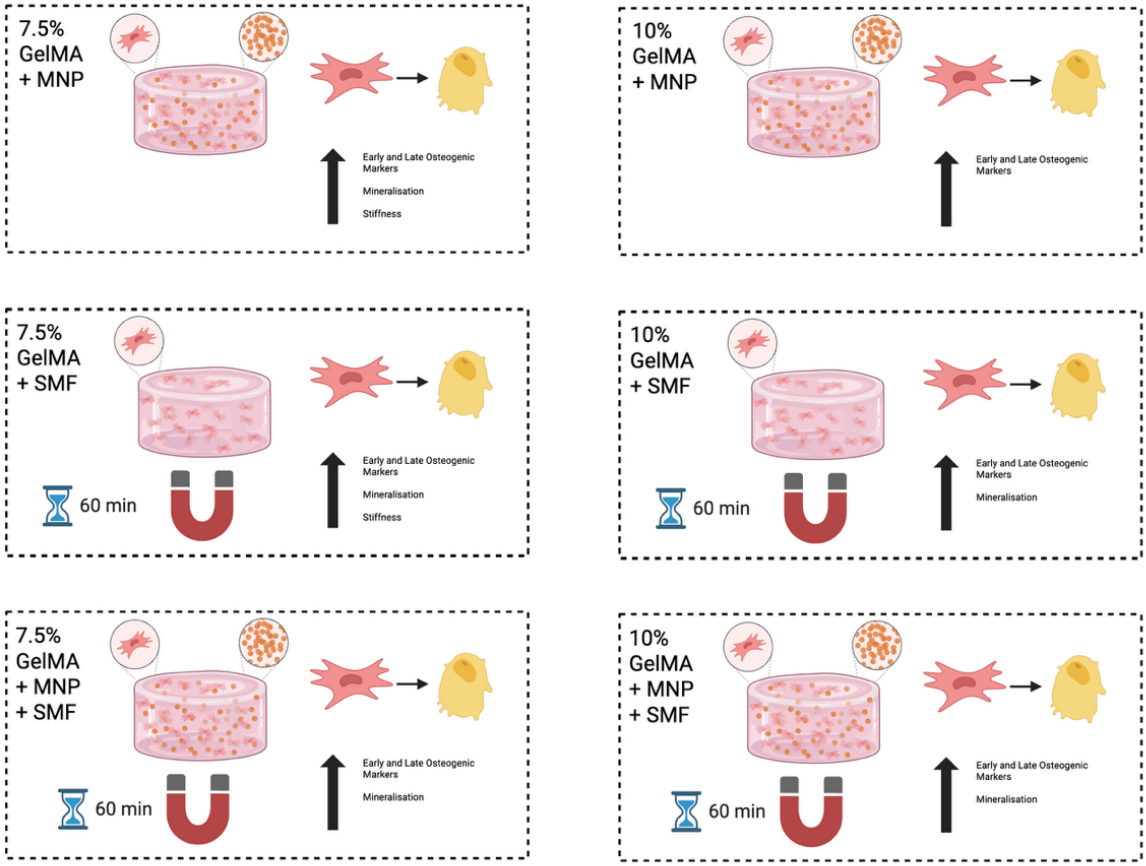

Figure 5-11: Summary of effects of magnetic nanoparticles and static magnetic fields on mesenchymal stromal cells in GelMA models

Summary of changes to GelMA hydrogels models, 7.5% and 10% w/v, and mesenchymal stromal cell (MSC) osteogenic commitment with magnetic nanoparticles (MNPs) and / or exposure to an intermittent static magnetic field (SMF). In 7.5% w/v GelMA hydrogels all magnetic conditions increased osteogenic gene expression, mineralisation and stiffness, with exception of the MNP + SMF condition which reduced stiffness. In 10% w/v GelMA hydrogels, all conditions increased osteogenic gene expression, with application of a SMF also promoting increased mineralisation. Created with Biorender.com

Mechanically, increasing GelMA concentration increased stiffness over 28 days (~2 kPa to 5 kPa). MNPs and SMF individually enhanced stiffness, but their combination slightly reduced stiffness in both concentrations (**Figure 5-10**). Since all hydrogels contained MSCs, this may be due to cell-mediated matrix remodelling over time, a phenomenon reported in other studies. Utilising a GelMA model, Martinez-Garcia et al., (2021) demonstrated that ADCs cultured in GelMA actively modulate both the stiffness and viscoelasticity of the hydrogel, progressively transforming it to a more fluid-like environment. They observed that cell-induced changes occurred earlier in softer (5% w/v) hydrogels and were delayed in stiffer (10% w/v) hydrogels (Martinez-Garcia, et al., 2021), which aligns with our observation of time dependent mechanical changes. While our data show an overall increase in stiffness, this may reflect progressive ECM deposition and mineralisation by MSCs driving bone formation. Additionally, Yan, et al., reported that their magnetic hydrogels containing iron oxide MNPs increased in stiffness under SMF actuation, influencing cell morphology and promoting mechanotransduction (Yan, et al., 2022). However, to fully understand if these dynamics occur in our model, it will be essential to investigate the mechanical properties of our hydrogels under active SMF application, as the real time effects of magnetic field activation on stiffness and viscosity remain unclear. The presence of MNPs and application of an intermittent SMF may modulate the observed remodelling process by cyclically influencing cell behaviour or matrix organisation. This could account for the slight reduction in stiffness when both are combined.

MSCs dispersed throughout the hydrogel exhibited more robust osteogenic differentiation and stemness marker expression in response to magnetic stimulation compared to MSC spheroids. In contrast, MSC spheroid cultures showed limited or decreased osteogenic gene expression under magnetic conditions, with some exceptions (**Figure 5-12**). This difference may arise from several mechanistic factors. Embedding pre-formed spheroids within a hydrogel increases cell to cell contacts while reducing cell to ECM interactions, which can interrupt mechanotransducive effects on individual cells (Yu, et al., 2020). Spheroids also commonly develop a necrotic core, limiting responsiveness of the innermost cells due to cell death. We observed development of a necrotic core in embedded spheroids within GelMA hydrogels over 10 days (**Figure 4-12**). Finally, the more elastic properties of the hydrogel may favour dispersed MSC models, which directly sense matrix stiffness, while spheroids do not respond to the same mechanical cues. Whitehead et al., (2021) demonstrated that the dynamic mechanical properties of viscoelastic alginate hydrogels significantly enhanced the osteogenic potential in MSC spheroids. Compared to elastic hydrogels, viscoelastic hydrogels promoted higher ALP activity and calcium deposition (Whitehead, et al., 2021).

This may explain the limited osteogenic response observed in our hydrogels, which exhibit more elastic than viscoelastic properties.

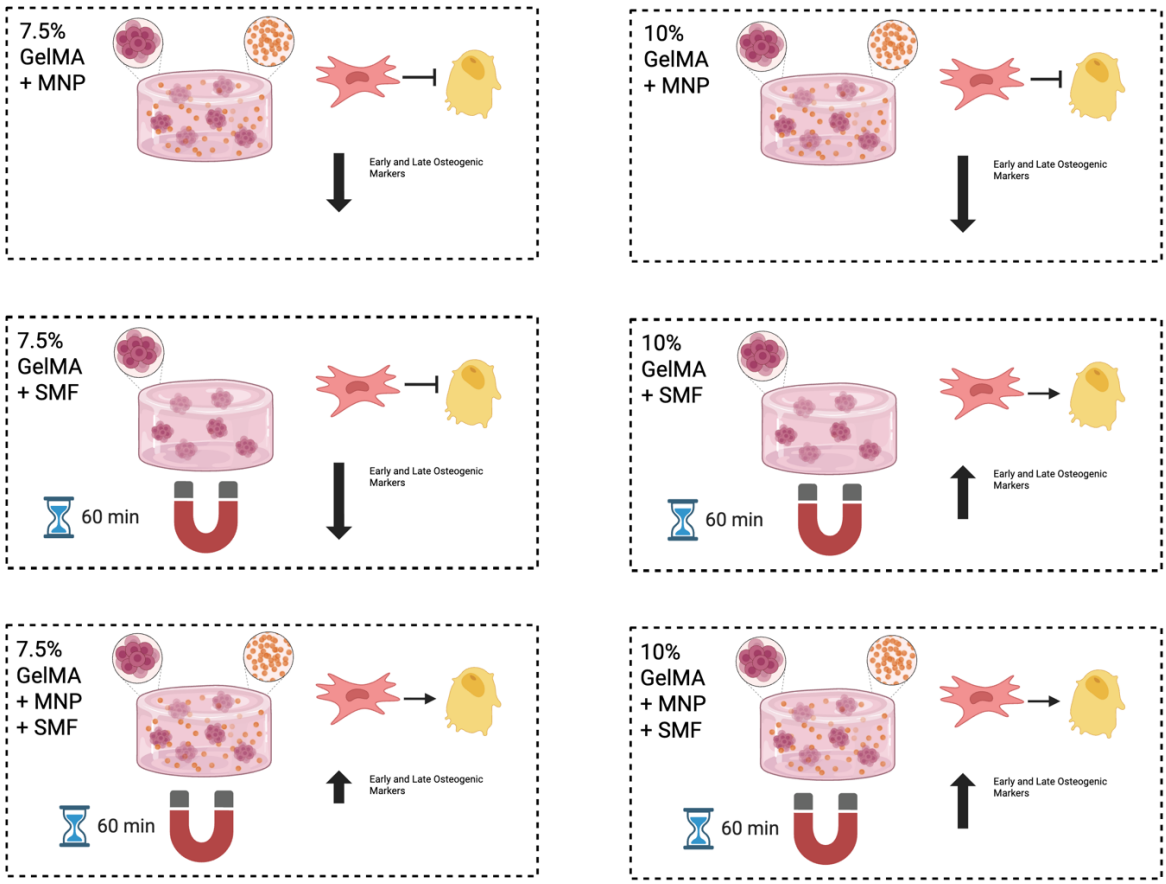

Figure 5-12: Summary of effects of magnetic nanoparticles and static magnetic fields on mesenchymal stromal cells spheroids in GelMA models

Summary of mesenchymal stromal cell (MSC) spheroid osteogenic commitment or inhibition in GelMA hydrogels models, 7.5% and 10% w/v, with magnetic nanoparticles (MNPs) and / or exposure to an intermittent static magnetic field (SMF). Magnetic conditions examined included MNP only, SMF only and combination of MNP and SMF. In 7.5% w/v GelMA hydrogels, addition of MNPs or application of a SMF did not lead to osteogenic gene expression in MSC spheroids however the combination of both showed slight upregulation of osteogenic markers. In 10% w/v GelMA hydrogels, only hydrogels under SMF actuation promoted osteogenic gene expression. Created with Biorender.com

Stemness markers remained stable or showed slight decreases across most conditions. Notably, Nestin increased in some conditions, suggesting a subset of MSCs retained self-renewal capacity alongside osteogenic differentiation. This balance between differentiation and maintenance highlights the magnetic hydrogel platforms potential to support a dynamic and sustainable MSC population. Some studies suggest that Nestin expression marks progenitor cells primed for differentiation. Although often considered a marker of stemness

or undifferentiated MSCs, its continued expression during lineage commitment indicates that Nestin is not exclusive to the most primitive undifferentiated state (Wong, et al., 2014). This suggests that Nestin may better represent a transitional progenitor phenotype, rather than a definitive stem cell marker. Therefore, relying solely on Nestin to identify true stemness may be insufficient. Incorporating additional markers, as we have with Alcam, could improve the accuracy of stem cell characterisation.

Shuai et al, developed a superparamagnetic scaffold model using iron oxide loaded polyglycolic acid, combined with a 65 mT SMF. They observed significantly enhanced osteogenic gene expression in MSCs (ALP, RUNX2, COL1, OCN) and demonstrated the *in vivo* biosafety of the system, despite gradual degradation. The incorporated iron oxide was primary removed by the spleen and subsequent metabolic pathways (Shuai, et al., 2020). The superparamagnetic characteristic of a magnetic scaffold is a key feature that enables magnetic responsiveness without remnant magnetisation, reducing the risk of nanoparticle aggregation and cytotoxicity. Our GelMA hydrogels similarly incorporate superparamagnetic MNPs, which likely contribute to the effective magnetic stimulation observed in our system using an intermittent SMF. The superparamagnetic behaviour ensures that magnetic effects are controllable and reversible, enhancing both the safety profile and functionality of our system for osteogenic applications. This shared property between our model and Shuai's supports the conclusion that incorporating superparamagnetic MNP is a valuable design strategy for magnetically responsive bone tissue engineering scaffolds.

In summary, our findings are broadly consistent with existing literature suggesting that MNP incorporation combined with SMF exposure may promote osteogenic differentiation in different hydrogel platforms. The superparamagnetic nature of the MNPs likely play a crucial role in enabling effective, safe controllable magnetic stimulation. Future investigations are warranted to delineate the precise signalling pathways driving osteogenesis within our GelMA hydrogel system.

5.6.3 Conclusion: Magnetically Hydrogel Bone Marrow Model Enhances MSC Osteogenesis

The magnetically responsive GelMA hydrogel provides a promising bone marrow model that can supports MSC osteogenic differentiation, potentially through the combined effects of MNP incorporation and intermittent SMF stimulation. This platform offers a

mechanically dynamic and physiologically relevant microenvironment and appears to promote osteogenic gene expression, mineralisation and maintenance of stemness in a manner that partially mimics *in vivo* conditions. The ability of the magnetic hydrogel to influence cellular behaviour and matrix mechanics suggests it as a potential tool for bone tissue engineering and regenerative medicine. Future studies should aim to clarify the underlying mechanotransducive pathways and optimise the system for translational applications in bone repair and regeneration.

Chapter 6: Mesenchymal Stromal Cell Response to Dynamic Magnetic Fields in a 3D Magnetic Hydrogel

6.1 Introduction

The previous chapter focused on the influence of a SMF on MSCs in a magnetic 3D hydrogel. However, DMFs have also been utilised as a promising tool for modulating cell behaviour through remote, non-invasive stimulation (Silva, et al., 2018). MSCs have shown enhanced osteogenic responses under a DMF, suggesting potential applications in the field of bone tissue engineering (Henstock, et al., 2014; Silva, et al., 2018). While most studies utilise 2D cell culture to examine the potential differentiation of DMFs, these systems fail to replicate the spatial environment of native tissue. To address this, we utilised the magnetic GelMA hydrogel, with incorporated magnetic nanoparticles, allowing for remote stimulation.

The research presented in this chapter was completed during a visiting researcher placement at the Universitat Politècnica de València (UPV) in Spain. The work was carried out with the support and guidance of Dr Gloria Gallego Ferrer, Dr Arantxa Martínez and Dr Jose Luis Aparicio Collado in the Centro de Biomateriales e Ingeniería (CBIT). A DMF bioreactor, compatible with multiwell plates, was used to apply alternating magnetic stimulation to cells. Developed by BC Materials (Basque Country, Spain), the system generates an alternating magnetic field up to 23 mT through displacement of a 48-well array of NdFeB magnets, at 0.3Hz with tuneable displacement. Cells placed on the bioreactor are subjected to a cyclical stimulation consistent of an active period (16 hours) and a rest period (8 hours). Due to limitations with available materials, primarily due to custom delays, the experimental work presented in this chapter was constrained.

The first part of this chapter focuses on the development and characterisation of the magnetic hydrogel model in the host institute, establishing its mechanical properties and assessing its biocompatibility for cell culture. Subsequently, the osteogenic capabilities of the DMF bioreactor on MSCs were investigated utilising the magnetic hydrogel.

6.1.1 Chapter Aims

This chapter builds on previously involving the development of a magnetic hydrogel by investigating the biological response MSCs embedded in a magnetic GelMA hydrogels under a dynamic magnetic field. The following objectives were set:

- Magnetic hydrogel fabrication. Magnetic GelMA hydrogels will be developed and optimised using available crosslinking methods and equipment in host institute.
- Magnetic hydrogel characterisation. The mechanical properties of the model will be determined. MSCs will be incorporated into the model and biocompatibility will be assessed *via* MSC viability.
- Osteogenic differentiation studies. Investigate MSC osteogenic response within the optimised magnetic GelMA hydrogel model when exposed to a DMF.

6.2: Materials and Methods

The following research was conducted at the placement host institute. As a result, certain materials and methods differ from those outlined in Chapter 2 due to variations in local protocols and available resources. The methods described in this section reflect the procedures and materials used specifically for this phase of the project.

6.2.1 Cell Culture

This chapter utilises human MSCs to investigate the effects of a DMF on osteogenic differentiation. All cell culture reagents and procedures are described below.

6.2.1.1 Cells and Reagents

Human bone marrow-derived MSCs from a single donor were used in the experiments described in this chapter. Cells were cultured in standard MSC growth medium composed of DMEM supplemented with 10% v/v FBS and additional supplements as detailed in **Tables 6-1** and **6-2**. All cell culture and cell incubation steps were carried out in a humidified incubator at 37°C with 5% CO_2, unless otherwise specified.

Media Type	Component	Manufacturer, Catalogue Number	Volume/ Concentration
MSC Expansion 10% DMEM	Dulbecco's Modified Eagles Medium (DMEM)	Biowest, France Cat No: L0102-500	430 mL
	Foetal Bovine Serum (FBS)	Capricorn Scientific, Germany Cat No: FBS-HI-11A	50 mL – 10% v/v
	Antibiotic Solution	Prepared in house (see table 6-2)	5 mL – 1% v/v (see Table 6-2 for component concentrations)
	L-glutamine*	Lonza Bioscience, Spain Cat No: BE17-605E	5 mL – 2mM
	Sodium Pyruvate*	Sigma-Aldrich, UK Cat No: S8636-100ML	5 mL – 1mM
	10X Minimum Essential Medium Non-essential Amino Acids (MEM-NEAA)	Biowest, France Cat No: X0557-100	5 mL – 1X
PromoCell Growth Media	MSC Growth Medium (PromoCell, Germany)	PromoCell, Germany Cat No: C-28009	50% v/v in MSC Expansion DMEM
Osteogenic Media	MSC Expansion 10% DMEM	Prepared in house	473.5 mL
	Dexamethasone 21-phosphate disodium salt	Sigma-Aldrich, Spain Cat No: D1159	500 µL – 1.1µM
	L-Ascorbic acid 2-phosphate sesquimagnesium salt hydrate	Sigma-Aldrich, Spain Cat No: A8960-5G	1 mL – 0.11µM
	β-Glycerophosphate disodium salt hydrate	Sigma-Aldrich, Spain Cat No: G9422-10G	25 mL – 52.8mM

Table 6-1: Composition of mesenchymal stromal cell culture media

Details the formulations used for (i) mesenchymal stromal cell expansion media, (ii) PromoCell Growth Media and (iii) osteogenic media for positive differentiation control. *Supplements were only added if basal DMEM formulation lacked L-glutamine or sodium pyruvate.

Reagent	Component	Manufacturer, Catalogue Number	Volume/ Concentration

Trypsin/PBS Solution	Trypsin/EDTA Solution	Gibco, Cat No: 25200-072	2 mL – 10% v/v
	Dulbecco's Phosphate-Buffer Solution (PBS) without Ca^{++}/Mg^{++}	Merk Cat No: 59331C-1000ML	18 mL – 90% v/v
Antibiotic Solution	Penicillin-Streptomycin	Gibco, Cat No: 15140-122	89 units/mL, 89 µg/mL
	Amphotericin B	Gibco, UK Cat No: 15290-018	0.27 µg/mL
Buffer Solution	Dulbecco's Phosphate Buffer Solution (PBS) without Ca^{++}/Mg^{++}	Merck, Spain Cat No: 59331C-1000ML	1X

Table 6-2: Cell culture reagents and buffer solutions

Summarises key reagents, media supplements and buffer compositions used throughout the study during all stages of cell culture.

6.2.1.2 Cell Thawing and Culture

PromoCell MSCs were expanded and stored at host institute in liquid nitrogen until use. Upon use, cryovials were rapidly thawed in 37 °C water bath, and cell freezing suspension was diluted with 1 mL of 10% DMEM before transfer to a 20 mL universal containing pre-warmed media. Cells were then centrifuged at 350g for 5 minutes at room temperature to pellet. The supernatant was aspirated, and the pellet resuspended in 1:1 mix of PromoCell Growth Media (PromoCell, Germany) and MSC Expansion 10% DMEM (**Table 6-1**) before seeding into T75 tissue culture flasks, then incubated at 37°C and 5% CO_2.

6.2.1.3 Osteogenic Media Control Differentiation Protocol

As a positive control for osteogenic gene expression, MSCs cultured in monolayer were treated with OGM (**Table 6-1**) alongside 28 day differentiation of MSCs conducted within GelMA hydrogels. Cells were maintained in OGM for either 14 or 28 days and at endpoints cells were lysed and RNA processed for gene analysis following protocols 6.2.2.2 RNA Extraction and Isolation, 6.2.2.3 Reverse Transcription, 6.2.2.4 Real-Time Quantitative Polymerase Chain Reaction.

6.2.2 Cell Analysis

6.2.2.1 Cell Viability Assay

MSC viability was evaluated using the LIVE/DEAD™ Viability/Cytotoxicity Kit (Invitrogen, L3224) as described in Section 2.2.1 Cell Viability Assay, except fluorescence imaging was performed using a Nikon Eclipse 80i imaging system with FITC and TRITC filter cubes to detect green and red fluorescence, respectively (**Table 6-3**). Image analysis and quantification were carried out using ImageJ as previously described.

Light Cube	Colour	Excitation	Dichroic Mirror	Emission
FITC	Green	482/25 nm	506 nm	536/40 nm
TRITC	Red	543/22 nm	562 nm	593/40 nm

Table 6-3: Fluorescence Filter Cubes and Specifications for Nikon Eclipse 80i Imaging System.

Outlines the fluorescent light/filter cubes used for imaging cell samples with Nikon Eclipse 80i fluorescent microscopy system

6.2.2.2 RNA extraction and Isolation

Total RNA was extracted from hydrogel encapsulated MSCs using the RNeasy Micro kit (Qiagen, UK), as described in Section 2.2.5 RNA Extraction and Isolation, except that NYZol reagent (NYZtech) was used in place of TRIzol for lysis and phase separation. RNA yield and purity were assessed using a NanoDrop™ One C spectrophotometer (Thermo Fisher Scientific).

6.2.2.3 Reverse Transcription

cDNA synthesis was performed using the High-Capacity cDNA Reverse Transcription Kit (Qiagen) following the manufacturer's protocol. All reagents, including RNA samples, were thawed and kept on ice throughout processing. RNA samples were first diluted with RNase-free water to a predetermined concentration, normalised across all samples, and 10 µL volume utilised for reverse transcription. The reverse transcription mix was prepared by adding 0.8 µL dNTP Mix, 2 µL RT Random Primers, 1 µL of MultiScribe Reverse Transcriptase, 1 µL RNase Inhibitor, 3.2 µL Nuclease-free water, and 2 µL of RT Buffer to each sample bringing the reaction volume to 20 µL. Reverse transcription was carried out at 25°C for 10 minutes, then 37°C for 120 minutes to synthesise cDNA, followed by 85°C for 5 minutes to inactive the reverse transcriptase. Synthesised cDNA was stored at -20°C prior to qPCR.

6.2.2.4 Real-Time Quantitative Polymerase Chain Reaction

Real-time quantitative reverse transcription polymerase chain reaction (RT qPCR) was performed using the QuantStudio™ 5 RT qPCR system (ThermoFisher) at the Facultultat de Medicina, Universitat de Valencia. Reactions were carried out in a final volume of 20 µl, comprising 10 µl PowerUp SYBR Green Master Mix (Applied Biosystems, UK), 0.1 µL forward primer (50 nM), 0.1 µL reverse primer (50 nM), 7.8 µL RNase free H_20 and 2 µL of template containing 4 ng of total cDNA. Cycling parameters and primer sequences used are found in **Tables 6-4** and **6-5** respectively. Quantitative gene expression was the comparative Ct (Δ ΔCt) method as described in Section 2.2.7 Real-Time Quantitative Polymerase Chain Reaction.

Stage	Temperature (°C)	Time	Cycles
Hold	95	20 seconds	1
Cycling	95	3 seconds	40
	60	30 seconds	
Melt Curve	95	15 seconds	1
	60	60 seconds	
	95	15 seconds	
	60	15 seconds	

Table 6-4: RT-qPCR Cycling conditions

Details the thermal cycling conditions used for fast RT-qPCR on the QuantStudio™ 5 Real-Time PCR system including each stage of the protocol and its parameters

Gene	Forward	Reverse
ALP	ATGAAGGAAAAGCCAAGCAG	CCACCAAATGTGAAGACGTG
BMP2	CAAGCCAAACACAAACAGCG	CCAACGTCTGAACAATGGCA
COL1A1	GCCAAGCCGAAGACATCCCA	GGCAGTTCTTGGTCTCGTCA
OCN1	GTGCAGAGTCCAGCAAAGG	TCAGCCAACTCGTCACAGTG
OPN	ACACATATGATGGCCGAGGTG	ATGGCCTTGTATGCACCATT
RUNX2	TCACAAATCCTCCCCAAGTA	GGCGGTCAGAGAACAAACTA
GAPDH*	GTCTCCTCTGACTTCAACAGCG	ACCACCCTGTTGCTGTAGCCAA

Table 6-5: RT-qPCR gene primers and sequences

Lists the genes and their corresponding forward and reverse primers used for RT-qPCR. *Denotes housekeeping gene

6.2.3 Dynamic Magnetic Field Bioreactor

A DMF was applied using a bioreactor in CBIT, UPV. The DMF bioreactor, developed by BCMaterials (Basque Country, Spain) generates an alternating magnetic field (0-23 mT) through the displacement of a 48 well array formation of NdFeB magnets. A frequency of 0.3 Hz and 10 mm displacement were applied on a programme with a 16-hour active stimulation period, followed by 8 hours of rest during which the cells were exposed to a low SMF of approximately 23 mT. The active period was delivered in 30-minute cycles, comprising 5 minutes magnetic stimulation (magnetic plate displacement) followed by 25 minutes rest. Magnetic field strength was confirmed using HIRST GM08 gaussmeter with transverse probe (HIRST, UK).

6.2.4 Magnetic Hydrogel Fabrication

A naturally derived gelatin methacryloyl (GelMA) based hydrogel embedded with MNPs was employed to enable magnetic actuation. This section details the key materials used for hydrogel synthesis, the fabrication protocol for magnetic hydrogels and the enzymatic digestion process for RNA isolation from cell-laden hydrogels.

6.2.4.1 Magnetic Hydrogel Components

The key materials used for magnetic hydrogel synthesis and subsequent enzymatic digestion are summarised in **Tables 6-6** and **6-7** respectively. **Table 6-6** lists the components and materials required to prepare GelMA hydrogels, with embedded MSCs. **Table 6-7** details the reagents and solutions for hydrogel digestion and the removal of MNPs from the final digested suspension.

Hydrogel Fabrication Component	**Manufacturer**	**Catalogue Number**
Gelatin Methacryloyl (GelMA) – Porcine Skin	Gelomics, Australia	SASKU0010
Lithium phenyl-2,4,6-trimethylbenzoylphosphinate (LAP)	Sigma-Aldrich	900889-5G
fluidMAG-DX	Chemicell, Germany	4104-1
Polydimethylsiloxane (PDMS)	ConRo Electronics, UK	1673921

Dulbecco's Phosphate Buffer Solution (PBS) without Ca^{++}/Mg^{++}	Merck, Spain	59331C-1000ML

Table 6-6: Components used for magnetic hydrogel fabrication

Summarises the hydrogel components, and materials employed in the synthesis of GelMA-based magnetic hydrogels.

Hydrogel Digestion Component	Manufacturer	Catalogue Number
Collagenase D from *Clostridium histolyticum*	Merck Life Science UK Limited, UK	11088866001
Ethylenediaminetetraacetic acid (EDTA)	Merck, Spain	E6758-500G
NYZol	NYZtech, Portugal	MB18502
Chloroform (≧99.8%)	Scharlau, Spain	CL02002500

Table 6-7: Reagents used for enzymatic digestion of hydrogels

Details the components employed in the breakdown of GelMA hydrogels and subsequent removal of magnetic nanoparticles and other inorganic residues

6.2.4.2 Magnetic Hydrogel Fabrication

Hydrogels were fabricated as outlined in Section 2.5.2 (Magnetic Hydrogel Fabrication), except that UV crosslinking was performed using an alternative setup. Crosslinking was carried out in a custom-built UV chamber (~1.5 mW/cm^2) for 10 minutes at room temperature to initiate polymerisation (**Figure 6-1**). Following polymerisation, hydrogels were incubated in DMEM at 37°C until further use.

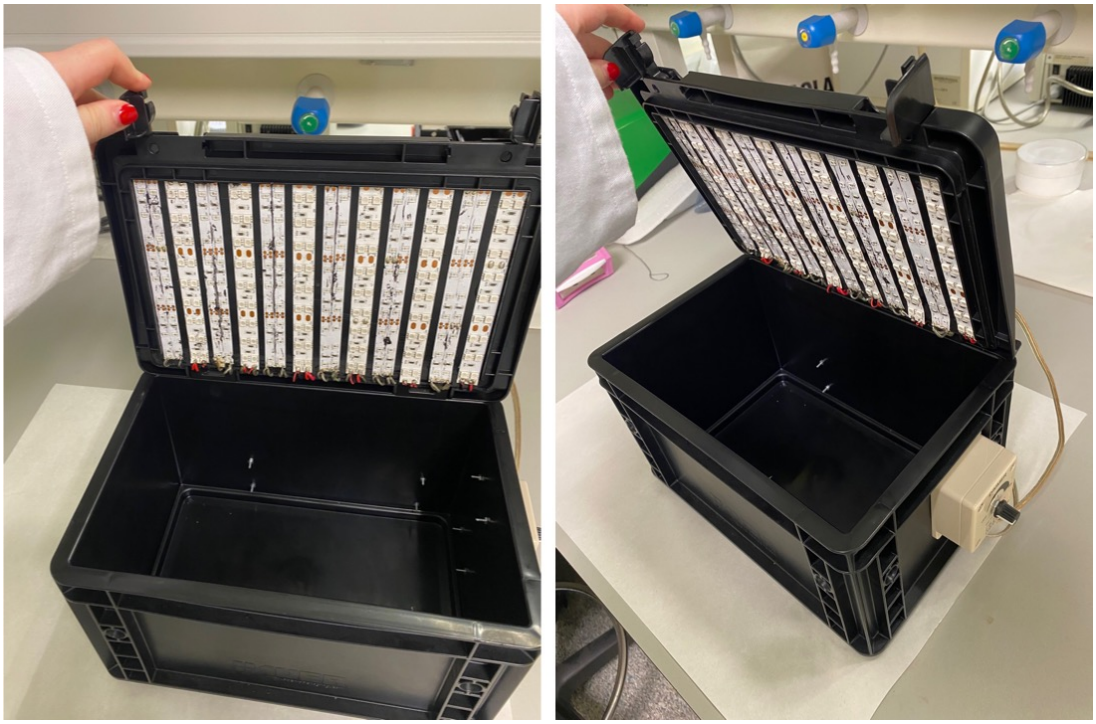

Figure 6-1: Custom built ultraviolet light crosslinker

Ultraviolet (UV) light crosslinker developed for researchers at CBIT, UPV. The UV light intensity at the bottom of the exposure chamber was measured at 0.2 mW/cm². However, positioning samples closer to the lid of the chamber increased exposure intensity to 1.5 mW/cm²

6.2.4.3 Magnetic Hydrogel Digestion and Cell Retrieval

RNA was extracted from hydrogels as described in Section 2.5.3 Magnetic Hydrogel: Digestion and Cell Retrieval, except that NYZol reagent (BioLine) was used in place of TRIzol for lysis and phase separation. All other steps, including enzymatic digestion with collagenase D, EDTA quenching and centrifugation were caried out as previously described.

6.2.5 Hydrogel Analysis

A range of mechanical, structural and surface characterisation techniques were employed to evaluate the physical properties of the hydrogels. The following subsections describe the methods used for assessing mechanical profiling, strength testing, wettability, and internal structure.

6.2.5.1 Rheology

A 20% w/v stock solution of unpolymerised GelMA was prepared as previously described (Section 6.2.4.2). Final GelMA concentrations of 7.5% and 10% w/v with MNP concentrations 0.25 mg/mL and 0.5 mg/mL, were prepared with 0.5% w/v LAP

photoinitiator and pipetted into the PDMS cylindrical moulds (13 mm diameter, 2 mm height). Samples were polymerised at the bottom of the UV chamber (~0.2 mW/cm^2) for 5 minutes and incubated in DMEM at 37 °C prior to testing.

Rheological measurements were conducted using an TA Instruments (DE, USA) rheometer, equipped with an 8 mm measuring plate. The gap was set by maintaining a contact force below 0.1N. All tests were performed at 37 °C. Storage modulus (G′) and loss modulus (G″) were measured over a frequency sweep, and a strain sweep of 0.01% to 20% to ensure measurements were within the linear viscoelastic region. Measurements were taken at 72 hours after polymerisation.

Measurements were repeated, and fabrication of hydrogels was completed as before however during crosslinking unpolymerised hydrogels were positioned closer to chamber lid, increasing exposure to 1.5 mW/cm^2 and crosslinking time increased to 10 minutes. Concentration of MNPs in hydrogels at this stage was reduced to 0.25 mg/mL with 0.5 mg/mL excluded from further measurements. Using the same rheological protocol the properties of these hydrogels were measured 72 hours after polymerisation. A final concentration at 10% w/v GelMA, with 0.25 mg/mL MNPs for magnetic system, was utilised for the following experiments.

6.2.5.2 Water Contact Angle

To investigate the biological compatibility of GelMA hydrogels synthesised with low crosslinking exposure, surface wettability was assessed *via* water contact angle measurements. GelMA hydrogels at 10% w/v with 0.25 mg/mL MNPs, as well as control hydrogels without MNPS, were prepared and polymerised. Measurements were performed 72 hours post-polymerisation. Contact angles were measured using a goniometer (Ossila). Prior to measurement, hydrogels were dried under ambient lab conditions for 5 minutes to improve consistency. Images were captured for 30 seconds at 20 frames per second with droplet rate was set at 2 µL/s. Analysis was completed using Ossila Contact Angle (version 4.1.5) after image capture to generate contact angle measurements (Young-Laplace).

6.2.5.3 Freeze Drying Hydrogel

To prepare hydrogels for analysis of internal structure using SEM, hydrogels were flash frozen by full immersion in liquid nitrogen and subsequently freeze-dried using a freeze

dryer (LyoQuest-85, Telestar), using the settings in **Table 6-8**. After freeze drying, samples were stored in parafilm sealed cell culture plates at room temperature until imaging.

Step	Ramp Rate	Shelf Temp (°C)	Time	Vacuum (mbar)
1	0.1	-10	2 hours	0
2	0.1	0	2 hours	0
3	0.1	5	∞	0

Table 6-8: LyoQuest-85 settings used for removal of fluid and drying hydrogels

Details the settings used on the LyoQuest-85 system for freeze drying of GelMA hydrogels

6.2.5.4 Scanning Electron Microscopy

Scanning electron microscopy (SEM) was performed at the Electron Microscopy Service (EMS), UPV using a Zeiss Ultra 55 (Carl Zeiss AG, Germany). Freeze dried hydrogel samples were mounted on aluminium pin stubs using conductive double-sided carbon tape. Samples were then prepared with a sputter coat of gold-palladium by EMS to improve surface conductivity. Imaging was conducted under high vacuum at an accelerated voltage of 5kV to examine both surface morphology and internal structure. TIF-format images were acquired using SmartSEM software.

6.3 Results

6.3.1 Mechanical Properties of GelMA Hydrogel Model

Magnetic hydrogels were prepared using local variations in equipment including a new UV crosslinker. Based on weaker crosslinking strength, these hydrogels were expected to be softer than previous formulations, with similar trends of increasing GelMA concentration improving mechanical properties, and addition of MNPs reducing mechanical properties, particularly with increased MNP concentration. Rheological measurements were performed to assess the effects of varying GelMA and MNP concentrations on hydrogel mechanical properties.

GelMA hydrogels with concentrations of 7.5% and 10% w/v, and MNP concentrations of 0.25 mg/mL and 0.5 mg/mL were examined using rheology. With 7.5% w/v GelMA concentration, G′ was 610 Pa at 72 hours post polymerisation. Adding 0.25 mg/mL MNPs increased G′ to 745 Pa indicating enhanced stiffness. However, increasing MNP concentration to 0.5 mg/mL significantly decreased G′ to 412 Pa, suggesting weaking of the

hydrogel. G″ followed a similar pattern, starting at 16 Pa, increasing to 17 Pa and decreasing to 13 Pa with 0.25 mg/mL and 0.5 mg/mL MNPs respectively. Increasing GelMA concentration to 10% w/v significantly increased G′ to 4271 Pa, although the wide range reflects greater hydrogel variability, compared to 7.5% w/v hydrogels. Adding MNPs reduced G′ to 1195 Pa and 803 Pa, for 0.25 mg/mL and 0.5 mg/mL respectively. Similarly, G″ increased in 10% w/v hydrogels, with 10% w/v GelMA at 67 Pa, and 52 Pa and 55 Pa with addition of MNPs (0.25 mg/mL and 0.5 mg/mL respectively) **(Figure 6-2, A)**.

A strain sweep was conducted from 0.01-20% to assess hydrogel strength under increasing strain. While 7.5% w/v hydrogels remained within their viscoelastic range, increased variability in G′ was observed with addition of 0.5 mg/mL MNPs. MNP concentrations showed increasing variation in G′ under increasing strain, in contrast to control hydrogels **(Figure 6-2, B)**.

Hydrogels were further examined following increased exposure to UV crosslinking, although 0.5 mg/mL MNP hydrogels were excluded at this stage. At 72 hours post polymerisation with increased crosslinking, G′ of 7.5% w/v GelMA increased to 921 Pa, which decreased to 754 Pa with addition of 0.25 mg/mL MNPs. G″ also increased to 57 Pa but showed a small decrease to 15 Pa with MNPs. For 10% w/v hydrogels, G′ decreased to 2015 Pa, with a narrower range indicating more consistent measurements; this was not affected by addition of MNPs. G″ remained at 74 Pa but increased to 155 Pa with MNP addition **(Figure 6-3, A)**. Under increasing strain, hydrogels with increased crosslinking showed stability in G′ under all conditions, with little variation between technical repeats **(Figure 6-3, B)**.

Tanδ values, were calculated from median G′ and G″ of measured hydrogels (**Table 6-9)**, were generally low across all GelMA conditions, remaining below 0.1. This indicates that the hydrogels maintain predominately elastic behaviour with the alternative crosslinking method.

Condition	**Control**
7.5% w/v GelMA	0.062
7.5% w/v GelMA + MNPs	0.020
10% w/v GelMA	0.038
10% w/v GelMA + MNPs	0.075

Table 6-9: Tanδ values of GelMA hydrogels with magnetic nanoparticles

Tanδ (=G″/G′) values of GelMA hydrogels (7.5% and 10% w/v) with 0.25 mg/mL magnetic nanoparticles (MNP) at 72 hours post polymerisation. Tanδ near 0 indicate the material shows more elastic behaviour, while close to 1 indicates viscous behaviour.

Due to improved consistency with measurements, the increased crosslinking protocol was utilised for subsequent hydrogel fabrications. With a limited supply of GelMA at this stage the 7.5% w/v condition was excluded, where all further experiments used the following two conditions: 10% w/v GelMA hydrogel (control) and 10% w/v GelMA hydrogel + 0.25 mg/mL MNPs.

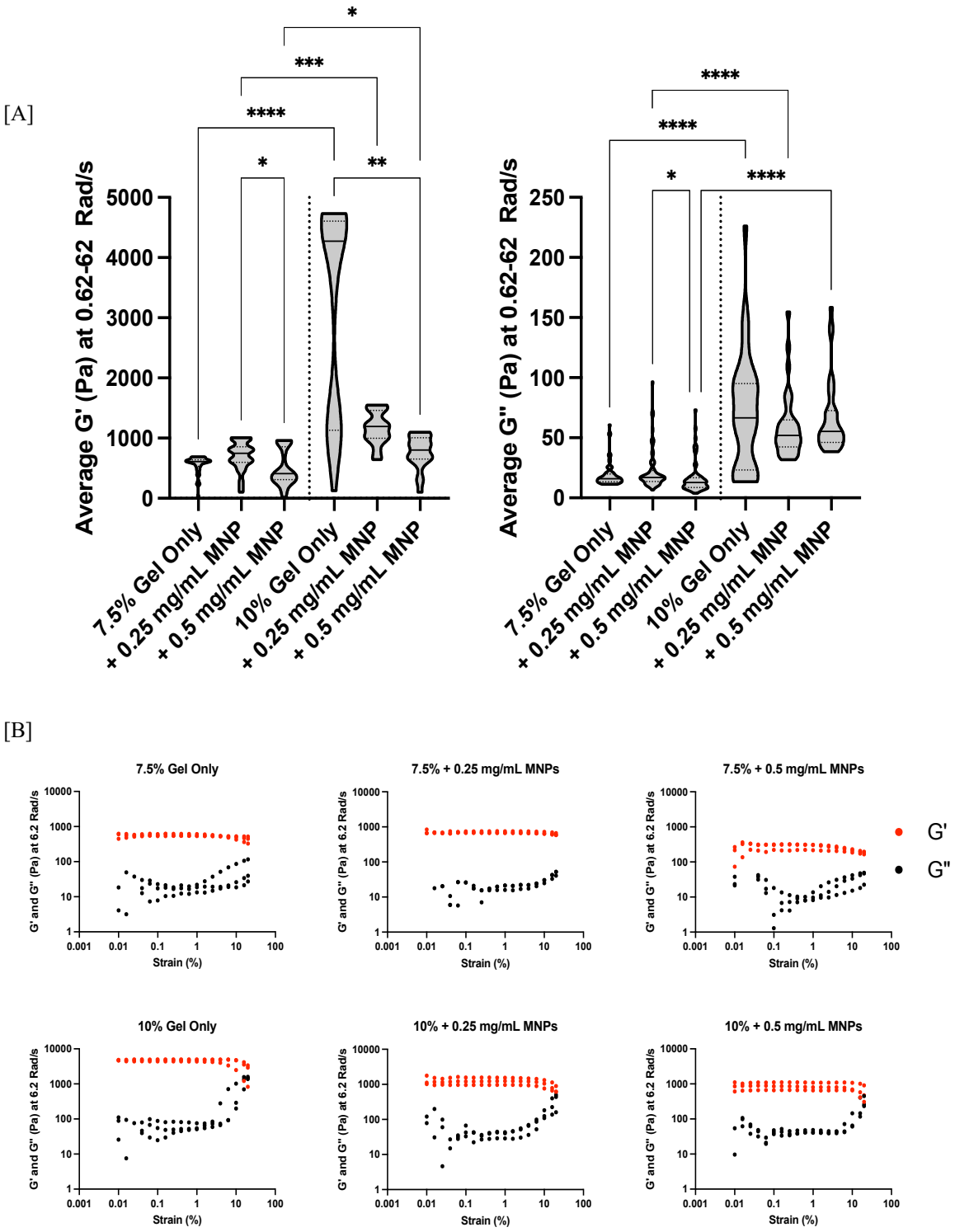

Figure 6-2: Mechanical properties are magnetic hydrogels are reduced with lower crosslinking exposure

GelMA hydrogels, 7.5% and 10% w/v, were prepared with 0.25 mg/mL and 0.5 mg/mL magnetic nanoparticles (MNPs). Measurements were obtained using a TA instruments rheometer. [A] Storage modulus (G′) and loss modulus (G″) were measured *via* strain sweep tests (0.01-0.1% strain, 1 Hz, 0.62-62 Rad/s). Truncated violin plots show distribution of G′ and G″ values with median (solid line) and interquartile range (dashed lines) (n=3). A Kruskal-Wallis test and post hoc Dunn's multiple comparison tests show significance between conditions [B] Amplitude sweeps of GelMA hydrogels, 7.5% and 10%

w/v, with addition of 0.25 mg/mL and 0.5 mg/mL magnetic nanoparticles (MNPs). Storage modulus (G′ – indicated by black circles) and loss modulus (G″ – indicated by red squares) were measured *via* strain sweep tests (0.01-20% strain, 1 Hz, 6.2 Rad/s) for hydrogels 72 hours post polymerisation (n=3).

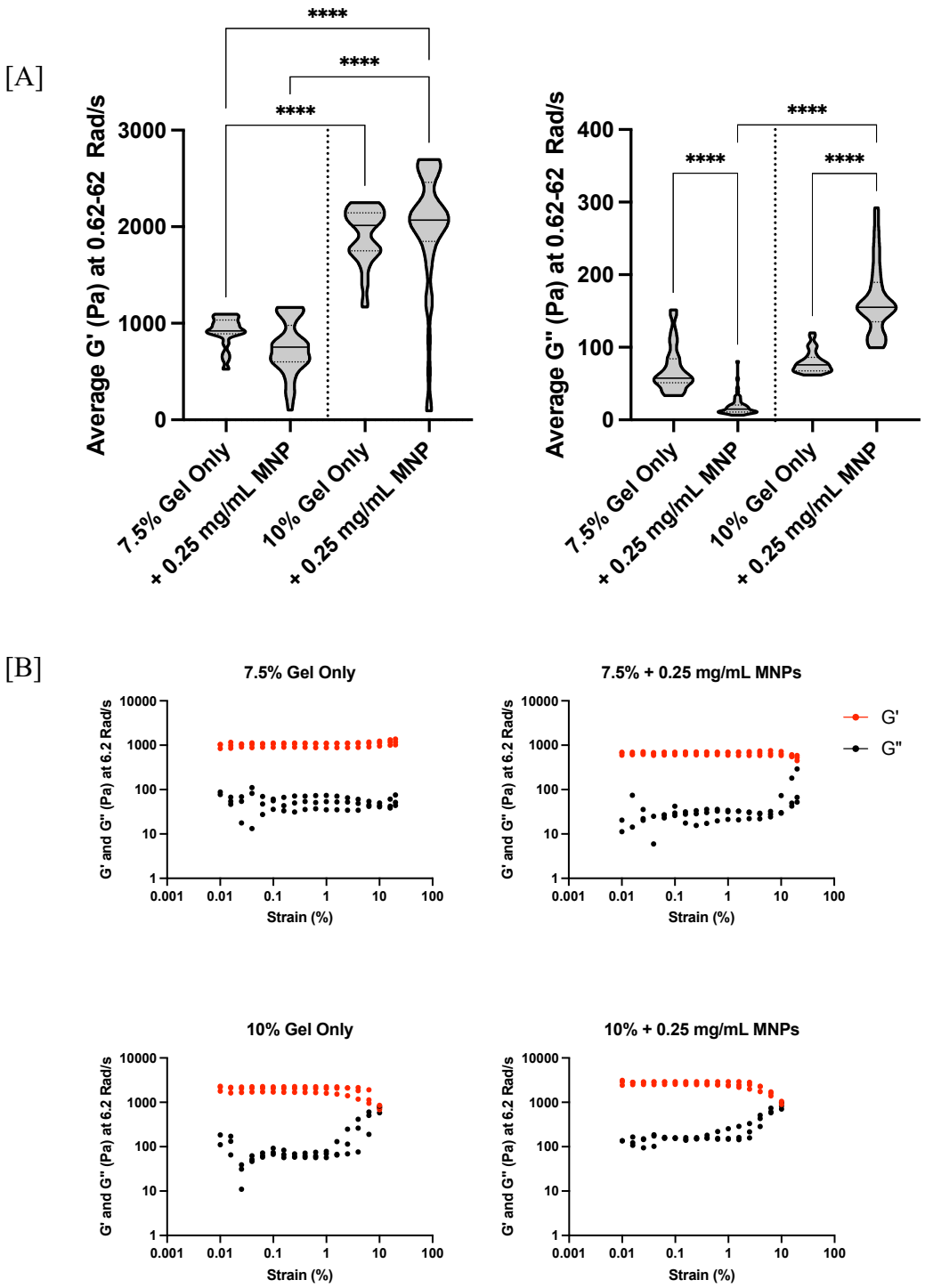

Figure 6-3: Mechanical properties of GelMA with magnetic nanoparticles improve after increased crosslinking exposure and duration

GelMA hydrogels, 7.5% and 10% w/v, were prepared with 0.25 mg/mL magnetic nanoparticles (MNPs) with increased exposure to ultraviolet crosslinking. Measurements were obtained using a TA instruments rheometer. [A] Storage modulus (G′) and loss modulus (G″) were measured *via* strain sweep tests (0.01-0.1% strain, 1 Hz, 0.62-62 Rad/s). Truncated violin plots show distribution of G′ and G″ values with median (solid line) and interquartile range (dashed lines) (n=3). A Kruskal-Wallis test and post hoc Dunn's multiple comparison tests show significance between conditions [B] Amplitude sweeps of GelMA hydrogels, 7.5% and 10% w/v, with addition of 0.25 mg/mL and 0.5 mg/mL magnetic nanoparticles

(MNPs). Storage modulus (G′ – indicated by black circles) and loss modulus (G″ – indicated by red squares) were measured *via* strain sweep tests (1-1000% strain, 1 Hz, 6.2 Rad/s) for hydrogels 72 hours post polymerisation (n=3).

6.3.2 Biocompatibility

To verify that the hydrogels remained biocompatible under new laboratory conditions, the effect of incorporating MNPs into GelMA hydrogels was assessed. Biocompatibility was evaluated using three complementary measures, wettability to confirm the hydrophilic nature, pore size and structure to ensure supportive environment for cell growth and MSC viability to confirm biocompatibility. Based on previous formations, hydrogels containing MNPs were expected to maintain hydrophilicity, retain open pore architecture without MNP aggregates and support MSC viability, demonstrating the material remained suitable for cell culture applications under local protocol variations.

6.3.2.1 Wettability

Wettability of GelMA hydrogels were measured using water contact angle measurements. Less than 90° corresponds to a hydrophilic material, with high wettability, while above 90° shows a hydrophobic material. Water contact angle measurements of 10% w/v GelMA hydrogels show a mean WCA of 51.9° (±2.4°). Addition of MNPs shows a statistically significant increase in WCA to 55.7° (±2.4°) **(Figure 6-4, A).**

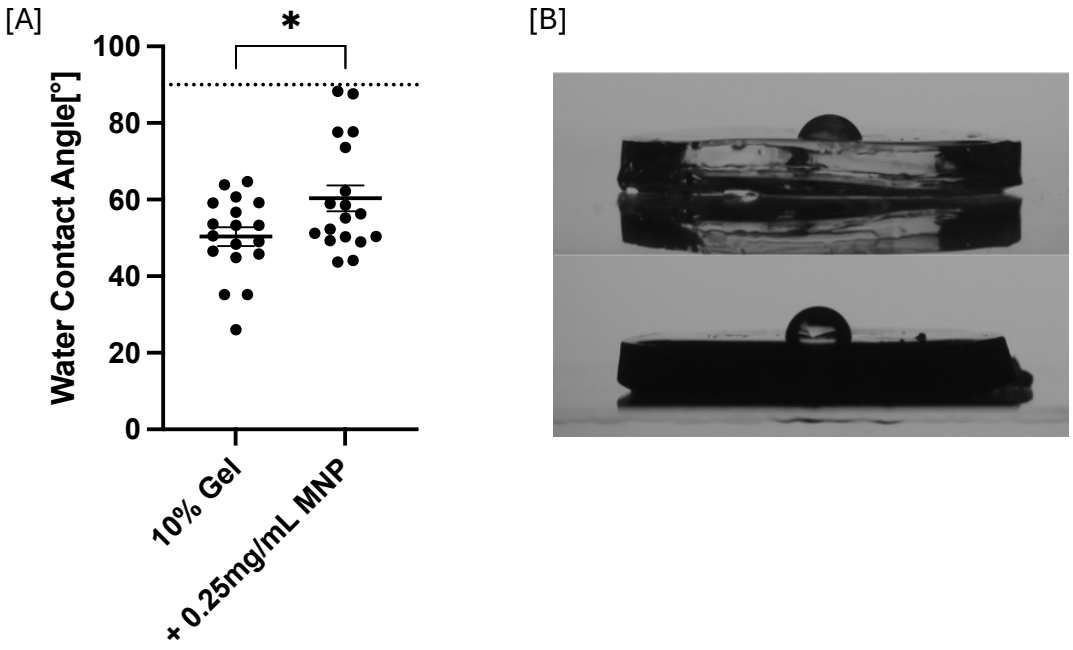

Figure 6-4: Wettability is maintained with reduced crosslinking exposure and duration

Wettability of 10% w/v GelMA hydrogels with 0.25 mg/mL magnetic nanoparticles (MNPs) were measured using water contact angle (WCA) measurements [A] WCA measurements from GelMA hydrogels were obtained (n=3). Dashed line shows 90°. Error bars show mean ± SEM. An unpaired t-test was completed to identify significance between conditions. [B] Captured images for analysis of water droplets on hydrogel surface. Top image: control, bottom image: MNP hydrogel

6.3.2.2 Hydrogel Morphology

SEM micrographs of GelMA hydrogels were collected for investigation of the hydrogel's internal structure. Pore diameter, pore area and pore circularity were measured from micrographs. The addition of 0.25 mg/mL MNPs to 10% w/v GelMA hydrogels significantly reduced mean pore diameter, from 39.6 µm to 35.3 µm, and mean pore area, from 1368 μm^2 to 986 μm^2. Circularity was measured, with all conditions ranging from 0.6-0.9 indicating a mixture of pore shapes. Pore circularity was significantly increased with the addition of MNPs, with control hydrogels showing mean circularity at 0.74 and MNP hydrogels showing an increase to 0.79 indicating a trend towards more circular pores in MNP hydrogels **(Figure 6-5)**.

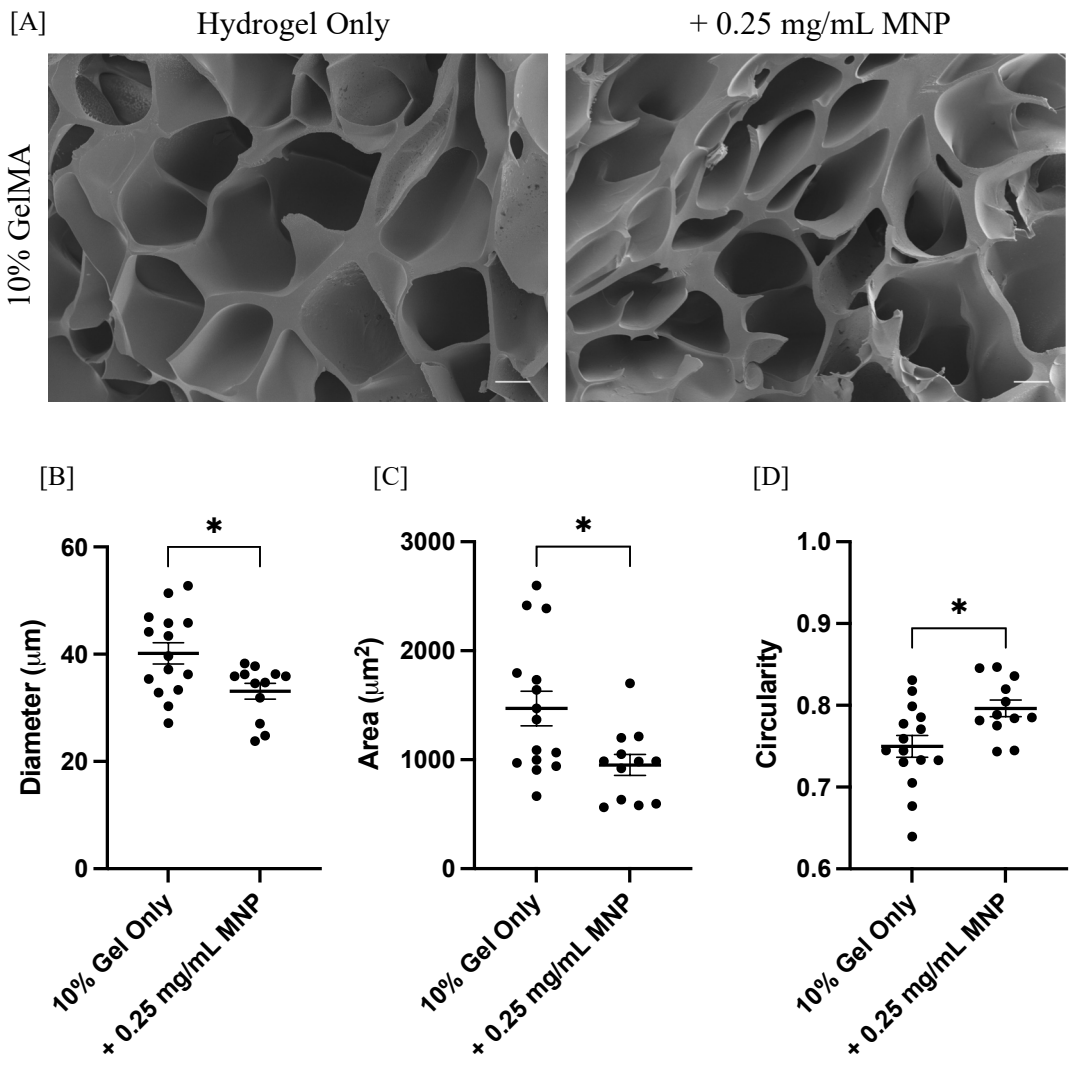

Figure 6-5: Hydrogel morphology is influenced by addition of magnetic nanoparticles

Freeze dried hydrogels were imaged using scanning electron microscopy (SEM) [A] SEM images of 10% w/v GelMA hydrogels with 0.25 mg/mL magnetic nanoparticles (MNPs) (n=3). Scale bar shows 20 μm. [B, C, D] Quantitative analysis of hydrogel morphology including pore diameter, area and circularity derived from SEM micrographs. Error bars show ± SEM. An unpaired t-test was completed to identify significance between conditions

6.3.2.3 Cell Viability

To investigate biocompatibility with MNPs, MSCs were embedded into hydrogels and cell viability was measured over 7 days. Light microscopy images of Calcein AM/ethidium-stained cells were collected at days 1, 3 and 7. Live cells were stained green with Calcein AM and dead cells stained with ethidium homodimer.

Cell viability was maintained in all hydrogels over 7 days with no significance identified between conditions. The only difference to note what that the variation in viability increased

with time in culture. In control hydrogels, day 1 viability was ~97.0% and ~98.2% in MNP hydrogels. Viability showed limited change at day 3, with ~95% viability in control hydrogels and ~95.1% in the MNP hydrogels. By day 7 viability was maintained at 97.2% and 98.2% in control and MNP hydrogels respectively. Unfortunately, due to limited GelMA availability long term viability could not be investigated.

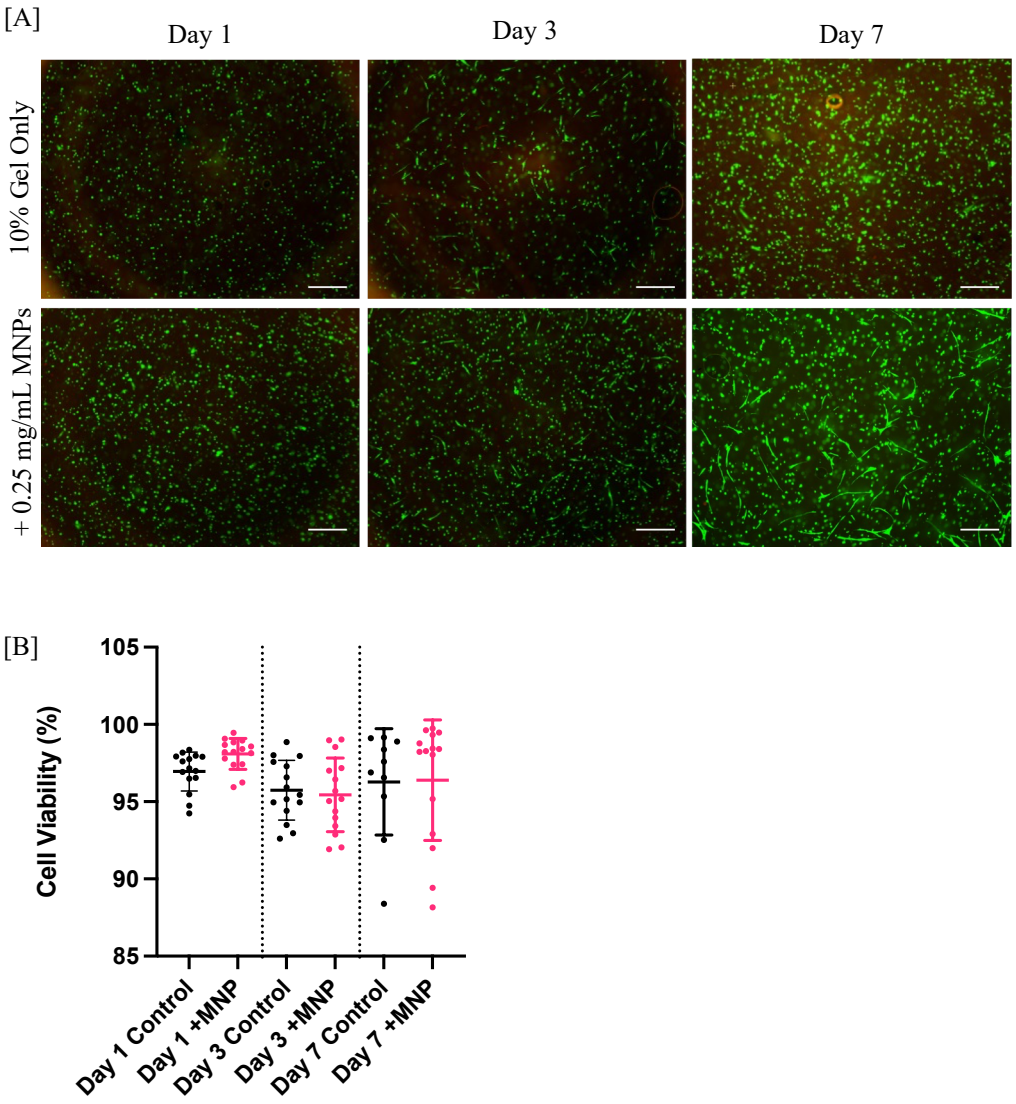

Figure 6-6: Mesenchymal stromal cell viability is maintained in GelMA over 7 days with increased crosslinking exposure and duration

Viability of mesenchymal stromal cells (MSCs) in GelMA hydrogels was assessed using LIVE/DEAD staining [A] Representative Live/Dead fluorescence microscopy images of MSCs stained with Calcein AM (live cells, green) and Ethidium homodimer-1 (dead cells, red) captured with Nikon Eclipse 80i fluorescent microscopy; scale bar shows 100 µm. [B] Quantification of cell viability (% live cells) calculated from fluorescence images. Error bars represent mean ± SEM. A one-way ANOVA and post hoc Tukey test was performed to identify significance between conditions

6.3.3 Osteogenic Commitment under a Dynamic Magnetic Field

Application of dynamic magnetic field resulted in MSCs showing some early commitment to an osteogenic lineage over 7 days. Based on these preliminary results, osteogenic commitment of MSCs in hydrogels under a DMF was investigated over 14 and 28 days. Hydrogels were digested and RNA was isolated and processed for RT-qPCR. Gene expression of both early and later osteogenic markers was measured and compared to control

(-MNP -DMF hydrogels). Due to limited technical repeats, no statistical analysis was performed.

For early osteogenic markers, ALP was downregulated in MSCs exposed to MNPs and/or DMF at day 14 but showed marked upregulation by day 28 across all conditions. Additionally, RUNX2 followed a similar trend, showing an initial downregulation at day 14, then upregulation compared to control levels at day 28. Furthermore, the later osteogenic marker OPN was also upregulated at day 28, supporting a move towards osteogenesis with the magnetic model is stimulated with a DMF.

The DMF alone did not indicate gene changes that differed from control, except with a marked increase in ALP at day 28. When considering signalling, BMP2 was actually reduced in all timepoints, and COL1 production did not indicate a change in magnetic hydrogels compared to control hydrogels.

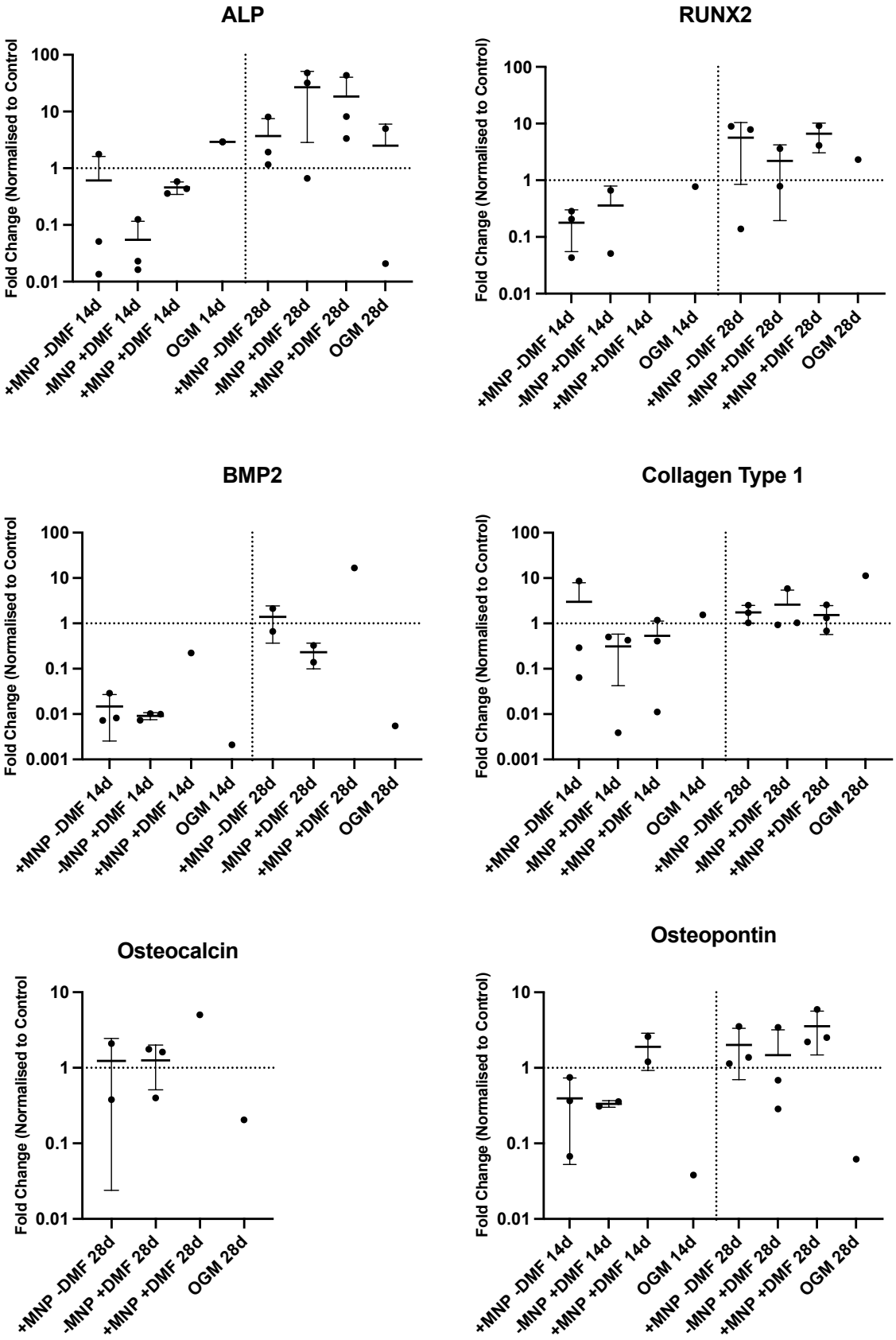

Figure 6-7: Exposure to a dynamic magnetic field shows minimal osteogenic gene expression compared to control

Mesenchymal stromal cell (MSC) commitment to osteogenic lineages in magnetic GelMA hydrogels was investigated over 28 days under dynamic magnetic field (DMF) actuation. MSCs were embedded in 7.5%

w/v GelMA hydrogels with or without magnetic nanoparticles (MNPs) and exposure to a SMF. Gene expression under magnetic fields over 28 days (n=1). Fold change was normalised to control. Bars represent mean, error bars represent SEM. Note that day 14 control measurements do not have Osteocalcin present and therefore are absent, and RUNX2 does not have +MNP +DMF at day 14.

6.4 Discussion

Chapter 5 demonstrated that an intermittent static magnetic field (SMF) for one hour per day was sufficient to stimulate an osteogenic response in MSCs within the magnetic hydrogel model optimised in Chapter 3. In the third year, of my PhD there was an opportunity to use a DMF bioreactor during a placement in CBIT, UPV. This aligned well with the overarching aims of my thesis; therefore, this chapter aimed to investigate the MSC response to a DMF within the magnetic hydrogel model.

As this work was conducted in a different lab, there were inevitably some variations in materials and methods, despite best efforts to standardise conditions. Notably a different UV crosslinker source was used, resulting in altered hydrogel properties and limitations in the availability of key materials reduced the number of biological replicates. Consequently, there are some differences in the data generated. Whilst direct comparisons with the SMF data cannot be made, the results presented in this chapter provide valuable insights into how a DMF may influence MSCs within the magnetic hydrogel model.

6.4.1 Dynamic Magnetic Field Regimes

In this study, a DMF was applied using a bioreactor developed by BCMaterials (Basque Country, Spain) for CBIT, UPV. The system generates a magnetic field, ranging from 0 to 23 mT by displacing an array of NdFeB magnets beneath a 48-well plate. The applied regime involved a frequency of 0.3 Hz and 10 mm displacement, delivered in a regime consisting of a 16 hour active period, followed by 8 hours rest. During the active period, magnetic stimulation occurred in 30 minute cycles with 5 minutes of magnetic displacement, followed by 25 minutes of rest. During the rest period, cells were exposed to a low SMF of approximately 23 mT (**Figure 6-8**).

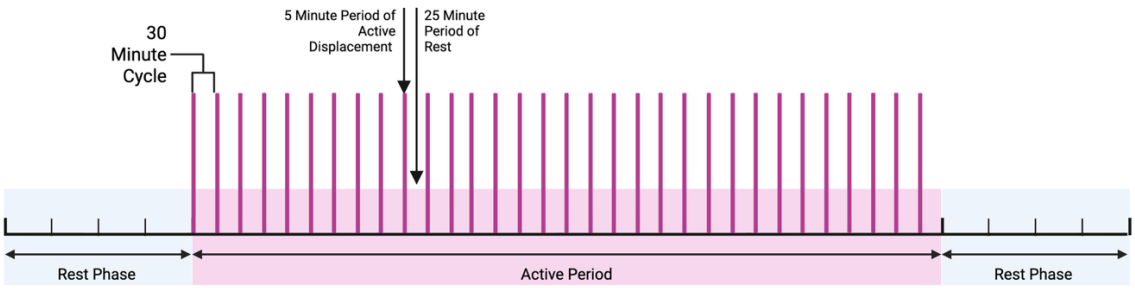

Figure 6-8: Schematic representation of bioreactor stimulation over a 24-hour period

The applied regime consisted of a 16-hour active period, followed by an 8-hour rest phase. During the active period, the bioreactor operated 30-minute cycles, each comprising 5 minutes of magnetic displacement, and 25 minutes of rest. This pattern was repeated continuously throughout the experimental duration. Created with Biorender.com

Two main types of DMF are typically reported in the literature:

(1) **pulsed or alternating electromagnetic fields**, characterised by switching the magnetic field on and off without physical movement, often involving variations in both intensity and direction.

(2) **magnetically driven dynamic culture systems**, which involve mechanical movement facilitated by magnetic components (Hao, et al., 2021; Tsai, et al., 2019; Varani, et al., 2021).

The DMF applied in this study falls into the latter category, as it relies on mechanical displacement of magnets to generate the alternating magnetic field (Guillot-Ferriols, et al., 2024). **Table 6-10** summarises the types of DMF systems discussed within this chapter.

Pulsed magnetic fields vary in strength but not direction, whereas alternating magnetic fields can vary in both strength and direction. Both are forms of low frequencies electromagnetic stimulation commonly used to promote bone healing and tissue regeneration (Guan, et al., 2024). Alternating magnetic fields in particular have been shown to promote osteogenic differentiation (Creecy, et al., 2012). These fields typically employ specific waveforms which create a time varying magnetic environment, inducing secondary electric fields in tissues and mimicking natural bioelectric signals (Varani, et al., 2021).

Dynamic culture systems aim to improve tissue engineering approaches by providing physical stimuli that enhances stem cell differentiation and nutrient exchange, surpassing the capabilities of static cultures. Traditional mechanical methods, such as stirring, may introduce sheer stress damage to cells or scaffolds, In contrast, magnetically driven dynamic

culture uses magnetic scaffolds embedded with nanoparticles that can be remotely actuated by an external magnetic field. This enables controlled, contact-free mechanical stimulation, reducing the risk of damage, making it a promising strategy for bone regeneration (Hao, et al., 2021; Tsai, et al., 2019).

Our regime employed a relatively low frequency in combination with a magnetic field strength of 23 mT. The stimulation was intermittent, consisting of a dynamic active phase followed by a rest phase, during which samples remained exposed to a 23 mT SMF. Hao et al., (2021) applied continuous magnetic fields of 5, 20 and 50 mT in their dynamic culture system. In contrast, our system used a controlled cyclic regime with defined stimulation and rest intervals. Interestingly, Aldebs et al., (2020) cultured control groups on their DMF bioreactor without activation, effectively exposing them to a SMF without dynamic stimulation. While our system did not include this specific control condition, including such a control in future studies could help delineate the effects of the dynamic component versus static exposure.

Type of Magnetic Field	Field Properties			Field Regime		Reference
	Strength	Frequency	Displacement	Exposure time	Duration	
Dynamic culture system	0.23 mT	0.3 Hz	10 mm	16 hours per day	14 and 28 days	Section: 6.2.3
Pulsed	1 mT	15 Hz	n/a	10 minutes, up to three times daily	4 days	(Celik, et al., 2021)
Alternating	0.3 mT	15 Hz	Sinusoidal	4 hours daily	7 days *in vitro*	(Li, et al., 2021)
Alternating	1 mT	45 Hz	Sinusoidal	8 hours per day	Up to 10 days	(Kim, et al., 2020)
Alternating	31.4 µT 62.8 µT	50 Hz	Sinusoidal	1 hour per day	48 hours	(Shapourzadeh, et al., 2020)
Pulsed	1 mT	15 Hz	n/a	8 hours per day	21 days	(Aldebs, et al., 2020)
Alternating	2 mT	60 Hz	Not defined	20 minutes	7 days *in vitro*, 14 days *in vivo*	(Guo, et al., 2025)
Alternating	1.7 mT	Not defined	Not defined	5 minutes	Up to 28 days	(Wang, et al., 2022)
Alternating	1 mT	15 Hz	Sinusoidal	4 hours per day	Up to 7 days	(Chen, et al., 2019)
Dynamic culture systems	5 mT 20 mT 50 mT	Not defined	Not defined	Constantly	Up to 14 days	(Hao, et al., 2021)

Table 6-10: Summary of magnetic field types, parameters and exposure regimes used in osteogenic studies

Studies are organised by magnetic field type: alternating, pulsed and dynamic culture systems. Where available, field properties such as strength, frequency, and displacement of magnetic system. In addition, exposure time (within 24 hours) and the experiment duration are included.

6.4.2 Dynamic Magnetic Field Promotes Osteogenic Gene Expression

The effects of DMF on the osteogenic differentiation of MSCs were investigated over 14 and 28 day periods using our magnetic GelMA hydrogel model within a dynamic culture system. Gene expression analysis of early and late osteogenic markers revealed time and condition dependent responses.

MSCs exposed to a DMF showed trends toward expression of key osteogenic markers, particularly at day 28, which may indicate a shift towards osteogenic commitment. While early markers like ALP showed variable trends, later stage markers (RUNX2, COL1 and OPN) were generally upregulated in the magnetic GelMA model under DMF. These preliminary findings suggest a potential synergistic effect of MNPs and DMF on osteogenic differentiation; however, the experiments were performed using a single biological replicate and further repetition is necessary to confirm these findings. Future studies should incorporate additional biological replicates, protein-level analyses, and functional assays, such as Alizarin Red S staining to determine whether these transcriptional changes correspond to functional osteogenesis.

Previous studies have explored the use of MNPs embedded within hydrogel scaffolds to enhance osteogenesis under DMF stimulation. For example, Wang et al., (2022) embedded RGD coated MNPs into agarose hydrogels and applied an alternating DMF (~1.7mT) to induce mild hyperthermia. This significantly upregulated osteogenic genes (ALP, RUNX2, and COL1) *via* the PI3K/AKT and MAPK pathways, while also promoting angiogenesis (Wang, et al., 2022). Li et al., (2022) incorporated MNPs into a 3D printed PVA/sodium alginate/HA scaffold, demonstrating strong ALP expression and matrix mineralisation after DMF exposure, with sustained biocompatibility over 21 days, regardless of MNP concentration (Li, et al., 2022) Additionally, Guo et al., (2025) developed a phosphate modified PGS scaffold, reinforced with MNP (iron oxide) laden hydrogel. Under DMF exposure (2 mT, 60 Hz), the model promoted osteogenic differentiation of MSCs, *via* activation of Piezo1/YAP/β-catenin mechanotransduction pathways (Guo, et al., 2025).

Aldebs et al., (2020) embedded MSCs into self-assembling RADA16 hydrogels containing iron oxide MNPs (10 nm, 0.5% w/v), and applied a pulsed DMF (1mT, 15 Hz) for 21 days. They observed a significant increase in ALP activity in magnetic scaffolds when combined with the DMF, particularly from day 21 (Aldebs, et al., 2020). Together these studies support the potential of MNP loaded hydrogels combined with DMF stimulation to promote

osteogenic differentiation, despite differences in exposure duration, field strength and frequency

Similarly, Hao et al., (2021) investigated a dynamic culture system, utilising 5, 20 and 50 mT magnets on magnetic chitosan-based scaffolds embedded with iron oxide MNPs. They found that 5 mT and 20 mT magnetic field significantly enhanced osteogenic differentiation, while 50 mT showed no significant effect compared to non-magnetic control (Hao, et al., 2021). Dong, et al., developed a magnetically responsive GelMA-based artificial periosteum (fibrous membrane surrounding bones) incorporating iron oxide MNPs that mimics the mechanical environment of the natural periosteum through controlled magnetic stretching. The remote application of a 200 mT SMF provided tensile stimulation, significantly enhancing osteogenic differentiation *via* MAPK/ERK activation (Dong, et al., 2025). These studies highlight the potential of magnetically enhanced dynamic culture systems to promote osteogenic differentiation.

Several groups have investigated the effects of DMFs on osteogenesis using hydrogels and scaffolds without embedded MNPs. Shapourzadeh et al., (2020) utilised a carboxymethyl cellulose grafted polycaprolactone scaffold seeded with ADSCs. When exposed to an alternating DMF (31.4 or 62.8 μT, 50 Hz) for 14 days, they observed enhanced osteogenic differentiation *via* increased matrix mineralisation (Shapourzadeh, et al., 2020). Similarly, Chen et al., (2019) developed a PCL/HA implant and applied an alternating DMF (1 mT, 15 Hz, 4 hours per day) both alone and in combination with VEGF. The magnetic stimulation significantly increased ALP activity, and upregulated osteogenic markers (OPN, COL1, RUNX2), with the effects linked to activation of the Wnt/β-Catenin signalling pathway (Chen, et al., 2019). Li et al., (2021) also reported enhanced osteogenesis using PCL and nano HA scaffolds, with embedded MSCs. An alternating DMF (0.3 mT, 15 Hz) for 4 hours daily increased expression of ALP, collagen production and calcium deposition via BMP and MAPK pathway activation (Li, et al., 2021). These studies suggest that magnetic stimulation alone, even without addition of MNPs, can enhance osteogenic differentiation through multiple intracellular pathways. This complements MNP-based studies and underscores the multifaceted role of magnetic cues in bone tissue engineering.

Kim et al., (2020) examined the effects of alternating DMF (1 mT, 45 Hz, 8 hours per day) combined with MNPs (10-14 nm, 50 μg/mL) on Saos-2 cells cultured without a 3D scaffold. They reported enhanced expression of osteogenic markers (OCN, ON, OPN), with the combination of DMF and MNPs produced synergistic effects promoting osteogenesis both

in vitro, and *in vivo* (Kim, et al., 2020). This demonstrates that even in the absence of a 3D scaffold, the interplay between MNPs and DMFs can effectively drive osteogenic differentiation.

While our focus has been on osteogenesis, DMF stimulation has also been shown to influence other MSC lineages. Celik et al, (2021) demonstrated that a single 10 minute exposure to a 1 mT pulsed DMF significantly promoted chondrogenesis in MSC seeded scaffolds. Interestingly, this one-time exposure was more effective than repeated exposures, significantly increasing the expression of key chondrogenic markers (SOX9, COLII and ACAN) (Celik, et al., 2021). Additionally, Song et al., demonstrated that DMFs (3 mT) enhanced early chondrogenic differentiation of MSCs in 2D culture by upregulating chondrogenic markers (ACAN, COLII), particularly at day 7. These effects were linked to the modulation of the Wnt/β-Catenin pathway *via* upregulation of sFRP2 which antagonises β-Catenin signalling (Song, et al., 2024). Together, these findings suggest that DMF stimulation can direct lineage specific differentiation depending on the exposure regime and experimental context.

It is noted that several of the studies applied linage specific differentiation media to both control and magnetic conditions, meaning the observed cellular responses cannot be attributed solely to the DMF, but rather reflect an enhancement of the chemically induced differentiation. For instance, chondrogenic differentiation media was used in Celik et al., (2021), and osteogenic differentiation media was applied in Aldebs et al., (2020), Chen et al., (2019), Guo et al., (2025) and Li et al., (2022), among others. In contrast, our study used standard cell culture media without differentiation supplements, with osteogenic media reserved only for the positive control. This suggest that the osteogenic gene expression observed in our magnetic GelMA hydrogels under DMF reflects a direct response to magnetic cues and MNPs, independent of exogenous chemical induction.

6.4.3 Conclusion: Role of Dynamic Magnetic Fields and Magnetic Nanoparticles in Promoting Osteogenesis

Overall, the collective evidence suggests that DMFs, particularly when combined with MNPs may contribute to enhanced osteogenic differentiation through multiple mechanotransducive pathways. In our dynamic culture system, the findings tentatively indicate that magnetic stimulation could promote osteogenic commitment even in the absence of exogenous differentiation supplements. Future studies should include functional

assays such as mineralisation and investigate the underlying signalling pathways to better understand the mechanisms involved to further elucidate the role of magnetic stimulation in bone tissue engineering.

Chapter 7: Magnetic Hydrogels for Bone Tissue Engineering

7.1 Project Summary

As outlined in Chapter 1, this project aimed to explore the potential of magnetic hydrogels, in combination with external magnetic fields, to enhance osteogenesis in MSCs. The central hypothesis was that the synergistic effect of an externally applied magnetic field and a magnetic hydrogel scaffold would accelerate and improve the differentiation of MSCs towards a bone-forming lineage.

The motivation for this study stems from the growing clinical demand for effective BTE solutions. With increasing global life expectancy, there is a corresponding rise in bone-related injuries, degenerative conditions and surgical interventions, requiring tissue grafts. While traditional grafting methods can be effective, they face several limitations such as donor site morbidity, limited graft availability and potential immune rejection. Therefore, developing alternative, biomimetic strategies – such as magnetic hydrogels - offers a promising avenue for improving bone regeneration

Moreover, understanding the cellular and molecular mechanisms through which MSCs respond to magnetic stimuli provides a foundation for innovative therapeutic strategies. This knowledge could lead to non-invasive, controllable methods for enhancing tissue repair and regeneration, thereby expanding the scope of regenerative medicine.

Throughout this project, progress was made toward engineering a magnetic hydrogel model, demonstrating not only the biocompatibility and functionality of the scaffold, but also providing preliminary evidence that magnetic stimulation can modulate MSC behaviour in ways conducive to osteogenesis. These findings contribute valuable insights into the design of advanced biomaterials that integrate physical cues into BTE strategies.

The overarching aims of this project were to:

- **Investigate MSC response to magnetic fields (Chapter 3):** Intermittent SMFs enhanced MSC proliferation, maintained migration, and promoted osteogenic commitment through BMP signalling, while other magnetic regimes showed limited or transient effects.

- **Develop and characterise magnetic GelMA hydrogels (Chapter 4):** Biocompatible, porous and elastic GelMA hydrogels incorporating superparamagnetic MNPs supported MSC viability and 3D culture, providing a scaffold suitable for remote magnetic stimulation.
- **Investigate the effects of static magnetic stimulation on MSCs within GelMA hydrogels (Chapter 5):** SMF and MNPs appear to synergistically enhance osteogenic gene expression and modulate hydrogel stiffness, with single MSCs responding more strongly than spheroids.
- **Investigating MSCs response to a dynamic magnetic field (Chapter 6):** Dynamic magnetic fields applied *via* a bioreactor appear to promote time dependent upregulation of osteogenic genes expression, particularly at later stages.

7.1.1 MSC Response to Magnetic Fields

Chapter 3 examined how different types of magnetic fields influence MSC behaviour – as essential aspect of BTE. Intermittent SMF exposure appeared to enhance MSC proliferation with trends towards upregulation of cell cycle promoters and downregulation of inhibitors, whereas constant SMFs and DMFs showed only transient effects. In migration assays, intermittent SMF supported wound closure at levels comparable to controls, whereas constant SMF slowed MSC migration and DMF significantly impaired migration. Gene expression revealed field-specific regulation of migration-related genes like Rac1 and RhoA.

Osteogenic commitment was most pronounced under intermittent SMF, with trend towards upregulation of early and late osteogenic markers, potentially mediated by BMP signalling. Other lineage markers were suppressed, while moderate activation of hypoxia and angiogenic pathways suggested a broader regenerative response.

Magnetic fields also influenced paracrine signalling. Intermittent SMF showed a strong but transient pro-inflammatory secretome; constant SMF exposure showed signs of metabolic stress; and DMF produced a more balanced profile of inflammatory and regenerative factors. It should be noted however that these interpretations are limited by the semi-quantitative nature of the cytokine assay and therefore provide inductive trends rather than definitive profiles. Evaluation of EVs from cell media showed that intermittent and constant SMF exposure generally preserved EV size and concentration, whereas DMF disrupted these parameters.

In summary, application of an intermittent SMF appeared to enhance key MSC functions - including proliferation, migration and early bone differentiation – with effects that may be mediated through BMP signalling and possibly YAP-mediated mechanotransduction. These findings suggest that intermittent SMF exposure for 1 hour per day could have potential in in MSC based regenerative approaches, although further studies are required to substantiate these findings.

7.1.2 Magnetic GelMA Hydrogel

Chapter 4 details the development of GelMA hydrogels incorporating dextran-coated MNPs to create magnetic, mechanically responsive scaffolds. MNPs exhibited dual magnetic behaviour: ferromagnetic under high magnetic fields and superparamagnetic under moderate fields, allowing reversible particle oscillation without aggregation.

The engineered GelMA hydrogels demonstrated bone marrow-like stiffness, elastic mechanical properties and supported uniform MNP dispersion throughout the matrix. The impact of MNP incorporation on hydrogel structure was dependent on GelMA concentration; higher MNP concentrations slightly reduced stiffness, potentially due to minor interference with the photo-crosslinking process. Both GelMA formulations (7.5% and 10% w/v) were porous and hydrophilic, promoting nutrient diffusion and MSC viability in the presence of MNPs. MSC spheroids maintained their shape and viability within the hydrogels, confirming suitability for 3D culture.

Overall, the magnetic GelMA hydrogels developed in this chapter are biocompatible, elastic and porous, offering natural adhesion sites that support MSC function. The embedded MNPs enable the potential for remote magnetic stimulation, making these hydrogels a promising platform for BTE applications.

7.1.3 The Effects of Static Magnetic Stimulation in on MSCs within GelMA Hydrogels

Chapter 5 examined how MNPs and SMFs influence the mechanical properties of GelMA hydrogels and osteogenic MSC differentiation over time. Hydrogel stiffness increased in the presence of MSCs and MNPs and was further enhanced by constant SMF exposure in cell-laden hydrogels. In contrast, acellular hydrogels remained largely unaffected by SMFs.

While the hydrogels retained predominantly elastic behaviour throughout, long term exposure to intermittent SMF slightly reduced stiffness.

MNPs and SMF each appeared to be associated with increased osteogenic gene expression, with the most pronounced effects on day 28 when both were applied in combination. Higher GelMA concentrations appeared to show more intense calcium staining, even in the absence of magnetic actuation; however, staining intensity tended to be highest under SMF stimulation. Over the 28-day culture period, stiffness increased with GelMA concentration. Interestingly, while MNPs and SMF alone enhanced stiffness, their combination unexpectedly reduced it - likely due to MSC mediated matrix remodelling. When comparing MSC configurations, dispersed MSCs tended to show stronger expression of osteogenic and stemness markers under SMF stimulation, whereas MSC spheroids appeared less responsive. Stemness markers were generally maintained over time, which may indicate level of self-renewal occurring alongside differentiation.

In summary, the combination of MNPs and SMF appeared to promote osteogenic differentiation within GelMA hydrogels, suggesting their potential as magneto-responsive biomaterials for BTE applications.

7.1.4 MSCs Response to a Dynamic Magnetic Field

In Chapter 6, the DMF was applied using a bioreactor that generated a magnetic field of 23mT through mechanical displacement of NdFeB magnetics in a 48 well plate. The stimulation protocol included a period of active magnetic displacement, followed by a rest phase under a low SMF. Over 14 and 28 days, gene expression analysis showed time- and condition-dependent increases in osteogenic markers under DMF, especially at day 28. Early markers such as ALP showed variable trends, while late-stage makers were generally upregulated in hydrogels containing MNPs exposure to DMF, which may suggest a trend towards osteogenic commitment. However, these findings should be interpreted cautiously, as they are based on a single biological repeat and therefore tentative, and indictive of possible effects rather than definitive outcomes. Further validation, including protein level analysis and quantitative assessment of mineralisation, is required to confirm that osteogenic gene expression translates into functional osteogenesis.

7.2 Final Discussion

We have developed a magnetically responsive bone marrow model that aims to mimic the bone microenvironment by providing dynamic mechanical stimulation and supporting osteogenic gene expression, evidence of mineralisation and maintenance of stemness under an intermittent SMF. Taken together, these observations suggest that the system may have potential for future applications in BTE and regenerative medicine.

7.2.1 Integrating 2D and 3D findings:

This project provides preliminary evidence that magnetic stimulation, particularly an intermittent SMF, may promote osteogenic differentiation. This effect was observed across both 2D and 3D systems, although it is important to note a limitation in the experimental time frames: up to 7 days for 2D culture and up to 28 days in 3D cultures.

In chapter 3, intermittent SMF upregulated osteogenic markers in 2D culture potentially *via* BMP signalling. In chapter 5, combining MNPs with SMF in GelMA hydrogels promoted upregulation of some osteogenic markers and showed evidence of matrix mineralisation in 3D. While most existing studies apply a constant SMF to 3D cultures, our decision to use intermittent SMF was based on its efficacy in 2D systems and the desire to assess whether shorter, less invasive stimulation could produce comparable osteogenic benefits in 3D.

In 2D cultures, BMP signalling emerged as a key mediator of osteogenic differentiation under intermittent SMF. However, 3D cultures induce new biophysical parameters – such as stiffness gradients and spatial confinement – that may modulate mechanotransducive signalling. It remains unclear whether BMP signalling remains dominant in 3D, or whether pathways like MAPK, Wnt/β-catenin or YAP/TAZ are also involved. Future studies should aim to elucidate these pathway contributions.

The model we have developed provides an adaptable research tool for investigating the complex effects of magnetic stimulation on stem cell differentiation. Its flexibility allows researchers to systematically test how variations in SMF duration type can influence cell behaviour across different culture conditions. Although a constant SMF was not tested over 28 days in GelMA hydrogels, future work could compare the long-term effects of intermittent vs constant SMF exposure in 3D environments. This is particularly relevant given findings by Bloise et al (2018), which showed that transitioning from 2D to 3D-substrate culture enhanced osteogenic responses under the same magnetic regime -indicating

a substrate-specific response (Bloise, et al., 2018; Petecchia, et al., 2015). As discussed in Chapter 4, Yan et al., (2022) also observed that application of a moderate magnetic field increased hydrogel stiffness, promoting two future directions for our model:

1. **Investigative SMF-induced changes in stiffness** by repeating rheological investigations with hydrogels under SMF actuation.
2. **Assess the osteogenic potential of a constant SMF** in the GelMA hydrogel model, particularly considering the established impact of stiffness on MSC lineage commitment.

Although we observed that the combination of SMF and MNPs caused slight decrease in bulk hydrogel stiffness over 28 days, osteogenesis and mineralisation still occurred over the same period. This suggests that bulk stiffness measurements may not fully reflect microscale changes at the cellular level. To address this, we suggest using atomic force microscopy (AFM) to quantify local stiffness variations between embedded cells and the surrounding matrix, as demonstrated in previous studies (Meng, et al., 2021; Yen, et al., 2020).

In Chapter 3 we observed that exposure to a SMF promoted osteogenic differentiation in 2D culture, which was observed in the absence of any osteogenic supplements. In Chapters 5 and 6, OGM applied to a 2D monolayer culture was utilised as a positive control for the 3D hydrogel studies. However, this positive control had important limitations. First, it represented a 2D system, whereas the main experiments were performed in 3D hydrogels. Second, and most importantly, the OGM did not behave as expected and resulted in downregulation of osteogenic markers. Therefore, the positive control did not function as an effective comparator in these chapters, which limits the strength of the conclusion regarding relative osteogenic potential.

Dexamethasone containing OGM was utilised in this study, as it is well established and widely adopted for inducing osteogenic differentiation *in vitro*, providing a standard reference condition (Hildebrandt, et al., 2009). However, it should also be acknowledged that dexamethasone OGM represents only one osteoinductive method. Alternative methods such as the use of BMP2 supplementation has also been shown to promote osteogenic differentiation and may provide more reliable positive controls (Zhou, et al., 2016). Future studies should incorporate a more 3D positive control, such as a cellular hydrogel cultured in a suitable osteoinductive media, to enable more robust comparison.

In addition, in both 2D and 3D studies, we utilised gene expression as the primary mechanism to investigate osteogenic differentiation and associated pathways. While the transcript level analysis provides insight into the cells state, i.e. the cells are primed towards an osteogenic phenotype, the absence of protein level validation represents an important limitation (Poliseno, et al., 2024). Without assessment of osteogenic protein expression and / or functional markers of matrix deposition, these experiments cannot definitively confirm the differentiated cell state. For example, Zhou, et al. (2021) utilised quantitative protein expression of RUNX2, alongside other assays, as additional confirmation of osteogenic differentiation in human pluripotent stem cells. Analysis of protein expression allowed them to verify transcriptional changes were translated into functional protein production, confirming cell change to an osteoblast like phenotype (Zhou, et al., 2021).

While our gene expression analyses suggest that cells are primed toward an osteogenic phenotype, several measurements exhibit large variability (as indicated by the sizeable SEM bars in the graphs). Such variability may reflect biological heterogeneity among samples, or technical differences in gene expression assays. Importantly, without protein level validation, these transcriptomic trends cannot definitively confirm osteogenic potential. Future studies should therefore include gene and protein analyses to reliably confirm osteogenic differentiation.

These findings underscore the complex interplay between magnetic stimulation, scaffold mechanics and cellular responses, emphasising the need for further detailed investigations. Optimising magnetic field parameters and hydrogel mechanical properties will be crucial for the effectiveness of magneto-mechanical stimulation in BTE applications.

7.2.2 Magnetic Stimulation and Extracellular Vesicles as Therapeutic agents in Osteogenesis and Regeneration

A key feature of this work is that osteogenic differentiation appeared to occur using magnetic stimulation alone, without the addition of traditional osteogenic supplements or exogenous bioactive molecules such as BMP2 (Zhou, et al., 2016). In contrast, many comparative studies pre-condition cells in osteogenic media (OGM) before apply magnetic fields, making it difficult to isolate the effect of the field itself, since osteogenesis has already been induced. The application of OGM can impact MSC behaviour. Castano-Izquierdo et al., (2007) reported that short term pre culture in OGM optimally primes MSCs for bone regeneration, whereas extended culture in OGM leads to over differentiation and diminished regenerative

potential, like due to reduced proliferation and adaptability. They also highlighted the role of pre-deposited ECM during pre-conditioning may contribute to osteoinductivity (Castano-Izquierdo, et al., 2007). Similarly, Hagmann et al., (2013) investigated the growth and differentiation potential of MSCs under different media compositions. They found that while osteogenic media promoted high MSC yield and enhanced osteogenic differentiation, it also reduced expression of stemness markers, thereby compromising the cells self-renewal ability, a key factor for long term regenerative potential(Hagmann, et al., 2013). In contrast to these studies, our work utilised standard cell culture media, which allows the observed effects of magnetic stimulation to be interpreted primarily as a response to physical cues rather than biochemical priming.

7.2.3 Osteogenesis and Angiogenic Crosstalk

Angiogenesis, the formation of new blood vessels, is regulated by both biochemical and mechanical cues. VEGF is a key biochemical regulator, known to drive matrix remodelling, include local ECM stiffening and activate signalling pathway including YAP/TAZ (Kretschmer, et al., 2021).

In our study, gene and cytokine data suggests that angiogenesis may be co-activated alongside osteogenesis under magnetic stimulation. Specifically, we noted upregulation of VEGF and other key angiogenic factors including FGF-2 and IL-6, supporting previous studies that report a co-orientated angiogenesis and osteogenesis. Wong et al. (2014) proposed that Nestin expression could be induced by hypoxia (Wong, et al., 2014). In our work, we observed upregulation of hypoxia related genes in 2D culture under intermittent SMF, as well as increased Nestin expression in the 3D magnetic hydrogel model under an intermittent SMF. This suggests that Nestin upregulation may be hypoxia-induced, potentially a downstream effect of static magnetic field stimulation.

In addition to VEGF upregulation, angiogenic cytokines were present under magnetic stimulation, indicating potential for vascular activation. Kretschmer et al., (2021) observed that substrate stiffness within the range of 0.5 kPa to 10 kPa promotes angiogenesis, facilitating endothelial cell migration and sprouting, while stiffer substrates beyond this range inhibit angiogenic processes. (Kretschmer, et al., 2021). Since our hydrogels fall within this angiogenic range, future studies could incorporate a co-culture system (e.g. with HUVECs) to directly investigate endothelial cell behaviour and vessel formation within

magnetic hydrogels environments. This would help to clarify the mechanisms of vascular-bone crosstalk promoted by magnetic stimulation.

Martino et al., (2010) observed that constant exposure to a 60 mT SMF increased HUVEC numbers after 2 days, while intermittent exposure (1 hour per day) had no effect on cell proliferation. Notably, VEGF expression did not change significantly under magnetic exposure (Martino, et al., 2010). These findings highlight the value of co-culture with MSCs, especially in systems where intermittent SMFs leads to VEGF upregulation, potentially supporting HUVEC angiogenesis indirectly via paracrine signalling.

7.2.4 Therapeutic Potential and Translation to Clinical Use

The magnetic GelMA model shows potential as a scaffold for static *in vitro* studies, and may also be applicable for advanced biofabrication and clinical delivery. Bioprinting provides high-throughput production of hydrogels, limiting variability in models (Huang, et al., 2017). We briefly explored bioprinting, although the magnetic print head in the system we used may limited ease of use and created challenges when printing cell laden hydrogels. Despite this we observed increased stiffness in bioprinted hydrogels. Viscoelasticity is a key parameter in determining the printability of hydrogels (Xuan, et al., 2025). Prior to crosslinking, GelMA exhibits thermoresponsive behaviour, with viscosity decreasing as temperature increases (Lipari, et al., 2025). At typical printing temperatures (~25-30°C), it behaves as a soft viscoelastic material - fluid enough for extrusion yet sufficiently structured to retain its shape post deposition. Upon UV crosslinking, GelMA transitions to a more elastic and mechanically stable hydrogel, providing enhanced structural integrity for tissue engineering constructs.

Theus et al., (2022) developed GelMA based bioinks incorporating superparamagnetic MNPs, showing that MNP incorporation slightly reduced mechanical properties, similar to what we observed in 7.5% w/v GelMA hydrogels. They hypothesised this was likely due to MNPs interfering with crosslinking (Theus, et al., 2022). Although developed for myogenesis, Hwangbo et al., (2022) bioprinted GelMA utilising an *in situ* extrusion crosslinking strategy, which improved printing prevision without compromising cell viability (Hwangbo, et al., 2020).

Bioprinting could also support vascularisation of hydrogels; Byambaa et al., (2017) developed 3D printed GelMA models using extrusion-based printing, demonstrating the

ability to create controlled architectures with embedded vascular structures, thereby promoting the formation of vascular networks within the tissue constructs (Byambaa, et al., 2017). Such refinements could enhance both the structural fidelity and biological functionality of magnetic GelMA constructs, advancing their translational potential in tissue engineering applications.

Given the injectability and *in situ* potential of hydrogels, there is a strong rationale for developing injectable magnetic hydrogels for use *in vivo*. Chai et al., (2022) developed an injectable GelMA scaffold for the bone defect regeneration *in vivo*. The scaffolds were injected into defects and crosslinked *in situ*. They demonstrated enhanced osteogenic differentiation and tissue regeneration (Chai, et al., 2022).

Regarding the *in vivo* safety of MNP incorporation, Jian et al., (2008) investigated the biodistribution and clearance of iron oxide MNPs *in vivo*. They observed MNPs predominately accumulate in the liver and spleen, without causing tissue damage or toxicity. Over several weeks, MNPs were gradually eliminated through macrophage phagocytosis, with steady decrease in iron content over time (Jain, et al., 2008).

As previously mentioned, our model appeared to induce osteogenesis in the absence of OGM, however preconditioning of MSCs *ex vivo* can significantly improve their survival, engraftment and osteogenic differentiation upon transplantation. Approaches such as hypoxia, three dimensional cultures, and preconditioning with pro-inflammatory cytokines have been shown to induce metabolic changes that enhance MSC survival and retention *in vivo* (Beegle, et al., 2015; Miceil, et al., 2023). Our system could be further enhanced by integrating bioactive strategies that precondition cells – for example, osteogenic promoter protein delivery *via* synthetic carriers or loading conditioned EVs into hydrogels to investigate their synergistic effects with magnetic cues. Saleem et al., observed that MSC conditioned media can promote osteogenesis in naïve cells by providing antioxidant and osteoinductive factors (Saleem, et al., 2021). Al-Sharabi et al., (2024) collected EVs from MSCs preconditioned with OGM, and demonstrated their ability to promote osteogenic differentiation. They further used EV loaded collagen membranes to enhance bone regeneration *in vivo* (Al-Sharabi, et al., 2024). These findings underscore the potential of magnetic stimulation as a controllable method to induce osteogenesis, which could be further enhanced by targeted bioactive priming strategies aimed at preserving regenerative capabilities while guiding differentiation.

Building on this, our work has demonstrated that EVs derived from SMF conditioned MSCs retained size and concentration, particularly under intermittent and constant SMF. These EVs should be tested for functional regenerative effects, such as promoting osteogenesis in naïve MSCs in the absence of magnetic fields or accelerating wound healing and proliferation. Wu et al., (2021) demonstrated that MSC derived exosomes stimulated with MNPs and SMFs significantly enhanced bone regeneration and angiogenesis *in vivo*, with improved bone formation collagen deposition and blood vessel formation. These exosomes also accelerated wound healing in a scratch assay using HUVECs over 24 hours (Wu, et al., 2021). Interestingly, Takeuchi et al (2019) observed that MSC derived exosomes significantly enhanced MSC migration and osteogenic potential, even without preconditioning. These exosomes promoted accelerated wound healing by upregulating key osteogenic and angiogenic gene expression. Furthermore *in vivo*, they accelerated bone formation and improved tissue regeneration compared to control groups (Takeuchi, et al., 2019).

In summary, this work highlights the potential of magnetic stimulation as a standalone tool to induce osteogenesis and tissue regeneration. It also emphasises the added promise of enhancing these effects through targeted bioactive priming strategies - such as the use of EVs - which could further optimise bone tissue engineering.

In clinical settings, magnetic stimulation could be applied both before and after stem cell or scaffold injection. Preconditioning with magnetic fields *in vitro* can prime cells for enhanced osteogenic differentiation prior to injection at the injury site. Post implantation, magnetic stimulation could be used to activate embedded nanoparticles, promoting further osteogenesis and tissue repair. One key advantage to our model is the use of an intermittent field, rather than a constant field which reduces the potential burden on surrounding tissue and allows for more controlled stimulation. This approach makes magnetic stimulation a viable, non-invasive adjunct therapy in BTE with minimal disruption to normal tissue function.

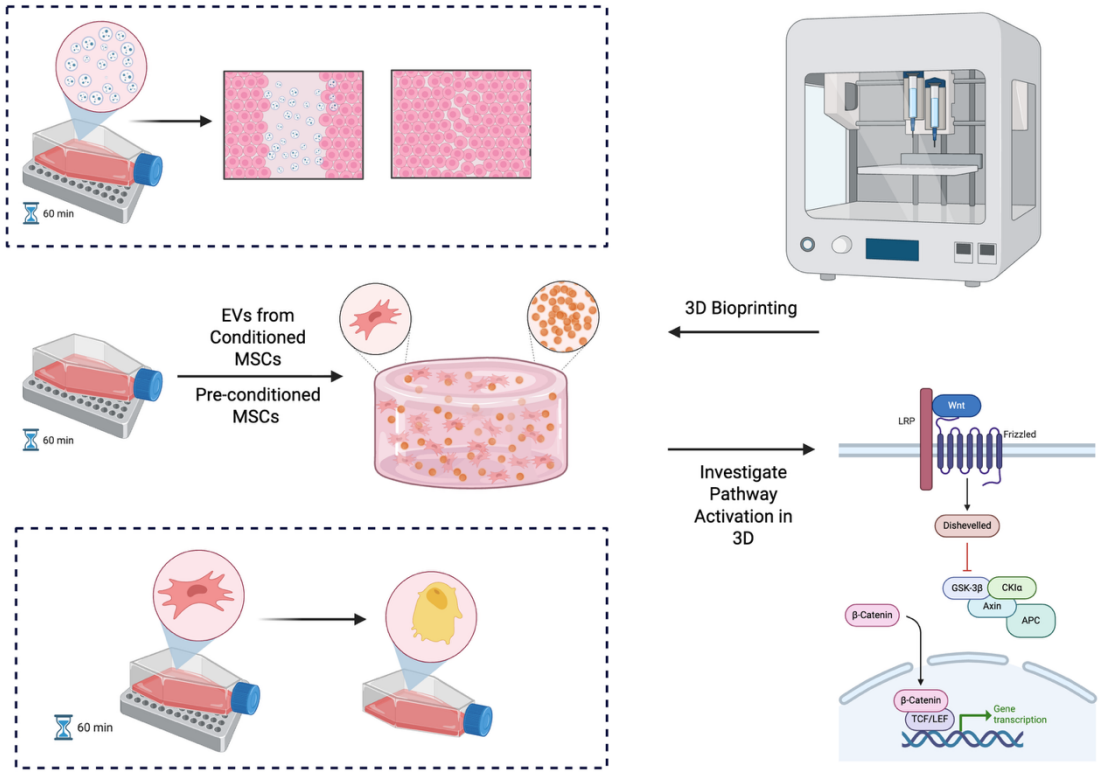

Figure 7-1: Schematic representation of suggestions for future investigations

Future work should focus on using extracellular vesicles (EVs) from static magnetic field (SMF) conditioned mesenchymal stromal cells (MSCs) for wound healing. Similarly, pre-conditioning of MSCs can support clinical applications. Both conditioned EVs and pre-conditioned MSCs can be loaded into hydrogels to enhance regenerative effects of further magnetic field stimulation. Additionally, 3D bioprinting will be explored to create customised scaffolds for tissue repair, while pathway activation in 3D should be investigated to refine the role of magnetic fields in promoting osteogenesis. Created with Biorender.com

7.3 Final Conclusion

This thesis provides preliminary evidence that magnetic hydrogels, particularly under intermittent SMF activation, may modulate MSC behaviour to support osteogenic differentiation without the use of chemical supplements. These findings contribute to the development of smart biomaterial systems that integrate biophysical and molecular cues to potentially enhance bone repair. The combination of magnetic stimulation with advanced biofabrication approaches may offer opportunities for translational applications, highlighting magnetic hydrogels as a promising platform for future regenerative medicine and bone tissue engineering research.

7.3.1 Recommendations for Future Work

- Comparing magnetic field regime in 3D
    - Compare intermittent vs constant SMF in 3D over long-term culture (28 days) to assess if constant SMF might produce stronger or complementary effects
    - Investigate how transitioning from 2D to 3D affects osteogenic responses under different magnetic regimes, focusing on identifying pathway activation contribution to osteogenic differentiation; confirm the role of BMP signalling or examine contribution of alternative pathways
    - Investigate calcium flux under magnetic field stimulation
- Magnetic Bioprinting and Injectable delivery
    - Evaluate alternative bioprinting platforms compatible with MNPs especially extrusion bases systems
- EV based therapies
    - Test EVs from SMF conditioned MSCs at promoting osteogenesis in naïve MSCs without magnetic stimulating
    - Investigate potential of SMF conditioned EVs at enhancing wound healing, or cell proliferation
- Angiogenesis and vascular bone crosstalk
    - Further investigate the angiogenic potential observed through gene and cytokine expression
    - Develop co-culture systems to observe endothelial behaviour, migration and tube formation within magnetic hydrogels
    - Investigation the interplay between osteogenesis and vascularisation under SMF
- *In vivo* and clinical translation
    - Assess integration with native bone *in vivo*, including host response and mechanical compatibility
    - Explore bioactive priming strategies to enhance the system such as: Delivery of pro-osteogenic proteins *via* synthetic vesicles, and loading hydrogels with magnetically conditioned EVs to test synergistic effects

Supplementary Information

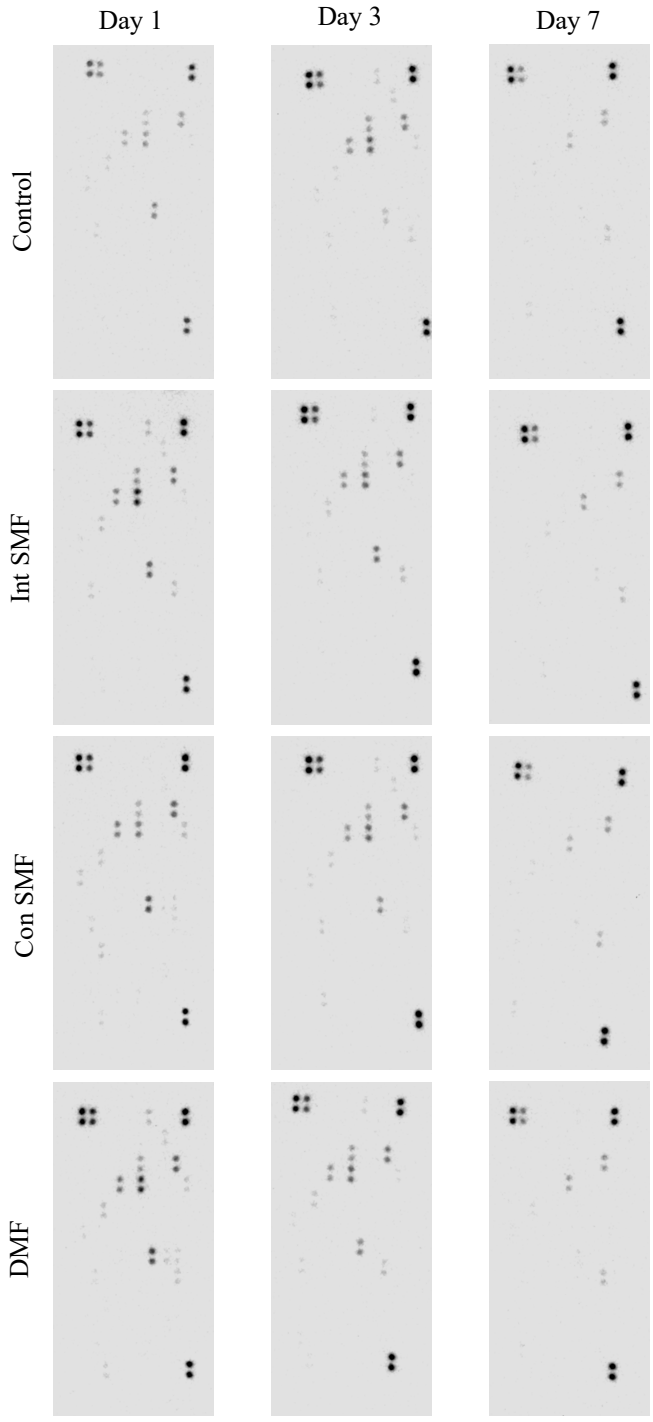

Supplementary Figure S 1: Cytokine expression on nitrocellulose membranes under magnetic conditions

Conditioned media from mesenchymal stromal cells (MSCs) was collected at days 1, 3 and 7 and analysed using the Human Cytokine Array immunoblot. Nitrocellulose membranes show cytokine profiles from MSC conditioned media at days 1, 3 and 7

Size Distribution Report by Intensity

v2.2

Malvern

Sample Details

Sample Name: chemicell fluidmag-DX 1 avg

SOP Name: Dextran coated magnetite.sop

General Notes: Average result created from record number(s): 4976 4977 4978

File Name:	Magnetic Microbeads.dts	**Dispersant Name:**	Water
Record Number:	4979	**Dispersant RI:**	1.330
Material RI:	1.59	**Viscosity (cP):**	0.8872
Material Absorbtion:	0.010	**Measurement Date and Time:**	11 July 2024 09:26:43

System

Temperature (°C):	25.0	**Duration Used (s):**	60
Count Rate (kcps):	365.5	**Measurement Position (mm):**	4.65
Cell Description:	Disposable sizing cuvette	**Attenuator:**	6

Results

			Size (d.nm...	% Intensity:	St Dev (d.n...
Z-Average (d.nm):	197.0	**Peak 1:**	225.5	100.0	90.59
PdI:	0.143	**Peak 2:**	0.000	0.0	0.000
Intercept:	0.932	**Peak 3:**	0.000	0.0	0.000

Result quality : Good

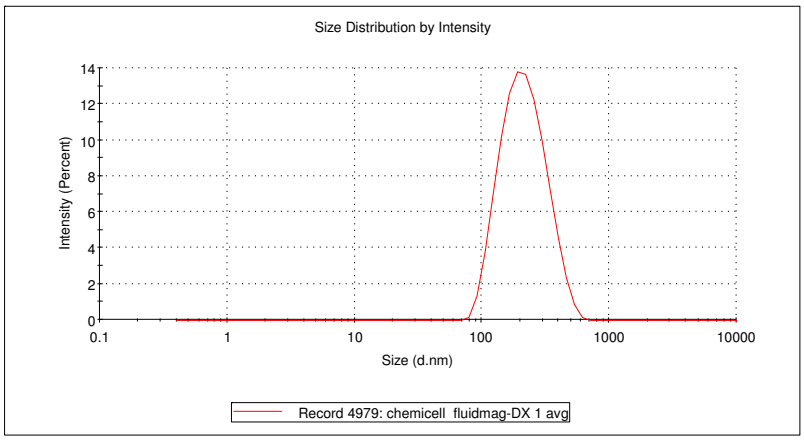

Malvern Instruments Ltd
www.malvern.com

Zetasizer Ver. 7.03
Serial Number : MAL1058114

File name: Magnetic Microbeads
Record Number: 4979
11 Jul 2024 10:36:12

Supplementary Figure S 2: Morphology and hydrodynamic size distribution of fluidMAG-Dx nanoparticles

Dynamic light scattering analysis of fluidMAG-Dx MNPs in suspension, showing various characteristics of magnetic nanoparticle morphology. Completed in collaboration with Liquid Research Ltd (Bangor, Wales).

References

Abdeen, A. A. et al., 2016. Temporal Modulation of Stem Cell Activity Using Magnetoactive Hydrogels. Advanced Healthcare Materials, 5(19).

Aigoin, J. et al., 2025. Comparative Analysis of Electron Microscopy Techniques for Hydrogel Microarchitecture Characterization: SEM, Cryo-SEM, ESEM, and TEM. ACS Omega, Volume 10, pp. 14687-14698.

Al-Bari, A. A. & Mamun, A. A., 2020. Current advances in regulation of bone homeostasis. FASEB BioAdvances, 2(11), pp. doi.org/10.1096/fba.2020-00058.

Aldebs, A. I. et al., 2020. Effect of Pulsed Electromagnetic Fields on Human Mesenchymal Stem Cells Using 3D Magnetic Scaffolds. Bio Electro Magnets.

Ali, A. et al., 2021. Review on Recent Progress in Magnetic Nanoparticles: Synthesis, Characterization, and Diverse Applications. Frontiers in Chemistry, Volume 9.

Allen, K. D., Thoma, L. M. & Golightly, Y. M., 2022. Epidemiology of osteoarthritis. Osteoarthritis and Cartilage, 30(2), p. doi.org/10.1016/j.joca.2021.04.020.

Al-Sharabi, N. et al., 2024. Osteogenic human MSC derived extracellular vesicles regulate MSC activity and osteogenic differentiation and promote bone regeneration in a rat calvarial defect model. Stem Cell Research and Therapy, 15(33).

Alveroğlu, E. et al., 2013. Fluorescence and magnetic properties of hydrogels containing Fe3O4 nanoparticles. Journal of Molecular Structure, Volume 1037.

Amini, Z. & Lari, R., 2021. A systematic review of decellularized allograft and xenograft–derived scaffolds in bone tissue regeneration. Tissue and Cell, Volume 69.

Annabi, N. et al., 2010. Controlling the Porosity and Microarchitecture of Hydrogels for Tissue Engineering. Tissue Engineering Part B: Reviews, 16(4).

Arya, P. N., Saranya, I. & Selvamurugan, N., 2024. Crosstalk between Wnt and bone morphogenetic protein signaling during osteogenic differentiation. World Journal of Stem Cells, 2024(16), p. 2.

Augusto, A. C. d. L. et al., 2022. Imaging Review of Normal andAbnormal Skeletal Maturation. Radiographics, p. 10.1148/rg.210088.

Bühring, H.-J.et al., 2009. Phenotypic Characterization of Distinct Human Bone Marrow–Derived MSC Subsets. Annals of the New York Academy of Sciences, 1176(1), pp. 124-134.

Bahamonde, M. & Lyons, K., 2001. BMP3: To Be or Not To Be a BMP. The Journal of Bone & Joint Surgery, 83(1).

Bai, J., Li, Y. & Zhang, G., 2017. Cell cycle regulation and anticancer drug discovery. Cancer Biology & Medicine, 14(4).

Bashir, S. et al., 2020. Fundamental Concepts of Hydrogels: Synthesis, Properties, and Their Applications. Polymers, 12(11).

Beegle, J. et al., 2015. Hypoxic Preconditioning of Mesenchymal Stromal Cells Induces Metabolic Changes, Enhances Survival, and Promotes Cell Retention In Vivo. Stem Cells, Volume 33.

Beird, H. C. et al., 2022. Osteosarcoma. Nature Reviews Disease Primers, Volume 8.

Bianco, P., 2014. "Mesenchymal" Stem Cells. The Annual Review of Cell and Developmental Biology, Volume 30, pp. 677-704.

Bianco, P. & Robey, P., 2015. Skeletal stem cells. The Company of Biologists, Volume 142, pp. 1023-1027.

Bloise, N. et al., 2018. The effect of pulsed electromagnetic field exposure on osteoinduction of human mesenchymal stem cells cultured on nano-TiO2 surfaces. PLOS One.

Boda, S. K., Thrivikraman, G. & Basu, B., 2015. Magnetic field assisted stem cell differentiation – role of substrate magnetization in osteogenesis†. Journal of Materials Chemistry B, Volume 3.

Bonewald, L. F. et al., 2003. Von Kossa Staining Alone Is Not Sufficient to Confirm that Mineralization In Vitro Represents Bone Formation. Calcified Tissue International, Volume 72, pp. 537-547.

Borok, M. J., Mademtzoglou, D. & Relaix, F., 2020. Bu-M-P-ing Iron: How BMP Signaling Regulates Muscle Growth and Regeneration. Journal of Developmental Biology, 8(1).

Brady, M. A., Talvard, L., Vella, A. & Ethier, C. R., 2015. Bio-inspired design of a magnetically active trilayered scaffold for cartilage tissue engineering.. Journal of Tissue Engineering and Regenerative Medicine, Volume 11.

Brady, R. T., O'Brien, F. J. & Hoey, D. A., 2015. Mechanically stimulated bone cells secrete paracrine factors that regulate osteoprogenitor recruitment, proliferation, and differentiation. Biochemical and Biophysical Research Communications, 459(1).

Brinkhof, B. et al., 2020. ALCAM (CD166) as a gene expression marker for human mesenchymal stromal cell characterisation. Gene, Volume 763.

Brookes, M. J. et al., 2021. Surgical Advances in Osteosarcoma. Cancers, Volume 13.

Bruels, R. G. M., Jiya, T. U. & Smit, T. H., 2008. Scaffold Stiffness Influences Cell Behavior: Opportunities for Skeletal Tissue Engineering. The Open Orthopaedics Journal, Volume 2.

Buemi, M. et al., 2001. Cell Proliferation/Cell Death Balance in Renal Cell Cultures after Exposure to a Static Magnetic Field. Nephron, Volume 87.

Byambaa, B. et al., 2017. Bioprinted Osteogenic and Vasculogenic Patterns for Engineering 3D Bone Tissue. Advanced Healthcare Materials.

Čamernik, K. et al., 2018. Mesenchymal Stem Cells in the Musculoskeletal System: From Animal Models to Human Tissue Regeneration?. Stem Cell Reviews and Reports, Volume 14.

Caley, M. P., Martins, V. L. C. & O'Toole, E. A., 2015. Metalloproteinases and Wound Healing. Advances in Wound Care, Volume 4.

Castano-Izquierdo, H. et al., 2007. Pre-culture period of mesenchymal stem cells in osteogenicmedia influences their in vivo bone forming potential. Journal of Biomedical Materials Research.

Castro, N. et al., 2020. Magnetic Bioreactor for Magneto-, Mechano- and Electroactive Tissue Engineering Strategies. Sensors, 20(12).

Celik, C. et al., 2021. Directionalities of magnetic fields and topographic scaffolds synergise to enhance MSC chondrogenesis. Acta Biomaterialia, Volume 119.

Chai, S. et al., 2022. Injectable Photo-Crosslinked Bioactive BMSCs-BMP2-GelMA Scaffolds for Bone Defect Repair. Frontiers in Bioengineering and Biotechnology, Volume 10.

Chan, W. C. W., Tan, Z., Tsun To, M. K. & Chan, D., 2021. Regulation and Role of Transcription Factors in Osteogenesis. International Journal of Molecular Sciences, 22(11).

Charde, S. H., Joshi, A. & Raut, J., 2023. A Comprehensive Review on Postmenopausal Osteoporosis in Women. Cereus.

Chaudhary, S. et al., 2013. Elucidating the Function of Penetratin and a Static Magnetic Field in Cellular Uptake of Magnetic Nanoparticles. Pharmaceuticals, 6(2).

Chaudhuri, O. et al., 2015. Hydrogels with tunable stress relaxation regulate stem cell fate and activity. Nature Materials, Volume 15.

chemicell, 2025. Product Information – fluidMAG-DX. [Online]
Available at: http://www.chemicell.com/products/nanoparticles/docs/PI_fluidMAG-DX_4104.pdf

chemicell, 2026. Magnetofection™. [Online]
Available at: http://www.chemicell.com/products/magnetofection/index.html#app
[Accessed 15 01 2026].

Chen, A. et al., 2012. The Global Economic Cost of Osteoarthritis: How the UK Compares. Arthritis, p. DOI: 10.1155/2012/698709.

Chen, J. et al., 2019. The combinatory effect of sinusoidal electromagnetic field and VEGF promotes osteogenesis and angiogenesis of mesenchymal stem cell-laden PCL/HA implants in a rat subcritical cranial defect. Stem Cell Research & Therapy, Volume 10.

Chen, Y. et al., 2023. Intermittent Exposure to a 16 Hz Extremely Low Frequency Pulsed Electromagnetic Field Promotes Osteogenesis In Vitro through Activating Piezo 1-Induced Ca2+ Influx in Osteoprogenitor Cells. Functional Biomaterials, 14(3).

Chithrani, B. D., Ghazani, A. A. & Chan, W. C. W., 2006. Determining the Size and Shape Dependence of Gold Nanoparticle Uptake into Mammalian Cells. Nano Letters, 6(4), pp. 662-668.

Cios, A., Ciepielak, M., Stankiewicz, W. & Szymański, Ł., 2021. The Influence of the Extremely Low Frequency Electromagnetic Field on Clear Cell Renal Carcinoma. International Journal of Molecular Sciences, Volume 22.

Clarke, B., 2008. Normal Bone Anatomy and Physiology. Clinical Journal of the American Society of Nephrology.

Clough, H. C. et al., 2021. Neutrally charged self-assembling peptide hydrogel recapitulates in vitro mechanisms of breast cancer progression. Materials Science and Engineering: C, Volume 127.

Comfort, N. et al., 2021. Nanoparticle Tracking Analysis for the Quantification and Size Determination of Extracellular Vesicles. Journal of Visualisd Experiements, 169(10).

Creecy, C. M. et al., 2012. Mesenchymal Stem Cell Osteodifferentiation in Response to Alternating Electric Current. Tissue Engineering, Part A: Research Advances, Volume 19.

Dahl, K. N., Ribeiro, A. J. S. & Lammerding, J., 2008. Nuclear Shape, Mechanics, and Mechanotransduction. Circulation Research, 102(11).

Dalby, M. et al., 2007. The control of human mesenchymal cell differentiation using nanoscale symmetry and disorder. Nature Materials, Volume 6.

D'Alimonte, I. et al., 2013. Wnt Signaling Behaves as a “Master Regulator” in the Osteogenic and Adipogenic Commitment of Human Amniotic Fluid Mesenchymal Stem Cells. Stem Cell Reviews and Reports, Volume 9.

Darbà, J. & Marsà, A., 2020. Hospital incidence, management and direct cost of osteogenesis imperfecta inSpain: a retrospective database analysis. Journal of Medical Economics.

Day, T. F., Guo, X., Garrett-Beal, L. & Yang, Y., 2005. Wnt/beta-catenin signaling in mesenchymal progenitors controls osteoblast and chondrocyte differentiation during vertebrate skeletogenesis. Developmental Cell, 8(5).

Day, T. & Yingzi, Y., 2008. Wnt and Hedgehog Signaling Pathways in Bone Development. The Journal of Bone & Joint Surgery, Volume 90.

Dobbenga, S., Fratilia-Apachitei, L. E. & Zadpoor, A. A., 2016. Nanopattern-induced osteogenic differentiation of stem cells – A systematic review. Acta Biomaterialia, Volume 46.

Dominici, M. et al., 2006. Minimal criteria for defining multipotent mesenchymal stromal cells. The International Society for Cellular Therapy position statement. Cryotherapy, 8(4).

Dong, G. et al., 2025. Effects of magnetic responsive GelMA hydrogel with tensile stimulation on proliferation, migration and osteogenic differentiation of periosteum-derived cells. International Journal of Biological Macromolecules, Volume 319.

Dormann, D. & Weijer, C. J., 2006. Imaging of cell migration. The EMBO Journal, Volume 25, pp. 3480-3493.

Doulatov, S., Notta, F., Laurenti, E. & Dick, J., 2012. Hematopoiesis: A Human Perspective. Cell Stem Cell, 10(2).

Drake, R., Vogl, W. A. & Mitchell, A. W. M., 2024. The Body. In: Gray's Anatomy for Students, Firth Edition. s.l.:Elsevier Inc..

Eaton, B. R. et al., 2020. Osteosarcoma. Paediatric Blood & Cancer.

Eberbeck, D. et al., 2010. Quantification of the aggregation of magnetic nanoparticles with different polymeric coatings in cell culture medium. JOURNAL OF PHYSICS D: APPLIED PHYSICS, Volume 43.

Edwards, S. D. et al., 2024. Enhanced osteogenesis of mesenchymal stem cells encapsulated in injectable microporous hydrogel. Scientific reports, Volume 14.

Ekegren, C. L., Edwards, R. E., Steiger, R. d. & Gabbe, B., 2018. Incidence, Costs and Predictors of Non-Union, Delayed Union and Mal-Union Following Long Bone Fracture. International Journal of Environmental Research and Public Health, Volume 15.

Elahi, K. C. et al., 2016. Human Mesenchymal Stromal Cells from Different Sources Diverge in Their Expression of Cell Surface Proteins and Display Distinct Differentiation Patterns. Stem Cells International, 2016(1), p. 5646384.

El-Rashidy, A. A. et al., 2021. Effect of Polymeric Matrix Stiffness on Osteogenic Differentiation of Mesenchymal Stem/Progenitor Cells: Concise Review. Polymers, 13(17).

Faia-Torres, A. B. et al., 2015. Osteogenic differentiation of human mesenchymal stem cells in the absence of osteogenic supplements: A surface-roughness gradient study. Acta Biomaterialia, Volume 28.

Fan, D. et al., 2020. Recent Advances of Magnetic Nanomaterials in Bone Tissue Repair. Frontiers in Chemistry, Volume 8.

Faroni, A., Workman, V. L., Saiani, A. & Reid, A. J., 2019. Self-Assembling Peptide Hydrogel Matrices Improve the Neurotrophic Potential of Human Adipose-Derived Stem Cells. Advanced Healthcare Materials, 8(17).

Fathi-Achachelouei, M. et al., 2019. Use of Nanoparticles in Tissue Engineering and Regenerative Medicine. Frontiers in Bioengineering and Biotechnology, Volume 7.
Fehlings, M. et al., 2015. The Aging of the Global Population The Changing Epidemiology of Disease and Spinal Disorders. Neurosurgery, Volume 77.

Filippi, M. et al., 2019. Magnetic nanocomposite hydrogels and static magnetic field stimulate the osteoblastic and vasculogenic profile of adipose-derived cells. Biomaterials, Volume 223.

Fitzimmons, R. E. B., Mazurek, M. S., Soos, A. & Simmons, C. A., 2018. Mesenchymal Stromal/Stem Cells in Regenerative Medicine and Tissue Engineering. Stem Cells International, 2018(1), p. 8031718.

Foo, J. B. et al., 2021. Comparing the Therapeutic Potential of Stem Cells and their Secretory Products in Regenerative Medicine. Stem Cells International.

Forlino, A., Cabral, W. A., Barnes, A. M. & Marini, J. C., 2012. New Perspectives on Osteogenesis Imperfecta. Nature Reviews Endocrinology.

Franco, A., Durme, B. V., Vlierberghe, S. V. & Dupont-Gillain, C., 2024. Misleading Pore Size Measurements in Gelatin and Alginate Hydrogels Revealed by Confocal Microscopy. Tissue Engineering Part C Methods, 30(7), pp. 307-313.

Garces, D. G. et al., 2023. The Effect of Gelatin Source on the Synthesis of Gelatin-Methacryloyl and the Production of Hydrogel Microparticles. Gels, 9(12), p. 927.

García-Bernal, D. et al., 2021. The Current Status of Mesenchymal Stromal Cells: Controversies, Unresolved Issues and Some Promising Solutions to Improve Their Therapeutic Efficacy. Frontiers in Cell and Developmental Biology, 9(650664).

Gasiorowski, J. Z., Murphy, C. J. & Nealey, P. F., 2013. Biophysical Cues and Cell Behavior: The Big Impact of Little Things. Annual Review of Biomedical Engineering , Volume 15.

GBD 2019 Fracture Collaborators, 2021. Global, regional, and national burden of bone fractures in 204 countries and territories, 1990–2019: a systematic analysis from the Global Burden of Disease Study 2019. The Lancet Healthy Longevity, 2(9).

Ge, Q. et al., 2017. VEGF secreted by mesenchymal stem cells mediates the differentiation of endothelial progenitor cells into endothelial cells via paracrine mechanisms. Molecular Medicine Reports, Volume 17.

Ghaben, A. L. & Scherer, P. E., 2019. Adipogenesis and metabolic health. Nature Reviews Molecular Cell Biology, Volume 20.

Golebiowska, A. A. & Nukavarapu, S. P., 2022. Bio-inspired zonal-structured matrices for bone-cartilage interface engineering. Biofabrication, Volume 14.

Gomez-Florit, M. et al., 2020. Natural-Based Hydrogels for Tissue Engineering Applications. Molecules, 25(24).

Grosso, A. et al., 2017. It Takes Two to Tango: Coupling of Angiogenesis and Osteogenesis for Bone Regeneration. Frontiers in Bioengineering and Biotechnology, Volume 5.

Guadix, J. A. et al., 2019. Principal Criteria for Evaluating the Quality, Safety and Efficacy of hMSC-Based Products in Clinical Practice: Current Approaches and Challenges. Pharmaceutics, 11(11).

Guan, S.-Y.et al., 2025. The impact of population ageing on musculoskeletal disorders in 204 countries and territories, 1990-2021: global burden and healthcare costs. Annals of the Rheumatic Diseases.

Guan, W. et al., 2024. Application of magnetism in tissue regeneration: recent progress and future prospects. Regenerative Biomaterials, Volume 11.

Guillot-Ferriols, M. et al., 2024. Piezoelectric Stimulation Induces Osteogenesis in Mesenchymal Stem Cells Cultured on Electroactive Two-Dimensional Substrates. ACs Publications, 6(22).

Guo, X. et al., 2025. Magnetically Guided Mechanoactive Mineralization Scaffolds for Enhanced Bone Regeneration. Advanced Functional Materials , Volume 35.

Gupte, M. J. et al., 2018. Pore size directs bone marrow stromal cell fate and tissue regeneration in nanofibrous macroporous scaffolds by mediating vascularization. Acta Biomaterialia, Volume 82.

Hagmann, S. et al., 2013. Different culture media affect growth characteristics, surface marker distribution and chondrogenic differentiation of human bone marrow-derived mesenchymal stromal cells. BMC Musculoskeletal Disorders, Volume 14.

Han, Y. et al., 2024. GelMA/TCP nanocomposite scaffold for vital pulp therapy. Acta Biomaterialia, 173(1), pp. 495-508.

Han, Y. et al., 2019. Mesenchymal Stem Cells for Regenerative Medicine. cells, Volume 8.

Hao, M. et al., 2021. Magnetic driven dynamic culture promotes osteogenesis of mesenchymal stem cell. Bioresources and Bioprocessing, 8(15).

Hao, X. et al., 2021. 3D printed structured porous hydrogel promotes osteogenic differentiation of BMSCs. Materials & Design, Volume 227.

Hart, N. H. et al., 2020. Biological basis of bone strength: anatomy, physiology and measurement. Journal of Musculoskeletal and Neuronal Interactions, Volume 20.

Hart, T. et al., 2024. The IMPACT Survey: the economic impact of osteogenesis imperfecta in adults. Journal of Rare Diseases.

Ha, Y. et al., 2018. Recent Advances Incorporating Superparamagnetic Nanoparticles into Immunoassays. ACS Applied Nano Materials, 1(2).

He, C. et al., 2010. Effects of particle size and surface charge on cellular uptake and biodistribution of polymeric nanoparticles. Biomaterials, 31(13), pp. 3657-3666.

Henstock, J. R. et al., 2014. Remotely Activated Mechanotransduction via Magnetic Nanoparticles Promotes Mineralization Synergistically With Bone Morphogenetic Protein 2: Applications for Injectable Cell Therapy. Stem Cells Translational Medicine , 3(11).

He, Y. et al., 2021. Effect of magnetic graphene oxide on cellular behaviors and osteogenesis under a moderate static magnetic field. Nanomedicine: Nanotechnology, Biology and Medicine, Volume 37.

Hildebrandt, C., Büth, H. & Thielecke, H., 2009. Influence of cell culture media conditions on the osteogenic differentiation of cord blood-derived mesenchymal stem cells. Annals of Anatomy, 191(1), pp. 23-32.

Hirasawa, T. & Kuratani, S., 2015. Evolution of the vertebrate skeleton: morphology, embryology, and development. Zoological Letters.

Hochmann, S. et al., 2023. The enhancer landscape predetermines the skeletal regeneration capacity of stromal cells. Bone.

Hong, R. Y. et al., 2008. Synthesis, characterization and MRI application of dextran-coated Fe3O4 magnetic nanoparticles. Biochemical Engineering Journal, Volume 42.

Hong, S. C. et al., 2011. Subtle cytotoxicity and genotoxicity differences in superparamagnetic iron oxide nanoparticles coated with various functional groups. International Journal of Nanomedicine, Volume 6.

Horton, E. R. et al., 2020. Extracellular Matrix Production by Mesenchymal Stromal Cells in Hydrogels Facilitates Cell Spreading and Is Inhibited by FGF-2. Advanced Healthcare Materials, 9(7).

Hoshyar, N., Gray, S., Han, H. & Bao, G., 2016. The effect of nanoparticle size on in vivo pharmacokinetics and cellular interaction. Nanomedicine, 11(6), pp. 673-692.

Ho, T.-C.et al., 2022. Hydrogels: Properties and Applications in Biomedicine. Molecules, 27(9).

Huang, E. E. et al., 2022. Novel Techniques and Future Perspective for Investigating Critical-Size Bone Defects. Bioengineering, 11(9).

Huang, Y. et al., 2017. 3D bioprinting and the current applications in tissue engineering. Biotechnology Journal, 12(8).

Hu, W. et al., 2019. Advances in crosslinking strategies of biomedical hydrogels. Biomaterials Science, 7(3).

Hu, Y. et al., 2021. Subchondral bone microenvironment in osteoarthritis and pain. Bone Research, Volume 9.

Hwangbo, H. et al., 2020. Bio-printing of aligned GelMa-based cell-laden structure for muscle tissue regeneration. Bioactive Materials, Volume 8.

International Osteoporosis Foundation, 2021. Fragility fractures cost European health care systems €56.9 billion annually. [Online]
Available at: https://www.osteoporosis.foundation/news/fragility-fractures-cost-european-health-care-systems-eu569-billion-annually-20210607-2118
[Accessed 2025].

Issa, B., Obaidat, I. M., Albiss, B. A. & Haik, Y., 2018. Magnetic Nanoparticles: Surface Effects and Properties Related to Biomedicine Applications. International Journal of Molecular Sciences, 14(11), pp. 21266-21305.

Jabalee, J., Hillier, S. & Franz-Odendaal, T. A., 2013. An investigation of cellular dynamics during the development of intramembranous bones: the scleral ossicles. Journal of Anatomy, p. doi.org/10.1111/joa.12095.

Jain, T. K. et al., 2008. Biodistribution, Clearance, and Biocompatibility of Iron Oxide Magnetic Nanoparticles in Rats. Molecular Pharmaceutics, 5(2).

James, A. W., 2013. Review of Signaling Pathways Governing MSC Osteogenic and Adipogenic Differentiation. Scientifica.

Jaworski, Z. F. G., 1981. Physiology and Pathology of Bone Remodeling: Cellular Basis of Bone Structure in Health and in Osteoporosis. Orthopedic Clinics of North America Volume 12, Issue 3, July 1981, Pages 485-512 .

Jin, S. et al., 2009. Swelling mechanism of porousP(VP-co-MAA)/PNIPAM semi-IPN hydrogelswith various pore sizes prepared by a freezetreatment. Polymer International, 58(2).

Katz, J. N., 2006. Total joint replacement in osteoarthritis. Best Practice & Research Clinical Rheumatology, 20(1).

Kim, J.-N.et al., 2015. Haversian system of compact bone and comparison between endosteal and periosteal sides using three-dimensional reconstruction in rat. Anatomy & Cell Biology.

Kim, M.-O.et al., 2015. Electromagnetic fields and nanomagnetic particles increase the osteogenic differentiation of human bone marrow-derived mesenchymal stem cells. International Journal of Molecular Medicine, Volume 35.

Kim, Y.-M.et al., 2020. Synergistic effect of electromagnetic fields and nanomagnetic particles on osteogenesis through calcium channels and p-ERK signaling. Journal of Orthopaedic Research.

Kou, M. et al., 2022. Mesenchymal stem cell-derived extracellular vesicles for immunomodulation and regeneration: a next generation therapeutic tool?. CDDPress, Volume 13.

Kranemann, T., Ersepke, T., Draack, S. & Schmitz, G., 20. Modeling and Measurement of the Nonlinear Force on Nanoparticles in Magnetomotive Techniques. IEEE Transactions on Ultrasonics, Ferroelectrics, and Frequency Control, 67(4), p. 2019.

Kretschmer, M., Rüdiger, D. & Zahler, S., 2021. Mechanical Aspects of Angiogenesis. Cancers.

Krinner, A. et al., 2009. Impact of oxygen environment on mesenchymal stem cell expansion and chondrogenic differentiation. Cell Proliferation, Volume 42.

Kulterer, B. et al., 2007. Gene expression profiling of human mesenchymal stem cells derived from bone marrow during expansion and osteoblast differentiation. BMC Genomics, 8(70).

Kurtz, S. M. et al., 2009. Future Young Patient Demand for Primary and Revision Joint Replacement: National Projections from 2010 to 2030. Clinical Orthopaedics and Related Research, Volume 9.

Kuss, M. et al., 2018. Effects of tunable, 3D-bioprinted hydrogels on human brown adipocyte behavior and metabolic function. Acta Biomaterialia, Volume 71.

Kusuma, G. D., Carthew, J., Lim, R. & Frith, J. E., 2017. Effect of the Microenvironment on Mesenchymal Stem Cell Paracrine Signaling: Opportunities to Engineer the Therapeutic Effect. Stem Cells and Development, Volume 26.

Kwon, J. H. et al., 2021. Senescence-Associated Secretory Phenotype Suppression Mediated by Small-Sized Mesenchymal Stem Cells Delays Cellular Senescence through TLR2 and TLR5 Signaling. cells, Volume 10.

Langenbach, F. & Handschel, J., 2013. Effects of dexamethasone, ascorbic acid and β-glycerophosphate on the osteogenic differentiation of stem cells in vitro. Stem Cell Research & Therapy, Volume 4.

Lang, J. et al., 2025. Molecular crosstalk in SP7-mediated osteogenesis: Regulatory mechanisms and therapeutic potential. Osteoporosis and Sarcopenia, 11(2).

Leach, J. K. & Whitehead, J., 2017. Materials-Directed Differentiation of Mesenchymal Stem Cells for Tissue Engineering and Regeneration. ACS Biomaterials Science & Engineering, 4(4).

Lee, K. et al., 2020. Osteogenic and Adipogenic Differentiation of Mesenchymal Stem Cells in Gelatin Solutions of Different Viscosities. Advanced Healthcare Materials, Volume 9.

Lee, S.-H., Kim, T.-S., Choi, Y. & Lorenzo, J., 2008. Osteoimmunology: cytokines and the skeletal system. BMB Reports, Volume 41.

Leisengang, S. et al., 2022. Neuroinflammation in Primary Cultures of the Rat Spinal Dorsal Horn Is Attenuated in the Presence of Adipose Tissue–Derived Medicinal Signalling Cells (AdMSCs) in a Co cultivation Model. Molecular Neurobiology, Volume 59, pp. 475-494.

Leon-Cecilla, A. et al., 2023. Alginate Hydrogels Reinforced by Dehydration under Stress—Application to a Soft Magnetic Actuator. gels.

Lestari, W. et al., 20216. Advancements and applications of gelatin-based scaffolds in dental engineering: a narrative review. Odontology, Volume 114, pp. 61-76.

Lewis, E. E. L. et al., 2014. The influence of particle size and static magnetic fields on the uptake of magnetic nanoparticles into three dimensional cell-seeded collagen gel cultures. Journal of Biomedical Materials Research Part B: Applied Biomaterials, Volume 6.

Li, H., Tan, C. & Li, L., 2018. Review of 3D printable hydrogels and constructs. Materials & Design, Volume 159.

Li, J. & Dong, S., 2016. The Signaling Pathways Involved in Chondrocyte Differentiation and Hypertrophic Differentiation. Stem Cells International.

Lin, C.-Y. & Kang, J.-H., 2021. Mechanical Properties of Compact Bone Defined by the Stress-Strain Curve Measured Using Uniaxial Tensile Test: A Concise Review and Practical Guide. Materials.

Lin, C.-Y.et al., 2025. Mechanotransduction pathways regulating YAP nuclear translocation under Yoda1 and vibration in osteocytes. Bone, Volume 190.

Lin, C.-H., Su, J. J.-M., Lee, S.-Y. & Lin, Y.-M., 2018. Stiffness modification of photopolymerizable gelatin-methacrylate hydrogels influences endothelial differentiation of human mesenchymal stem cells. Journal of Tissue Engineeing and Regenerative Medicine, Volume 12.

Lin, G. L. & Hankenson, K. D., 2011. Integration of BMP, Wnt, and notch signaling pathways in osteoblast differentiation†. Journal of Cellular Biochemistry.

Lipari, S. et al., 2025. Thermally Cured Gelatin-Methacryloyl Hydrogels Form Mechanically Modulating Platforms for Cell Studies. Biomacromolecules, Volume 26.

Li, Q. et al., 2017. Correlation between particle size/domain structure and magnetic properties of highly crystalline Fe3O4 nanoparticles. Scientific Reports, Volume 7, p. 9894.

Li, Q., Xu, R., Lei, K. & Yuan, Q., 2022. Insights into skeletal stem cells. Bone Research, 10(61).

Li, R. et al., 2014. BMP-2 mRNA expression after endothelial progenitor cell therapy for fracture healing. Journal of Orthopaedic Trauma, Volume 28.

Li, S., Liu, G. & Hu, S., 2024. Osteoporosis: interferon-gamma-mediated bone remodeling in osteoimmunology. Frontiers in Immunology, Volume 15.

Liu, J. et al., 2022. Mesenchymal stem cells and their microenvironment. Stem Cell Research & Therapy , 13(429).

Liu, Q. et al., 2020. Recent Advances of Osterix Transcription Factor in Osteoblast Differentiation and Bone Formation. Frontiers in Cell and Developmental Biology, Volume 8.

Liu, Y. & Chen, Q., 2020. Senescent Mesenchymal Stem Cells: Disease Mechanism and Treatment Strategy. Current Molecular Biology Reports, 6(4).

Liu, Y. et al., 2023. Sustained delivery of a heterodimer bone morphogenetic protein-2/7 via a collagen hydroxyapatite scaffold accelerates and improves critical femoral defect healing. Acta Biomaterialia, Volume 162.

Liu, Z. et al., 2020. Recent Advances on Magnetic Sensitive Hydrogels in Tissue Engineering. Frontiers in Chemistry, 8(124).

Liu, Z. et al., 2023. The Mechanotransduction Signaling Pathways in the Regulation of Osteogenesis. International Journal of Molecular Sciences, 24(18).

Livak, K. J. & Schmittgen, T. D., 2001. Analysis of Relative Gene Expression Data Using RealTime Quantitative PCR and the 2(^-DDCT) Method. Methods, 25(4), pp. 402-408.

Li, W. et al., 2021. Low-frequency electromagnetic fields combined with tissue engineering techniques accelerate intervertebral fusion. Stem Cell Research & Therapy, Volume 12.

Li, W. et al., 2020. Static magnetic fields accelerate osteogenesis by regulating FLRT/BMP pathway. Biochemical and Biophysical Research Communications, 527(1).

Li, X. et al., 2019. Iron oxide nanoparticles promote the migration of mesenchymal stem cells to injury sites. International Journal of Nanomedicine, Volume 14.

Li, Y. et al., 2022. Graphene Oxide-loaded magnetic nanoparticles within 3D hydrogel form High-performance scaffolds for bone regeneration and tumour treatment. Composites Part A: Applied Science and Manufacturing, Volume 152.

Li, Y. et al., 2017. Senescence of mesenchymal stem cells. International Journal of Molecular Medicine, 39(4).

Londhe, P. V. et al., 2025. Magnetic hydrogel (MagGel): An evolutionary pedestal for anticancer therapy. Coordination Chemistry Reviews, Volume 522, p. 216228.

Lou, X. et al., 2020. Thermo/photo dual-crosslinking chitosan-gelatin methacrylate hydrogel with controlled shrinking property for contraction fabrication. Carbohydrate Polymers, Volume 236.

Lou, Z. et al., 2019. Notch Signaling in Osteogenesis, Osteoclastogenesis, and Angiogenesis. The America Journal of Pathology, 189(8).

Lu, A.-H., Salabas, E. L. & Schüth, F., 2007. Magnetic Nanoparticles: Synthesis, Protection, Functionalization, and Application. Angewandte Chemie, 46(8).

Lu, T. et al., 2015. Effect of pulsed electromagnetic field therapy on the osteogenic and adipogenic differentiation of bone marrow mesenchymal stem cells. Genetics and Molecular Research, 14(3).

Lv, J. et al., 2015. Enhanced angiogenesis and osteogenesis in critical bone defects by the controlled release of BMP-2 and VEGF: implantation of electron beam melting-fabricated porous Ti6Al4V scaffolds incorporating growth factor-doped fibrin glue. Biomedical materials, Volume 10.

Maas, S. L. N. et al., 2015. Possibilities and limitations of current technologies for quantification of biological extracellular vesicles and synthetic mimics. Journal of Controlled Release, Volume 200, pp. 87-96.

Mackie, E. J. et al., 2008. Endochondral ossification: How cartilage is converted into bone in the developing skeleton. The International Journal of Biochemistry & Cell Biology, Volume 40, p. doi.org/10.1016/j.biocel.2007.06.009.

Maisenbacher, T. C. et al., 2025. reatments, cost and healthcare utilization of patients with segmental bone defects.. Bone and Joint Research, 14(4).

Mamidi, N., Ijadi, F. & Norahan, M. H., 2023. Leveraging the Recent Advancements in GelMA Scaffolds for Bone Tissue Engineering: An Assessment of Challenges and Opportunities. Biomacromolecules, 25(4).

Mandal, A., Clegg, J. R., Anselmo, A. C. & Mitragotri, S., 2020. Hydrogels in the clinic. Bioengineering & Translational Medicine, 5(2).

Manjua, A. C., Alves, V. D., Crespo, J. G. & Portugal, C. A. M., 2019. Magnetic Responsive PVA Hydrogels for Remote Modulation of Protein Sorption. ACS Applied Materials & Interfaces, Volume 11.

Manjua, A. C., Cabral, J. M. S., Ferreira, F. C. & Portugal, C. A. M., 2021. Magnetic Field Dynamic Strategies for the Improved Control of the Angiogenic Effect of Mesenchymal Stromal Cells. Polymers, Volume 13.

Manzini, B. M., Machado, L. M. R., Noritomi, P. Y. & Lopes de Silva, J. V., 2021. Advances in Bone tissue engineering: A fundamental review. Journal of Biosciences, Volume 46.

Marędziak, M. et al., 2017. Static magnetic field enhances the viability and proliferation rate of adipose tissue-derived mesenchymal stem cells potentially through activation of the

phosphoinositide 3-kinase/Akt (PI3K/Akt) pathway. Electromagnetic Biology and Medicine, Volume 36.

Markey, A. et al., 2016. Peptide hydrogel in vitro non-inflammatory potential. Journal of Peptide Science.

Martinez-Garcia, F. D. et al., 2021. Adipose Tissue-Derived Stromal Cells Alter the Mechanical Stability and Viscoelastic Properties of Gelatine Methacryloyl Hydrogels. International Journal of Molecular Sciences, Volume 22.

Martino, C. F. et al., 2010. Effects of Weak Static Magnetic Fields onEndothelial Cells. Bioeclectromagnetics, Volume 31.

Marycz, K., Kornicka, K. & Röcken, M., 2018. Static Magnetic Field (SMF) as a Regulator of Stem Cell Fate – New Perspectives in Regenerative Medicine Arising from an Underestimated Tool. Stem Cell Reviews and Reports, Volume 14.

Matsumoto, G. et al., 2012. Bone regeneration by polyhedral microcrystals from silkworm virus. Scientific Reports, Volume 2.

Matsumoto, G. et al., 2015. Polyhedral microcrystals encapsulating bone morphogenetic protein 2 improve healing in the alveolar ridge. Journal of Biomaterials Applications, 30(2).

Mattix, B. et al., 2014. Biological magnetic cellular spheroids as building blocks for tissue engineering. Acta Biomaterialia, 10(2).

Maurer Magnetic, 2025. Convert magnetic units. [Online]
Available at: https://maurermagnetic.com/en/demagnetizing/technology/convert-magnetic-units/

Ma, Y. et al., 2022. Osteogenic differentiation of the MSCs on silk fibroin hydrogel loaded Fe3O4@PAA NPs in static magnetic field environment. Colloids and Surfaces B: Biointerfaces, Volume 220.

Meinel, L. et al., 2004. Bone Tissue Engineering Using Human Mesenchymal Stem Cells: Effects of Scaffold Material and Medium Flow. Annals of Biomedical Engieering, 32(1), pp. 112-122.

Meng, H., Chowdhury, T. T. & Gavara, N., 2021. The Mechanical Interplay Between Differentiating Mesenchymal Stem Cells and Gelatin-Based Substrates Measured by Atomic Force Microscopy. Frontiers in Cell and Developmental Biology, Volume 9.

Miceil, V. et al., 2023. Different priming strategies improve distinct therapeutic capabilities of mesenchymal stromal/stem cells: Potential implications for their clinical use. World Journal of Stem Cells, 15(5).

Mndlovu, H., Kumar, P., du Toit, L. C. & Choonara, Y. E., 2024. A review of biomaterial degradation assessment approaches employed in the biomedical field. NPJ Materials Degradation, 8(66).

Mostafa, N. Z. et al., 2012. Osteogenic Differentiation of Human Mesenchymal Stem Cells Cultured with Dexamethasone, Vitamin D3, Basic Fibroblast Growth Factor, and Bone Morphogenetic Protein-2. Connective Tissue Research, Volume 53.

Mukasheva, F. et al., 2024. Optimizing scaffold pore size for tissue engineering: insights across various tissue types. Frontiers in Bioengineering and Biotechnology, Volume 12.

Nallusamy, J. & Das, R. K., 2021. Hydrogels and Their Role in Bone Tissue Engineering: An Overview. Journal of Pharmacy & BioAllied Sciences, Volume 13.

Nauth, A. et al., 2018. Critical-Size Bone Defects: Is There a Consensus for Diagnosis and Treatment?. Journal of Orthopaedic Trauma, Volume 32.

Nikukar, H. et al., 2013. Osteogenesis of Mesenchymal Stem Cells by Nanoscale Mechanotransduction. ACS Nano, 7(3).

Nowak, J., Wiekhorst, F., Trahms, L. & Odenbach, S., 2014. The influence of hydrodynamic diameter and core composition on the magnetoviscous effect of biocompatible ferrofluids. Journal of Physics: Condensed Matter, Volume 26.

Nowlan, N. et al., 2010. Mechanobiology of embryonic skeletal development: Insights from animal models. Birth Defects Research Part C: Embryo Today, p. doi.org/10.1002/bdrc.20184.

Ongaro, A. et al., 2014. Pulsed Electromagnetic Fields Stimulate Osteogenic Differentiation in Human BoneMarrow and Adipose Tissue DerivedMesenchymal Stem Cells. Bioelectromagnetics, Volume 25.

Oryan, A., Kamali, A., Moshiri, A. & Eslaminejad, M. B., 2017. Role of Mesenchymal Stem Cells in Bone Regenerative Medicine: What Is the Evidence?. Cells Tissues Organs, Volume 204.

Osugi, M. et al., 2012. Conditioned media from mesenchymal stem cells enhanced bone regeneration in rat calvarial bone defects. Tissue Engineering Part A, Volume 18.

Parekh, S. H. et al., 2011. Modulus-driven differentiation of marrow stromal cells in 3D scaffolds that is independent of myosin-based cytoskeletal tension. Biomaterials, 32(9).

Park, J. et al., 2011. The Effect of Matrix Stiffness on the Differentiation of Mesenchymal Stem Cells in Response to TGF-β. Biomaterials, 32(16).

Paun, I. A. et al., 2018. 3D Biomimetic Magnetic Structures for StaticMagnetic Field Stimulation of Osteogenesis. International Journal of Molecular Science, Volume 19.

Peffers, M. J., Milner, P. I. & Clegg, P. D., 2010. Regulation of SOX9 in normal and osteoarthritic equine articular chondrocytes by hyperosmotic loading. Osteoarthritis Cartilage, Volume 18.

Perez, J. R. et al., 2018. Tissue Engineering and Cell-Based Therapies for Fractures and Bone Defects. Frontiers in Bioengineering and Biotechnology, Volume 6.

Petecchia, L. et al., 2015. Electro-magnetic field promotes osteogenic differentiation of BM-hMSCs through a selective action on Ca2+-related mechanisms. Nature Scientific Reports, Volume 5.

Petit, I., Jin, D. & Rafii, S., 2007. The SDF-1–CXCR4 signaling pathway: a molecular hub modulating neo-angiogenesis. Trends in Immunology, 28(7).

Philip, S., Bulbule, A. & Kundu, G. C., 2004. Matrix metalloproteinase-2: Mechanism and regulation of NF-κB-mediated activation and its role in cell motility and ECM-invasion. Glycoconjugate, Volume 21, pp. 429-441.

Pimentel de Araujo, F. et al., 2021. Staphylococcus aureus clones causing osteomyelitis: a literature review (2000–2020). Journal of Global Antimicrobial Resistance, Volume 26, pp. 29-36.

Podhorská, B. et al., 2020. Revealing the True Morphological Structure of Macroporous Soft Hydrogels for Tissue Engineering. Applied Sciencies, 10(19), p. 6672.

Poliseno, L., Lanza, M. & Pandolfi, P. P., 2024. Coding, or non-coding, that is the question. Cell Research, Volume 34, pp. 609-629.

Presen, D. M., Traweger, A., Gimona, M. & Redl, H., 2019. Mesenchymal Stromal Cell-Based Bone Regeneration Therapies: From Cell Transplantation and Tissue Engineering to Therapeutic Secretomes and Extracellular Vesicles. Frontiers in Bioengineering and Biotechnology, Volume 7.

Prestwich, T. C. & MacDougald, O. A., 2007. Wnt/β-catenin signaling in adipogenesis and metabolism. Current Opinion in Cell Biology, 19(6).

PromoCell, 2026. Human Mesenchymal Stem Cells (hMSC). [Online]
Available at: https://promocell.com/uk_en/human-mesenchymal-stem-cells-hmsc.html?sku=C-12974
[Accessed 07 01 2026].

Rahman, M. S. et al., 2015. TGF-β/BMP signaling and other molecular events: regulation of osteoblastogenesis and bone formation. Bone Research, Volume 3.

Raicevic, G. et al., 2011. The source of human mesenchymal stromal cells influences their TLR profile as well as their functional properties. Cellular Immunology, 270(2), pp. 207-216.

Reginster, J.-Y. & Burlet, N., 2006. Osteoporosis: A still increasing prevalence. Bone.

Restrepo, R., Park, H. J. & Shreiber, V. M., 2014. Bacterial osteomyelitis in pediatric patients: a comprehensive review. Skeletal Radiology, Volume 53, pp. 2195-2210.

Ricarte, R. G. & Shanbhag, S., 2024. A tutorial review of linear rheology for polymer chemists: basics and best practices for covalent adaptable networks†. Polymer Chemistry, Volume 15, pp. 815-846.

Robert, A. W., Marcon, B. H., Dallagiovanna, B. & Shigunov, P., 2020. Adipogenesis, Osteogenesis, and Chondrogenesis of Human Mesenchymal Stem/Stromal Cells: A Comparative Transcriptome Approach. Frontiers in Cell and Development Biology, Volume 8.

Robertson, S. et al., 2018. Control of cell behaviour through nanovibrational stimulation: nanokicking. Philosophical Transactions of the Royal Society A: Mathematical, Physical and Engineering Sciences, Volume 376.

Rodriguez, A.-M.et al., 2005. The human adipose tissue is a source of multipotent stem cells. Biochimie, 87(1), pp. 125-128.

Romeo, S. et al., 2016. Lack of effects on key cellular parameters of MRC-5 human lung fibroblasts exposed to 370mT static magnetic field. Nature Scientific Reports, Volume 6.

Sadri, M. et al., 2017. Static Magnetic Field Effect on Cell Alignment, Growth, and Differentiation in Human Cord-Derived Mesenchymal Stem Cells. Cellular and Molecular Bioengineering, Volume 10.

Salama, A. M. et al., 2025. Injectable Hydrogel Technologies for Bone Disease Treatment. ACS Applied Bio Materials, 8(4).

Saleem, R. et al., 2021. Conditioned Medium from Bone Marrow Mesenchymal Stem Cells Restored Oxidative Stress-Related Impaired Osteogenic Differentiation. International Journal of Molecular Sciences, 22(24).

Schaller, V. et al., 2009. Effective magnetic moment of magnetic multicore nanoparticles. Physical Review B, Volume 80.

Schemitsch, E., 2017. Size Matters: Defining Critical in Bone Defect Size!. Journal of Orthopaedic Trauma, Volume 31.

Selvaraj, V., Sekaran, S., Dhanasekaran, A. & Warrier, S., 2024. Type 1 collagen: Synthesis, structure and key functions in bone mineralization. Differentiation.

Serguienko, A., Wang, M. Y. & Myklebost, O., 2018. Real-Time Vital Mineralization Detection and Quantification during In Vitro Osteoblast Differentiation. Bioloical Procedures Online, 20(14).

Shaikh, A. et al., 2023. Cell cycle regulators and bone: development and regeneration. Cell & Bioscience, Volume 13.

Shapourzadeh, A., Atyabi, S.-M., Irani, S. & Bakhshi, H., 2020. Osteoinductivity of polycaprolactone nanofibers grafted functionalized with carboxymethyl chitosan: Synergic effect of β-carotene and electromagnetic field. Internatinoal Journal of Biological Macromolecules, Volume 150.

Sharifi, S., Sharifi, H., Akbari, A. & Chodosh, J., 2021. Systematic optimization of visible light-induced crosslinking conditions of gelatin methacryloyl (GelMA). Scientific Reports, Volume 11, p. 23276.

Sharma, U. N., Ostrovidov, S., Datta, S. & Kaji, H., 2015. Overview of Magnetic Hydrogel Fabrication, Its Basic Characteristics, and Potential Uses in Biomedical Engineering. Bioengineering, 12(11), p. 1142.

Shea, J. E. & Miller, S. C., 2005. Skeletal function and structure: Implications for tissue-targeted therapeutics. Advanced Drug Delivery Reviews, Volume 57, p. doi.org/10.1016/j.addr.2004.12.017.

Sheng, G., 2015. The developmental basis of mesenchymal stem/stromal cells (MSCs). BMC Developmental Biology, Volume 15.

Shi, H. et al., 2022. A Review Into the Insights of the Role of Endothelial Progenitor Cells on Bone Biology. Frontiers in Cell and Developmental Biology, Volume 10.

Shirley, R., Fazekas, J., McNally, M. & Ramsden, A., 2018. Costs and renumeration of osteomyelitis treatment involving free flaps: implications of return to theatre. Journal of Bone and Joint Infection, Volume 3.

Shuai, C. et al., 2020. Magnetically actuated bone scaffold: Microstructure, cell response and osteogenesis. Composites Part B: Engineering, Issue 192.

Shuai, C. et al., 2018. Physical stimulations and their osteogenesis-inducing mechanisms. International Journal of Bioprinting, 4(2).

Sia, I. G. & Berbari, E. F., 2006. Osteomyelitis. Best Practice & Research Clinical Rheumatology, 20(6), pp. 1065-1081.

Silva, E. D. et al., 2018. Multifunctional magnetic-responsive hydrogels to engineer tendon-to-bone interface. Nanomedicine: Nanotechnology, Biology and Medicine, 14(7).

Singh, D. et al., 2015. Bench-to-bedside translation of magnetic nanoparticles. Nanomedicine, 9(4), pp. 501-516.

Singh, N., Jenkins, G. J. S., Asadi, R. & Doak, S. H., 2010. Potential toxicity of superparamagnetic iron oxide nanoparticles (SPION). Nano Reviews, 1(1), p. 5358.

Singh, R. K. et al., 2023. Coordinated Biophysical Stimulation of MSCs via Electromagnetized Au-Nanofiber Matrix Regulates Cytoskeletal-to-Nuclear Mechanoresponses and Lineage Specification. Advanced Functional Materials, Volume 33.

Song, J. et al., 2024. Alteration in cartilage matrix stiffness as an indicator and modulator of osteoarthritis. Bioscience Reports, 44(1).

Song, K. et al., 2024. Pulsed electromagnetic fields potentiate bone marrow mesenchymal stem cell chondrogenesis by regulating the Wnt/β-catenin signaling pathway. Journal of Translational Medicine.

Stetfeld, J., McKenna, S. A. & Patel, T. R., 2016. Dynamic light scattering: a practical guide and applications in biomedical sciences. Biophysical Reviews, Volume 8.

Steward, A. J. & Kelly, D. J., 2014. Mechanical regulation of mesenchymal stem cell differentiation. Journal of Anatomy, 227(6).

Sun, X. & Kaufman, P. D., 2018. Ki-67: more than a proliferation marker. Chormosoma, Volume 127, pp. 175-186.

Su, N. et al., 2019. Bone function, dysfunction and its role in diseases including critical illness. International Journal of Biological Sciences, 15(4), p. doi: 10.7150/ijbs.27063.

Sun, Y. et al., 2023. A static magnetic eld enhances the repair of osteoarthritic cartilage by promoting the migration of stem cells and chondrogenesis. Jounral of Orthopaedic Translation, Volume 39.

Sun, Y. et al., 2022. Mechanical Stimulation on Mesenchymal Stem Cells and Surrounding Microenvironments in Bone Regeneration: Regulations and Applications. Frontiers in Cell and Developmental Biology, Volume 10.

Taichman, R. S., 2005. Blood and bone: two tissues whose fates are intertwined to create. The American Society of Hematology.

Takeuchi, R., Katagiri, W., Endo, S. & Kobayashi, T., 2019. Exosomes from conditioned media of bone marrow-derived mesenchymal stem cells promote bone regeneration by enhancing angiogenesis. PLOS One.

Tang, J., Wang, X., Lin, X. & Wu, C., 2024. Mesenchymal stem cell-derived extracellular vesicles: a regulator and carrier for targeting bone-related diseases. Cell Death Discovery, Volume 10.

Tang, S. et al., 2024. Nanocomposite magnetic hydrogel with dual anisotropic properties induces osteogenesis through the NOTCH-dependent pathways. NPG Asia Materials, Volume 16.

Testa, S. et al., 2020. Skeletal Muscle-Derived Human Mesenchymal Stem Cells: Influence of Different Culture Conditions on Proliferative and Myogenic Capabilities. Frontiers in Physiology, Volume 11.

Theus, A. S. et al., 2022. 3D bioprinting of nanoparticle-laden hydrogel scaffolds with enhanced antibacterial and imaging properties. iScience, 25(9).

Thorat, N. D. et al., 2013. Enhanced colloidal stability of polymer coated La0.7Sr0.3MnO3 nanoparticles in physiological media for hyperthermia application. Colloids and Surfaces B: Biointerfaces, Volume 111, pp. 264-269.

Tran, K. A. et al., 2021. Dynamic Tuning of Viscoelastic Hydrogels with Carbonyl Iron Microparticles Reveals the Rapid Response of Cells to ThreeDimensional Substrate Mechanics. ACS Applied Materials & Interfaces, Volume 13.

Tsai, H.-H.et al., 2019. The Effects of Different Dynamic Culture Systems on Cell Proliferation and Osteogenic Differentiation in Human Mesenchymal Stem Cells. International Journal of Molecular Sciences, Volume 20.

Turinetto, V., Vitale, E. & Giachino, C., 2016. Senescence in Human Mesenchymal Stem Cells: Functional Changes and Implications in Stem Cell-Based Therapy. Internatinal Journal of Molecular Sciences, Volume 17.

Turnbull, G. et al., 2018. 3D bioactive composite scaffolds for bone tissue engineering. Bioactive Materials, 3(3).

Varani, K. et al., 2021. Pulsed Electromagnetic Field Stimulation in Osteogenesis and Chondrogenesis: Signaling Pathways and Therapeutic Implications. International Journal of Molecular Sciences, 22(809).

Velasco-Rodriquez, B. et al., 2021. Hybrid Methacrylated Gelatin and Hyaluronic Acid Hydrogel Scaffolds. Preparation and Systematic Characterization for Prospective Tissue Engineering Applications. International Journal of Molecular Sciences, 22(13).

Viswanathan, S. et al., 2019. Mesenchymal stem versus stromal cells: International Society for Cell & Gene Therapy (ISCT®) Mesenchymal Stromal Cell committee position statement on nomenclature. Cytotherapy, 21(10), pp. 1019-1024.

Vogel, R. et al., 2016. A standardized method to determine the concentration of extracellular vesicles using tunable resistive pulse sensing. Journal of Extracellular Vesicles, 5(1), p. 31242.

Wang, C. et al., 2020. 3D printing of bone tissue engineering scaffolds. Bioactive Materials, 5(1).

Wang, C., Min, S. & Tian, Y., 2023. Injectable and Cell-Laden Hydrogel in the Contained Bone Defect Animal Model: A Systematic Review. Tissue Engineering and Regenerative Medicine, Volume 20.

Wang, J. et al., 2016. Inhibition of Viability, Proliferation, Cytokines Secretion, Surface Antigen Expression, and Adipogenic and Osteogenic Differentiation of Adipose-Derived Stem Cells by Seven-Day Exposure to 0.5 T Static Magnetic Fields. Stem Cells International.

Wang, L. et al., 2022. Mild hyperthermia-mediated osteogenesis and angiogenesis play a critical role in magnetothermal composite-induced bone regeneration. Nanotoday, Volume 43.

Wang, S. et al., 2024. Magnetocaloric-Responsive Hydrogel Nanoarchitectonics for Pyroptosis-Relay-Immunotherapy to Suppress Post-Operation Tumor Recurrence and Metastasis. Advanced Functional Materials, 34(22), p. 231494.

Wang, W. & Yeung, K. W. K., 2017. Bone grafts and biomaterials substitutes for bone defect repair: A review. Bioactive Materials.

Whitehead, J. et al., 2021. Hydrogel mechanics are a key driver of bone formation by mesenchymal stromal cell spheroids. Biomaterials, Volume 269.

Whitty, C. et al., 2022. Sustained delivery of the bone morphogenetic proteins BMP-2 and BMP-7 for cartilage repair and regeneration in osteoarthritis. Osteoarthritis and Cartilage Open, 4(1).

Wong, A., Ghassemi, E. & Yellowley, C. E., 2014. Nestin expression in mesenchymal stromal cells: regulation by hypoxia and osteogenesis. BMC Veterinary Research, Volume 10.

World Health Organization, 2023. Osteoarthritis. [Online]
Available at: https://www.who.int/news-room/fact-sheets/detail/osteoarthritis
[Accessed August 2024].

Wu, B. et al., 2022. A narrative review of diabetic bone disease: Characteristics, pathogenesis, and treatment. Frontiers in Endocrinology, Volume 13, p. doi.org/10.3389/fendo.2022.1052592.

Wu, D. et al., 2021. Bone mesenchymal stem cells stimulation by magnetic nanoparticles and a static magnetic field: release of exosomal miR-1260a improves osteogenesis and angiogenesis. Journal of Nanobiotechnology, Volume 19.

Wu, E. et al., 2024. Application of gelatin-based composites in bone tissue engineering. Heliyon, 10(16).

Wu, H. et al., 2022. Static Magnetic Fields Regulate T-Type Calcium Ion Channels and Mediate Mesenchymal Stem Cells Proliferation. Cells, Volume 11.

Xiang, C. et al., 2022. A Porous Hydrogel with High Mechanical Strength and Biocompatibility for Bone Tissue Engineering. Functional Biomaterials, 13(3).

Xiao, S. et al., 2019. Gelatin Methacrylate (GelMA)-Based Hydrogels for Cell Transplantation: an Effective Strategy for Tissue Engineering. Stem Cell Reviews and Reports, Volume 15, pp. 664-679.

Xia, Y. et al., 2018. Magnetic field and nano-scaffolds with stem cells to enhance bone regeneration. Biomaterials, Volume 183.

Xie, L., Zeng, X., Hu, J. & Chen, Q., 2015. Characterization of Nestin, a Selective Marker for Bone Marrow Derived Mesenchymal Stem Cells. Stem Cells International, 2015(1).

Xuan, X. et al., 2025. Three-Dimensional Printable Magnetic Hydrogels with Adjustable Stiffness and Adhesion for Magnetic Actuation and Magnetic Hyperthermia Applications. Gels, 11(1).

Xu, C. et al., 2020. Endothelial progenitor cells promote osteogenic differentiation in co-cultured with mesenchymal stem cells via the MAPK-dependent pathway. Stem Cell Research & Therapy, Volume 11.

Xu, C. et al., 2024. Bone tissue engineering scaffold materials: Fundamentals, advances, and challenges. Chinese Chemical Letters, Volume 35.

Xu, C. et al., 2024. Delivery of miR-15b-5p via magnetic nanoparticle-enhanced bone marrow mesenchymal stem cell-derived extracellular vesicles mitigates diabetic osteoporosis by targeting GFAP. Cell Biology and Toxicity, Volume 40.

Xue, N. et al., 2022. Bone Tissue Engineering in the Treatment of Bone Defects. Pharmaceuticals, 15(7).

Xue, X., Hu, Y., Deng, Y. & Su, J., 2021. Recent Advances in Design of Functional Biocompatible Hydrogels for Bone Tissue Engineering. Advanced Functional Materials, Volume 31.

Xu, F. et al., 2012. Release of Magnetic Nanoparticles from Cell-Encapsulating Biodegradable Nanobiomaterials. ACS Nano, 6(8).

Xu, L. et al., 2017. Tissue source determines the differentiation potentials of mesenchymal stem cells: a comparative study of human mesenchymal stem cells from bone marrow and adipose tissue. Stem Cell Research & Therapy, 8(275).

Yang, H.-W.et al., 2024. A Printable Magnetic-Responsive Iron Oxide Nanoparticle (ION)-Gelatin Methacryloyl (GelMA) Ink for Soft Bioactuator/Robot Applications. Polymers, 16(1).

Yang, Q., Liu, R. & Wang, X., 2025. Engineering Marrow-Mimetic Hydrogel Platforms Enhance Erythropoiesis: A Mechanobiology-Driven Approach for Transfusion Red Blood Cell Production. Gels, 11(8).

Yang, W. et al., 2016. Surface topography of hydroxyapatite promotes osteogenic differentiation of human bone marrow mesenchymal stem cells. Materials Science and Engineering: C, Volume 60.

Yan, K. et al., 2025. Unveiling distinctions between mesenchymal stromal cells and stem cells by single-cell transcriptomic analysis. Heliyon, 11(e42311).

Yan, T. et al., 2021. Magnetic nanocomposite hydrogel with tunable stiffness for probing cellular responses to matrix stiffening. Acta Biomaterialia, Volume 138.

Yen, M.-H., Chen, Y.-H., Liu, Y.-S. & Lee, O. K.-S., 2020. Alteration of Young's modulus in mesenchymal stromal cells during osteogenesis measured by atomic force microscopy. Biochemical and Biohysical Research Communications, Volume 526.

Yi, B., Xu, Q. & Liu, W., 2022. An overview of substrate stiffness guided cellular response and its applications in tissue regeneration. Bioactive Materials, Volume 15.

Yin, Y. et al., 2018. The Effects of a Pulsed Electromagnetic Field on the Proliferation and Osteogenic Differentiation of Human Adipose-Derived Stem Cells. Medical Science Monitor, Volume 24.

Young, D. A., Choi, Y. S., Engler, A. J. & Christman, K. L., 2014. Stimulation of adipogenesis of adult adipose-derived stem cells using substrates that mimic the stiffness of adipose tissue. Biomaterials, Volume 34.

Yuan, Z. et al., 2018. Development of a 3D Collagen Model for the In Vitro Evaluation of Magnetic-assisted Osteogenesis. Nature Scientific Reports, Volume 8.

Yu, C.-F.et al., 2017. Dual roles of tumour cells-derived matrix metalloproteinase 2 on brain tumour growth and invasion. Molecular Diagnostics, Volume 117, pp. 1828-1836.

Yue, K. et al., 2015. Synthesis, properties, and biomedical applications of gelatin methacryloyl (GelMA) hydrogels. Biomaterials, Volume 72.

Yue, S., He, H., Li, B. & Hou, T., 2020. Hydrogel as a Biomaterial for Bone Tissue Engineering: A Review. Nanomaterials, 10(8).

Yue, Z.-G.et al., 2011. Surface Charge Affects Cellular Uptake and Intracellular Trafficking of Chitosan-Based Nanoparticles. Biomacromolecules, 12(7).

Yun, H.-M.et al., 2016. Magnetic nanocomposite scaffolds combined with static magnetic field in the stimulation of osteoblastic differentiation and bone formation. Biomaterials, Volume 85.

Yu, S. J. et al., 2020. Three-Dimensional Spheroid Culture on Polymer-Coated Surface Potentiate Stem Cell Functions via Enhanced Cell–Extracellular Matrix Interactions. ACS Biomaterials Science and Engineering, 6(4).

Yusuf, F. & Brand-Saberi, B., 2012. Myogenesis and muscle regeneration. Histochemistry and Cell Biology, Volume 138.

Zennifer, A. et al., 2023. 3D bioprinting and photocrosslinking: emerging strategies & future perspectives. Biomaterials Advances, Volume 134, p. 112576.

Zhang, H. et al., 2018. Moderate-intensity 4 mT static magnetic fields prevent bone architectural deterioration and strength reduction by stimulating bone formation in streptozotocin-treated diabetic rats. Bone, Volume 107.

Zhang, K. et al., 2023. Static Magnetic Field Promotes Proliferation, Migration, Differentiation, and AKT Activation of Periodontal Ligament Stem Cells. Cells Tissues Organs, Volume 212.

Zhang, L. et al., 2025. Sonic Hedgehog potentiates BMP9-induced osteogenic differentiation of mesenchymal stem cells. Genes & Diseases, 12(3).

Zhang, L., Yang, G., Johnson, B. N. & Jia, X., 2019. Three-dimensional (3D) printed scaffold and material selection for bone repair. Acta Biomaterialia, Volume 84.

Zhang, N., Lock, J., Sallee, A. & Liu, H., 2015. Magnetic Nanocomposite Hydrogel for Potential Cartilage Tissue Engineering: Synthesis, Characterization, and Cytocompatibility with Bone Marrow Derived Mesenchymal Stem Cells. ACS Applied Materials & Interfaces, Volume 7.

Zhang, Y. et al., 2018. Extremely low frequency electromagnetic fields promote mesenchymal stem cell migration by increasing intracellular Ca2+ and activating the FAK/Rho GTPases signaling pathways in vitro. Stem Cell Research & Therapy, Volume 9.

Zheng, L. et al., 2018. Static magnetic field regulates proliferation, migration, differentiation, and YAP/TAZ activation of human dental pulp stem cells. Journal of Tissue Engineering and Regenerative Medicine, Volume 12.

Zhou, B. et al., 2023. GelMA-based bioactive hydrogel scaffolds with multiple bone defect repair functions: therapeutic strategies and recent advances. Biomaterials Research, 15(27).

Zhou, N. et al., 2016. BMP2 induces chondrogenic differentiation, osteogenic differentiation and endochondral ossification in stem cells. Cell & Tissue Researcher, Volume 366.

Zhou, P. et al., 2021. Establishing a deeper understanding of the osteogenic differentiation of monolayer cultured human pluripotent stem cells using novel and detailed analyses. Stem Cell Research & Therapy, 12(41).

Zhu, G. et al., 2021. Bone physiological microenvironment and healing mechanism: Basis for future bone-tissue engineering scaffolds. Bioactive Materials, 6(11).

Zhu, S., Chen, W., Masson, A. & Li, Y.-P., 2024. Cell signaling and transcriptional regulation of osteoblast lineage commitment, differentiation, bone formation, and homeostasis. Cell Discovery, Volume 10.

Zhu, Y. et al., 2023. Bioprinted PDLSCs with high concentration GelMA hydrogels exhibit enhanced osteogenic differentiation in vitro and promote bone regeneration in vivo. Clinical Oral Investigations, Volume 27.